

UCSF

UC San Francisco Electronic Theses and Dissertations

Title

Silicon Membranes for Extracorporeal Membrane Oxygenation (ECMO)

Permalink

<https://escholarship.org/uc/item/4qr8v9cz>

Author

Abada, Emily

Publication Date

2019

Peer reviewed|Thesis/dissertation

Silicon Membranes for Extracorporeal Membrane Oxygenation (ECMO)

by
Emily Abada

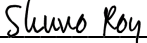
DISSERTATION
Submitted in partial satisfaction of the requirements for degree of
DOCTOR OF PHILOSOPHY

in
Bioengineering

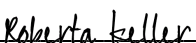
in the
GRADUATE DIVISION

of the
UNIVERSITY OF CALIFORNIA, SAN FRANCISCO
AND
UNIVERSITY OF CALIFORNIA, BERKELEY

Approved:

DocuSigned by:
 Shuvo Roy
C1B7512AE288433... Chair

DocuSigned by:
 Phillip Messersmith
C15846A65D784FC... Phillip Messersmith

DocuSigned by:
 Roberta Keller
C15846A65D784FC... Roberta Keller

Committee Members

Copyright 2019

by

Emily Abada

This dissertation is dedicated to my parents Laura and David Abada, my siblings Sharon and Benjamin

Abada, and Brian Archer - אני לדודי ודודי לי.

ACKNOWLEDGMENTS

In my time as a graduate student, I have had the honor to work with many inspiring scientists and engineers, and to grow as a bioengineer and as a person. It has been a fulfilling journey to pursue such interesting and meaningful research, surrounded by supportive colleagues and friends. I am grateful to all the people who have been around me and encouraged me throughout this part of my life.

First, I am immensely grateful to my advisor, Professor Shuvo Roy, for being a constant source of guidance, support, and encouragement. As a mentor, I am thankful to have trained under someone so inspired and innovative as an engineer, who always motivated me to learn and advance myself. Under Dr. Roy's guidance, I have grown so much as an individual. His confidence, positivity, creativity, and intellect are qualities I aspire to manifest in my future, as I continue to pursue my personal and professional growth. Beyond being my principal investigator, I truly could not have done so much without his compassion and support of me throughout my time as his student.

Here at UCSF, I have gotten to know many scientists, engineers, and clinicians who have inspired and influenced my research through their unique perspectives. I would like to thank the members of my thesis committee – Professor Phillip Messersmith and Dr. Roberta Keller – for their support and advice on my research. I am grateful to have had the opportunity to learn from their expertise. Throughout my project, I have also learned much from the clinical fellows on the oxygenator team, who see and treat ECMO patients day-to-day. Working with Drs. Ajay Dharia and David Blauvelt has brought me meaningful perspective on how to think of medical technology and the patients who receive our therapies. It has also been an exciting adventure to collaborate with Colin Yee at UCSF. His intellectual curiosity and drive have pushed me forward into fascinating scientific directions I would not have endeavored alone. Among all my colleagues, I would especially like to thank Deepika Sarode – the most dedicated and genuine undergraduate student who I am also happy to call a friend. It has been a privilege to mentor her and be a part of her journey, as she has become an accomplished scientist in her own right.

The Roy Lab has been a welcoming and supportive environment, full of people who are motivated to do good and help others around them. Members of the Roy Lab are always there to lend a hand, give advice or constructive feedback, and bring their unique talents to collaborate with others. My labmates have been there through many rough moments, and also to celebrate the good times. It has been fulfilling to get to know them as professional scientists, and as individuals. My life as a graduate student would not have been complete without my fellow Roy Lab graduates and dear friends Drs. Zohora Iqbal, Aishwarya Jayagopal, and Shang Song. All of you made me feel so welcome in the lab (and away from it), and I feel lucky to have crossed paths in graduate school. Some of my favorite times in the last few years were when we all were taking a tea break, having a deep chat over some coffee, or heading out to get the best ice cream in San Francisco.

I wish to thank those in my personal life who have supported me with unconditional love throughout my education. I am always grateful for my parents Laura and David Abada, and my siblings Sharon and Benjamin Abada, for their encouragement and motivation to continue. I am also thankful for the love and support of my longtime friends Kimia Sohrabi, Lida Wang, and Isaac Lu, who have always been caring and empathetic in both good and bad moments. Finally, I am truly grateful for the love, endless kindness, and understanding of my husband Brian Archer. I would like you all to know how honored I am to have so many inspirational and caring people in my life who have stood by me throughout this time.

The following dissertation includes previously published work, and the coauthors of these publications deserve recognition.

Artificial Organs, 2017;42(2):166-173

Biomedical Microdevices, 2018;20:86

ABSTRACT

Silicon Membranes for Extracorporeal Membrane Oxygenation (ECMO)

by

Emily Abada

In cases of severe lung or heart failure, extracorporeal membrane oxygenation (ECMO) is a life-saving therapy in which a patient's blood is passed into a circuit outside of their body to provide respiratory support. The circuit's main component is the membrane oxygenator that drives oxygen into the blood from a sweep gas source and removes excess carbon dioxide from the blood. At present, clinical use of ECMO is limited by its high risk profile, owing to two intertwined risks: thrombosis from the large circuit, and bleeding from the anticoagulation needed to prevent thrombosis. Improvements to the gas exchange efficiency and hemocompatibility of the oxygenator could enable the development of a longer-term supportive ECMO therapy, intended as a bridge-to-transplant or destination therapy for chronic lung failure. Here we describe a novel blood oxygenator concept based on parallel plate silicon membranes developed for high precision geometry, mechanical rigidity, and high efficiency membrane transport. Using these membranes, we create blood oxygenator prototypes consisting of arrays of silicon membranes, and endeavor to improve the efficiency and hemocompatibility of this concept.

First, multiple types of silicon membranes were evaluated systematically for mechanical rigidity and oxygen exchange efficiency, indicators of suitability for a future oxygenator. The combination of a silicon micropore membrane (S μ M) and a 5 μ m-thick polydimethylsiloxane (PDMS) layer maximized both qualities, withstanding over 260 cmHg of applied pressure and producing 0.03 mL/min of O₂ flux. These membranes were then assembled into prototype flow cells, and tested for *in vitro* and *in vivo* oxygenation, successfully yielding an oxygen permeability of 1.92 ± 1.04 ml O₂ STP/min/m²/cmHg. From this benchmark, we then attempted to optimize the surface hemocompatibility of the Si-PDMS

composite through application of multiple polyethylene glycol (PEG)-based coatings. Although successful application of PEG to the surfaces was demonstrated, none of the coatings appeared to reduce protein adhesion to the S μ M -PDMS membranes. Finally, we inserted turbulence-inducing spacer meshes into the channels of the S μ M-PDMS prototypes to disrupt the transport boundary layer adjacent to the membranes, with the goal of substantially improving oxygenation. Though a threefold increase in oxygen flux was observed *in vitro* with the spacer meshes, the disruptive turbulence resulted in thrombosis and channel occlusion within the channels despite heavy anticoagulation of the blood. In summary, the work in this dissertation demonstrates the successful construction and testing of S μ M-PDMS oxygenator prototypes, laying the foundation for future work to optimize this concept and create a large-scale blood oxygenator that can expand the clinical use of this life-saving therapy.

TABLE OF CONTENTS

CHAPTER 1 ECMO OXYGENATOR DEVELOPMENT – LOOKING TOWARDS THE FUTURE OF RESPIRATORY SUPPORT.....	1
1.1 INTRODUCTION	1
1.2 NEEDS FOR DESIGNING AN OXYGENATOR	4
1.2.1 Hemocompatibility/Anticoagulation	4
1.2.2 Gas Exchange Efficiency/Portability	8
1.3 CURRENT ECMO OXYGENATOR DESIGNS	12
1.3.1 Standard of Care: Hollow Fiber Oxygenators.....	12
1.3.2 Hollow Fiber Derivatives	15
1.3.2.1 ECCO ₂ R.....	15
1.3.2.2 Pumpless ECMO (Novalung)	16
1.4 CURRENT RESEARCH DIRECTIONS.....	17
1.4.1 Improvements to Hollow Fiber Devices	17
1.4.2 Microfluidic Artificial Lungs	20
1.5 SILICON MEMBRANE OXYGENATOR.....	25
1.6 RESEARCH OBJECTIVE	30
CHAPTER 2 EVALUATION OF SILICON MEMBRANES FOR EXTRACORPOREAL MEMBRANE OXYGENATION (ECMO).....	31
2.1 INTRODUCTION	31
2.2 MATERIALS AND METHODS	32
2.2.1 Membrane Fabrication	32
2.2.2 Failure Point Testing	38

2.2.3	Oxygen Flux and Permeability <i>In Vitro</i>	40
2.3	RESULTS AND DISCUSSION.....	42
2.3.1	Failure Point Testing.....	42
2.3.2	Oxygen Flux and Permeability <i>In Vitro</i>	44
2.4	CONCLUSION	49
CHAPTER 3 SILICON MICROPORE-BASED PARALLEL PLATE MEMBRANE		
OXYGENATOR		
50		
3.1	INTRODUCTION.....	50
3.2	MATERIALS AND METHODS	51
3.2.1	Fabrication of the Silicon-PDMS Membrane and Flow Cell.....	51
3.2.2	Oxygen Diffusion Through Membranes	52
3.2.3	Blood Oxygenation in an <i>In Vivo</i> Porcine Model	54
3.2.4	Model Formulation.....	56
3.3	RESULTS.....	57
3.3.1	Membrane Fabrication	57
3.3.2	Oxygen Diffusion of the Membranes.....	59
3.3.3	Blood Oxygenation in an <i>In Vivo</i> Porcine Model	59
3.4	DISCUSSION.....	61
CHAPTER 4 PEG-SILANE COATING VARIATIONS ON SILICON AND PDMS FOR		
IMPROVED HYDROPHILICITY		
64		
4.1	INTRODUCTION	64
4.2	MATERIALS AND METHODS	66
4.2.1	Silane Application.....	66

4.2.1.1	Substrates.....	66
4.2.1.2	PEG-Silane Application.....	67
4.2.2	Analysis of Silane Layers.....	69
4.2.2.1	Contact Angle	69
4.2.2.2	ELISA	69
4.2.2.3	Ellipsometry.....	70
4.2.2.4	AFM.....	71
4.2.2.5	Statistical Analysis.....	71
4.3	RESULTS.....	72
4.3.1	Contact Angle.....	72
4.3.2	ELISA.....	73
4.3.3	Ellipsometry	74
4.3.4	AFM	75
4.4	DISCUSSION.....	77
4.5	CONCLUSION	82
CHAPTER 5 IMPROVED OXYGENATION VIA TURBULENT BOUNDARY LAYER		
DISRUPTION		
84		
5.1	INTRODUCTION.....	84
5.2	MATERIALS AND METHODS	87
5.2.1	Silicon Membrane Design.....	87
5.2.2	Spacers	88
5.2.3	Oxygenator Device Design and Assembly.....	89
5.2.4	Oxygen Flux and Pressure Drop <i>In Vitro</i>	90

5.2.5	Hemocompatibility <i>In Vivo</i>	91
5.2.6	Scanning Electron Microscopy (SEM)	94
5.3	RESULTS AND DISCUSSION.....	95
5.3.1	Oxygen Flux and Pressure Drop <i>In Vitro</i>	95
5.3.2	Hemocompatibility <i>In Vivo</i>	101
5.3.3	Examination of Devices	104
5.3.4	Scanning Electron Microscopy (SEM)	106
5.4	CONCLUSION	107
CHAPTER 6 CONCLUSIONS AND FUTURE DIRECTIONS		109
APPENDIX.....		113
A.1. FUNCTIONAL OXYGENATOR COATINGS FOR IMPROVED GAS		
EXCHANGE AND HEMOCOMPATIBILITY.....		113
A.1.1	INTRODUCTION.....	113
A.1.2	MATERIALS AND METHODS	116
A.1.2.1	Substrates and Precursor Coatings	116
A.1.2.1.1	Substrates	116
A.1.2.1.2	Aminosilane Precursor Application.....	116
A.1.2.1.3	Poly(acrylic acid) (PAA) Immobilization.....	117
A.1.2.2	Secondary Reactions.....	118
A.1.2.2.1	Hyaluronic Acid Application.....	118
A.1.2.2.2	L-Histidine and Lysine Attachment to PAA.....	118
A.1.2.3	Coating Characterization	119
A.1.2.3.1	Contact Angle – Wettability	119

A.1.2.4	Gas Permeability and Hemocompatibility Evaluation	120
A.1.2.4.1	Oxygen Flux <i>In Vitro</i>	120
A.1.2.4.2	<i>In Vivo</i> Gas Exchange and Hemocompatibility	122
A.1.2.4.3	Scanning Electron Microscopy (SEM)	127
A.1.2.4.4	Platelet Immunohistochemistry (IHC)	128
A.1.2.4.5	Statistical Analysis	128
A.1.3	RESULTS	129
A.1.3.1	Coating Characterization	129
A.1.3.1.1	Contact Angle	129
A.1.3.2	Gas Permeability and Hemocompatibility Evaluation	132
A.1.3.2.1	Oxygen Permeability <i>In Vitro</i>	132
A.1.3.2.2	<i>In Vivo</i> Gas Permeability and Hemocompatibility	137
A.1.3.2.3	Scanning Electron Microscopy (SEM)	143
A.1.3.2.4	Platelet Immunohistochemsitry (IHC)	145
A.1.4	DISCUSSION	146
A.1.5	CONCLUSION	150
A.2.	IN VIVO GAS EXCHANGE THROUGH OXYGENATOR PROTOTYPES	151
A.2.1	INTRODUCTION	151
A.2.2	METHODS	151
A.2.2.1	Oxygen Flux and Pressure Drop <i>In Vitro</i>	151
A.2.2.2	Gas Exchange and Hemocompatibility <i>In Vivo</i>	152
A.2.2.3	Scanning Electron Microscopy (SEM)	153
A.2.2.4	Statistical Analysis	154

A.2.3	RESULTS.....	154
A.2.3.1	Oxygen Flux and Pressure Drop <i>In Vitro</i>	154
A.2.3.2	Gas Exchange and Hemocompatibility <i>In Vivo</i>	155
A.2.3.3	Scanning Electron Microscopy (SEM).....	158
A.2.4	DISCUSSION.....	159
	REFERENCES.....	161

LIST OF FIGURES

Fig. 1.1: Diagram of ECMO operation in veno-arterial (VA) configuration.....	2
Fig. 1.2: Schematic of oxygen and carbon dioxide exchange through an ECMO oxygenator.....	4
Fig. 1.3: Current generation of hollow fiber oxygenators	13
Fig. 1.4: Examples of improvements to hollow fiber membrane gas exchange devices	18
Fig. 1.5: Microfluidic blood oxygenator schematics and actualizations	21
Fig. 1.6: Silicon membranes for artificial organ devices, highlighted for use as ECMO membranes	25
Fig. 2.1: Fabrication of SNM membranes	33
Fig. 2.2: Fabrication of $S_{\mu}M$ (a-d), and application of PDMS (e-g) to form $S_{\mu}M$ -PDMS.....	35
Fig. 2.3: SEM images of membranes.....	37
Fig. 2.4: Diagram of bubble/rupture point testing setup.....	39
Fig. 2.5: Schematic of <i>in vitro</i> oxygen permeability testing setup	42
Fig. 2.6: Bubble or rupture points of silicon membranes related to pore size	43
Fig. 2.7: Plots of (a) oxygen flux and (b) pore area-normalized mass transfer coefficient from silicon membranes downselected from bubble point experiments.	45
Fig. 2.8: SNM flux measurements plotted against continuum flow and Knudsen flow predictions.	47
Fig. 3.1: Schematic of the fabrication of the silicon micropore membranes (1a) and of the PDMS transfer process (1b) to achieve 3-5 micron thick PDMS layer bonded to the silicon micropore membranes.	52
Fig. 3.2: Diagram (a) and picture (b) of experimental setup to measure oxygen diffusion into water.....	54

Fig. 3.3: The S μ M membrane was fabricated with the windows of pores as seen under bright field and individual pores as seen by SEM imaging (a and b).....	58
Fig. 3.4: O ₂ permeability for three separate flow cells \pm SD.....	60
Fig. 3.5: Picture of flow cell with top and bottom half of the blood flow path exposed after <i>in vivo</i> test.	60
Fig. 3.6 Comparison of model output with experimental water data (a) and experimental blood data (b) showing the partial pressure of oxygen at a particular water or blood flow rate at a certain sweep gas pressure before and after (both experimentally and model-predicted) the device.	61
Fig. 4.1: Substrates for functionalization with PEG-silane.....	67
Fig. 4.2: Characterization methods of PEG-silane surfaces	70
Fig. 4.3: Contact angle of PEG-silane on (a) Si, (b) Si-PDMS, and (c) PDMS	73
Fig. 4.4: Albumin fouling ELISA results for (a) Si, (b) Si-PDMS, and (c) PDMS.....	74
Fig. 4.5: Ellipsometry results on Si substrates.....	75
Fig. 4.6: AFM topographic scans of 3 μ m x 3 μ m spots on (a) Si, (b) Si-PDMS, and (c) PDMS substrates.....	76
Fig. 5.1: Coarse and fine spacer meshes cut to fit in flow cell channels	88
Fig. 5.2: Design views of oxygenator flow cell with spacers	90
Fig. 5.3: Schematic of gas permeability testing setup, showing a spacer insert in one half of the flow cell.	91
Fig. 5.4: <i>In vivo</i> testing of S μ M-PDMS devices with spacers.	94
Fig. 5.5: (a) Transoxygenator pressure and (b) area-normalized flux of oxygenator with and without spacers.....	95

Fig. 5.6: <i>In vivo</i> flux of O ₂ and CO ₂ in device without spacers	102
Fig. 5.7: Disassembled flow cells (a-c) and spacer meshes (d) after blood exposure	104
Fig. 5.8: Example SEM micrographs of S _μ M post-blood exposure, taken at 500X magnification.	106
Fig. A. 1.1: <i>In vitro</i> testing methods for biomolecule-coated membranes	119
Fig. A. 1.2: Assembly of 4-membrane parallel plate flow cell used for <i>in vitro</i> and <i>in vivo</i> testing	122
Fig. A. 1.3: Set up of <i>in vivo</i> gas exchange circuits for experiments 1 and 2.....	124
Fig. A. 1.4: Contact angle of biomolecule coatings on Si-PDMS membranes and Si and PDMS materials controls for Experiment 1.....	130
Fig. A. 1.5: Contact angle of biomolecule coatings on Si-PDMS membranes and Si and PDMS materials controls for Experiment 2.....	131
Fig. A. 1.6: <i>In vitro</i> oxygen flux of biomolecule coatings on individual Si-PDMS membranes from Experiment 1, normalized by membrane porous area.....	133
Fig. A. 1.7: <i>In vitro</i> oxygen flux of biomolecule coatings on individual Si-PDMS membranes from Experiment 2, normalized by membrane porous area.....	134
Fig. A. 1.8: Experiment 2 – <i>In vitro</i> oxygen flux of assembled parallel plate devices containing coated membranes, normalized by membrane porous area	135
Fig. A. 1.9: Experiment 1 – Oxygenation of blood through assembled parallel plate devices <i>in vivo</i>	138
Fig. A. 1.10: Experiment 1 – Area-normalized O ₂ and CO ₂ flux <i>in vivo</i> of each parallel plate device, with a blood flow rate of 20 mL/min.....	139

Fig. A. 1.11: Experiment 2 – Oxygenation of blood through assembled parallel plate devices <i>in vivo</i>	141
Fig. A. 1.12: Experiment 2 – Area-normalized O ₂ and CO ₂ flux <i>in vivo</i> of each parallel plate device, with a blood flow rate of 20 mL/min.....	142
Fig. A. 1.13: Experiment 1 – 200X magnification SEM images of gross cell/platelet on membranes removed from the <i>in vivo</i> devices after 2 hours of blood contact	144
Fig. A. 1.14: Experiment 2 – 200X magnification SEM images of gross cell/platelet on membranes removed from the <i>in vivo</i> devices after nearly 4 hours of blood contact	145
Fig. A. 1.15: Experiment 2 – 40X magnification IHC cross-stain of platelet adhesion (CD41, FITC green) and platelet activation (CD62p, Cy-3 red).....	146
Fig. A. 2.1: Setup of <i>in vivo</i> testing circuit for replicates of the no spacers control device in Chapter 5.....	153
Fig. A. 2.2: <i>In vitro</i> testing comparison of replicate devices to the original data from Chapter 5 (Fig. 5.5).....	155
Fig. A. 2.3: <i>In vivo</i> O ₂ and CO ₂ area-normalized flux comparison of replicate devices to the original data from Chapter 5 (Fig. 5.5).....	156
Fig. A. 2.4: Disassembly of oxygenator devices after 2 hours of exposure to heparinized blood.	158
Fig. A. 2.5: SEM micrographs of replicate devices at 200X and 1000X magnification	159

LIST OF TABLES

Table 1.1: ECMO operation requirements for patients by age in units of mL/kg/min.	9
Table 1.2: Comparison of advantages and disadvantages of current and future gas exchange devices.....	28
Table 2.1: List of variables and constants for membrane transport equations.....	36
Table 2.2: Dimensions of SNM and S μ M as measured by SEM.	37
Table 2.3 Failure points of nanopore and micropore membranes	43
Table 4.1: Reaction conditions for PEG protocols.	68
Table 5.1: Dimensions of meshes used as spacers.....	89
Table 5.2: Variables, geometric data of the S μ M-PDMS oxygenator, and constants used in calculations	98
Table 5.3: Results of theoretical calculations for Reynolds number and Sherwood number for spacer-filled channel	100
Table 5.4: Raw ABG data collected from no spacers device during <i>in vivo</i> experiment	102
Table A. 1.1: Raw ABG data collected from the three coated devices during Experiment 1	139
Table A. 1.2: Raw ABG data collected from the four devices during Experiment 2	143
Table A. 2.1: Raw ABG data collected from all three replicate devices during <i>in vivo</i> experiment.	157

CHAPTER 1

ECMO OXYGENATOR DEVELOPMENT – LOOKING TOWARDS THE FUTURE OF RESPIRATORY SUPPORT

1.1 INTRODUCTION

For patients with life-threatening lung or heart failure, common clinical approaches to respiratory support, such as mechanical ventilation, may not sufficiently meet patient requirements. As a last option, extracorporeal membrane oxygenation (ECMO) is a method of providing sustained respiratory support by exchanging oxygen and carbon dioxide directly with blood, giving the patient's lungs time to recover. In ECMO, a patient's venous blood is taken outside of their body and pumped through a mechanical oxygenation device containing an array of gas-permeable membranes (Fig. 1.1) ^{1,2}. These membranes separate two compartments: one for the patient's blood, and one for a sweep gas, typically oxygen mixed with room air. Gases are exchanged through the membrane via diffusion, powered by concentration gradients between the oxygen in the sweep gas and the deoxygenated, carbon dioxide-rich blood. The oxygenated blood can then be returned to the patient's circulation. ECMO can therefore deliver complete respiratory support by simultaneously oxygenating and removing carbon dioxide from a patient.

While ECMO can be a life-saving treatment for critically ill patients, its clinical use is severely limited due to the high risk of complications, primarily either thrombosis events or hemorrhage due to excessive anticoagulation^{3,4}. Blood in an ECMO circuit travels through complex flow paths outside the body, and comes into contact with several square meters of foreign materials. Beyond the oxygenator

itself, a complete ECMO system includes many other circuit components including at least one catheter, many meters of tubing, and a pump. To mitigate the high risk of thrombosis, clinicians need to supply high doses of anticoagulation to patients, typically short-acting unfractionated heparin to block thrombin activity. However, though heparin administration is needed to prevent thrombosis, excessive anticoagulation can result in hemorrhage/bleeding events, which are the most common complications of ECMO in every patient demographic. Given these risks to patients, ECMO is typically only used as a salvage therapy to treat patients who have not been successfully recovered by any other method.

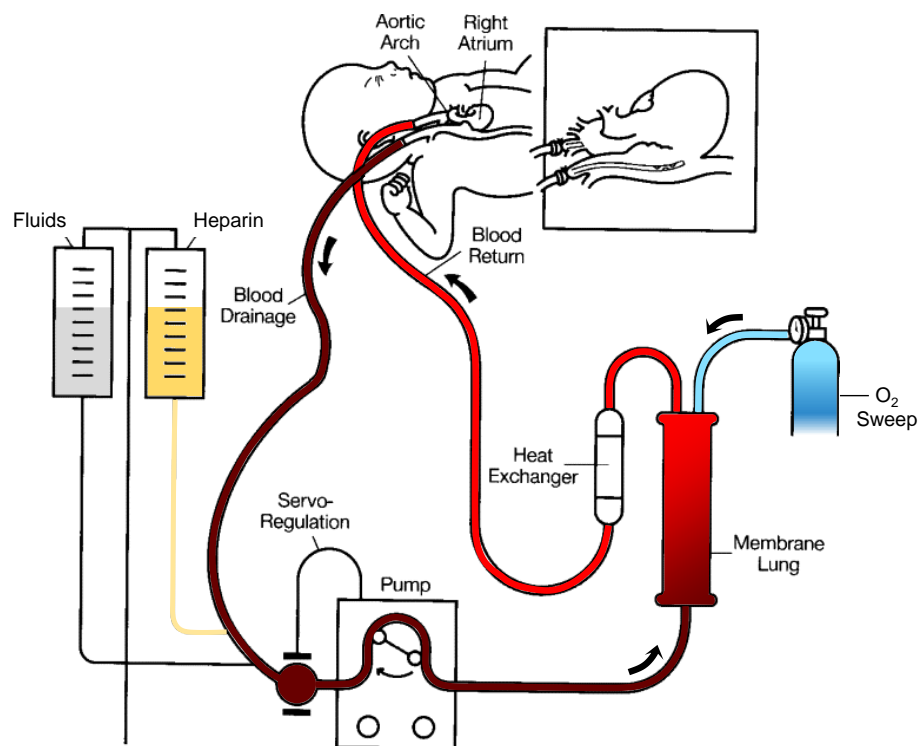


Fig. 1.1: Diagram of ECMO operation in veno-arterial (VA) configuration. Deoxygenated blood is removed from the right atrium of the patient via a catheter and passed through the extracorporeal circuit. The blood first passes through a pump and is supplied with heparin and fluids as needed. Afterwards, the blood enters the membrane oxygenator and receives oxygen coming from the sweep gas. Once the blood is oxygenated, it is reheated before being returned to the patient's aortic arch through another catheter. In this VA configuration, the patient's lungs and heart are supplied by the ECMO circuit. Adapted from Frenckner and Radell ².

As of the 2019 ELSO registry, over 12,000 patients per year were supported by ECMO worldwide ⁴. While ECMO use in general has been steadily rising since the year 2000, the adult ECMO population in particular has dramatically increased in the last 10 years, now making up the largest group of ECMO patients. Historically, ECMO has been primarily a therapy for neonates rather than adults, as neonates are less likely to suffer from unrecoverable chronic lung conditions that would contraindicate ECMO ^{5,6}. However, the success of the CESAR trial and the advent of the H1N1 pandemic in 2006 and 2009, respectively, led to the surge in ECMO for adult patients ^{3,7,8}. Adult candidates for ECMO are more likely to suffer from chronic, progressive lung disease without long-term treatment endpoints such as chronic obstructive pulmonary disease (COPD), pulmonary fibrosis, or end-stage lung failure ⁹⁻¹¹. For these patients, ECMO can be used as a bridge-to-transplant, often with favorable outcomes compared to mechanical ventilation ^{6,12,13}. Bridge-to-transplant patients have consistently shown better treatment outcomes with active rehabilitation programs using a semi-ambulatory ECMO circuit, though these patients still require constant monitoring by care teams within the intensive care unit.

These bridge-to-transplant programs have spurred considerable clinical interest in increasingly portable ECMO systems that deliver sufficient respiratory support while minimizing circuit complexity and thrombogenicity ^{13,14}. In an ideal case, an ambulatory ECMO system would effectively exchange O₂ and CO₂ with minimal anticoagulation and clinician intervention, enabling use outside of the intensive care unit (ICU), and possibly outside of the hospital. Beyond improving bridge-to-transplant outcomes, a portable ECMO circuit with reduced thrombosis risk could make ECMO a more viable treatment option for other patient groups who may benefit from more frequent or prolonged oxygenation. With technology advances, an ambulatory, hemocompatible ECMO could be envisioned as a destination therapy for chronic lung failure patients.

1.2 NEEDS FOR DESIGNING AN OXYGENATOR

The design of an ECMO circuit, particularly the oxygenator, requires consideration of many design elements, as well as human factors for the clinician or patient. An ideal ECMO circuit would effectively exchange O_2 and CO_2 through its membranes, while minimizing thrombosis and hemorrhage risk to the patients. For an ambulatory ECMO circuit, the overall size and complexity of the circuit are also paramount, as well as durability over an extended treatment duration.

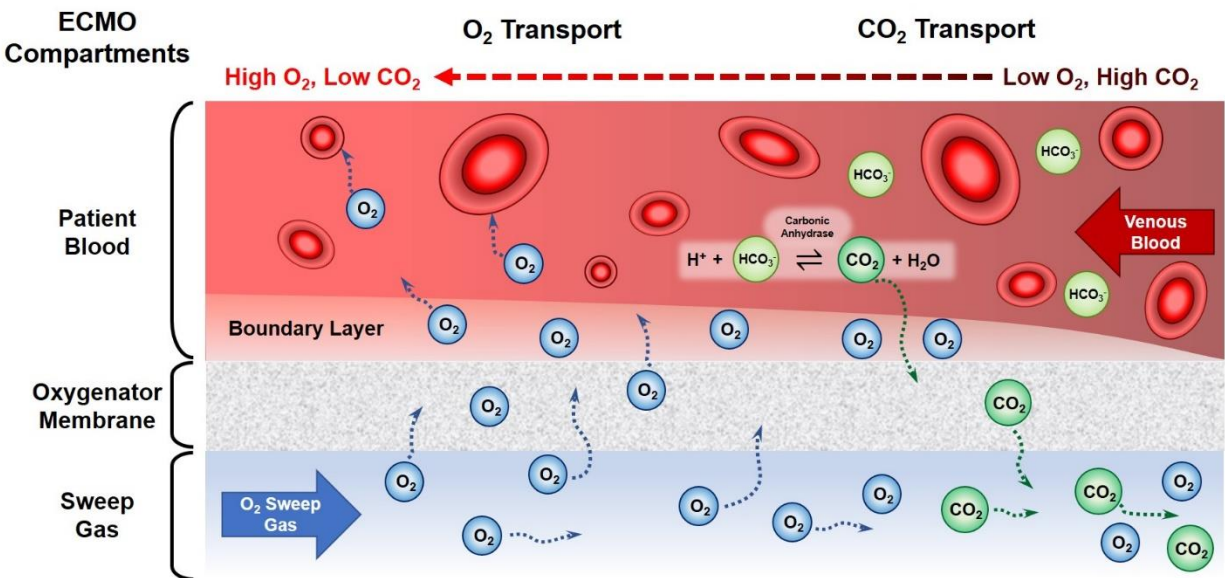


Fig. 1.2: Schematic of oxygen and carbon dioxide exchange through an ECMO oxygenator. Oxygen in the flowing sweep gas diffuses through the oxygenator membrane pores. Once in the blood compartment, the oxygen enters a diffusion boundary layer that sequesters much of it due to the dominant effects of viscosity over convection. Eventually the oxygen diffuses into the bulk of the plasma, where it can be taken up by hemoglobin in red blood cells. Meanwhile, carbonic anhydrase enzyme maintains an equilibrium between dissolved carbon dioxide and bicarbonate ion as part of the blood's pH buffering system. Excess dissolved carbon dioxide in venous blood can diffuse through the membrane and into the sweep gas, where it is carried away by the flowing oxygen.

1.2.1 Hemocompatibility/Anticoagulation

In order to provide sufficient respiration, ECMO requires a patient's entire cardiac output to travel through a complex and potentially turbulent extracorporeal circuit, and come into contact with a large area of foreign materials. Given the obvious likelihood of thrombosis under these circumstances,

clinicians must continuously dose of patients with anticoagulants throughout ECMO treatment, and frequently adjust their anticoagulation regimens as complications arise. On the whole, patient complications on ECMO are overwhelmingly centered around either clotting or bleeding events, indicating either inadequate or excessive anticoagulation, respectively. From multiple retrospective surveys of ECMO patients, several of the most common complications include mechanical failure of the ECMO system, circuit clotting, and surgical site hemorrhage ^{3,11}. Furthermore, long-term ECMO circuit performance is known to deteriorate as a result of fibrin and cellular deposition on the membrane surfaces, reducing gas exchange efficiency over time and increasing pressure resistance from the oxygenator ¹⁵. These complications indicate a lack of hemocompatibility of the circuit itself, necessitating substantial blood anticoagulation that – in turn – raises the risk of bleeding. Therefore, improving hemocompatibility to the greatest extent possible could improve patient outcomes on long-term ECMO.

Blood responsiveness to various disturbances in medical devices is a combination of three factors, comprising Virchow's triad: the overall blood coagulatory status, mechanical forces on blood movement, and any blood-materials interactions with foreign surfaces ^{16,17}. The first of these factors – the blood's overall coagulatory status – is typically addressed through clinical administration of continuous systemic heparin in an ECMO circuit, rather than through device design ^{18,19}. In the context of ECMO circuitry, the latter two factors can be addressed through engineering of the blood flow path throughout the circuit, and modifying the material surfaces to improve blood interactions.

Flowing blood is subjected to a number of mechanical stimuli, typically a combination of velocity, pressure, and shear stress. Alterations to any of these mechanical forces individually or in combination can lead to a disruption of hemostasis, leading to thrombus formation. Shear stress on blood cells outside of typical physiologic ranges can lead to thrombosis through a number of different mechanisms including platelet activation, red blood cell hemolysis, and collection of pro-coagulatory factors in regions of uneven shear stress. Hemolysis can also contribute to the development of acute

kidney injury in ECMO patients, and therefore presents a significant clinical concern beyond thrombosis²⁰. Interestingly, both low ($< 50 \text{ s}^{-1}$) and high ($> 1500 \text{ s}^{-1}$) shear rates have been shown to produce hemolysis and thrombosis in ECMO circuits, indicating that thrombosis is best prevented when shear rates are kept as consistent as possible^{21,22}. Higher shear rates are particularly associated with significantly increased platelet activation and red blood cell hemolysis, while lower shear rates also lead to increased red blood cell hemolysis and higher fibrin deposition. Low flow velocities – particularly regions of near stagnancy – are also highly associated with thrombus deposition in ECMO circuits. Given the complexity of most ECMO circuitry, especially the oxygenator, many stagnant zones can develop and have been shown to consistently lead to clot formation in the same regions. Some of these zones include the connectors throughout the circuit; the oxygenator inlet, in which flow is distributed throughout the membranes; and around the impellers of centrifugal blood pumps²³⁻²⁵. Low flow regions are likely regions of low shear stress as well, and likely lead to thrombus formation through increasing local density of coagulatory proteins. In addition to shear stress, hydrostatic pressure on red blood cells can lead to hemolysis and subsequent thrombosis. High hydrostatic pressure is typically accompanied by higher flow velocities and shear rates, creating a potent combination for thrombus formation. Historically in ECMO, most of the resistance in the circuit originated from the oxygenator, since blood must pass through a dense array of membranes packed into a small volume. As such, most modern ECMO designs endeavor to minimize the pressure drop across the oxygenator unit, preventing one of the possible sources of hemolysis in the oxygenator^{20,26,27}. Still, regardless of hydrostatic pressure, shear rate alone is a significant contributor to hemolysis. Ultimately, from a flow mechanics perspective, ideal ECMO operation would maintain consistent physiologic shear stress throughout the entire circuit flow path, with as few regions of stagnancy as possible. Blood flow velocity should be kept at a relatively high rate for the device size to prevent stagnancy, but pressure drop in the oxygenator circuit should also be minimized to prevent the use of high hydrostatic pressure at high blood flow rates.

The third arm of Virchow's triad – blood-materials interactions – arises from the absence of native vascular endothelium throughout the artificial ECMO circuitry. Healthy vascular endothelial cells secrete many different molecules to prevent both platelet activation and thrombin generation via the coagulation cascade. Since ECMO circuits contain no endothelium, blood proteins, platelets, and cells immediately react to the foreign materials in the circuit. Although systemic heparin administration can deter thrombin formation by increased antithrombin activity, circulating blood proteins quickly adsorb to the circuit materials and encourage clot formation by recruiting other proteins, cells, and platelets to the surfaces. Beyond increasing thrombosis risk, protein deposition on oxygenator membranes limits O₂ and CO₂ exchange through the membranes, gradually reducing ECMO effectiveness over time¹⁵. Foremost among these proteins is fibrinogen which converts into fibrin when enzymatically cleaved by thrombin, making it a crucial step in thrombogenesis^{28,29}. When adsorbed to a surface, fibrinogen undergoes significant conformational changes that also trigger platelet adhesion and activation, acting as a trap for the platelets to form a “white” fibrin clot^{29,30}. Fibrinogen and other proteins show differential binding when adsorbing to surfaces with different chemistries, with fibrinogen binding preferentially to hydrophobic surfaces compared to other blood proteins like albumin^{31,32}. In addition, protein binding to material surfaces cycles through a dynamic process known as the Vroman Effect: proteins that are more adsorbent to a specific surface displace less adsorbent proteins over time^{31,33,34}. Essentially, fibrinogen may displace other proteins that initially adsorbed onto a surface – such as albumin – if fibrinogen is more adsorptive to that surface. This means that some common methods of reducing fibrinogen adsorption, such as albumin passivation of a surface, will rapidly become ineffective once fibrinogen is available to adsorb. Aside from surface chemistry, the topography of a biomaterial surface can influence thrombogenicity via protein binding and platelet interactions, depending on the length scale of the surface features. Blood cells and proteins may perceive rough surface features as similar to exposed endothelial basement membrane fibers (10-300 nm), leading to thrombotic reactions in an attempt to repair the

damaged endothelium³⁵. Most studies generally indicate that surface topography starts to influence protein binding when roughness is as low as 30-50 nm, although fibrinogen also shows significant adsorption onto surfaces with < 30 nm scale topography that allow further denaturing of its rod-shaped structure^{36,37}. In contrast, platelets are more responsive to topographies with roughnesses greater than 50 nm, definitively in the hundreds of nanometers range, since any lower surface roughness is essentially smooth to platelets^{38,39}. However, some studies have shown that platelet adhesion in particular can be reduced using intentionally structured nanomaterial surfaces. Organized structures on the order of hundreds of nanometers, such as pillars or nanotubes, reduce the amount of available surface for platelets to contact, and can lower platelet adhesion compared to a completely smooth surface³⁹. Still, a smooth biomaterial surface would be the ideal topography to reduce thrombogenicity when considering both platelet and protein adhesion to surfaces. Between surface chemistry and topography, a smooth and hydrophilic surface would be the most likely to reduce materials-related thrombogenicity on oxygenator membranes.

1.2.2 Gas Exchange Efficiency/Portability

Beyond hemocompatibility and anticoagulation, another significant consideration for oxygenators is the efficiency of the membranes at blood-gas exchange of O₂ and CO₂. To act as a total lung replacement, a blood oxygenator must be able to: 1. Supply a patient's entire oxygen requirements, 2. Ventilate carbon dioxide adequately, and 3. Maintain rates of O₂ and CO₂ exchange at a blood flow rate equivalent to the patient's cardiac output. All three parameters are dependent on a patient's size and age, and clinicians should continuously evaluate and adjust ECMO support based on individual patient needs. As such, the values in Table 1.1 are generalized for each demographic⁴⁰.

Table 1.1: ECMO operation requirements for patients by age in units of mL/kg/min.

Age Demographic	O₂ Exchange	CO₂ Exchange	Blood Flow Rate
Units	mL/kg/min	mL/kg/min	mL/kg/min
Neonate	6	3-6	100
Pediatric	4-5	3-6	80
Adult	3	3-6	60

For example, an adult patient with a mass of ~70 kg would require 210 mL/min of oxygenation and 315 mL/min of CO₂ ventilation, while at a blood flow rate of 4.2 L/min through the ECMO circuit. The current market-leading oxygenator – the Maquet Quadrox-i series – has been independently evaluated to supply 125 mL/min/m² of area-normalized oxygen flux at 4 L/min blood flow^{27,41}. With a membrane surface area of 1.8 m², its total oxygen output would be around 225 mL/min, successfully meeting the needs of a 70 kg adult ECMO patient.

ECMO circuits perform both O₂ and CO₂ exchange with blood, as in healthy lungs, although the exchange mechanism of each gas is distinct. Providing adequate oxygenation through the ECMO circuit is crucial for most hypoxic lung failure patients (arterial pO₂ < 60 mmHg). Once O₂ enters the bloodstream, it can only be stored as a dissolved gas until it is taken up by hemoglobin in red blood cells. Also, given that hemoglobin has a finite capacity for oxygen storage, the amount of blood oxygenation that can be achieved is limited by the oxygen dissociation curve of hemoglobin^{42,43}. As such, O₂ transport in ECMO is driven by the pressure gradient between the oxygen in the sweep gas compartment, and the dissolved oxygen gas in the bloodstream. In contrast, CO₂ levels in the blood are primarily modulated by the bicarbonate buffering system, which involves enzymatic conversion of dissolved CO₂ into bicarbonate ion: [HCO₃]⁻. The vast majority of the body's CO₂ is stored as bicarbonate ion (90% in arterial blood, 60% venous), with some amounts of dissolved CO₂ gas (5% arterial, 10% venous) and some CO₂ bound to hemoglobin as carboxyhemoglobin (5% arterial, 30% venous)^{44,45}. With most of the body's CO₂ stored

as acidic bicarbonate ion, the main complication of hypercapnic respiratory failure is reduced blood pH and respiratory acidosis ($\text{pH} < 7.32$). CO_2 ventilation in ECMO is controlled by the flow rate of the oxygen sweep gas: as dissolved CO_2 exits the bloodstream and transits the ECMO membranes, the gaseous CO_2 is rapidly swept away by the flowing O_2 to continuously eliminate the CO_2 in the sweep gas. Between the two gases, O_2 is poorly soluble in blood, whereas CO_2 is over 20 times more soluble due to the bicarbonate buffering system⁴⁵. The Henry's Law solubility coefficients of the gases in mL gas (100 mL plasma)⁻¹ mmHg⁻¹ are 0.003 for O_2 and 0.069 for CO_2 ^{45,46}. Therefore, oxygenation is significantly more difficult in ECMO than CO_2 ventilation. Due to the poor solubility of O_2 in blood, oxygenators are typically designed to have large surface areas (1-2 m² for adults) and operate at high blood flow rates (2-7 L/min for adults) to maximize O_2 flux through the membranes. These conditions are usually conducive to CO_2 ventilation as well, since sufficient CO_2 removal can still be achieved with lower blood flow rates (~500 mL/min for adults) and reduced surface area.

Given the difficulty of oxygenation through ECMO, it is important to optimize oxygen delivery in ECMO at each stage of transport from the sweep gas to the hemoglobin. Improvements to oxygenator efficiency would also translate to improvements in hemocompatibility by minimizing blood-contacting surface area, overall device size, and hydrostatic pressure drop across the device. As O_2 enters the oxygenator from the sweep gas, the O_2 must travel by diffusion through the oxygenator membranes, after which the O_2 enters the bloodstream. At this point, the O_2 enters a fluidic boundary layer near the surface of the membrane. Diffusion boundary layers form at the interface of a solid and a flowing liquid, and it is in these regions where viscous forces are dominant over convective forces. In the case of O_2 , the boundary layer essentially sequesters most of the oxygen near the membrane surface, reducing the pressure gradient of oxygen across the ECMO membranes and thereby lowering transmembrane O_2 flux. Eventually, the O_2 diffuses out of the boundary layer and into the bulk of the flowing plasma, where it is finally be taken up by the hemoglobin in red blood cells. While the membranes themselves present some

resistance to oxygen transfer, by far the most significant resistance to O₂ transport in conventional ECMO is this blood boundary layer, possibly comprising ~80-100% of the total resistance to transport⁴⁷⁻⁴⁹.

Overcoming the resistance of the blood-side boundary layer is a significant challenge in oxygenator development. Most oxygenators are designed to operate in laminar flow regimes in order to avoid fluidic turbulence and thrombosis, yet this laminar flow prevents convective forces from interfering with the boundary layer. Designing fluid flows that minimize the effect of the boundary layer may be one strategy to create a more efficient oxygenator that maximizes transport with minimal membrane area and blood volume. Based on Blasius solutions to laminar boundary layer equations, the thickness of the boundary layer (δ) grows along the membrane surface at position x in inverse proportion to the square root of the Reynolds number⁵⁰:

$$\delta \approx \frac{4.9x}{\sqrt{\text{Re}_x}} \quad \text{Eq. 1.1.1}$$

This means that boundary layer thickness is related to the inverse of the blood velocity: higher blood flow rates reduce the boundary layer thickness. Essentially, operating ECMO at higher blood flow rates should allow for more efficient gas exchange across the membranes, which is confirmed by manufacturer data. Also, generating secondary fluid flows – as in turbulent boundary layers – could disrupt the formation of the boundary layer and encourage more transport^{51,52}. However, these concepts must be balanced with pro-thrombotic concerns of generating high pressure resistance and uneven shear stresses. Overall, boundary layer disruption is likely a powerful method to create a more efficient ECMO oxygenator, yet should be considered holistically alongside hemocompatibility strategies.

Designing a more efficient oxygenator can be a critical factor in creating a truly ambulatory ECMO circuit. With a small and efficient oxygenator, other components of the ECMO circuit could possibly be reduced or eliminated. For example, an oxygenator with a low priming volume and a low pressure drop could allow the circuit to be operated without a pump, which is a major potential source of

ECMO thrombosis. In this configuration, the patient's own heart flow would be able to pump blood through the oxygenator without additional assistance.

1.3 CURRENT ECMO OXYGENATOR DESIGNS

Considering the development of a future ambulatory ECMO circuit, examining various oxygenator modalities may elucidate what design concepts make for superior oxygenator performance. Specifically, this section will briefly evaluate oxygenators in the commercial and research landscapes through the lenses of hemocompatibility and portability potential.

1.3.1 Standard of Care: Hollow Fiber Oxygenators

From 1971 onwards, clinical ECMO units have used hollow fiber technology to create membrane oxygenators^{53,54}. In these devices, blood from the pump enters a manifold containing a bundle of tightly-packed fibers, around which the blood must navigate towards the exit (Fig. 1.3). These fibers are hollow and contain the oxygen-rich sweep gas. As the blood navigates around the hollow fibers, gas exchange of O₂ and CO₂ is facilitated through the fiber membranes. Since their introduction, they have been the standard of care, and currently the only type of oxygenators clinically available.

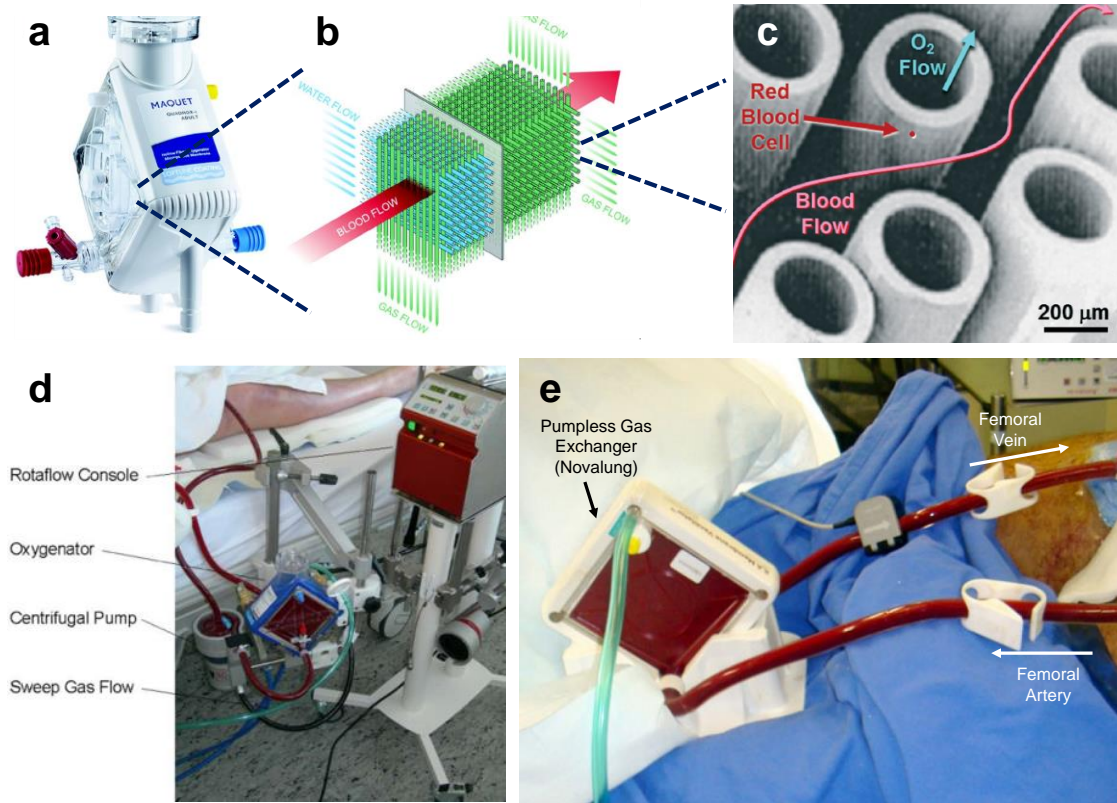


Fig. 1.3: Current generation of hollow fiber oxygenators. (a)-(c) shows the Maquet Quadrox oxygenator unit going from (a) the packaged device, to (b) a general diagram of blood and sweep gas flow, then to (c) SEM imaging of hollow fibers in cross section ^{41,55}. (d) shows a functioning circuit with the Quadrox device, with visibly increased O₂ saturation after blood exits the oxygenator ⁵⁶. In contrast, (e) shows the pumpless Novalung ECCO₂R device in a femoral arteriovenous configuration ⁵⁷.

The complexity of the blood flow paths around the hollow fiber membranes creates unique hemocompatibility challenges, but offers some benefits to gas exchange efficiency. Blood flowing around the hollow fibers can be subjected to many zones of stagnant flow and uneven shear stresses, leading to a pro-thrombotic state. Furthermore, in studying the locations of clots within hollow fiber devices, researchers have pointed to certain locations that tend to nucleate clots, some of which are inherent to the design of hollow fiber devices. Notably, these areas include the flow distributor region at the device inlet, in which the blood first contacts the hollow fibers, and any corners of the manifold such as in the market-leading Maquet Quadrox series ^{25,58}. Systemic heparinization is required to likelihood of clotting due to

these uneven flow paths. However, the complex flow paths around the hollow fibers are capable of generating secondary flows, which can disrupt the diffusion boundary layer and increase gas exchange through the device ^{22,51,52}. Also, as hollow fiber technology has advanced, the devices currently on the market are able to operate at high blood flow rates while maintaining a low pressure drop reducing hemolysis resulting from high hydrostatic pressure. For example, the adult Maquet Quadrox oxygenator yields only 8.4 mmHg of pressure drop per liter per minute of blood flow rate ²⁷.

From a materials perspective, hollow fibers have largely converged on a few material choices and coating combinations. Though some hollow fiber oxygenators are still made of polypropylene (PP), polymethylpentene (PMP) has become the optimal polymer choice for hollow fiber membranes because it features a microporous structure with an extremely thin (~0.1 μm) liquid-tight outer skin ^{59,60}. This allows the transit of O_2 and CO_2 with minimal resistance through the micropores, while also preventing leakage of blood plasma into the sweep gas. As a hemocompatible coating, most manufacturers have conjugated heparin to the fiber surfaces, in addition to systemic heparin administration for anticoagulation. However, heparin has a relatively short bioactivity period of only a few hours, and some researchers have linked heparin coatings with heparin-induced thrombocytopenia ⁶¹⁻⁶⁵. Therefore, heparin coatings may only benefit hollow fiber membranes over a short span within the ECMO support timeline. Some makers have instead employed polymeric coatings, often with a negative surface charge, although these are currently less common and their composition is typically proprietary ⁶⁶⁻⁶⁸.

The dimensions of current hollow fiber oxygenators can provide a benchmark upon which to evaluate other technologies. Using 3M Membrana OXYPLUS PMP membranes as a contemporary example, hollow fibers are generally around 300-400 μm in diameter with a wall thickness of ~90 μm ^{59,69}. They are packaged in sheets at a density of 44 fibers per inch as specified by the manufacturer. The market-leading adult model Maquet Quadrox-i oxygenator contains 1.8 m^2 of membrane surface area with 215 mL of priming volume, and recommended blood flow can range from 0.5-7 L/min ⁴¹.

1.3.2 Hollow Fiber Derivatives

Using hollow fiber membranes as a foundation, a few notable oxygenator derivatives have been developed to fill specific application niches. Examining these devices can elucidate what design priorities are valuable in each setting, and may be relevant for the development of similar gas exchange devices.

1.3.2.1 ECCO₂R

Although adequate O₂ and CO₂ exchange is critical for ECMO patients, oxygenation is typically a clinical priority over CO₂ ventilation, partially due to poor solubility of O₂ in blood. However, there are some clinical indications where specifically CO₂ removal is critical. In hypercapnic cases of respiratory failure, body's inability to ventilate CO₂ leads to high concentrations of bicarbonate ion in blood, which reduces blood pH and results in respiratory acidosis (pH < 7.32). Patients who suffer from acute hypercarbia as in an asthma attack or COPD exacerbation may see a significant benefit from ECMO for CO₂ removal compared to mechanical ventilation^{70,71}. One further consideration is that prioritizing CO₂ removal is mostly pertinent in cases of acute hypercapnia. Many adult patients have chronic conditions that have altered their respiratory physiology over time, such as COPD; these patients often develop compensated respiratory acidosis, with elevated pCO₂ values (pCO₂ > 50 mmHg) but normal physiologic blood pH (pH > 7.35). For these patients, CO₂ removal may not be as critical, since their blood pH is not acidotic.

A newer therapy of extracorporeal carbon dioxide removal (ECCO₂R) has been specifically developed to address this population of acute hypercapnic patients. Given that CO₂ is significantly more soluble in blood than O₂, blood CO₂ ventilation can be achieved with far less surface area, smaller catheters, and at lower blood flow rates than ECMO for oxygenation^{42,72}. Blood flow rates for ECCO₂R range between 0.3-1 L/min (generally around 0.5 L/min), and surface area of 0.3-0.7 m²^{70,71,73}. Most studies on ECCO₂R have shown positive patient outcomes compared to mechanical ventilation treatment alone, although the available clinical data is insufficient for conclusive evidence of ECCO₂R's benefits⁷⁰.

Compared to conventional ECMO, ECCO₂R therapy may result in an increased risk of thrombosis to patients. Many studies have speculated that the lower flow rates of ECCO₂R lengthen the time that blood is in contact with foreign materials in the circuit, contributing to an increased likelihood of thrombosis^{70,71,74}. The lower flow rates may also yield lower shear stresses on blood cells, leading to the same outcome⁷⁵. As of 2019, the leading ECCO₂R system – the Hemolung RAS, manufactured by ALung Technologies – has received the CE mark in 2013, and is undergoing two prospective clinical trials in the United States and the United Kingdom, primarily to evaluate the safety and efficacy of the ECCO₂R device for acute COPD exacerbations^{76,77}.

1.3.2.2 Pumpless ECMO (Novalung)

One of the most prominent contributors to thrombosis in ECMO is the pump needed to drive flow throughout the circuit, at flow rates equivalent to the patient's cardiac output (2-7 L/min for adults). Elimination of the pump alone could reduce the overall likelihood of thrombotic events in the circuit, and improve portability through size and weight reduction^{55,78,79}. To achieve pumpless operation, blood flow through the circuit would be entirely driven by the natural pressure gradients of the patient's heart, meaning a low-resistance oxygenator is paramount to pumpless operation. For adults, pulmonary artery to left atrium pressure differential is ~15 mmHg for veno-venous operation⁷⁹, while the mean arterial pressure of 60-80 mmHg could be used to drive flow in an arterio-venous configuration^{80,81}. Furthermore, without a pump to drive flow, a pumpless device would likely operate with only a fraction of the patient's entire cardiac output, meaning flow through the device – and therefore oxygenation support – would be limited^{80,82}. Still, a pumpless, low-flow gas exchange device could be used for ECCO₂R therapy, or as a device intended for respiratory assistance rather than complete support.

The Novalung iLA device, now produced by Xenios, is intended as a respiratory assistance therapy for bridge-to-transplant cases. Similar to other ECMO and ECCO₂R devices, the Novalung is constructed of PMP hollow fibers with a heparin coating, and designed with a low pressure resistance of

only ~15 mmHg at a flow rate of 2.5 L/min^{80,83}. Generally, a fraction of the body's cardiac output is shunted through the Novalung device for respiratory assistance, which is connected in an arterio-venous configuration between femoral arteries and veins (Fig. 1.3e)^{81,83}. The device has a surface area of 1.3 m² and is rated between 0.5-4.5 L/min of blood flow, although typical blood flows are mostly kept to ~1.5 L/min^{54,55,80}. Using the device, supportive carbon dioxide removal – but only minimal oxygenation – has been demonstrated in patients, essentially making the Novalung another type of ECCO₂R device⁸⁰. As the system is completely pumpless, the Novalung circuit uses less priming volume compared to conventional ECMO (~250 mL), and greatly simplifies the clinical monitoring of the device⁸². However, the pumpless Novalung operates at a relatively low blood flow rate similar to other ECCO₂R devices, and so has shown somewhat increased platelet activation in some tests⁸².

1.4 CURRENT RESEARCH DIRECTIONS

Research groups worldwide are endeavoring to build novel gas exchange devices that improve upon the hemocompatibility and efficiency of current hollow fiber ECMO oxygenators. Some researchers have been attempting to optimize versions of hollow fiber oxygenators, while others have been studying alternative membranes and gas exchange paradigms altogether.

1.4.1 Improvements to Hollow Fiber Devices

One prominent research objective involves the optimization of hollow fiber membrane assembly with the goal of constructing a portable lung assistance device. Multiple groups have used hollow fiber membranes to construct new devices that improve upon the efficiency and hemodynamics of existing ECMO units. Efforts at the University of Michigan and University of Pittsburgh have separately developed portable paracorporeal lung assistance devices through optimization of hollow fiber packaging^{52,79,84,85}. The Pittsburgh approach centers around the integration of a centrifugal pump in the same unit as the oxygenator (Fig. 1.4a)^{84,86}, while the Michigan device aims for pumpless flow through the circuit. Both devices improve overall circuit portability through the consolidation of circuit components. Other

efforts have attempted to improve gas exchange efficiency through unconventional boundary layer disruption techniques such as oscillation of the hollow fiber bundles, rotation of the hollow fiber bundle, or introducing pulsatility to the blood flow into the fiber bundles⁸⁷⁻⁸⁹. None of these techniques has been integrated into a larger-scale oxygenator, but all address the desire for improved gas exchange via boundary layer disruption and increased mixing.

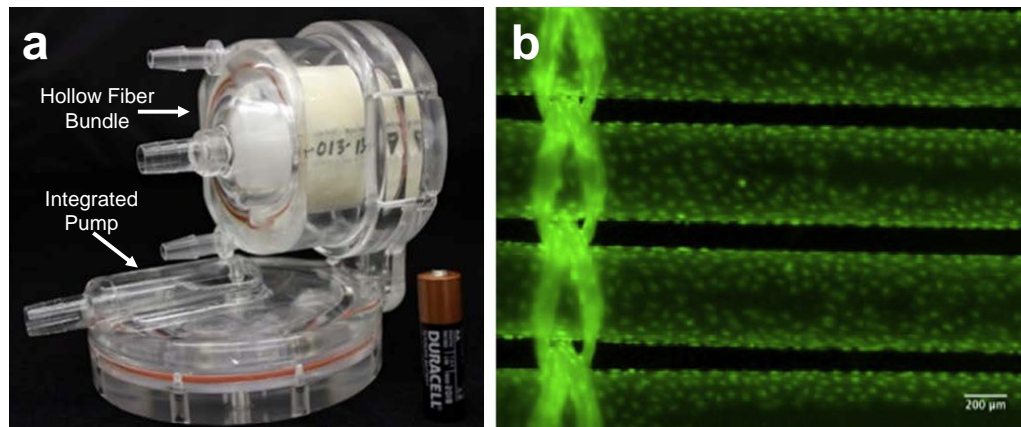


Fig. 1.4: Examples of improvements to hollow fiber membrane gas exchange devices. (a) shows the University of Pittsburgh pediatric ambulatory lung with integrated blood pump – an advancement in compactness and portability⁸⁶. (b) shows endothelialization of perfused PMP hollow fibers with human cord blood derived cells at Hannover Medical School⁹⁰.

Improvements to hemocompatible coatings on hollow fibers are also a notable area of research and development. Generally, these alternative coatings tend to emphasize high hydrophilicity, or add a new functionality to the membranes beyond their original capabilities. Zwitterionic coatings have gained considerable traction as biomaterial coatings, including on oxygenator membranes. The combination of positive and negative ionic residues on the same molecule imbues surfaces with unparalleled hydrophilicity, drawing a hydration layer to the surface that prevents protein adhesion and thrombosis^{91,92}. On oxygenator membranes specifically, zwitterionic coatings that have been tested have include phosphorylcholine derivatives⁹³⁻⁹⁵, carboxybetaine bonded to dopamine⁶⁵, and sulfobetaine⁹³. The

majority of these studies have shown favorable reductions in protein fouling on surfaces and platelet activation, often with little to no significant reduction in gas exchange with coating application.

More advanced coatings on hollow fibers have attempted to imbue an additional functional benefit to the coatings beyond reducing protein fouling. Work by Arazawa, et al. at the University of Pittsburgh combined an enzymatic coating (carbonic anhydrase) with an acidic sweep gas to enhance carbon dioxide removal through hollow fibers⁷³. This combination leveraged the equilibrium between bicarbonate ion and dissolved CO₂ in the blood to drive increased carbon dioxide ventilation compared to either the sweep gas or the coating alone. Other coatings attempt to mimic the native vascular endothelium by continuously eluting the natural anticoagulant – nitric oxide – into the bloodstream^{96,97}. Nitric oxide (NO) is naturally secreted by healthy endothelial cells to quell platelet activation, and therefore could be highly beneficial to a potent anticoagulation strategy for ECMO. Some examples of NO-releasing coatings include the NOrel polymer coatings developed at the University of Michigan for over a decade^{96,98,99}, and the copper-embedded elastomer coatings from Carnegie Mellon University^{100,101}.

Another intriguing approach to enhancing ECMO hemocompatibility is the endothelialization of the hollow fibers themselves to create a “biohybrid” artificial lung (Fig. 1.4b). Theoretically, endothelialization of the oxygenator membranes would achieve the ultimate hemocompatible surface by becoming a functional vascular endothelium, similar to alveolar capillaries in the native lung¹⁰². Multiple research groups have studied the establishment of a confluent endothelial cell layer onto surface-modified hollow fiber membranes. Cell types have included bovine aortic endothelial cells⁸⁹, and human umbilical cord blood endothelial cells^{90,103,104}. Generally, research has demonstrated that, under physiologic levels of shear stress *in vitro*, the endothelial cells can be successfully seeded and maintained on oxygenator fibers for up to 28 days of culture. However, the *in vivo* feasibility and longevity of this endothelial layer has yet to be thoroughly demonstrated. When exposed to blood, bovine endothelialized hollow fibers have

shown reduced thrombosis compared to uncoated membranes with over an hour of exposure, but also significantly reduced oxygen permeability^{55,89}. More recent studies on human cord blood cells have not yet explored the gas exchange consequences of endothelialization or hemocompatibility. The viability of the endothelial layer over long-term exposure to blood and highly oxygenated sweep gas has not been studied, since the few experiments that expose endothelium to blood have only studied cell viability over a few hours. Any defects in the conformity of the endothelium could expose the hollow fiber membrane surfaces to blood, possibly triggering thrombus formation despite the endothelial coating. Also, the immunologic consequences of patient blood to this endothelium have not yet been explored, especially if the cell source is autologous or xenogenic to the patient. Significantly more research will need to be conducted on the feasibility of endothelialized oxygenator membranes, but – if long-term gas transfer and biocompatibility is demonstrated with these units – they could be a significant benefit to overall ECMO hemocompatibility.

1.4.2 Microfluidic Artificial Lungs

Moving away from hollow fibers altogether, many research groups have developed prototype artificial lungs based on synthetic microfluidic capillary beds, which attempt to create a synthetic lung structure by mimicking native alveolar vasculature. These microfluidic devices use advanced microelectromechanical systems (MEMS) production techniques, including soft lithography of silicone elastomers, to emboss highly organized microchannel structures into flat sheets of materials such as polydimethylsiloxane (PDMS). With unparalleled precision and reproducibility, many of these flat silicone sheets can be stacked in parallel plate layers that alternate between sweep gas and blood flow channels, forming the oxygenator membrane structures. By routing blood through highly organized microchannels, researchers hope to mimic the hemodynamic and gas transfer qualities of the native lung, which hollow fiber membranes are inherently incapable of recreating. While no large-scale microfluidic

prototypes currently exist, research in this field presents unique solutions to concerns with hollow fiber ECMO, and provides an intriguing direction for a potential future artificial lung.

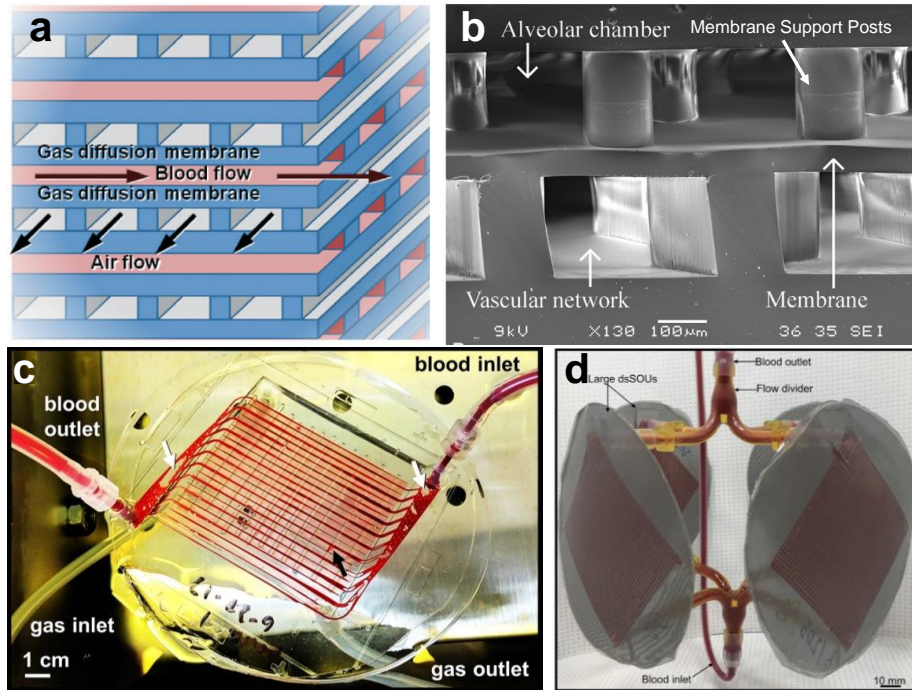


Fig. 1.5: Microfluidic blood oxygenator schematics and actualizations. (a) shows a schematic of a stacked array of microfluidic channels in parallel plate configurations⁵⁵. (b) shows an SEM cross section of such a device separating the sweep gas in the alveolar chamber from the blood in the vascular network¹⁰⁵. (c) shows the blood-perfused capillary bed of a branched microfluidic oxygenator¹⁰⁶, while (d) shows the current largest microfluidic oxygenator consisting of four microfluidic units in parallel¹⁰⁷.

Dimensions of microfluidic oxygenators vary widely between each research group's devices⁵⁵.

One of the earliest iterations of a microfluidic oxygenator by Lee, et al. (2008) used a relatively thick 130 μm PDMS membrane, and comparatively thin 15 μm blood flow channels¹⁰⁸. Subsequent early devices by the Draper Lab^{105,109-111}, McMaster University¹¹², and the University of Michigan^{113,114} substantially reduced the PDMS membrane thickness into the tens of microns, ranging from 10-63 μm . Blood capillary heights of these early devices either attempted to mimic ultrathin alveolar vasculature (10-20 μm)^{55,113}, or design significantly wider channels to ensure low-resistance flow (80-200 μm)^{105,112}. Although ECMO membranes are not generally significant contributors to O_2 and CO_2 transfer resistance, microfluidic

oxygenators can create extremely thin gas exchange membranes that effectively make membrane resistance negligible. PDMS has a naturally high permeability to both O₂ and CO₂¹¹⁵⁻¹¹⁸, and does not lead to gas emboli formation or plasma leakage. Still, because PDMS is a flexible material, the thin PDMS membranes need to be sufficiently structurally supported so as not to collapse into the blood flow channels. Most researchers have settled on blood channel widths of 50-60 μm to ensure adequate channel support without collapse¹⁰⁶. The most recent generation of microfluidic oxygenators has converged on PDMS membrane thicknesses of 30-60 μm – thinner than PMP hollow fiber wall thickness – and blood channel capillary heights of 30-100 μm^{106,107,119}. The McMaster University research group has also explored the reinforcement of their PDMS membranes with stainless steel wire meshes, which provide significant structural rigidity and robustness under pressure^{107,120}. Ongoing efforts within these groups have endeavored to increase device scale to oxygenate large scale animals, with the goal of reaching human scale. The largest microfluidic oxygenators so far have used priming volumes of 7-8 mL to handle 12-17 mL/min of blood flow, using 14-32 cm² of effective gas exchange surface area – maximally ~63 cm² when multiple units are arrayed^{106,107}. In terms of overall portability, some researchers have designed novel packaging techniques to keep the microfluidic oxygenators as compact as possible. Researchers at McMaster University and the University of Michigan have explored rolling their oxygenator beds into cylindrical structures, or in a cup-shaped bundle^{79,107,121}. At this prototype stage of development, though, it is difficult to determine the extent to which microfluidic oxygenators can improve overall ECMO portability by achieving pumpless operation, or using room air as a sweep gas instead of O₂⁵⁵.

The most significant advantages to microfluidic oxygenators are the highly controlled flow paths that can be constructed with MEMS precision, and the high oxygen transfer that can be achieved using micromachined gas exchange channels. Blood flow paths can be divided throughout the artificial capillary bed using natural scaling and branching patterns similar to native lung structure, altering hydraulic diameter between larger and smaller channels to retain consistent flow dynamics. Among microfluidic

ECMO research groups, the University of Michigan group has extensively utilized Murray's Laws of parent-daughter vessel construction to guide branching angles and microchannel heights^{106,114}. The Draper Lab group has used biomimetic branching angles as well, but generally single-height blood flow channels that do not vary with parent-daughter branching¹¹¹. By contrast, the McMaster University group has opted for simple 90° capillary branching angles and no variance in capillary height, demonstrating that biomimetic branching angles are not a requirement for microfluidic design^{112,121,122}. In theory, distributing blood flow in a biomimetic branching manner should improve the flow path arm of Virchow's triad by keeping flow rates and shear stresses on platelets consistent throughout the entirely smooth, laminar flow path. Ordinarily, keeping blood flow paths entirely laminar in a microfluidic device would prevent any boundary layer mixing, reducing the oxygenation potential of such a geometry. However, microfluidic devices can be designed with channel heights in the tens of microns, nearing alveolar capillary channel heights of 8 μm^{55,112,113}. This means that the boundary layer essentially encompasses the entire microchannel, and therefore transfer resistance is negligible. Furthermore, MEMS soft lithography techniques could be used to emboss mixing structures onto the PDMS microchannels and create gas transfer-enhancing flow paths, though these have yet to be tested for hemocompatibility¹²³.

As with hollow fibers, many researchers developing microfluidic oxygenators have applied coatings on top of PDMS to improve the hemocompatibility of the surface. Though it is bioinert, PDMS alone is a naturally hydrophobic material, and thus attracts considerable protein deposition onto the surface that could trigger thrombus formation. For microchannels specifically, improving the hydrophilicity of PDMS also ensures that all channels will become properly wetted with fluid. Surface modification of PDMS is possible with plasma treatment followed by silane bonding chemistry to covalently attach hydrophilic moieties to the surface. Coatings that have been studied on microfluidic oxygenators specifically include polyethylene glycol¹²⁴, and zwitterionic polymers including sulfobetaine¹²⁵. In addition, research groups have attempted to build an endothelialized microfluidic PDMS

oxygenator^{111,126}. The most significant research on this topic, conducted at RWTH Aachen University, has successfully cultured human vascular endothelial cells on RGD-modified PDMS for up to 33 days, though O₂ and CO₂ exchange was significantly reduced compared to unmodified PDMS^{126,127}.

While initial work on microfluidic ECMO devices have demonstrated proof-of-concept, the biggest hurdle to further development is the scale-up of this technology to a full-scale, human-sized device. At the prototype stage, assembly of oxygenators involves laborious PDMS molding and layer-by-layer stacking, currently done by manually. In the future, automated MEMS tooling could be used to greatly simplify and standardize this process⁵⁵. Microfluidic ECMO devices are currently operating at a prototype scale that is significantly smaller than full-scale hollow fiber membrane devices, but have shown promising comparability of gas transfer. Using more recent prototypes as examples, oxygen transfer rates range from 88-130 mL/min/m²^{106,121}. At the higher end of this range, a microfluidic oxygenator may be comparable to a hollow fiber device such as the Maquet Quadrox-i series. Still, no device has come close to providing enough total oxygen flux for human respiratory support. Hemocompatibility results for microfluidic oxygenators are mixed thus far. With the help of hemocompatible coatings, short term patency of microfluidic devices over the range of hours has been demonstrated in many studies, with a few experiments showing patency of > 18 h¹¹⁴. However, blood flow through the very narrow artificial capillary beds results in high pressure gradients and shear stresses across prototype oxygenators. One recent example from Thompson, et al (2018) demonstrated a pressure drop of 66 mmHg at a blood flow rate of 17 mL/min, while a Maquet Quadrox-i has a pressure drop of only 8.4 mmHg per L/min of blood flow^{27,106}. Despite efforts to improve hemodynamics through controlled branching design, the artificial capillary beds inherently present a significant resistance to blood flow, potentially resulting in hemolysis and thrombosis from the uneven shear stresses and high hydrostatic pressure. Scale up of the devices may be able to mitigate this issue by routing blood flow through more channels, thereby reducing pressure drop. Considering the advantages and drawbacks of

microfluidic oxygenators, this research presents unique solutions to the hemodynamic issues with current ECMO devices, and scale up of the technology could put this concept on a competitive level with hollow fiber membranes.

1.5 SILICON MEMBRANE OXYGENATOR

For over a decade, our lab has developed porous silicon membranes with high precision and reproducibility, made using scalable MEMS technology from the silicon integrated circuits industry¹²⁸⁻¹³¹. These membranes possess a mechanically rigid – yet thin – structure, and can be readily arrayed in parallel plate configurations for controlled exchange of materials between two separated compartments. With a range of pore sizes from < 10 nm to $1 \mu\text{m}$, silicon membranes can readily reproduce a variety of physiologic filtration functions, by way of their unprecedented selectivity and filtration efficiency. As such, silicon membranes can serve as individual filtration units for the construction of large-scale artificial organ devices, including as an artificial lung device.

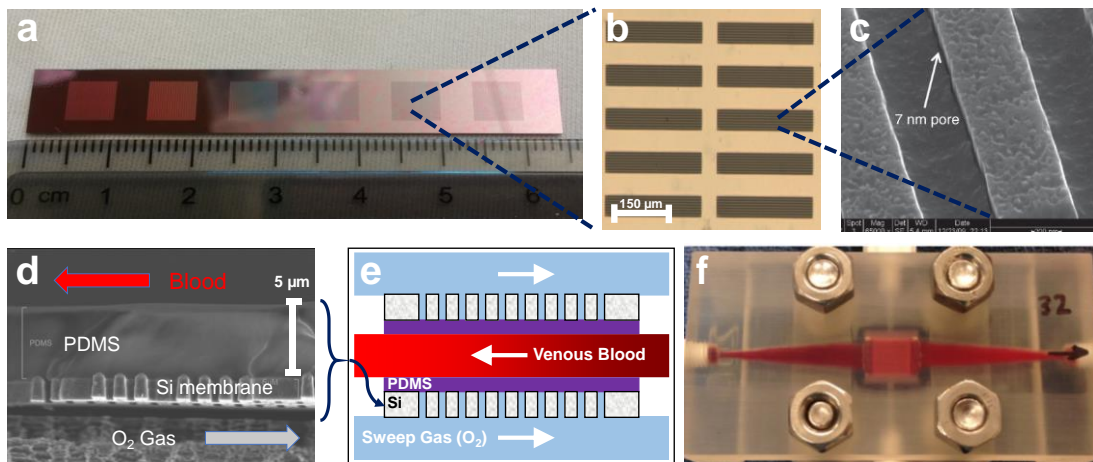


Fig. 1.6: Silicon membranes for artificial organ devices, highlighted for use as ECMO membranes. (a)-(c) show the hierarchy of highly precise silicon structures from a macroscopic (6.5 cm^2 membrane) to nanometer scale. (d) shows a cross section of a silicon-PDMS composite membrane, intended for liquid-tight blood oxygenation. (e) shows a schematic of a blood oxygenator assembly using the composite membranes, and (f) shows an early proof-of-concept prototype using a 1 cm^2 silicon membrane to conduct blood oxygenation¹³².




By developing and characterizing silicon membranes, our lab has prototyped artificial organ replacements for the kidneys, pancreas, and lungs. Significant research in our lab has focused on renal filtration using nanoporous (~10 nm pore) silicon membranes (SNM) to controllably filter small solutes. Compared to a hollow fiber renal dialyzer, the SNM allow for highly selective filtration of over relatively short (200-500 nm) diffusion distances^{131,133,134}. With highly efficient membrane filtration, the SNM can be arrayed into a compact artificial kidney, intended for long-term implantation as a renal replacement therapy¹³⁵⁻¹³⁷. In addition to filtration, the silicon membranes are capable of supporting cell populations through protective encapsulation in one of the device compartments¹³⁸⁻¹⁴⁰. The silicon membranes can permit an encapsulated population of cells to interact with small molecules and nutrients in a patient's bloodstream, while also protecting the cells from larger entities such as the patient's immune cells. Using silicon membranes in the sub-micron (~500 nm) range for immunoisolation has led to the design of a bioartificial pancreas device^{138,139}. Through separation of an islet chamber from the bloodstream, a population of autologous or xenogenic pancreatic islets can be viably kept for sustained blood glucose regulation.

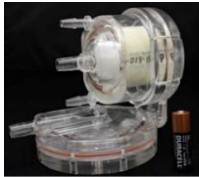
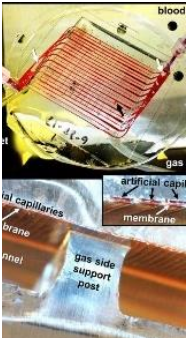

Further research has investigated the sustained hemocompatibility of silicon membrane devices, including membranes coated with hemocompatible polymers such as polyethylene glycol^{131,135} and sulfobetaine methacrylate^{91,141,142}. Given that silicon membranes are rigid, flat sheets, prototype devices are assembled with the silicon membranes in parallel plate configurations, similar to microfluidic oxygenator devices. Laminar flow throughout the devices is achieved at flow rates up to 60 mL/min *in vivo*, with computationally optimized shear stress throughout the blood flow path⁹¹. Membranes can be assembled into devices with blood flow channels ranging from 50 μm to 3 mm in height, allowing a high degree of tailoring to meet the needs of a particular application^{91,132,139}. Since the silicon membranes are mechanically rigid, blood flow channels can be kept very wide (1-8 cm range) relative to their height to ensure low pressure resistance throughout the entire flow path^{135,139,143}. Compared to a microfluidic

oxygenator, high rates of blood flow with very low pressure drop can be achieved with silicon membrane geometries, while keeping the membrane's mass transfer resistance exceptionally low due to material thinness. Devices with zwitterionic coatings on silicon substrates have shown sustained patency and hemocompatibility for 26 days of implantation into a flowing blood porcine model, indicating a high degree of hemocompatibility of both the coated silicon and the parallel plate assembly⁹¹.

As with the kidney and pancreas, silicon membranes have been studied as a potential oxygenator membrane. Early studies in 2009 with SNM demonstrated that O₂ transfer can occur through silicon membranes, possibly at an enhanced level due to free molecular flow inside of the silicon nanopores¹⁴⁴. Subsequent work by Yeager moved to the use of a microporous silicon membrane surmounted with an ultrathin layer of PDMS to construct a rigid, liquid-tight oxygenator membrane^{54,145}. In this work, a proof-of-concept oxygenator was built using a 1 cm² silicon membrane, through which some O₂ and CO₂ exchange was observed with ovine blood. Still, at this small prototype stage, much about the oxygenator concept was not yet established. These preliminary gas exchange rates were only measured through a small membrane, and systematic characterization the gas permeance of different silicon membranes had not been conducted. The design of the device prototype had not been optimized for hemocompatibility, and no coatings other than PDMS were used to minimize surface thrombogenicity. Future work from these experiments would need to systematically determine gas exchange through membranes, and optimize a larger-scale oxygenator prototype to further the silicon membrane oxygenator concept. A comparison of a hypothetical silicon membrane oxygenator to current and future gas exchange devices can be found in Table 1.2

Table 1.2: Comparison of advantages and disadvantages of current and future gas exchange devices. Critical size parameters are specified, with notes about overall circuit portability potential. Flow hemodynamics, surface materials, and gas exchange properties of each device are characterized.

Device	Dimensions δ_m : wall thickness h_c : channel height SA: surface area	Flow Path and Hemodynamics	Blood-Materials Interactions	Gas Exchange Efficiency
<p>Hollow Fiber Oxygenator – Maquet Quadrox-i Adult⁴¹</p> 	<p>δ_m: 90 μm h_c: ?, est. 200 μm¹⁴⁶ SA: 1.8 m^2</p> <p>Advantages - Full-scale device</p> <p>Disadvantages - Thick membranes - Not compact or ambulatory - Pump required</p>	<p>Advantages - Low resistance</p> <p>Disadvantages - Uneven shear \rightarrow hemolysis, platelet activation - Stagnant regions \rightarrow thrombosis</p>	<p>Advantages - PMP: liquid barrier, permits gas diffusion</p> <p>Disadvantages - Heparin coatings unstable over time - Membrane fouling over time</p>	<p>Advantages - Secondary flows induce boundary layer disruption - High flow rates \rightarrow high O_2, CO_2 flux</p> <p>Disadvantages - Thick membranes, long diffusion distances</p>
<p>ECCO₂R – Hemolung¹⁴⁷</p> 	<p>δ_m: 90 μm h_c: ?, est. 200 μm SA: 0.59 m^2</p> <p>Advantages - Full-scale device - Compact design</p> <p>Disadvantages - Only CO_2 support - Not ambulatory, still requires pump</p>	<p>Advantages - Low resistance</p> <p>Disadvantages - Uneven shear - Low flow rates \rightarrow hemolysis - Stagnant regions</p>	<p>Advantages - PMP: liquid barrier, gas diffusion</p> <p>Disadvantages - Heparin coatings unstable over time - Membrane fouling</p>	<p>Advantages - Secondary flows induce boundary layer disruption</p> <p>Disadvantages - Low flow rates \rightarrow only CO_2 support</p>
<p>Pumpless ECCO₂R – Novalung⁵⁷</p> 	<p>δ_m: 90 μm h_c: ?, est. 200 μm SA: 1.3 m^2</p> <p>Advantages - Full-scale device - Pumpless</p> <p>Disadvantages - Only CO_2 support - Not ambulatory - Requires cardiac functionality</p>	<p>Advantages - Ultra-low resistance - Pumpless usage</p> <p>Disadvantages - No control over flow rates - Uneven shear and stagnant zones - Low flow rates \rightarrow hemolysis</p>	<p>Advantages - PMP: liquid barrier, gas diffusion</p> <p>Disadvantages - Heparin coatings unstable over time</p>	<p>Advantages - Secondary flows induce boundary layer disruption</p> <p>Disadvantages - Low flow rates \rightarrow only CO_2 support - No control over flow rates \rightarrow unknown respiratory support</p>

Device	Dimensions δ_m : wall thickness h_c : channel height SA: surface area	Flow Path and Hemodynamics	Blood-Materials Interactions	Gas Exchange Efficiency
<p>U. Pitt. Pediatric Lung Assist (Hollow Fiber) ⁸⁶</p> 	<p>δ_m: 90 μm h_c: ?, est. 200 μm SA: 0.3 m^2</p> <p>Advantages</p> <ul style="list-style-type: none"> - Full-scale pediatric device - Ambulatory with compact circuit <p>Disadvantages</p> <ul style="list-style-type: none"> - Pump required 	<p>Advantages</p> <ul style="list-style-type: none"> - Integrated pump \rightarrow lower total size <p>Disadvantages</p> <ul style="list-style-type: none"> - High resistance - Complex pump flows due to integrated design - Uneven shear and stagnant zones - Device failure in limited early trials 	<p>Advantages</p> <ul style="list-style-type: none"> - PMP: liquid barrier, gas diffusion <p>Disadvantages</p> <ul style="list-style-type: none"> - Currently no coating, future: zwitterionic 	<p>Advantages</p> <ul style="list-style-type: none"> - Secondary flows induce boundary layer disruption <p>Disadvantages</p> <ul style="list-style-type: none"> - Low flow rates \rightarrow less efficient gas exchange
<p>U. Michigan Microfluidic Oxygenator ^{106,125}</p> 	<p>δ_m: 30 μm h_c: 30 μm SA: 31.5 cm^2 (gas exchange)</p> <p>Advantages</p> <ul style="list-style-type: none"> - Compact, efficient circuit <p>Disadvantages</p> <ul style="list-style-type: none"> - Prototype scale, not human size \rightarrow future size TBD - Soft lithography scale up unknown 	<p>Advantages</p> <ul style="list-style-type: none"> - Controlled laminar flow paths - Biomimetic capillary bed <p>Disadvantages</p> <ul style="list-style-type: none"> - High resistance - High shear stresses - Long term patency unknown 	<p>Advantages</p> <ul style="list-style-type: none"> - PDMS: liquid barrier, ultrathin - Possible zwitterion coating <p>Disadvantages</p> <ul style="list-style-type: none"> - Zwitterionic coating longevity unknown 	<p>Advantages</p> <ul style="list-style-type: none"> - Thin blood channels \rightarrow efficient gas exchange <p>Disadvantages</p> <ul style="list-style-type: none"> - No boundary layer disruption
<p>Silicon Membrane Oxygenator</p> 	<p>δ_m: 5 μm (PDMS) h_c: 50 μm – 3 mm SA: ?</p> <p>Advantages</p> <ul style="list-style-type: none"> - Stackable array - Silicon MEMS scale up <p>Disadvantages</p> <ul style="list-style-type: none"> - Prototype scale, not human size \rightarrow future size TBD 	<p>Advantages</p> <ul style="list-style-type: none"> - Controlled laminar flow paths - Even shear - Low resistance - Long-term flow path patency <p>Disadvantages</p> <ul style="list-style-type: none"> - Scale up flow path not optimized yet - Not biomimetic 	<p>Advantages</p> <ul style="list-style-type: none"> - PDMS: liquid barrier, ultrathin <p>Disadvantages</p> <ul style="list-style-type: none"> - Hemocompatible coatings unknown 	<p>Advantages</p> <ul style="list-style-type: none"> - Thin membranes \rightarrow efficient gas exchange - Tunable flow path height <p>Disadvantages</p> <ul style="list-style-type: none"> - No boundary layer disruption

1.6 RESEARCH OBJECTIVE

Between hollow fiber and microfluidic oxygenators, there exists a need for a blood oxygenator with maximal gas exchange efficiency and long-term hemocompatibility. Such a device could be conceived as part of a portable, ambulatory ECMO circuit for long-term support of patients in need of a bridge-to-transplant or destination lung replacement therapy. To achieve this goal, the technology used to make this oxygenator would need to improve upon the existing hemocompatibility issues with blood flow paths around hollow fibers (uneven flow paths, areas of stagnancy) or through microfluidic circuits (high pressure resistance and shear stress). Furthermore, the oxygenator would need to be optimized for efficient gas exchange and long-term blood-materials contact, similar or better than existing oxygenators.

This work endeavors to develop a prototype device that uses silicon membrane technology to build a hemocompatible blood oxygenator, capable of efficient O₂ and CO₂ exchange with blood. In this work, various generations of silicon membranes with pore sizes from 10 nm to 1 μm, with and without an additional PDMS layer, were systematically tested for suitability as oxygenator membranes (Chapter 2). The membrane selected from this work was then deployed in larger oxygenator prototype flow cells to evaluate the membranes' *in vitro* and *in vivo* performance (Chapter 3). These foundational studies were the basis for making further improvements to the surface hemocompatibility (Chapter 4) and boundary layer mixing (Chapter 5) of silicon membrane devices. Ultimately, we hope to expand upon this work to continue the scale-up of a compact and hemocompatible blood oxygenator founded upon silicon membrane technology.

CHAPTER 2

EVALUATION OF SILICON MEMBRANES FOR EXTRACORPOREAL MEMBRANE OXYGENATION (ECMO)

Substantial portions of this chapter have been published in Biomedical Microdevices (2018);20:86

2.1 INTRODUCTION

Extracorporeal membrane oxygenation (ECMO) is a clinical alternative to mechanical ventilation by which oxygen is delivered to the blood and carbon dioxide is removed. Since its initial development, ECMO has become a well-established treatment that is used on nearly 8,000 neonatal, pediatric, and adult patients annually worldwide^{3,7,54}. Despite ECMO's effectiveness as a treatment, its use remains limited due to its high risk profile¹⁴⁸. The large membrane area and tortuous blood flow path around the hollow fibers can cause blood clotting within the circuit; in turn, the high systemic anticoagulation prescribed to prevent these clots can cause devastating bleeding. Clotting and bleeding are the most common causes of complications in patients, pointing to the need for a smaller, more efficient ECMO system with reduced dependence on high systemic anticoagulation^{149,150}.

Advances in microelectromechanical systems (MEMS) technology may be able to address the deficiencies of hollow fiber membranes through innovative approaches to high flux gas exchange membranes, and overall device design⁵⁵. Past work in our lab has developed silicon nanopore membranes (SNM) for use in blood-contacting devices^{131,135,139,151}. Since then, we have expanded this concept to include membranes with larger, micron-scale pores employed for gas transport applications^{132,143}. One potential disadvantage of these silicon micropore membranes (S μ M) is that they are far more susceptible

to transmembrane leakage of gas bubbles or blood plasma compared to the smaller pore SNM. To address this potential limitation of S μ M, we have developed a method of applying a solid layer of polydimethylsiloxane (PDMS) to the surface of the S μ M – an adaptation derived from PDMS microfluidic oxygenators¹⁴³. PDMS is highly permeable to both oxygen and carbon dioxide, making it capable of facilitating respiratory gas exchange. With the combination of the silicon membrane and PDMS layer, the composite “S μ M-PDMS” is imbued with several possible advantages, whereby the silicon membrane mechanically reinforces the PDMS while preventing transmembrane leakage.

The purpose of this work is to examine the effect of SNM and S μ M design on pressure resilience and maximum gas flux. An ideal ECMO membrane would be robust enough to withstand high sweep gas pressures, which would lead to a greater pressure gradient that would drive oxygen into the blood. SNM and S μ M may have different advantages when considered as potential ECMO membranes: the SNM can withstand higher sweep pressures with a smaller pore size, while the higher pore area of the S μ M may yield a higher oxygen flux. As such, both types of silicon membranes were evaluated for the effects of pore size, pore area, and distribution on maximum gas pressure prior to gas bubble formation. Subsequently, the most robust membranes were examined for gas transport efficiency, which would determine the final suitability of the silicon membranes for ECMO applications.

2.2 MATERIALS AND METHODS

2.2.1 Membrane Fabrication

Following prior work in this lab, the SNM and S μ M were created with a uniform pore distribution and high level of pattern fidelity^{131,135,143}. Briefly, SNM are created from a silicon wafer starting with thermal oxidation growth of SiO₂ followed by low pressure chemical vapor deposition (LPCVD) of polysilicon, which is then patterned through dry etching (Fig. 2.). Controlled, tunable growth of another layer of sacrificial SiO₂ on top of this polysilicon defines the width of the future pores in the membrane. An anchor layer is then patterned through wet etching. A second layer of polysilicon is

deposited with LPCVD flush with the existing layers, followed with a blanket etch of the polysilicon until the sacrificial oxide is exposed. The SNM are then protected with deposited low temperature oxide, and original silicon wafer is etched away through deep reactive ion etching (DRIE) to expose the sacrificial oxide on both sides. Finally, the oxide is etched away in a wet etching process to yield the nanometer-scale pores. S μ M are manufactured with a simpler process, in which the pores are directly patterned into a single layer of polysilicon on top of silicon oxide (Fig. 2.2a-d). The initial oxide only is etched away to create the pores. Pore sizes for SNM were intended to be 11, 30, and 40 nm as defined by oxide thickness, while S μ M pores were intended to be 500 and 1000 nm as defined by the lithography step.

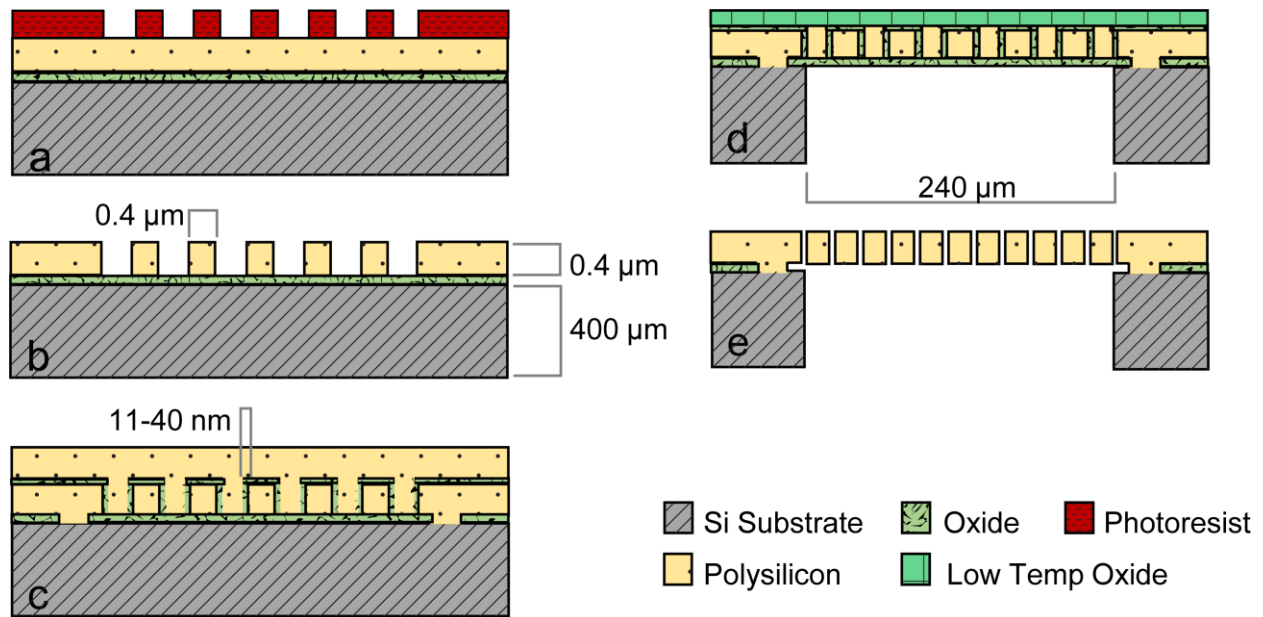


Fig. 2.1: Fabrication of SNM membranes. Step (c) shows the deposition of sacrificial oxide to form pores, which is removed through wet etching in step (e).

To create S μ M-PDMS, a 5 μ m-thick layer of PDMS is made using a multistep sacrificial layer method, and then applied to the surfaces of the S μ M via O₂ plasma bonding (Fig. 2.2e-g). A ~300 μ m layer of Sylgard 184 PDMS (Dow Corning: 4019862) is mixed at a 10:1 monomer-to-crosslinker ratio, spin coated onto a silicon wafer, and then cured for 2 hours in an 80°C oven. After a brief oxygen plasma

treatment to make the surface wettable (Harrick Plasma PDC-001, Harrick Plasma, Ithaca, NY USA), a 5% w/w solution of polyvinyl alcohol in water is spin coated on top of the first PDMS layer and cured for 1 hour at 60°C (Sigma Aldrich: P8136-250G). Finally, mixed Sylgard 184 is diluted with hexanes (Sigma Aldrich: 227064-1L) at a 1:1 ratio, spin coated on top of the PVA to a thickness of ~5µm, and cured at 80°C for 2 hours. The cured PDMS is cut from the wafer into strips, and placed into the plasma oven along with the SµM. Following plasma treatment, the SµM are briefly dipped into DI water, and the strips of PDMS are placed face down on top of the membranes such that the 5 µm PDMS layer is in contact with the polysilicon face of the membrane. The plasma bond is strengthened with 70°C heat and pressure to ensure even contact. After 12 hours of bonding, the excess PDMS is cut from the membrane and the membranes are allowed to soak in 70°C DI water until the PVA layer completely dissolves creating the SµM-PDMS membrane.

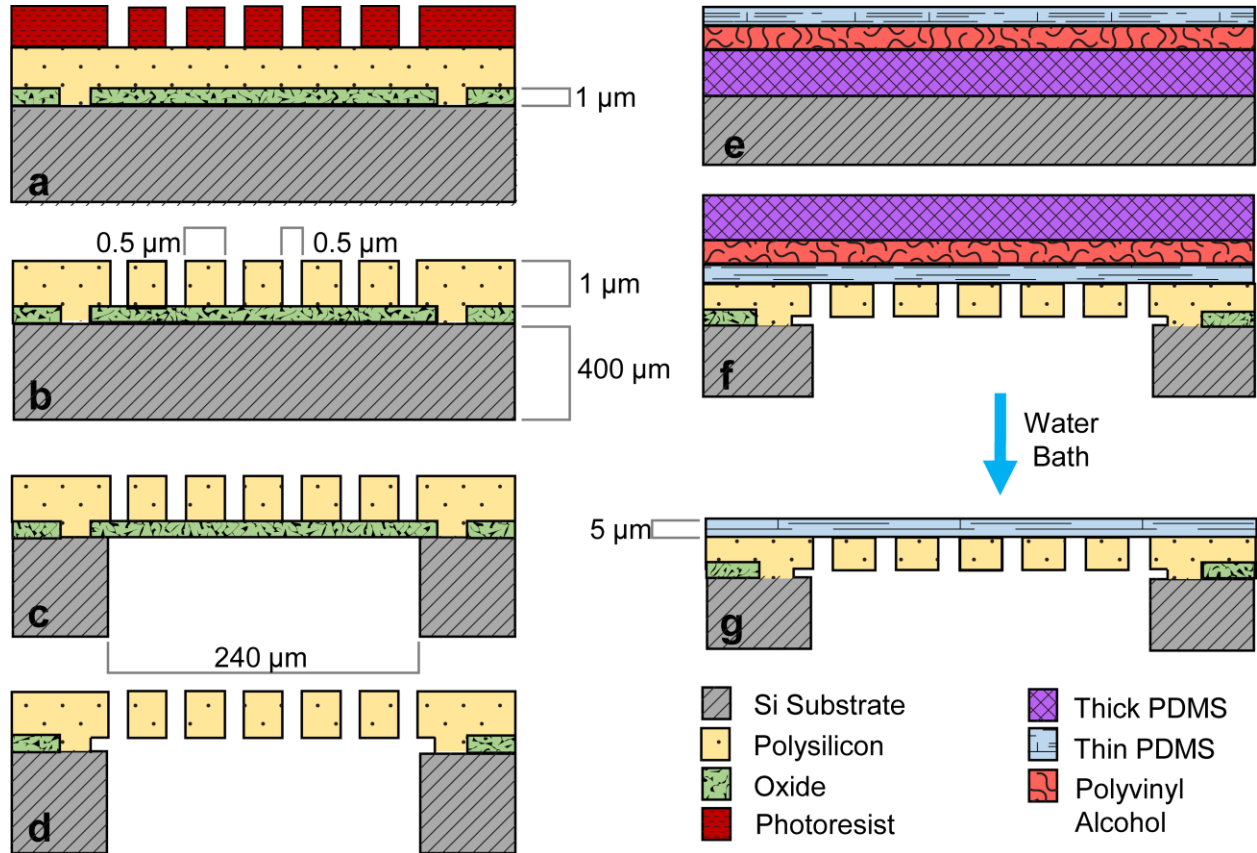


Fig. 2.2: Fabrication of SμM (a-d), and application of PDMS (e-g) to form SμM-PDMS. Adapted from Dharia, et al (2017).

Pore widths were validated through hydraulic permeability testing and SEM imaging of membranes. Hydraulic permeability testing was performed on SNM after wet etching of the pores¹⁵². By establishing a ~5 cmHg pressure gradient of water across the membrane, the volume flow rate of the permeate from the membrane could be measured through timed collection. From the following equation, the actual pore width of the membrane could be related to the permeate flow rate, pressure drop, and other length dimensions of the pore:

$$w = \left(\frac{12\mu h \Delta Q_{perm}}{L \Delta P} \right)^{1/3} \quad \text{Eq. 2.1}$$

All variables and constants for transport equations can be found in Table 2.1. Hydraulic permeability testing showed that the SNM had pore sizes of 10.2 ± 0.6 , 22.3 ± 3.4 , and 33.0 ± 3.1 nm. The measured pore sizes indicated that the SNM were patent, and that the pore sizes were on the same order of magnitude as intended. Since the pores of the S μ M were large enough to be easily visualized, light microscopy was used to measure the size of S μ M pores (Leica DM4000M, Leica Microsystems, Buffalo Grove, IL USA), and hydraulic permeability testing was unnecessary. SEM imaging was used to confirm the pore widths of SNM and S μ M, and the thickness of the PDMS layer of the S μ M-PDMS was determined to be $\sim 5\mu\text{m}$ (Fig. 2.3).

Table 2.1: List of variables and constants for membrane transport equations.

Variable	Units	
Pore Width (w)	m	
Pore Length (L)	m	
Pore Depth (h, δ_m)	m	
Membrane Area (A_m)	m ²	
Pressure (P)	cmHg	
Flow Rate (Q)	m ³ s ⁻¹	
Bubble Point Shape Factor (κ)	---	
Hydraulic Diameter (D_H)	m	
Flux (J)	mL O _{2,STP} min ⁻¹	
Total Mass Transfer Coefficient (k_T)	cm O _{2,STP} ³ m ⁻² min ⁻¹ cmHg ⁻¹	
Permeability (P_m)	mol O ₂ m ⁻¹ min ⁻¹ cmHg ⁻¹	
Constants	Units	Value
Surface Tension – Water/Air (σ)	mN/m	72.75
Contact Angle – Water on Si (θ)	Degrees	40
Density of Oxygen (ρ_{STP})	kg m ⁻³	1.429
Henry’s Law Constant (H)	mol H ₂ O · atm O ₂ /mol O ₂	$4.2 \cdot 10^4$
Molar Concentration of Water (c_L)	mol/L	55.5

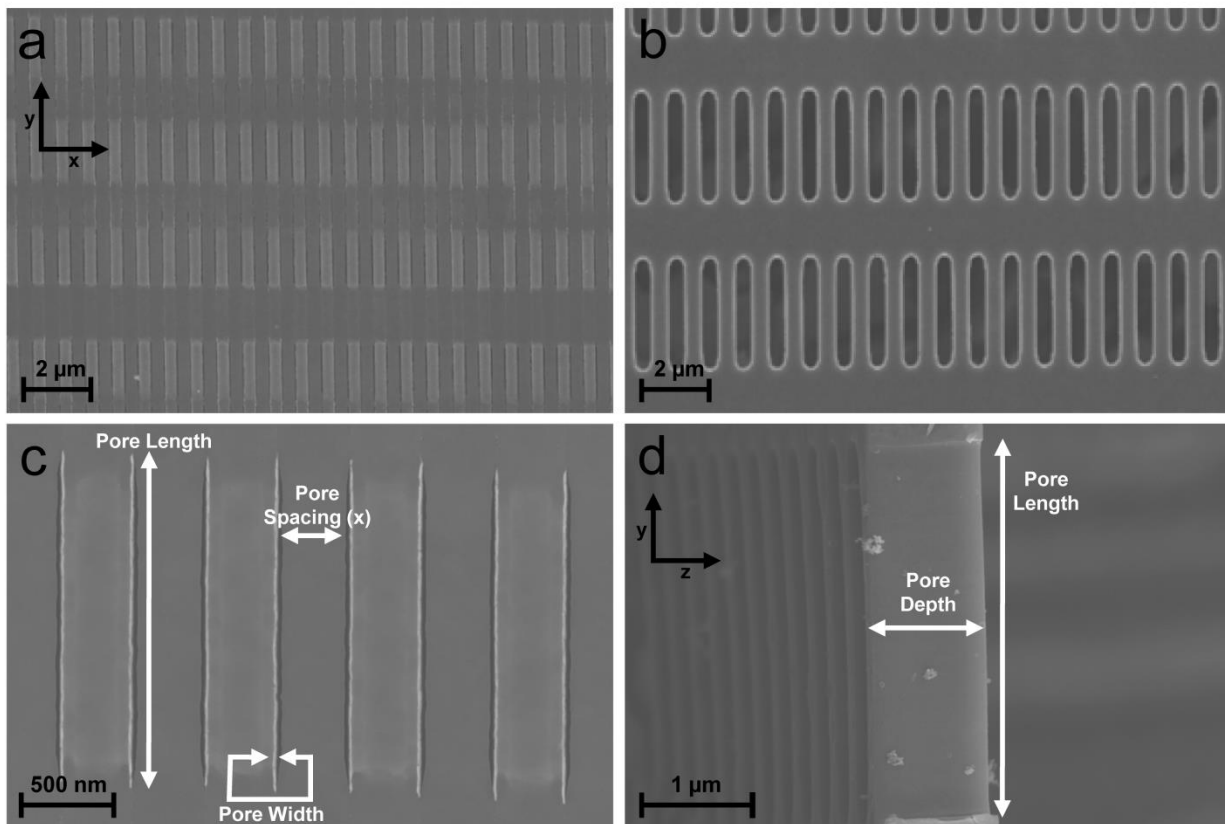


Fig. 2.3: SEM images of membranes. (a) and (b) are 1.82k magnification plan view images of 30 nm and 500 nm pore membranes, respectively. (c) is a 25k magnification plan view image of a 30 nm-pore wide membrane with dimensions labeled. (d) is a cross sectional image of a 500 nm pore membrane showing pore depth.

Table 2.2: Dimensions of SNM and S_μM as measured by SEM.

Dimensions	Nanopore Membranes (SNM)			Micropore Membranes (S _μ M)	
	Pore Width (nm)	10.4	29.0	39.1	600.8
Pore Length (μm)	2.17	1.83	1.92	.46	3.45
Pore Depth (nm)	400	400	400	1000	1000
Pore Spacing (nm)	386	368	362	400	468.9
Pores Per Membrane	1.56E+07	1.56E+07	1.56E+07	3.16E+06	2.10E+06
Pore Area (m ²)	3.60E-07	7.02E-07	9.36E-07	5.53E-06	7.36E-06
Membrane Area (m ²)	1.91E-05	1.91E-05	1.91E-05	1.48E-05	1.48E-05
Porosity (Pore Area/Membrane Area)	1.89%	3.67%	4.90%	37.33%	49.68%

2.2.2 Failure Point Testing

The failure point of the membranes was investigated to determine the maximum sweep gas pressure that the membranes could support prior to gas bubble formation in liquid. Failure point can be further characterized as either bubble point or rupture point, depending on the cause of the bubble formation. Bubble point is defined as the gas pressure at which the largest pore of a wetted membrane will become completely de-wetted, leading to gas bubbles on the liquid side of the membrane. Rupture point is the pressure at which the membrane will break due to the mechanical strain arising from the deflections upon application of gas pressure, causing gas bubbles to traverse the membrane. Unlike rupture point, which is an irreversible and non-repeatable measurement, bubble point testing is both reversible and consistent because the membrane remains intact upon completion of the test. Silicon membranes with smaller pores will require higher gas pressure to de-wet and reach bubble point than those with larger pores. Ultimately, they may reach their rupture pressure before they reach their bubble point.

For this study, a selection of membranes was used with pore sizes ranging from approximately 10 nm to 1 μm , and classified as either SNM (pore size < 100 nm) or S μM (pore size > 500 nm). To visually measure bubble or rupture point, SNM and S μM were diced into 1x 1 cm square membranes, completely wetted with water, and mounted inside of a gasket-sealed transparent acrylic flow cell (Fig. 2.4). One side of the membrane was exposed to circulating deionized water at a flow rate of 1 mL/min, allowing visualization of gas bubbles in the liquid. The opposite side of the membrane was connected upstream to an air-filled syringe pump (kdScientific Gemini 88, Holliston, MA USA) and a pressure gauge (Druck DPI 104, General Electric, Billerica, MA USA); air flow was blocked downstream of the flow cell. The side of the membrane with the polysilicon pores was oriented to face the water to mimic the configuration of membranes when in contact with blood. Measurements of bubble point gas pressure (cmHg) were taken by pressurizing the air using the syringe pump until bubbles were observed in the liquid. Each

membrane was re-tested upon completion of the first test to determine if the membrane had ruptured or had reached a repeatable bubble point. A ruptured membrane would permit bubbles at very low gas pressures – significantly lower than during the first test – while a membrane that reached its bubble point would become pressurized to the same level as the initial test.

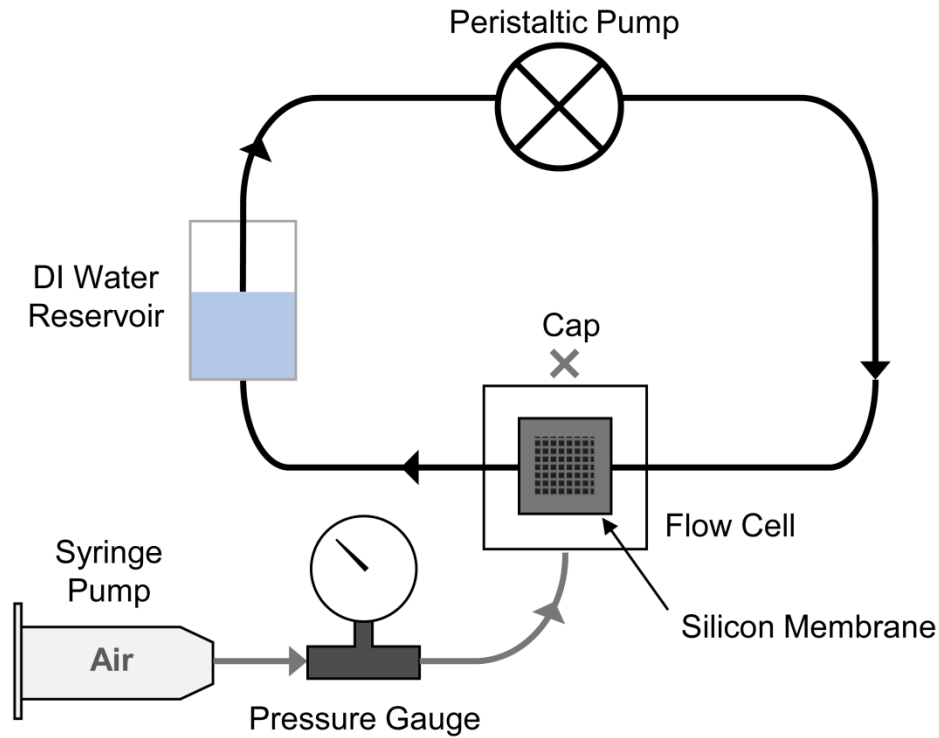


Fig. 2.4: Diagram of bubble/rupture point testing setup. The membrane in the flow cell is shown with bubbles traversing the membrane as bubble or rupture point has been reached.

The bubble point of any membrane can be described by the following equation:

$$\Delta P = \frac{4\sigma \cdot \cos(\theta) \cdot \kappa}{D_H} \quad \text{Eq. 2.2}$$

where κ is an empirical, unitless “shape factor” constant that applies to non-cylindrical pore membranes and ΔP has units of Pa¹⁵³. Given that hydraulic diameter is inversely proportional to bubble point

pressure, membranes with larger pore sizes will reach bubble point with less pressure than membranes with smaller pores.

2.2.3 Oxygen Flux and Permeability *In Vitro*

Following bubble/rupture point testing, SNM and S μ M that withstood the highest gas pressure without gas emboli were chosen for subsequent experiments. These membranes were assessed for their gas permeability at a constant, low pressure below the bubble/rupture point of all membranes (Fig. 2.5). The SNM and S μ M membranes were diced to a size of 1 cm x 6.5 cm, thoroughly dried, and mounted into a gasket-sealed polyether ether ketone (PEEK) flow cell with a channel height of 200 μ m. For gas permeability testing, the membranes were diced larger than for the bubble point testing in order to ensure adequate gross gas transport. For this test, the face of the membrane with polysilicon pores was exposed to circulating, nitrogen-sparged water at a rate of 10 mL/min and hydrostatic pressure of under 5.17 cmHg, and the backside was exposed to pressurized pure oxygen sweep gas. In this experiment, the gas flow was not blocked downstream of the flow cell, but instead permitted to flow completely through. An optical oxygen probe (NeoFoxGT with FOSPOR probe, Ocean Optics, Dunedin, FL, USA) was placed downstream of the flow cell on the liquid side to detect oxygen transport across the membrane. The gas pressure of the oxygen sweep gas was raised to 26 cmHg, and oxygen flux into the water was measured by the probe. Flux (J , mL O₂/min) was determined using the measured oxygen concentration in μ mol/L before and after adding oxygen to the circuit ($[O_2]_i$ and $[O_2]_f$, respectively), with a conversion of 22.4 L O₂/mol at STP:

$$J = \left([O_2]_f - [O_2]_i \right) \cdot 10^{-6} \frac{\text{mol}}{\mu\text{mol}} \cdot 22.4 \frac{\text{L}}{\text{mol}} \cdot Q \quad \text{Eq. 2.3}$$

Q is the flow rate of water in mL/min. From the flux, the coupled mass transfer coefficient (κ , mL O₂ min⁻¹ m⁻² cmHg⁻¹) was determined to represent the total transport efficiency of oxygen through the sweep gas, the membrane, and the liquid. To obtain this value, the flux from Eq. 2.3 is normalized by the total

pressure driving force between the gas and liquid ($\Delta P_{gas-liquid}$, cmHg), as well as the membrane area (A_m , m²):

$$k_T = \frac{J}{\Delta P_{gas-liquid} \cdot A_m} \quad \text{Eq. 2.4}$$

For the calculations in this study, the membrane area was taken to be the total area of open pores on the membrane. The mass transfer coefficient can be further broken down into its measurable parameters, where $P_{O_2, gas}$ is the gas driving pressure (cmHg) and P_{O_2, H_2O} is the partial pressure of oxygen in the water measured using the oxygen probe (cmHg):

$$k_T = \frac{\Delta[O_2] \cdot Q}{\left(P_{O_2, gas} - \frac{P_{O_2, H_2O, f} - P_{O_2, H_2O, i}}{2} \right) \cdot A_m} \quad \text{Eq. 2.5}$$

Both the oxygen flux and mass transfer coefficient can be used to aid our understanding of the influence of membrane design on gas transfer, and thereby, help determine if silicon membranes are suitable for ECMO.

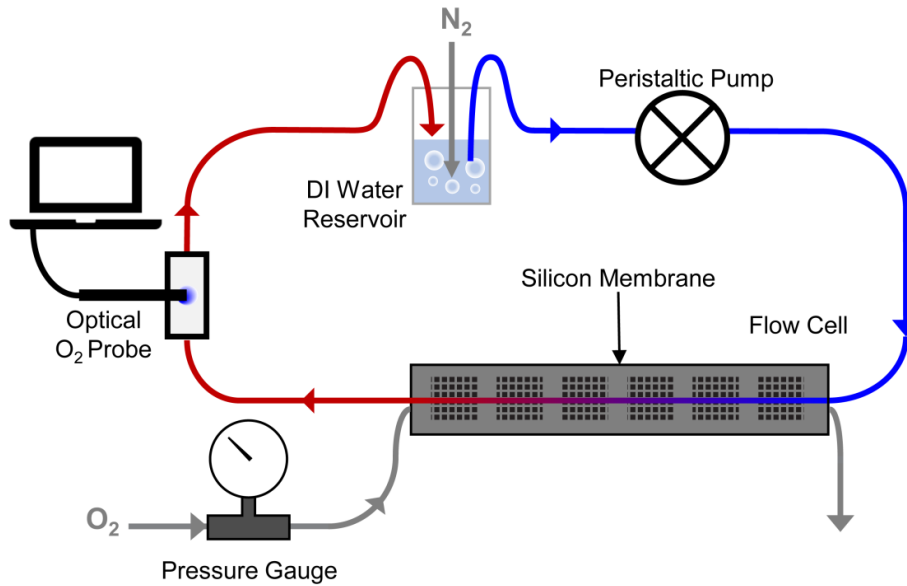


Fig. 2.5: Schematic of *in vitro* oxygen permeability testing setup. Water is shown as blue when deoxygenated, and red when oxygenated after contact with the silicon membrane.

2.3 RESULTS AND DISCUSSION

2.3.1 Failure Point Testing

Failure point data for the SNM, $S_{\mu}M$, and $S_{\mu}M$ -PDMS are shown in Table 2.3 and Fig. 2.6. The $S_{\mu}M$ without PDMS showed bubble points at approximately 84.1cmHg for 500 nm pores, and 43.9cmHg for 1000 nm. These bubble points were found to be repeatable, indicating that the micropore membranes had not ruptured. The smaller pore $S_{\mu}M$ had a higher bubble point than the larger pore membrane, which is consistent with Eq. 2.2. While the SNM without PDMS produced identifiable bubble points, the $S_{\mu}M$ -PDMS showed no membrane rupture or bubbles during the course of the test. Instead, the membranes did not rupture prior to the maximum gas pressure permitted by the syringe pump testing system – approximately 260 cmHg.

Table 2.3 Failure points of nanopore and micropore membranes. The 11 nm pore SNM and 1000 nm pore S μ M with PDMS both exceeded the maximum pressure of the syringe pump without bubbling or rupturing. Maximum pressure of the syringe pump was somewhat variable due to inconsistent syringe pump performance, leading to differences between the membrane maximum pressures.

Pore Size (nm)	11	30	40	500	1000	1000+PDMS
Failure Point (cmHg)	310 \pm 67.4 (MAX)	220 \pm 59.5 (rupture)	170 \pm 26.7 (rupture)	84.1 \pm 4.95 (bubble)	43.9 \pm 2.99 (bubble)	276 \pm 65.6 (MAX)

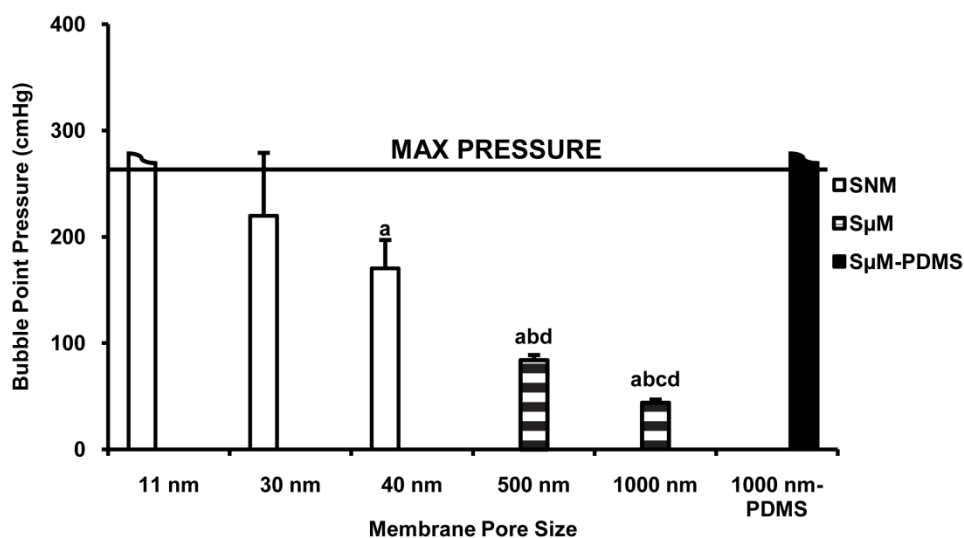


Fig. 2.6: Bubble or rupture points of silicon membranes related to pore size. Significant difference ($p < 0.05$) is indicated above chart bars: difference from from 11 nm SNM shown by (a), 30 nm shown by (b), 40 nm shown by (c), and 1000 nm-PDMS membrane. Maximum pressure indicated by dashed line.

The two SNM with relatively larger pore sizes ruptured at pressures of 220 cmHg and 170cmHg for membranes with 30 and 40 nm pores, respectively. This rupture point was the result of the membranes breaking while under pressure, which was verified through light microscopy. The 40 nm pore SNM ruptured at a lower pressure than the 30 nm pore SNM likely due to the fact that the larger pore membrane was reinforced with less additional silicon than the smaller-pore counterpart. The SNM with the smallest pores (~11 nm) did not rupture or reach bubble point before the syringe pump system reached its maximum pressure. Ultimately, the two types of membranes with the highest bubble/rupture points were the S μ M-PDMS, and the 11 nm pore size SNM. These membranes were able to resist rupture before

the conclusion of the test, indicating that they would be able to withstand greater than ~260 cmHg of pressure prior to the formation of gas emboli in blood. This pressure is comparable to that of existing hollow fiber oxygenators, which can be used at pressures up to 260 cmHg (50 psi) clinically ^{154,155}. Microfluidic, PDMS-based oxygenators are comparatively used at sweep gas pressures of 16 cmHg or lower to prevent rupture ¹⁵⁶. For example, Potkay (2011) used a sweep gas pressure of 16.0 cmHg, while Hoganson (2010) and Lee (2008) used lower pressures of 0.475 cmHg and 1-2 cmH₂O, respectively ^{105,108,113}.

2.3.2 Oxygen Flux and Permeability *In Vitro*

From the initial set of membrane types, the S μ M-PDMS and 11 nm pore SNM were selected for further testing to determine oxygen flux through each membrane, since they were able to resist failure prior to the end of the test. Since one of the membrane types selected was the S μ M-PDMS, an additional group of 500 nm pore S μ M without PDMS was also tested for gas permeability. It was essential to compare the transport of the S μ M with and without PDMS to determine if the PDMS layer had a significant impact on gas transport. Gas permeability testing was conducted for all chips at a sweep gas pressure below the failure point of all membranes (26 cmHg) to achieve comparative tests of gas flux.

The oxygen flux from each membrane (using Eq. 2.3) is shown in Fig. 2.7a. Based on Eq. 2.5, the coupled mass transfer coefficient was also determined for each membrane, taking the area to be the area of open pores on the membranes (Fig. 2.7b). The PDMS coated membranes produced the most oxygen flux at 0.03 mL/min. As can be seen in Fig. 2.7a, the oxygen flux from the S μ M with and without PDMS are indistinguishable and values for both membranes were also insignificantly different. The PDMS layer, therefore, provides little resistance to oxygen transport. Compared to the S μ M, the SNM showed significantly lower oxygen flux – only 40% of the S μ M flux. Higher transport through the S μ M is likely due to the significantly greater open pore area of S μ M compared to the SNM. However, the mass transfer coefficient of the SNM when normalized by actual pore area is significantly higher by an order of

magnitude. This result would indicate that, per pore, more transport is exhibited by the smaller pore membranes – pointing to a nonlinear relationship between pore area and gas flux¹⁴⁴. Despite the higher transport per pore of the SNM, compared to the S μ M, overall more gas transport was generated when using membranes of higher porosity.

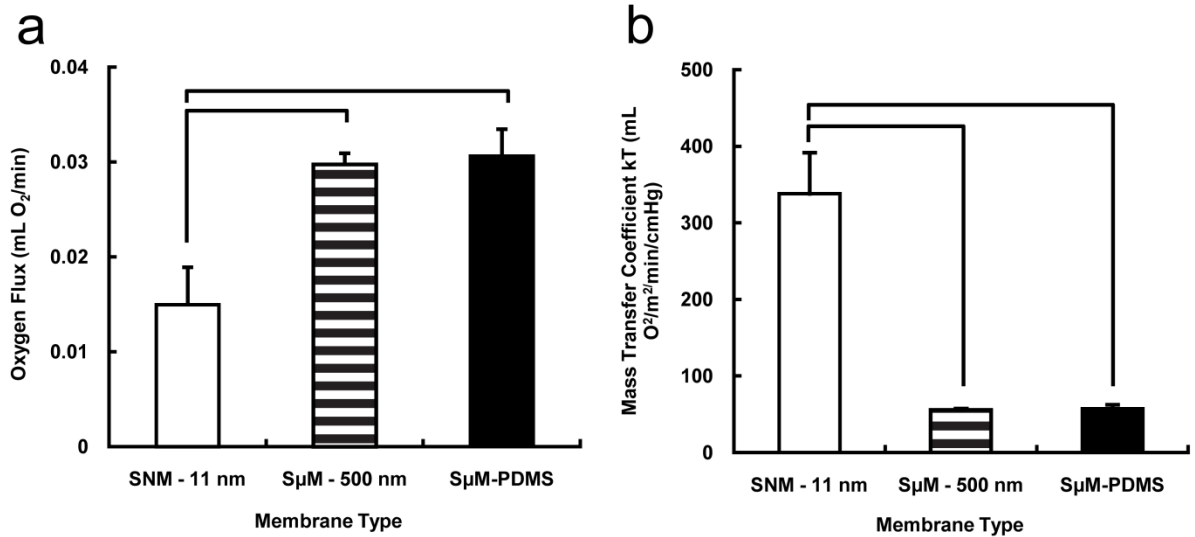


Fig. 2.7: Plots of (a) oxygen flux and (b) pore area-normalized mass transfer coefficient from silicon membranes downselected from bubble point experiments. Bars above chart indicate significant difference by one way ANOVA ($p < 0.05$).

A few hypotheses may help explain this nonlinear behavior. One possibility is that the small pores of the SNM are capable of inducing free molecular (Knudsen) flow of the oxygen gas. In a Knudsen flow regime, the frequency of gas molecule collisions with solid walls increases relative to the frequency of intermolecular collisions. This effect leads to higher gas flux through nanochannels that would otherwise be expected with Navier-Stokes continuum flow¹⁴⁴. To determine if Knudsen flow occurs through a nanochannel, the Knudsen number can be calculated as the ratio between the mean free path of the gas (λ) and the width of the channel (w):

$$Kn = \frac{\lambda}{w} \quad \text{Eq. 2.6}$$

The mean free path of oxygen is known to be 63 nm, making the Knudsen number equal to 6.19 through an 11 nm pore SNM. This Knudsen number falls short of the threshold for free molecular flow ($Kn \geq 10$), but is higher than the Knudsen number for continuum flow ($Kn \leq 0.01$). A Knudsen number between 0.01 and 10 implies that the SNM are in a “transitional” flow regime between free molecular flow and continuum flow.

To determine which flow regime most accurately describes the flux data, the experimental flux data through the SNM can be compared to predictions of Knudsen flow and continuum flow. In a continuum flow regime, the volume flow rate in mL/min can be calculated using:

$$Q_{continuum} = \frac{w^3 L (\rho_{in} + \rho_{out}) \Delta P}{12\mu \quad 2\rho_{out} \quad h} \quad \text{Eq. 2.7}$$

The corresponding volume flow rate in a Knudsen regime can be calculated through:

$$Q_{Knudsen} = C \frac{v_m w L}{4P_{out}} \Delta P \quad \text{Eq. 2.8}$$

where C is a geometry-dependent shape factor and v_m is the mean molecular speed. Formulas for calculating both C and v_m can be found in Fissell et al. 2011¹⁴⁴. Using Eq. 2.7 and Eq. 2.8, the volume flow rates for continuum and Knudsen flow were predicted for theoretical SNM pore sizes from 1-100 nm using the same experimental conditions as in the oxygen permeability test. The predictions are plotted against the measurements of SNM oxygen flux in Fig. 2.8. Ultimately, the average of the SNM measurements (9.57E-10 mL/min/pore) was an order of magnitude beneath the continuum prediction (6.91E-08 mL/min/pore), and several orders of magnitude below the Knudsen prediction (9.18E-06 mL/min/pore). This result differs from data in Fissell (2011), in which transport through SNM pores matched Knudsen predictions better than continuum models. However, the experiments of the Fissell study were conducted using an SNM between two gas compartments, whereas the experiments in this study involved membranes between a gas and liquid compartments. Considering the different study

conditions, even if the SNM induce Knudsen flow, the benefits of free molecular flow may be outweighed by transport behavior in the liquid compartment.

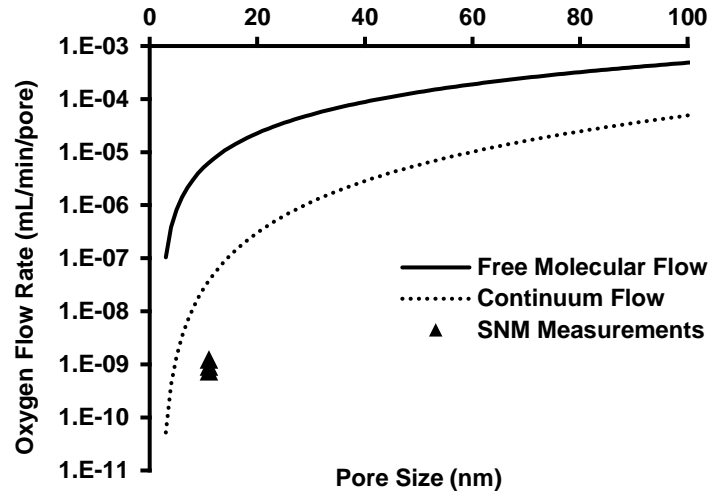


Fig. 2.8: SNM flux measurements plotted against continuum flow and Knudsen flow predictions.

Following the Knudsen calculations, the transport between the membrane and the liquid was examined to determine if transport within the liquid compartment was responsible for the nonlinearity between pore size and flux. From the analytical modeling described for this testing system in Dharia, et al (2017), the total coupled mass transfer coefficient can be related to mass transfer through the membrane and the liquid:

$$\frac{1}{k_T} = \frac{\delta_m}{P_m \cdot \rho_{STP}} + \frac{H}{c_L \cdot k_{O_2, H_2O}} \quad \text{Eq. 2.9}$$

The first entity in this equation represents transport through the membrane itself: δ_m is membrane thickness (m), represents membrane permeability ($\text{cm}_{STP}^3 \text{cm cm}^{-1} \text{min}^{-1} \text{cmHg}^{-1}$), and ρ_{STP} is the density of oxygen at standard temperature and pressure (mol/m^3). The second part represents transport through of gas through the liquid phase of the system: H is the Henry's Law Constant, c_L is the molar concentration of water. When using silicon membranes for gas-into-liquid transport, it can be assumed that transport

within the gas regime is instantaneous, and contributes little to transport resistance. By extension, transport through the silicon membrane can also be assumed instantaneous since the pores are filled with gas, reducing the mass transfer coefficient to:

$$\frac{1}{k_T} = \frac{H}{c_L \cdot k_{O_2, H_2O}} \quad \text{Eq. 2.10}$$

Essentially, this reduction leaves liquid phase as the largest determinant of transport in this regime, although the amount of open membrane area dictates how much of the membrane contributes to transport. Considering the importance of the liquid phase to overall gas transport, we speculate that the high area-normalized transport in SNM is due to phenomena within the liquid phase boundary layer. As oxygen gas exits the membrane, it enters a microns thick boundary layer that collects oxygen near the surface before it can diffuse into the liquid bulk. Within the boundary layer, the pores of both SNM and S μ M behave as point/area sources for oxygen, which can diffuse outwards laterally into the spaces between pores. The effect of this lateral diffusion implies the membranes yield a higher oxygen flux than the pore area alone would suggest, creating a nonlinear relationship between open pore area and oxygen flux. In S μ M, pore size and pore spacing are of similar magnitude, and the additive effect of the boundary layer lateral diffusion is likely minimal when flux is normalized by pore area. Comparatively, the pores of SNM are far smaller than the spacing between pores, and contribution of this accumulated oxygen to overall flux is far more evident than for the S μ M. The effect of this nonlinear relationship drives the transport of SNM to appear higher when normalized by open pore area, since the pores comprise such a small fraction of the overall membrane surface area. However, the accumulated oxygen in the boundary layer of the SNM is not sufficient to outdo the advantage of the overall open pore area of the current S μ M.

From the S μ M-PDMS flux data, the oxygen transport rates of the membranes were found to be 0.03 mL O₂/min, with a membrane area of 6.5e-4 m² at a 10 mL/min liquid flow rate. Although the device conditions of this study were not optimized for scale up, it is possible to use this transport data to

determine the operating conditions of a theoretical full-scale oxygenator. To oxygenate a 3.5 kg neonate with an oxygen requirement of 6 mL/kg/min, a total of 700 membranes would be needed with a membrane area of 0.455 m². This surface area is similar to that of the Maquet QUADROX-i Neonatal (0.38 m²), and could be reduced with fabrication of more porous membranes. However, at the flow rate used in this study, a scaled up device with 700 membranes and 0.455 m² of area would be capable of 7 L/min of blood flow, which far exceeds the 0.35 L/min cardiac output of a neonate. Ultimately, a future S μ M ECMO device will require optimization of the device design to fully scale the flow rate and oxygen transport to match patient requirements.

One drawback of this study is the limited range of pore sizes of membranes available. Between the SNM and S μ M, there is an unaddressed transitional range of 50-500 nm pores. It is possible that a membrane with pores in the transitional range would be better suited to meet bubble point and gas flux metrics than either the SNM or S μ M. A membrane with pores between 100-500 nm may have a higher bubble point than the current S μ M for more pressure resistance, while also retaining the higher pore area of the S μ M for more gas flux.

2.4 CONCLUSION

This study demonstrates that silicon membranes can be used with high sweep gas pressures and yield high-efficiency oxygenation *in vitro*, opening up possibilities for use as ECMO membranes. The highest gas transfer and rupture resistance was seen with the S μ M coated with PDMS, making this type of membrane the most suitable silicon membrane for ECMO. Subsequent research on device design would be required to scale the membranes to meet clinical oxygenation needs. Further optimization of the device design would be needed to establish the effects of channel height, liquid flow rate, and membrane pore distribution on oxygen flux. With optimization of the device design, silicon membranes could be employed for robust, high efficiency oxygenation.

CHAPTER 3

SILICON MICROPORE-BASED PARALLEL PLATE MEMBRANE OXYGENATOR

Substantial portions of this chapter have been published in Artificial Organs (2018); 42:2 166-173

3.1 INTRODUCTION

Extracorporeal membrane oxygenation (ECMO) is a life support system that circulates the blood through an oxygenating system to temporarily (days to months) support heart or lung function during cardiopulmonary failure until organ recovery or replacement. Over the past two decades, ECMO has become more common, and is now used to treat nearly 8000 patients annually worldwide, including a fivefold increase over the past decade in the adult population^{3,157,158}. Still, commercially available ECMO systems have considerable drawbacks and limitations, including the most common complication of bleeding¹⁵⁹. There have been several approaches to improve on ECMO technology including further refinement of hollow fiber membrane technology, or use of microfluidic soft lithography to approximate human lung architecture⁵⁵. However, these approaches have inherent limitations that lead to membrane fouling and risk of thrombosis, necessitating the use of high levels of anticoagulation. As an alternative to these systems, our lab has adopted an alternative strategy utilizing MEMS (microelectromechanical systems) fabrication techniques to create novel gas exchange membranes consisting of a rigid silicon micropore membrane (S μ M) support structure bonded to a thin film of gas-permeable polydimethylsiloxane (PDMS). The silicon membrane support structure provides structural integrity, which allows for the PDMS layer to be an order of magnitude thinner than commercially available polymer membranes¹⁶⁰. We anticipate that the composite S μ M-PDMS membranes will yield efficient

oxygen transport, and can be arranged in a parallel plate design that can be readily modified to finely tune the blood flow path to allow for optimized hemocompatibility. The goal is to house the S μ M-PDMS membranes in a compact design with an improved hemocompatibility profile compared to the current standard of care. In this paper, we develop a proof-of-concept parallel plate membrane oxygenator and demonstrate *in vivo* feasibility in a porcine model.

3.2 MATERIALS AND METHODS

3.2.1 Fabrication of the Silicon-PDMS Membrane and Flow Cell

The fabrication of the S μ M-PDMS membrane is based on prior work in this lab on silicon nanopore membranes, with adaptations specific to this project^{128,131,138,160}. Briefly, the prior work describes a process by which controlled growth of silicon dioxide produces arrays of sub-100 nm rectangular pores within silicon wafers (Fig. 3.a). For this study, the process was modified to utilize lithographic patterning to define pore dimensions at the 500 nm-1000 nm range. To create the PDMS layer of the composite membrane, a multilayered sacrificial substrate was used to transfer the thin layer (3-5 μ m) of polydimethylsiloxane (PDMS) to the S μ M (Fig. 3.b). A thick layer of Sylgard 184 PDMS (Dow Corning, Midland, MI) was mixed at a monomer-to-crosslinker ratio of 10:1, spin coated (500 RPM for 10s) onto a 4 inch silicon wafer, and cured for 2 hours at 80°C. Then, the surface was treated with O₂ plasma (100W, 20s, 200SCCM) to make the surface wettable. Subsequently, a second sacrificial layer of polyvinyl alcohol (PVA) 5% w/w in water was spin coated (1000 RPM, 30s) onto the PDMS layer, cured at 60°C for 1 hour, and slowly cooled to room temperature. As the final thin layer of PDMS, mixed Sylgard 184 was diluted with hexanes (Sigma Aldrich) at a 1:1 ratio, and spin coated directly on top of the layer of PVA (6000 RPM, 300s). The thick PDMS-PVA-thin PDMS construct was peeled off the silicon wafer and bonded to the S μ M membrane using oxygen plasma to activate both surfaces (100W, 20s, 200 SCCM). After at least 12 hours of bonding time, the membranes were submerged

in 70°C water for 3-4 hours to fully dissolve the PVA layer and release the thick PDMS layer, leaving the thin PDMS layer (3-5 microns) bonded to the S μ M.

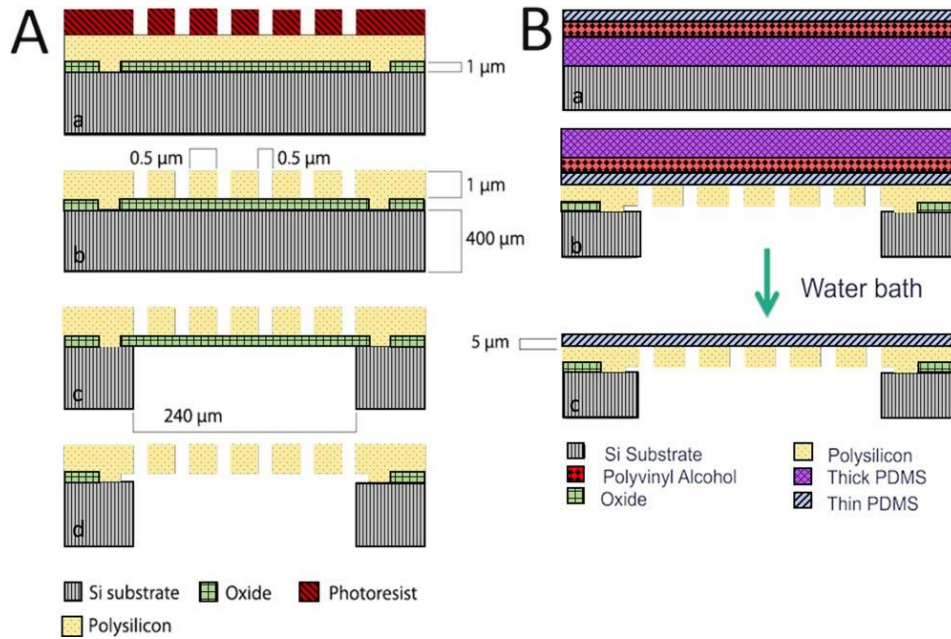


Fig. 3.1: Schematic of the fabrication of the silicon micropore membranes (1a) and of the PDMS transfer process (1b) to achieve 3-5 micron thick PDMS layer bonded to the silicon micropore membranes.

3.2.2 Oxygen Diffusion Through Membranes

Oxygen diffusion through the S μ M-PDMS membranes was determined by measuring the oxygen concentration change in degassed water after passing over the membrane, similar to previous work and shown in Fig. 3.2^{161,162}. A 6.5 cm x 1 cm PDMS-S μ M membrane was mounted into a machined polyether ether ketone (PEEK) flow cell with a water channel height of 200 microns, such that the PDMS would be in contact with the water while the silicon support structure was exposed to sweep gas. Oxygen was then removed from water by bubbling in nitrogen gas to establish a low starting concentration of oxygen in the water. This degassed water was pumped across the membrane at a rate of 10 mL/min (Cole Palmer pump) with an optical oxygen sensor (NeoFox inline optical oxygen sensor - Ocean Optics, Dunedin, FL) at the distal end of the device (Fig. 3.2). For each measurement, pure oxygen was used to pressurize the sweep

gas and the resulting oxygen flux into the water from the membrane was determined by the oxygen sensor. The pressurized sweep gas of pure oxygen was held between 2 and 10 PSI to establish a trans-membrane partial pressure gradient of between 800 and 1200 mmHg. The upper range of these pressures was chosen to be less than half the pressure at which mechanical failure occurred of the S μ M-PDMS membrane.

At the end of each test, the oxygen supply was removed and the sweep gas was vented. The coupled oxygen permeability coefficient k_{O_2} was determined using the following formula ($\text{mL O}_2 \text{ min}^{-1} \text{ m}^{-2} \text{ cmHg}^{-1}$), where is $\Delta[\text{O}_2]$ the concentration of oxygen before and after the device ($\text{ml O}_2 \text{ ml water}^{-1}$), Q_{H_2O} is the flow rate of fluid (ml water min^{-1}), A_m is the membrane area (m^2), and P_{O_2} is the partial pressure of oxygen in the sweep gas and in the water at the start and end of the membrane (cm Hg).

$$k_{O_2} = \frac{\Delta[\text{O}_2] \cdot Q_{H_2O}}{\left(P_{O_2, gas} - \frac{P_{O_2, H_2O, f} + P_{O_2, H_2O, i}}{2} \right) \cdot A_m} \quad \text{Eq. 3.1}$$

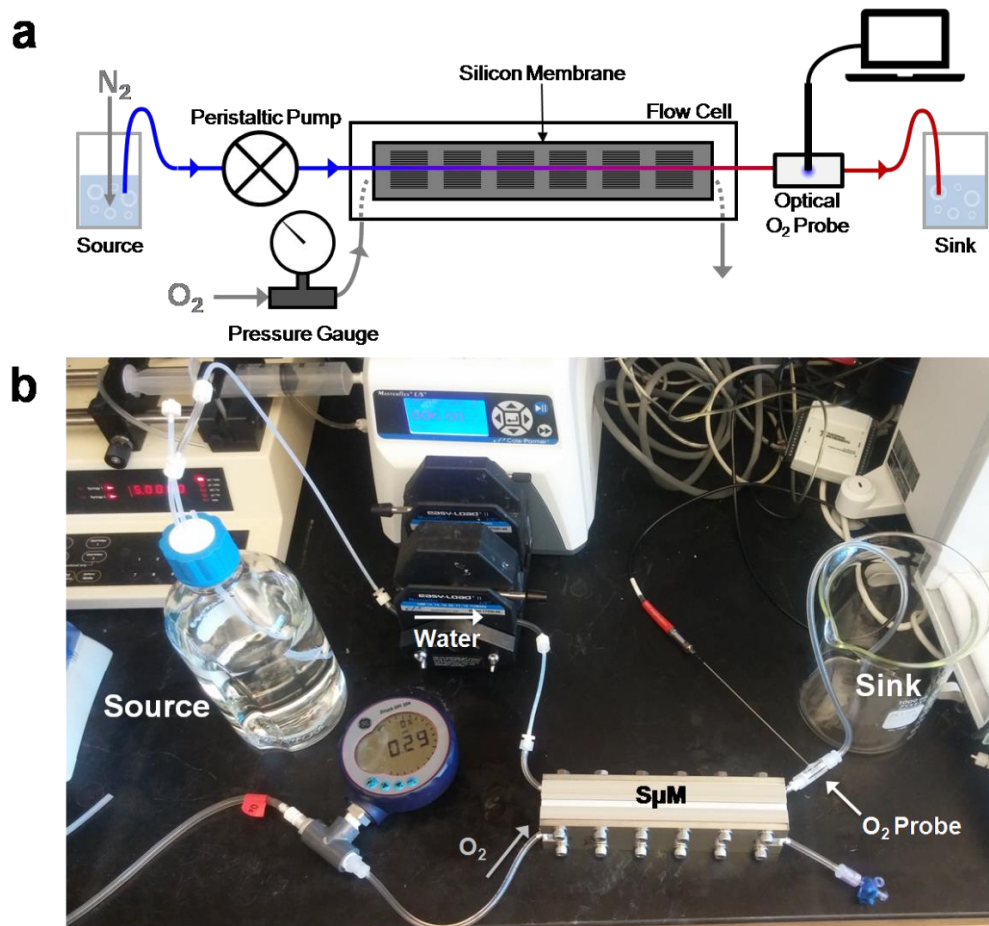


Fig. 3.2: Diagram (a) and picture (b) of experimental setup to measure oxygen diffusion into water.

3.2.3 Blood Oxygenation in an *In Vivo* Porcine Model

Oxygen permeability for the S μ M-PDMS membranes arranged in a parallel plate geometry was determined in an *in vivo* porcine model. Four membranes were secured into each half of a titanium flow cell using epoxy (Epoxy Technology OD2002) for eight total membranes per device (Figure 4). The two halves were then assembled using 125 μ m silicone gaskets to guide the sweep gas path, as well as seal the blood path. The channel height of the blood flow path was estimated to be approximately 100-125 μ m for each of the devices, with some uncertainty related to gasket compression. The channel flow path was roughly 4 cm wide and 6.5 cm long. Each flow cell was tested for leaks with deionized water prior to each

experiment. Over a series of three separate experiments, ~55 kilogram Yorkshire pigs were sedated, anesthetized, anticoagulated with heparin to goal ACT > 400 seconds, and their trachea were intubated. Two 16 French venous sheaths were placed into the right internal jugular and the left femoral vein of each pig. Using a mixture of nitrogen and oxygen as the inhaled gas, the pig's peripheral oxygen saturation was lowered to 80% for the entirety of the study. After the pigs reached a steady oxygen saturation state, a sweep gas of pure oxygen was applied to the backside of the silicon membranes. Blood was pulled from the femoral vein and pumped through the blood channel of the flow cell and returned to the animal via the internal jugular vein. In these experiments, blood flow rate was mostly kept at 25 mL/min, with some samples taken at 15 and 50 mL/min to examine the effect of flow rate on oxygen flux into blood. Samples of blood were taken proximal and distal of each the device simultaneously every 15 minutes for 3 hours. Blood samples were run on an iStat ABG - G8 cartridge to determine O₂ content in ml O₂ per ml of blood (Eq. 3.2)⁴³, where Hg is the hemoglobin of the blood (mg ml⁻¹), SaO_2 is the percent of hemoglobin that are bound to oxygen, and PaO_2 is the partial pressure of oxygen in the blood (mm Hg).

$$[O_2] = 1.36 \cdot Hg \cdot SaO_2 + 0.0031 \cdot PaO_2 \quad \text{Eq. 3.2}$$

The difference in oxygen content pre- and post-device was used to determine the gas permeability of the membranes in this device. This analysis was based on a modified Eq. 3.1, where Q_{H_2O} is broken into

V_{blood} (volume of blood within the device in ml) and t (residence time within the device in minutes)

(Eq. 3.3).

$$k_{O_2} = \frac{\Delta[O_2] \cdot V_{blood}}{\left(P_{O_2, gas} - \frac{P_{O_2, blood, f} + P_{O_2, blood, i}}{2} \right) \cdot t \cdot A_m} \quad \text{Eq. 3.3}$$

At the conclusion of the study, the animal was sacrificed as per protocol that was approved by the Institutional Animal Care and Use Committee (IACUC) at SurpassInc CRO (Mountain View, CA) and the assembly was dismantled and inspected for gross clots and membrane defects.

3.2.4 Model Formulation

A model to predict and describe oxygen transport in the PDMS-S μ M oxygenator was developed to provide insight into variables to focus on for future refinement. Similar to prior gas transport models, this model also accounts for non-porous regions of the membranes which create a heterogeneous gas exchange surface. For details on model derivations please see supplementary information, where the result is the equation:

$$\frac{q_L c_L}{H} \frac{dp_{L,b}}{dx} = k_o w_L (p_{C,b} - p_{L,b}) \quad \text{Eq. 3.4}$$

where q_L is the volumetric flowrate in the liquid, c_L is the liquid molar concentration, H is the Henry's law coefficient for oxygen in water, w_L is the channel width, x is the distance along the membrane length, p is partial pressure of oxygen in the sweep gas and at the liquid boundary layer, and k_o represents the overall mass transfer coefficient through:

$$\frac{1}{k_o} = \frac{H}{c_L k_L} + \frac{\delta_m}{P_m \rho_{STP}} \quad \text{Eq. 3.5}$$

In blood, hemoglobin acts as a sink for oxygen, dramatically decreasing the change in blood plasma oxygen concentration compared to that of pure water. The rate of change of occupied oxygen sites in blood hemoglobin (dC_{bound}) relative to the rate of change of free plasma oxygen (dC) can be related through a rearrangement of the Hill equation¹⁶³:

$$m = \frac{dC_{bound}}{dC} = np_{50}^n H C_H^{sat} \frac{p^{n-1}}{[p_{50}^n + p^n]^2} \quad \text{Eq. 3.6}$$

which depends on the saturated oxyhemoglobin concentration C_H^{sat} , the serum oxygen partial pressure at which fifty percent of oxygen sites on hemoglobin are saturated p_{50}^n , and the cooperative binding factor n . The m parameter can be then incorporated into the differential equations for the change in blood side oxygen concentration ¹⁶³:

$$q_L \frac{d(C + C_{bound})}{dx} = k_o w_L (p_{G,b} - p_{L,b}) \quad \text{Eq. 3.7}$$

$$\frac{q_L c_L (1+m)}{H} \frac{dp_{L,b}}{dx} = k_o w_L (p_{G,b} - p_{L,b}) \quad \text{Eq. 3.8}$$

For the case of no hemoglobin, $m = 0$ and Eq. 3.8 simplifies to Eq. 3.4.

The external mass transfer coefficients for the liquid channel can be taken as $k = Sh D_\infty / d_h$

where Sh is the Sherwood number and d_h is the hydraulic diameter of the flow channel. For a long, thin rectangular channel, the Sherwood number can be approximated by ¹⁶⁴:

$$Sh = 1.65 \left(\text{Re} Sc \frac{d_h}{L} \right)^{0.33} \quad \text{Eq. 3.9}$$

where $\text{Re} = \rho u_b d_h / \mu$ and is the ratio of momentum forces to viscous forces, and $Sc = \mu / \rho D_\infty$, and is the ratio of momentum diffusivity and mass diffusivity. In both cases, ρ is the solvent density and μ is the solvent viscosity.

3.3 RESULTS

3.3.1 Membrane Fabrication

Silicon micropore membranes were fabricated using a MEMS-based approach. The resulting wafers were diced into ~1cm x 6.5 cm rectangular membranes with a total porous region of 2.16 cm², comprising 9000 windows of pores with a pore density of 8.67E6 pores/cm². The pores were either 4 μm

long, 1 μm thick with a width of either 500 nm or 1 μm , depending on the specific device. The membranes had consistent pore distribution with a high level of pattern fidelity (Fig. 3.3). A thin layer of PDMS was plasma-bonded to the surface of the silicone micropore membrane to create a membrane to function as a membrane oxygenator that is resistant to mechanical deformation, while minimizing the membrane thickness. These composite membranes consisted of a thin gas permeable membrane coupled with a highly porous rigid support structure which were then secured into a flow cell.

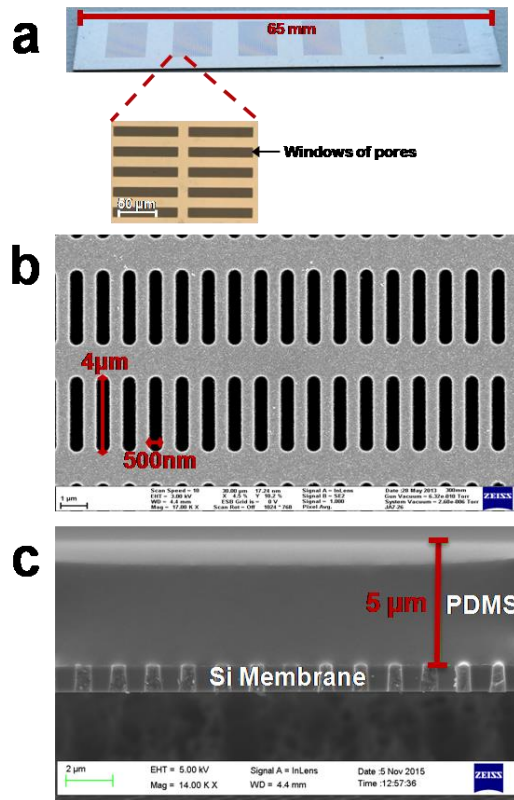


Fig. 3.3: The S μ M membrane was fabricated with the windows of pores as seen under bright field and individual pores as seen by SEM imaging (a and b). A thin layer of PDMS was bonded to the surface of the membrane and imaging was accomplished with SEM (c). This shows both the rigid silicon support structure and a gas permeable membrane consisting of PDMS.

3.3.2 Oxygen Diffusion of the Membranes

Oxygen permeability of the S μ M-PDMS membranes was determined using a water-based testing system to obtain reproducible, non-destructive data. From Eq. 3.1, oxygen permeability for S μ M-PDMS membranes was found to be $3.03 \pm 0.42 \text{ mL O}_2 \text{ min}^{-1} \text{ m}^{-2} \text{ cmHg}^{-1}$.

Testing in a simplified system was critical to develop the model of oxygen transport in our membrane oxygenator. We needed to determine the oxygen permeability of PDMS treated with plasma, which is known to be lower than that of untreated PDMS but is not defined in the literature¹¹⁵. To do this, we used the experimentally-derived pure water data to implicitly determine the membrane permeability by fitting experimental water data to the theoretical model (Eq. 3.8). Minimization of the square of the difference between model output (with changing P_m) and experimental data resulted in an optimized value of $P_m = 309.5 * 10^{-10} \text{ cm}^3_{\text{STP}} \text{ cm cm}^{-2} \text{ s}^{-1} \text{ cmHg}^{-1}$ (Barrer). Fig. 3.6a depicts experimental water results and model output using this membrane permeability under three operating conditions. As per model predictions, the results confirm that higher flow rates lead to smaller changes in water oxygen partial pressure due to shorter system residence time. Furthermore, at a given flow rate, higher driving pressure leads to greater overall oxygen diffusion into the working fluid. Finally, by determining of the oxygen permeability of the PDMS, we were able to apply the model to the subsequent blood testing and validate the model.

3.3.3 Blood Oxygenation in an *In Vivo* Porcine Model

Oxygen transport into whole blood was accomplished using an *in vivo* porcine model to determine the oxygen transport of the S μ M-PDMS membrane. Using Eq. 3.3, the oxygen permeability of the S μ M-PDMS membranes into whole blood was found to be $1.92 \pm 1.04 \text{ mL O}_2 \text{ min}^{-1} \text{ m}^{-2} \text{ cmHg}^{-1}$ (Fig. 3.4). No occlusive clots were noted over the S μ M-PDMS membranes after disassembly, although small non-occlusive clots were noted at the exits of the devices (Fig. 3.5).

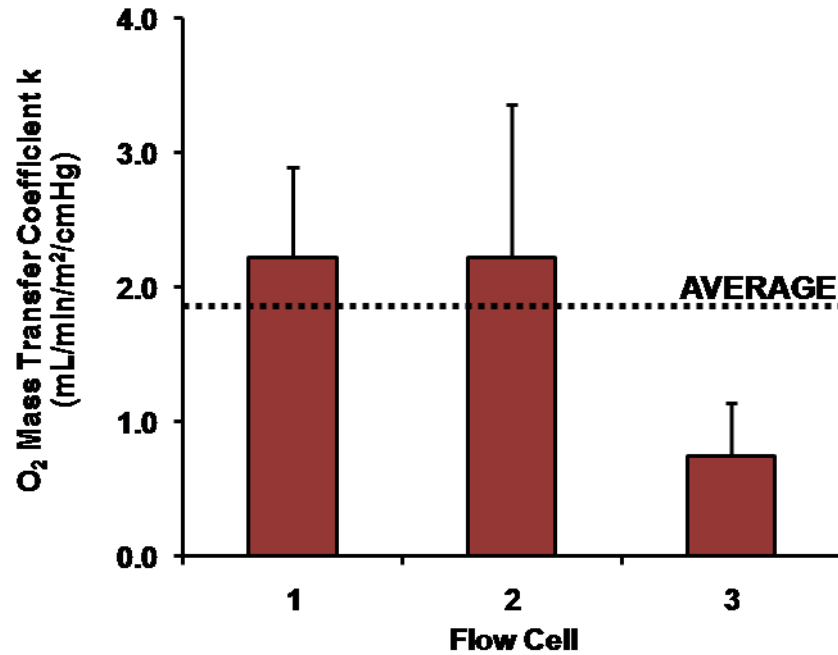


Fig. 3.4: O₂ permeability for three separate flow cells ± SD. Combining all flow cells, average gas permeability was found to be 1.92 ± 1.04 ml O₂ STP/min/m²/cm Hg (n=7 for each of the three flow cells).

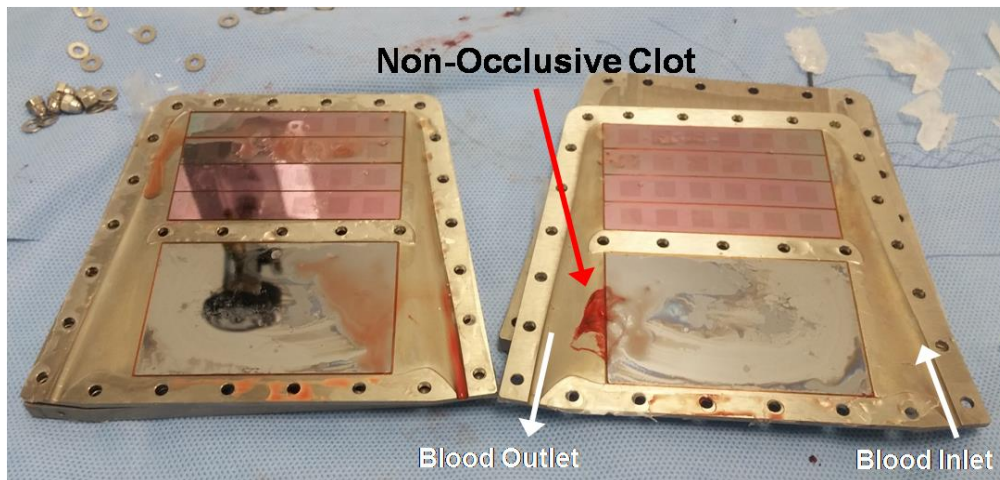


Fig. 3.5: Picture of flow cell with top and bottom half of the blood flow path exposed after *in vivo* test. Fig. 3.6b compares the model output with experimental blood data. Most of the experimental blood data was collected at a flow rate of 25 mL/min, with the model prediction well within the standard deviation of the experimental results. At blood flow rates of 15 mL/min and 50 mL/min, where only one to two data points were collected, there still appears to be relatively close agreement with the model.

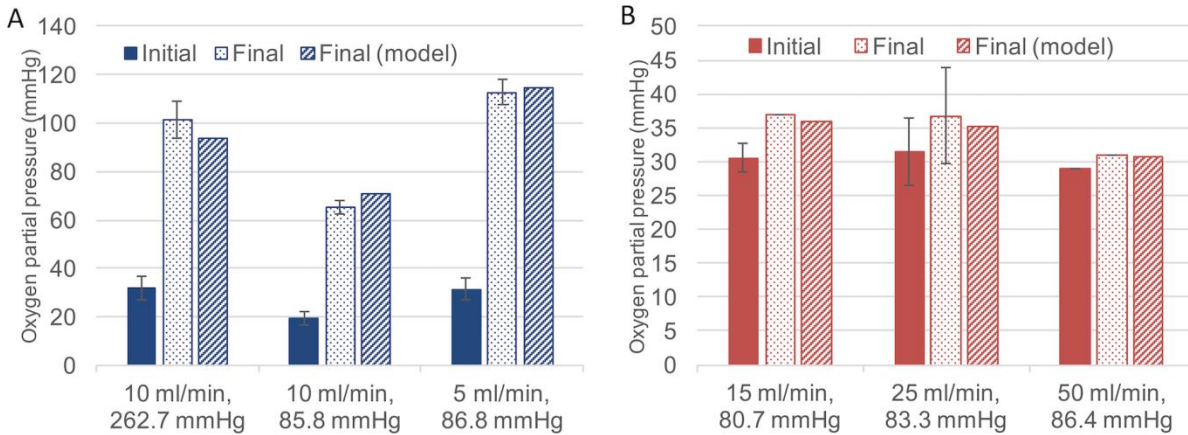


Fig. 3.6 Comparison of model output with experimental water data (a) and experimental blood data (b) showing the partial pressure of oxygen at a particular water or blood flow rate at a certain sweep gas pressure before and after (both experimentally and model-predicted) the device.

3.4 DISCUSSION

In this study, we designed and built a parallel plate silicon membrane oxygenator, and developed an accompanying analytic model to predict gas transport. Initial testing and model development was performed in a simplified water setup with subsequent validation *in vivo*. Consistent with the model, the porcine *in vivo* testing showed a silicon membrane oxygenator able to achieve effective oxygen flux.

There are several advantages of the $S_{\mu}M$ -PDMS membrane when compared to hollow fiber membrane technology. By using the porous rigid support structure of the silicon membrane, the layer of highly gas permeable PDMS can be an order of magnitude thinner than hollow fiber membranes. This thinness prevents the membrane itself from hindering gas exchange through the oxygenator, as has been shown in Abada et al (2018) ¹⁶⁰. Additionally, the ability to resist mechanical deformation with the underlying rigid support structure allows this device to be operated at sweep gas pressure over 258 mm Hg (5 psig), thus creating a high driving pressure of oxygen into the blood. These advantages of thinness and mechanical resistance are unique to this design since other technologies, such as hollow fiber membranes and microfluidic devices, would be at risk for mechanical failure and air embolism if using

such high sweep gas pressures with thin membranes. Although additional work is needed to further improve the efficiency of the membranes, this can necessitate less surface area required to achieve adequate gas exchange and will improve hemocompatibility by decreasing foreign material to blood contact. In regards to improving hemocompatibility, perhaps more important is the ability to precisely control the blood flow path, including the shear stress and pressure drop, within the device. In this device, since the membranes are flat sheets, a laminar flow pattern is established and engineered to prevent areas of high shear and turbulence while avoiding areas of stagnation. This can be seen as an advantage when being compared to the relatively disorganized blood flow path of hollow-fiber membranes. The clear tradeoff in establishing a laminar, more organized blood flow pattern is that the liquid-side boundary layer becomes more significant to gas flux resistance, and has the potential to strongly limit gas transport^{161,165}. Since this was a proof-of-concept experiment, there remain several limitations to the data. First, we used relatively low blood flow rates to generate the gas transport data. The flow rate was limited in part to size of the overall device as well as the narrow channel height. Given the small channel height, the flow rates were kept such that the pressure drop across the device was not excessive. Additionally, considerable variability of oxygen transport measurements was observed both between devices, and during a single experiment using the same device. This variability could be related to the use of different blood flow rates, error in the measurement tools, variable blood flow from transient clots, or air bubbles initially in the device. The difference between the mass transfer coefficient between the water studies and the blood can be explained by different channel heights, flow paths, flow rates, and membrane fouling after exposure to blood, but the exact reason for the difference will need further study.

This work can be used to guide the design and fabrication of future generations of devices. The first modification will be focused on optimizing the balance between smaller channels with superior gas transport with taller channels that have acceptable pressure drop and shear stress to avoid hemolysis and activation of the coagulation cascade¹⁹. In this version of the device, there was a large pressure drop

across the device of just over 100 mmHg, compared to current membrane oxygenators that have an overall pressure drop of less than 40 mmHg. Future devices will likely require larger channel heights to decrease pressure drop, which will need to be assessed effects on mass transfer. The modeling that was developed in this work aims to predict how system changes, such as changes in membrane geometry and blood flow properties, would affect the rates of oxygen transport. The data from the water tests were used to define the oxygen permeability of our plasma-treated membranes, which was then used in the subsequent blood studies. This model built on prior work in the literature to describe oxygen transport by incorporating membrane geometry to better predict gas flux. Still, since the model has only been validated for a small number of flow rates with a single channel height, we will need additional data to ensure the model continues to perform well under a variety of flow rates and channel heights.

Future iterations of the next generation S μ M-PDMS membrane oxygenator will build upon the flow path and mass transfer data collected in this study. As a focus of this future work, gas transfer efficiency may be improved through studying disruption of the liquid-side boundary layer, overcoming the liquid mass transport resistance. This disruption can include the use of surface mixers or the use of sound waves to increase the rates of gas transport^{166,123,167}. While these techniques have the potential to increase gas transport efficiency, they will need to be closely examined for negative effects on device hemocompatibility. Once the flow cell and membrane are fully optimized, additional studies will need to be conducted to specifically answer if this approach does indeed improve hemocompatibility of membrane oxygenators, and how this ultimately affects the whole ECMO system. While the S μ M-PDMS membrane oxygenator is still early in development, this initial work provides the rationale and the tools to proceed with investigating the use of silicon micropore membranes for the use of ECMO systems.

CHAPTER 4

PEG-SILANE COATING VARIATIONS ON SILICON AND PDMS FOR IMPROVED HYDROPHILICITY

4.1 INTRODUCTION

Polydimethylsiloxane (PDMS) elastomers have long been used in the development of biomedical microfluidic devices owing to their machinability, mechanical strength, and biological inertness^{168,169}. An additional property of PDMS – high gas permeability to oxygen and carbon dioxide – has led researchers to design extracorporeal membrane oxygenation (ECMO) devices consisting of stacked layers of PDMS forming capillary-like blood channels^{55,106,112,170}. These PDMS oxygenators optimize blood flow dynamics through precisely engineered parallel plate channels, while utilizing the high gas permeability and mechanical strength of PDMS to effectively exchange gas with the blood. Similarly, we have developed a parallel plate oxygenator consisting of composite silicon-PDMS membranes that are capable of robust, efficient gas transfer^{143,160}. Compared to the PDMS microfluidic devices, the use of a PDMS film surface reinforced by silicon micropore membranes (S μ M) allows us to build composite membranes that leverage the nonreactivity of PDMS, as well as the mechanical robustness of the S μ M-PDMS combination¹⁶⁰. Crucial to any PDMS-based blood oxygenation devices is the ability of PDMS to withstand continuous blood contact without thrombosis within the blood channels⁵⁵. In order to meet clinical needs of ECMO patients, the PDMS-based oxygenators must be able to remain patent for a minimum of 6 hours, and not trigger formation of thrombi that occlude the channel or travel downstream

to the patient . As such, ensuring the hemocompatibility of PDMS is highly important to PDMS oxygenator development.

While PDMS is not a bioactive material, it is naturally very hydrophobic, demonstrating water contact angles around 100-120°^{168,171}. Hydrophobic materials in contact with blood are known to attract proteins and cells to their surfaces, causing rapid biofouling and clot formation^{15,172}. Furthermore, hydrophobic microfluidic devices are subject to poor wettability and consequently poor flow performance^{124,173}. To address the hydrophobicity and biocompatibility of PDMS, many researchers working on PDMS microfluidic devices have devised treatments that attempt to engineer a stable, hydrophilic surface^{173,174}. Physical surface modifications, commonly oxygen plasma treatment, can create a suitably hydrophilic surface on PDMS through the creation of surface hydroxyl groups¹⁷⁴⁻¹⁷⁶. However, PDMS undergoes continuous rearrangement as uncrosslinked polymers migrate throughout the bulk structure, leading to “hydrophobic recovery” as the surface hydroxyl groups migrate into the bulk^{177,178}. Due to the hydrophobic recovery of PDMS, developing a surface coating that maintains hydrophilicity over time is critical. Another approach to attaining PDMS hydrophilicity is to chemically modify the surface by attaching hydrophilic surface coatings. Considerable research has been conducted on a variety of hydrophilic surface coatings to PDMS, which can be covalently modified with silane groups after activating the PDMS surface through plasma treatment^{124,174,179-181}. An ideal coating for a blood-contacting PDMS surface would be hydrophilic, omniphobic to both cell and protein adhesion, and would remain stable on the surface for extended periods of time.

One common surface coating that is frequently used in biomaterials research is polyethylene glycol (PEG), which has historically been an effective coating to improve hemocompatibility^{124,174,182,183}. The hydrophilic PEG chains on a surface sterically hinder the adhesion of cells and proteins, combining physical deterrence and hydrophilicity. A silane derivative of PEG can be used to modify silicon or PDMS – both constituents of our $S_{\mu}M$ -PDMS membranes. In our past work with silicon membranes, we

have developed protocols to attach PEG as an alkoxy silane to silicon surfaces, and shown that PEG attachment reduces protein fouling and cell/platelet adhesion^{131,135,184}. Although these studies showed clear benefits to PEG application, another recent study from our lab using the same protocol showed no improvement in omniphobicity with PEG-modified silicon, calling into question if this protocol would be successful over time¹⁴¹. Other research groups have also shown substantial hemocompatibility benefits with PEG on PDMS, including near-negligible fouling and sustained stability^{124,178,181}. One such protocol, described in Kovach, et al (2014), was specifically developed improve the hemocompatibility of a PDMS-based blood oxygenator, and uses the same PEG-silane derivative as our previous work¹²⁴. If we employ PEG-silane to modify our oxygenator membranes, we would need to determine the optimal protocol conditions that result in a stable, hydrophilic chemical modification to our silicon-PDMS composite.

In this study, we examine multiple protocols for the application of PEG-silane to silicon and PDMS substrates to determine which, if any, improves hydrophilicity and *in vitro* protein fouling resistance. After applying PEG-silane films to the surfaces, we also perform additional characterization using ellipsometry and atomic force microscopy (AFM) to determine what attributes of the films result in superior fouling resistance. Using this information, we speculate if any modification of PEG may be able to protect the μM -PDMS membranes from sustained blood contact.

4.2 MATERIALS AND METHODS

4.2.1 Silane Application

4.2.1.1 Substrates

Three substrates were prepared for testing the coating protocols, as seen in Fig. 4.. The first substrate – abbreviated as Si – consisted of 1 cm² pieces of silicon cut from 400 μm -thick double side polished, p-type wafers. This substrate was similar to past work from our lab^{131,141,142}, and was used to compare results between this work and prior studies. As a surrogate for silicon membranes, pieces of Si substrate were bonded on one face with a 5 μm -thick layer of PDMS, creating the Si-PDMS substrate.

Briefly, this PDMS layer was formed from spin-coated Sylgard 184 PDMS (Dow Corning, Midland, MI, USA) mixed at a 10:1 elastomer-to-crosslinker ratio, and then diluted 1:1 with hexanes (Millipore Sigma, Burlington, MA, USA). Further processing methods can be found in Dharia, et al (2017)¹⁴³. The final substrate consisted of undiluted Sylgard 184 PDMS mixed at a 10:1 elastomer-to-crosslinker ratio, which was cast into a 3 mm-thick sheet and cut into 1 cm² discs. These discs – abbreviated as PDMS – were intended to mimic the PDMS microchannels from Kovach, et al. (2014)¹²⁴ and also act as a material control for the Si-PDMS group.

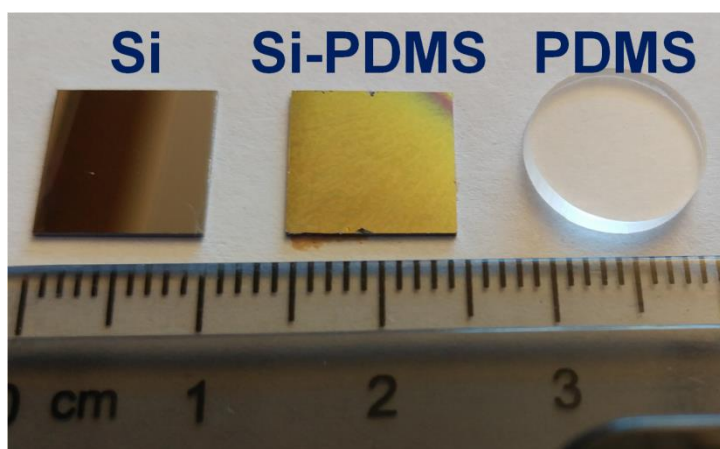


Fig. 4.1: Substrates for functionalization with PEG-silane.

4.2.1.2 PEG-Silane Application

Three different protocols were used to attach the PEG silane to the surfaces of the substrates. A comparison of the silanization methods can be found in Table 4.1. The first protocol (1A, Table 4.1) was adapted from previously described methods used in our lab^{131,139}. First, Si-PDMS and PDMS samples were treated with oxygen plasma (Harrick Plasma PDC-001, Harrick Plasma, Ithaca, NY) for 30 seconds at high power (~30 watts) to produce reactive hydroxyl groups on the surfaces. Si samples were activated with a 20-minute exposure to “piranha” solution, consisting of a 3:1 mixture of sulfuric acid (96%) and hydrogen peroxide (30%). After activation, all samples were then submerged in a 1% solution of PEG-

silane (6-9 monomer chain length, Gelest SIM6492.7, Morrisville, PA, USA) in pure ethanol within a glass petri dish. This mixture was heated to 70°C for 2 hours and mixed with a magnetic stir bar. Finally, after functionalization, the samples were washed three times each in ethanol and deionized water for 3 minutes per wash, totaling 6 washes.

Based on the methods described in Kovach et al (2014), a second protocol (2, Table 4.1) was employed to attach the PEG-silane with a higher silane density ¹²⁴. After plasma or piranha treatment of the surfaces, the substrates were submerged in a 1:1 mixture of PEG-silane and anhydrous acetone (SeccoSolv C992H04, Millipore Sigma, Burlington, MA) in a glass petri dish. This solution was kept at room temperature for 1 hour with no stirring. These samples were then washed twice each with acetone, ethanol, and water for 3 minutes per wash.

As a bridge between both PEG silanization protocols, a third method was adapted from both methods (1B, Table 4.1). After surface activation, the substrates were immersed in a 1% solution of PEG-silane in anhydrous acetone for 2 hours at 70°C under agitation by a magnetic stir bar. Due to the elevated temperature, the acetone in this protocol largely evaporated during functionalization, and was replenished as needed throughout the experiment. This solvent evaporation allowed a much higher concentration of the PEG silane to collect on the surfaces of the substrates. Washes were conducted in a manner similar to the first protocol.

Table 4.1: Reaction conditions for PEG protocols.

Reaction Condition	Protocol		
	1A	1B	2
Solvent	Ethanol	Acetone	Acetone
PEG Concentration	1%	1%	50%
Activation	O ₂ Plasma	O ₂ Plasma	O ₂ Plasma
Reaction Time	2h	2h	1h
Temperature	70°C	70°C	21°C
Stirring Applied	Stirring	Stirring	Static
Storage Time	7 days	7 days	7 days

4.2.2 Analysis of Silane Layers

4.2.2.1 Contact Angle

Contact angle, which measures hydrophilicity of a surface, was used to assess successful application of the silane coatings. Changes to the contact angle after applying a coating would indicate if surface modification had occurred, though wettability changes alone do not definitively confirm the presence of a coating. Sessile drop measurements using deionized water were recorded for each sample using a Biolin Scientific Theta Lite optical tensiometer (Stockholm, Sweden) with OneAttension software¹⁴¹. Samples were measured for contact angle on the day of coating (Day 0), stored in ambient air, and analyzed again 6 days later (Day 6) to mimic sample processing conditions in Kovach, et al¹²⁴. In waiting 6 days for further study, the hydroxyl surface groups created by plasma treatment could dissipate through hydrophobic recovery, allowing restoration of the underlying native surface^{177,178,185-187}.

4.2.2.2 ELISA

After 7 days of storage, the coatings were evaluated for *in vitro* protein fouling using a surface enzyme-linked immunosorbent assay (ELISA) of human serum albumin (HSA, A3782, Millipore Sigma, Burlington, MA, USA)^{141,142}. Briefly, each sample is incubated in a 1 mg/mL solution of HSA in PBS for 1.5 h at 37°C. The HSA is rinsed off with 0.5 mL PBS five times, and any unbound sites on the samples are then blocked with a 1 mg/mL solution of bovine serum albumin (BSA, ≥98%, Millipore Sigma, Burlington, MA) in PBS for 1.5 h at 37°C. Subsequently, the samples are rinsed again, transferred to new containers, and incubated for 1.5 h with a 10 µg/mL solution of anti-HSA antibody conjugated with horseradish peroxidase (ab19183, Abcam, Cambridge, MA). Samples are rinsed again, transferred to new containers, and treated with 0.5 mL of an aqueous solution of 0.5 mg/mL *o*-phenylenediamine (oPD, VWR Inc., Visalia, CA), 0.03% H₂O₂, and 0.05M citrate phosphate buffer (pH 5.0, Millipore Sigma, Burlington, MA). The reaction was protected from light for 7-10 minutes at room temperature to allow for color development, and then stopped with a 1M solution of H₂SO₄. Light absorbance of the solutions was

measured at 490 nm in triplicate. Protein adsorption data was normalized to two controls: a positive control of tissue culture polystyrene (TCPS), and a negative control of the uncoated substrate without HSA added. Since three different substrates were functionalized, the data for each substrate was normalized separately to a negative control of the same material.

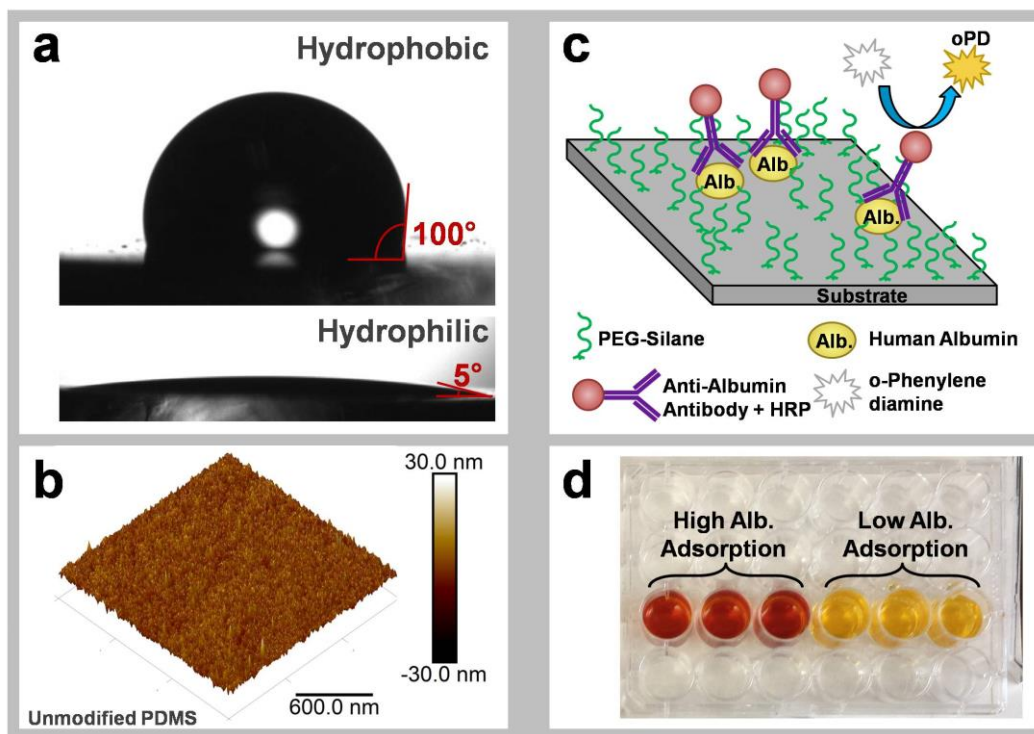


Fig. 4.2: Characterization methods of PEG-silane surfaces: (a) contact angle of hydrophilic and hydrophobic surfaces, (b) AFM scan showing topography of unmodified PDMS, (c) schematic of protein fouling ELISA showing the steps to yield oPD color change, and (d) example of high and low albumin adsorptivity in the protein ELISA

4.2.2.3 Ellipsometry

The thickness of the PEG coatings on the Si substrates was measured using a LSE Stokes ellipsometer (Gaertner Scientific, Skokie, IL). Methods are described in Iqbal, et al ¹⁴¹. Only the Si substrates could be assessed using ellipsometry because the ellipsometer used requires a reflective surface within 1 μm of the top of the sample, and both the Si-PDMS and PDMS substrates do not meet this

requirement. One Si sample of each coating group was characterized by measuring thickness in three locations on the surface, which were then averaged. The thickness measurements from the unmodified substrate were taken to be the thickness of the native oxide on Si, and the average thickness of the unmodified group was subtracted from all groups as a baseline.

4.2.2.4 AFM

The coated substrates were examined through atomic force microscopy (AFM) to visualize the morphology of the coatings. 3 μm by 3 μm surface scans of one sample of each group were taken in air using a MultiMode III (Digital Instruments, Santa Barbara, CA, USA) and Scanasyst-Fluid+ AFM probes (Bruker AFM probes, Santa Barbara, CA, USA) in PeakForce QNM tapping mode. The scans were processed using NanoScope Analysis software to obtain root mean square (RMS) roughness values for the substrates.

4.2.2.5 Statistical Analysis

A minimum of three measurements was taken for all samples in the contact angle and ELISA experiments. Statistical significance was determined using Graphpad Prism 8.2.0 (San Diego, CA, USA). Contact angle measurements were analyzed through two-way ANOVA. Tukey post-hoc tests were used to determine statistical difference ($p < 0.05$) between the same coating conditions on Day 0 and Day 6 of the experiment, and between different coating conditions at the same time point. ELISA measurements were analyzed for each substrate independently through one-way ANOVA, with Tukey post-hoc tests to determine significant difference between different coating conditions on the same substrate. Ellipsometry measurements on silicon were averaged for each substrate. The average thickness value of the unmodified Si substrate was considered native oxide, and this value was subtracted from all groups to normalize the data to the unmodified group. Significant difference in thickness was determined by one-way ANOVA with Tukey post-hoc tests.

4.3 RESULTS

4.3.1 Contact Angle

Measurements of contact angle (average \pm SD) taken on days 0 and 6 after coating application are shown in Fig. 4.3. Data from Si substrates (Fig. 4.3a) shows the hydrophobic recovery of the unmodified substrate after piranha activation, reaching 25° on Day 6. The contact angles of all PEG-modified groups are significantly higher than the unmodified group, and remain stable from Day 0 to Day 6. The contact angles of PEG 1A and 1B on Si were similar at $\sim 41^\circ$, while the contact angle of PEG 2 was significantly lower than the other PEG groups on both days – around 30° . The measurements of unmodified Si and PEG 1A on Si are similar to those published in Iqbal, et al., and also close to the manufacturer-specified contact angle of 36° ¹⁴¹. The steady contact angle over time indicates that a stable film of PEG may be present on all the Si modified surfaces. Both the Si-PDMS (Fig. 4.3b) and PDMS (Fig. 4.3c) substrates show that the unmodified PDMS surfaces are strongly hydrophobic – around 102° – and that plasma activation temporarily renders the PDMS hydrophilic^{124,185}. With the Si-PDMS substrates, all PEG-modified groups have similar contact angles at Day 0, generally $\sim 45^\circ$, which is similar to the Si substrates. However, by Day 6, all of the PEG groups exhibited statistically significant hydrophobic recovery, possibly indicating that any PEG coating may have degraded over time. Compared to the other two substrates, the PEG-modified PDMS pieces showed much lower contact angles on Day 0; all were insignificantly different at $\sim 24^\circ$. On Day 6, only the PEG 1A group showed hydrophobic recovery, and the PEG 1B and 2 groups remained stable.

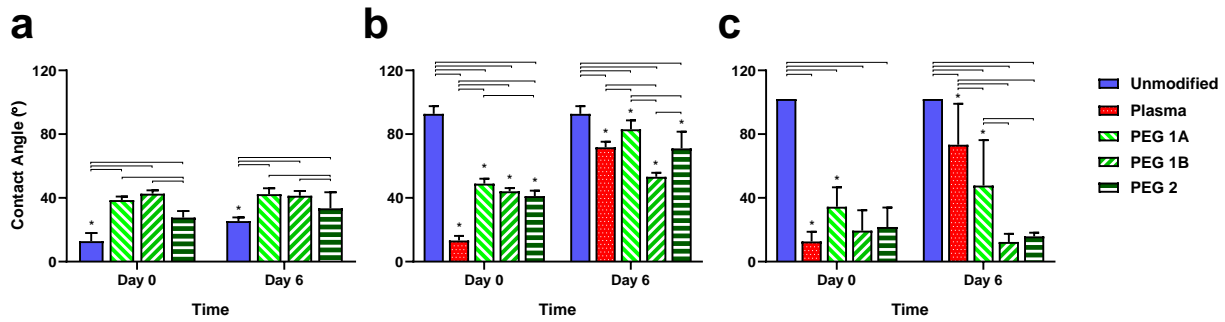


Fig. 4.3: Contact angle of PEG-silane on (a) Si, (b) Si-PDMS, and (c) PDMS. Statistical comparisons were drawn between the same coating conditions on Day 0 and Day 6, noted by * if $p < 0.05$, and between different coating conditions on the same day, noted by the bars above the columns if $p < 0.05$.

Based on the known contact angle of PEG-silane, it is likely that the Si and Si-PDMS surfaces were successfully PEG-modified in all groups on Day 0, though this result cannot be confirmed without additional characterization. Results on Day 6 indicate that the PEG was stable on the Si substrates, but the substantial hydrophobic recovery on Si-PDMS surfaces may indicate that the PEG on the surfaces was inconsistent, or degraded over time. Day 0 contact angles of PEG-modified PDMS groups were significantly lower than the manufacturer’s published values for contact angle. However, this data is consistent with values published by Kovach, et al, which showed a maximum contact angle of 27.2° with the PEG 2 protocol on cast PDMS¹²⁴. Two of the PEG groups – 1B and 2 – showed a steady contact angle over time, indicating that stable PEG modification had likely occurred. The PEG 1A group also showed less hydrophobic recovery than the plasma group, which may also point to some modification.

4.3.2 ELISA

Protein fouling results from the albumin ELISA are in Fig. 4.4. Within the Si group (Fig. 4.4a), unmodified Si showed a relative fouling of 33.8% of TCPS, which is less than the ~45% fouling in Iqbal, et al¹⁴¹. Relative to the unmodified control, only PEG 1B showed significantly less albumin fouling, at 23.7% of TCPS – 30.1% less than the unmodified control. While older data from our lab has shown a strong fouling reduction with the PEG 1A protocol on Si¹⁴², more recent data has shown that PEG-silane

makes little difference to protein fouling¹⁴¹. The Si-PDMS substrates (Fig. 4.4b) showed no significant difference between the unmodified and any of the PEG groups. Plasma treatment of Si-PDMS slightly increased albumin fouling compared to the unmodified group from 28.7% to 37.8% of TCPS. Within the PDMS group (Fig. 4.4c), the unmodified, plasma-treated, and PEG 1A groups showed the same level of fouling. Interestingly, the PEG 1B and PEG 2 groups showed a strong reduction in protein fouling, with both reaching the same low level as the PDMS experimental negative control – 0% on the graph.

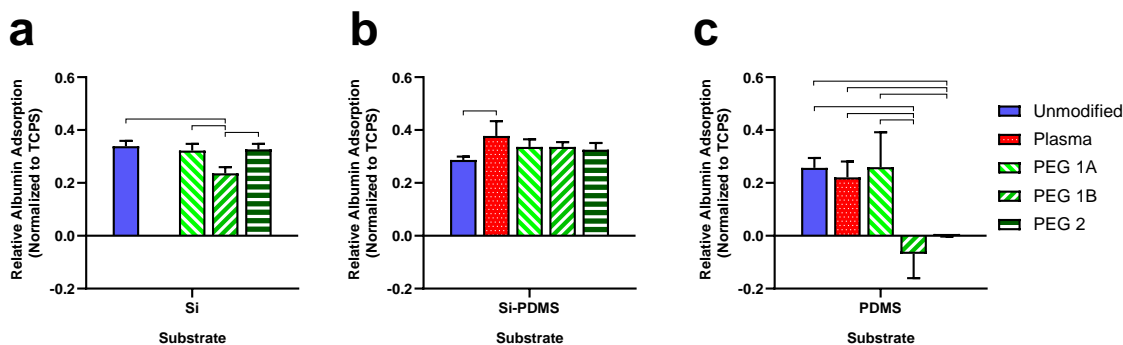


Fig. 4.4: Albumin fouling ELISA results for (a) Si, (b) Si-PDMS, and (c) PDMS. Significant difference within each substrate group ($p < 0.05$) is shown by the bars above the graphs.

Ultimately, PEG modification only strongly reduced protein fouling on the PDMS substrates, with some reduction seen with PEG 1B on silicon as well. Therefore, the PEG 1B protocol overall was the most effective at reducing albumin fouling of the surface. By contrast, the PEG 1A did not reduce fouling on any substrate, and the PEG 2 protocol was only effective on PDMS.

4.3.3 Ellipsometry

Ellipsometry measurements of coating thickness on Si substrates can be found in Fig. 4.5. PEG 1A had a thickness of 2.38 nm, which was not different from the unmodified group. The PEG 1B and PEG 2 groups had significantly thicker coatings at 12.4 and 17.5 nm, respectively. These coatings were significantly thicker than the unmodified and PEG 1A groups, though not different from each other.

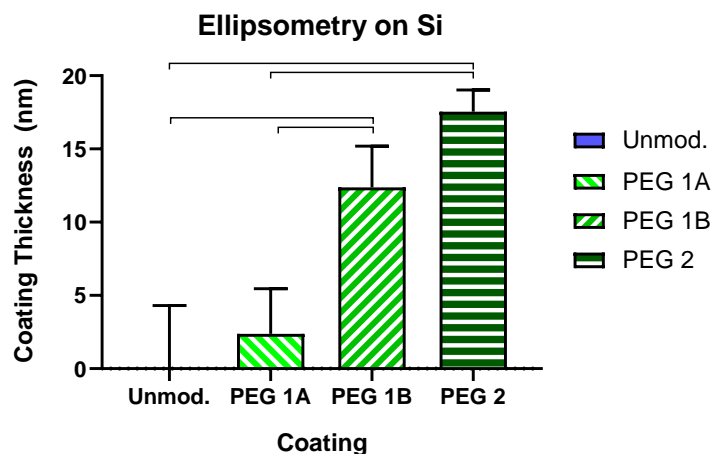


Fig. 4.5: Ellipsometry results on Si substrates, taking the thickness of the native oxide on the unmodified substrate to be a baseline. Significant difference is shown by the bars above the graph.

4.3.4 AFM

Topographic surface scans of the Si, Si-PDMS, and PDMS substrates can be seen in Fig. 4.6, with the corresponding roughness values below the scans. From the Si scans (Fig. 4.6a), most of the surfaces are smooth and featureless, except for the “islands” on the PEG 2 surface. Within both the Si-PDMS and PDMS samples, the unmodified PDMS surfaces start with a natural texture, with similar RMS values of 2.42 and 2.28 respectively. Plasma treatment then smoothens the texture, although the PDMS sample acquired several surface cracks¹⁸⁷. While the PEG-modified Si-PDMS were all nearly as smooth as the plasma sample, the PEG-modified PDMS pieces show a variety of wrinkled textures on the surfaces. Specifically, the PEG 1B sample shows a pronounced wrinkling of the entire surface, spanning ~60 nm in height. The PEG 1A substrate shows a similar texture, though less pronounced, while the PEG 2 substrate shows overall fewer, faint wrinkles. Compared to the plasma-treated PDMS, the presence of this wrinkled texture on all three PEG groups suggests that films may be present on the surfaces. Given the depth of the wrinkled patterns, these films are likely on the order of tens of nanometers thick.

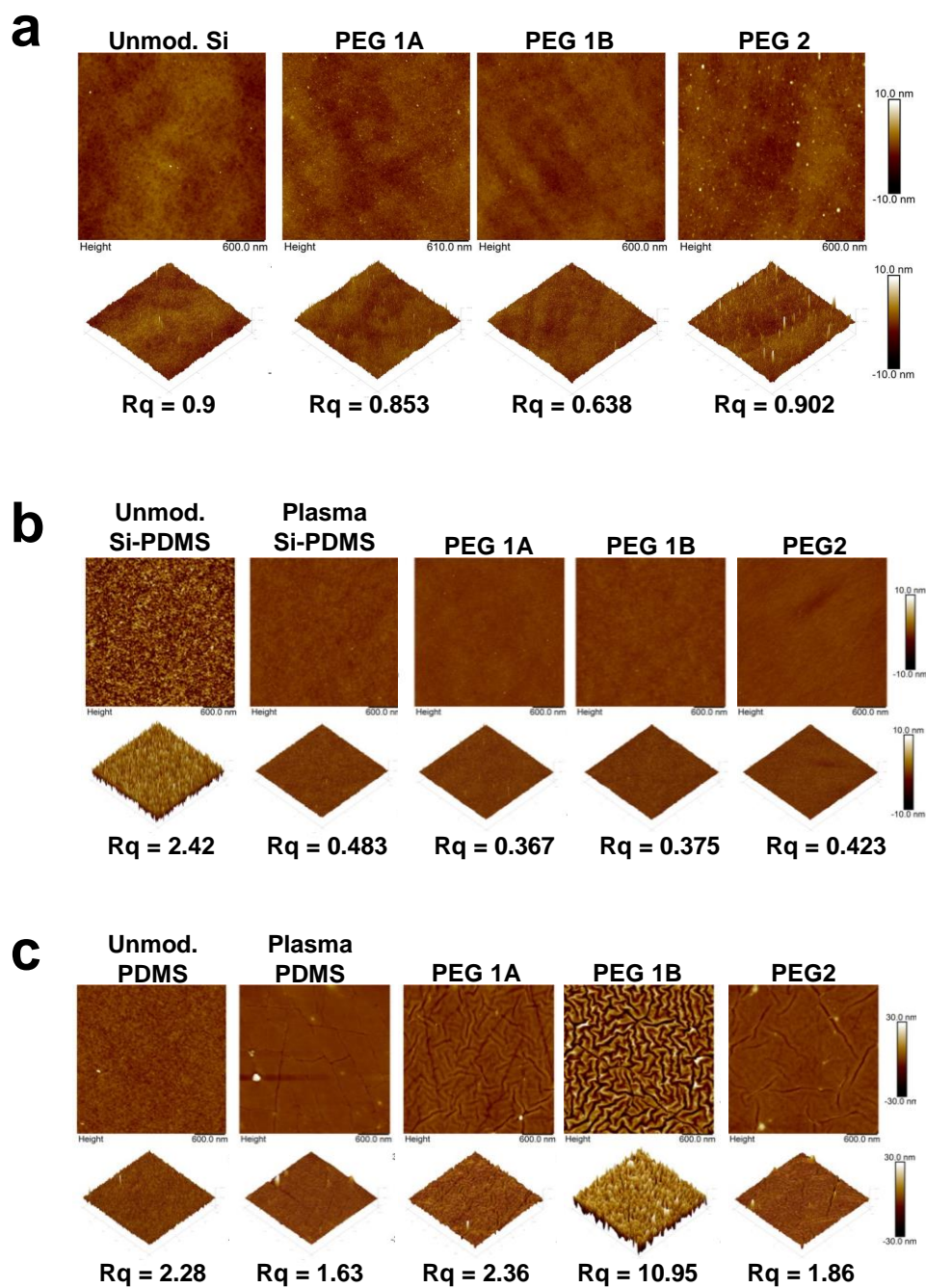


Fig. 4.6: AFM topographic scans of $3\ \mu\text{m} \times 3\ \mu\text{m}$ spots on (a) Si, (b) Si-PDMS, and (c) PDMS substrates. Each scan is shown in top view and at an angle. The Si and Si-PDMS scans are scaled to heights of -10 to 10 nm. The PDMS scans are scaled from -30 to 30 nm due to the increased feature roughness. Roughness values (Rq) are shown below the corresponding scans.

4.4 DISCUSSION

In this study, we examined multiple application protocols of PEG-silane to determine which protocol, if any, would improve the future biocompatibility of a PDMS surface for blood oxygenation. Since our membrane material was akin to the Si-PDMS substrate in this work, we sought a coating that would be stable on that substrate surface, possibly increase hydrophilicity, and reduce protein fouling. Ultimately, none of the coating protocols was able to meet all criteria. Comparing the results between all substrates may explain why the PEG-silane was ineffective on Si-PDMS specifically, and broadly how the PEG modification is altered by each protocol.

From the contact angle measurements, the wettability of the PEG-modified Si and PDMS substrates indicates that successful PEG modification may have taken place, particularly with the PEG 1B and PEG 2 groups. However, all of the PEG-modified groups on Si-PDMS showed a substantial degree of hydrophobic recovery, indicating that any surface modification present may be unstable. Both the Si-PDMS and PDMS substrates involved application of the PEG-silane to PDMS surfaces, so the discrepancy in hydrophobic recovery between the substrates was surprising. One reason behind this difference may be related to the ways in which the Si-PDMS film and the PDMS discs were formed. The PDMS discs were cast from an undiluted mixture of the elastomer and curing agent, while the PDMS film on Si-PDMS was created from hexane-diluted elastomer that was spin coated to achieve the thin film. It is possible that the hexane dilution altered the plasma reactivity of the Si-PDMS film compared to the undiluted PDMS discs. However, hexane dilution of PDMS has often been used as a solvent extraction method to remove uncrosslinked PDMS from the bulk, which should improve the overall stability of the PDMS film¹⁸⁸. Indeed, the thinness of the Si-PDMS film should also increase stability compared to the undiluted PDMS pieces, since thin layers of spin-coated PDMS have been shown to form stronger crosslinks than thicker, bulk PDMS¹⁸⁹. Another explanation may be that the height difference between the two substrates – 3 mm thick for PDMS, 400 μm for Si-PDMS – may have influenced the PEG

modification efficacy. Without additional analysis techniques to examine coating thickness or graft density, it is difficult to determine if the film composition on PDMS and Si-PDMS was the cause of the less stable Si-PDMS modifications. Nonetheless, it is at least probable to conclude that PEG films were present on Si and PDMS, and may have initially been present on Si-PDMS.

Based on the ELISA results, the PEG 1B protocol was the most effective at reducing protein fouling on any substrate, although none of the PEG protocols reduced fouling on Si-PDMS. While the PEG 1B protocol was effective on both Si and PDMS, only the PDMS substrates showed a substantial reduction in albumin fouling. Similarly, the PEG 2 protocol only showed a strong reduction in fouling on the PDMS substrate, akin to results from Kovach, et al. The PEG 1B protocol was the only group on Si that showed any reduction in fouling, and the Si-PDMS substrates showed no difference with any protocol of PEG-silane. It is possible that the increased hydrophilicity of those two PEG modifications, as seen in Fig. 4.3c on PDMS, may have led to lower HSA fouling in the ELISA, since proteins are apt to adsorb to more hydrophobic surfaces. However, there does not appear to be a relationship between lower contact angle and decreased protein fouling for either the Si or Si-PDMS substrates. For instance, the Si PEG 1B group showed significantly less fouling than any other Si group, yet the contact angle of the PEG 1B group was around the same as the unmodified and PEG 1A groups. Similarly, despite the significant differences in contact angle between the Si-PDMS PEG groups, all PEG-modified groups showed the same protein adsorption. Considering only the contact angle and HSA ELISA of the substrates, there does not appear to be a concrete relationship between hydrophilicity and reduced protein fouling.

Ellipsometry and AFM data provide additional information about how the different protocols of PEG-silane affected the resulting layers of PEG modification. The ellipsometry data on Si shows that PEG film thickness varied strongly with the different protocols, with the PEG 1A protocol resulting in an extremely thin film and the PEG 1B and PEG 2 protocols resulting in substantially thicker films. Given that the PEG-silane is a small molecule with a molecular weight of 459-591 Da, we would expect a

monolayer to have a film thickness of less than 1 nm¹⁹⁰. In this case, the PEG 1A protocol is closest to a monolayer, and the PEG 1B and PEG 2 protocols are clearly beyond a monolayer in thickness. Instead, it is likely that the PEG-silane has formed multilayers on these surfaces. This formation may have occurred through either covalent bonding of the reactive silane terminuses to each other, or through hydrogen bonding interactions throughout the films^{191–193}. Additional characterization would be needed to determine the structure of these multilayers.

The AFM topography scans may point to a similar film thickness trend on the PDMS pieces. Though the scans revealed little on Si and Si-PDMS, the PDMS pieces show particularly prominent surface textures. It is known that plasma oxidation leads to the formation of a glassy SiO₂ layer on PDMS surfaces, which can form microscopic cracks under physical stress^{187,194,195}. Evidence of stress-induced cracking can indeed be seen on the plasma-treated PDMS, but additional wrinkled texturing is obvious on all of the PEG-modified samples. The surfaces indicate that the PEG-silane films have experienced “buckling”, which occurs when a rigid film deforms due to thermal or mechanical stresses on a more elastic, underlying substrate^{196,197}. PDMS is certainly an elastic substrate, as it is often used for testing film buckling. The flexibility of the cut PDMS discs in this study likely caused any films on the surface, particularly the glassy SiO₂ layer, to become mechanically stressed due to extensive handling during processing¹⁷⁸. Additionally, the PEG 1A and PEG 1B samples were heated during functionalization, likely causing additional thermal stresses on those films¹⁹⁸. As can be seen in Fig. 4.6c, the PEG 1A and 1B samples do show a denser pattern of buckling compared to the PEG 2 sample, which was not heated. Comparatively, the Si and Si-PDMS substrates were backed by rigid silicon pieces, and so would not be affected by those handling stresses. Given the amplitude of the buckling observed on the PDMS samples, the thickness of the PEG-silane films on PDMS can be speculated. The depth of the wrinkles on the PEG 1A sample appears to be ± 5 nm, likely indicating a sub-5 nm film, while the depth of the PEG 1B wrinkles was ± 30 nm, indicating a film in the tens of nanometers. While these estimates do not

definitively calculate the PEG-silane film thicknesses, they do point to a substantial difference between PEG 1A and PEG 1B on PDMS. Since the PEG 2 film is less buckled than the others, its thickness is difficult to determine from buckling depth. Still, it appears that the film thicknesses on PDMS follow a similar trend to the ellipsometry measurements on Si.

Ultimately, while it is likely that PEG-silane modification occurred in all cases, the protein fouling resistance of the resulting films appears the most related to the films' thickness and structure, rather than any innate fouling resistance conveyed by PEG-silane as a monolayer. The PEG 1A protocol, which likely yielded monolayer films, did not reduce fouling on any substrate. Many studies have indicated that PEG monolayer films should reduce protein fouling of a substrate^{124,128,174,178}, although others have shown no reduction in fouling with PEG application¹⁴¹. In this study, it is possible that the protocol resulted in a low grafting density of PEG, or that the short chain length of the PEG-silane produced a film too thin to be protective¹⁹⁹. The latter seems likely, given the apparent relationship between protein fouling and film thickness. Indeed, the most fouling resistance was seen with multilayer films of agglomerated PEG-silane, particularly the PEG 1B groups.

Still, the fouling reduction with thick PEG-silane films was not universal for all groups, indicating that other factors in addition to thickness may influence omniphobicity. One possibility is that the multilayers may be structurally unstable, especially if the PEG-silane molecules are noncovalently attached to each other¹⁹³. If the multilayer films are weakly bound, the ELISA processing steps may be sloughing off the PEG-silane during the test. This would lead to lower apparent HSA binding, as the bound HSA would be removed with the PEG-silane. However, not all PEG multilayer films showed lower protein fouling, and – lacking additional characterization techniques – it is difficult to determine what types of bonds exist within the PEG multilayers. Since the PDMS PEG 1B and PEG 2 samples were the only groups that showed substantial protein fouling resistance, those samples may provide the clearest indicators of omniphobicity. Notably, buckling is associated with film delamination from the underlying

substrate, meaning that the thin films may detach from the surface when they become buckled²⁰⁰. It is possible that the buckled films on the PDMS samples specifically may have become delaminated, particularly during the ELISA handling processes, and that this delamination led to seemingly lower protein fouling as any bound HSA would be removed during the test. Further experiments on film stability, similar to the shear rate experiments found in Iqbal, et al., would be valuable towards determining if the PEG-silane multilayers are stable, and if buckling leads to destructive delamination^{91,201}.

Much of the work in this study was limited by a lack of additional characterization of the PEG-silane films, and so the hypotheses in this discussion are not substantially supported by the data. First, XPS data is essential to identifying the composition of the films on the surface, and high-resolution XPS scans could even provide some insights to the film structure. This information could indicate the presence of covalent bonds within the PEG-silane multilayers, possibly supporting some of the speculation about the multilayer stability. Contact angle alone can indicate that a substrate surface has been modified, but cannot prove that the modification is as intended by the protocol. Also, the film thicknesses were ultimately only measured on Si substrates, and so the film thicknesses on Si-PDMS and PDMS are unknown. A spectroscopic ellipsometer with multiple angles, rather than a single wavelength ellipsometer with a fixed angle, would be able to provide a more complete picture of film thickness on PDMS. In addition, the stability of the PEG-silane films in aqueous flow conditions was not assessed, possibly using methods described in Iqbal, et al⁹¹. This testing would provide insight into how stable the PEG-silane layers are, particularly if delamination of the buckled layers had occurred. Finally, no hemocompatibility testing was conducted in this study, so the blood response to the PEG-silane layers is unknown. Based on the protein fouling data, we can speculate that there would be little difference in thrombogenicity between PEG-functionalized substrates and their unmodified controls, but this cannot be proven without blood contact with the surfaces.

4.5 CONCLUSION

In this study, multiple application protocols of PEG-silane were compared on three substrates, with a goal towards determining future suitability in a blood-contacting device made of silicon membranes. The resulting films yielded inconsistent contact angle and protein fouling between substrates, and none of the films significantly improved the hydrophilicity or omniphobicity of the desired Si-PDMS substrate. Additional thickness and topography data revealed that two of the protocols formed thick multilayers of PEG-silane on the surfaces rather than monolayers, and that the thicker coatings tended to correlate with improved resistance to protein fouling. However, this fouling reduction may have been due to unstable bonds within the multilayers, or delamination of the PEG-silane layer entirely. Ultimately, while additional characterization is necessary, this study indicates that PEG-silane does not effectively reduce protein fouling or improve hydrophilicity, and that certain application protocols may result in unstable films.

Future work will focus on determining an alternative coating on Si-PDMS that increases the hydrophilicity of the surface, lowers protein fouling, and remains stable on the surface over time. As an alternative to PEG, recent research has explored the use of zwitterionic coatings such as sulfobetaine, carboxybetaine, and phosphorylcholine, which are strongly polar molecules with both positively and negatively charged functional groups^{91,93,125,141,174,180}. These coatings have been shown to increase hydrophilicity and omniphobicity beyond PEG, and successful application of zwitterionic coatings to PDMS has been achieved with multiple protocols. Another option may be heparin coatings, similar to those currently used in ECMO hollow fiber oxygenators²⁰². Although the bioactivity of heparin is short-lived, heparin-derived coatings on PDMS could substantially improve the hemocompatibility of the PDMS surfaces at least acutely. Lastly, since the silicon membranes are intended for use in an oxygenator, it may be possible to leverage a functional coating that improves gas transfer, possibly in addition to improving hemocompatibility. Arazawa, et al, designed a coating consisting of immobilized

carbonic anhydrase enzyme, which – in conjunction with an acidic sweep gas – was highly effective at CO₂ removal from blood by creating a locally acidified environment ⁷³. An acidic biomolecule immobilized on PDMS may be able to facilitate higher CO₂ removal as well. Continuing work on the SμM-PDMS oxygenator will focus on determining if one of these alternative coatings is best able to improve the oxygenator's hemocompatibility and functionality.

CHAPTER 5

IMPROVED OXYGENATION VIA TURBULENT BOUNDARY LAYER DISRUPTION

5.1 INTRODUCTION

Over the last several decades, extracorporeal membrane oxygenation (ECMO) has been a life-saving supportive treatment for critically ill patients with severe lung or heart failure. In recent years, increasing use of ECMO has led to more interest in a compact ECMO device for patient transportation or ambulation. Current hollow fiber ECMO systems are large and most often require patients to be bedbound, resulting in muscle deconditioning and poorer patient outcomes. Clinical advances in cannulation and patient management have led many ECMO centers to introduce awake and ambulatory physical therapy programs for patients^{14,203,204}. These programs' successes have directed ECMO research towards the development of smaller ECMO devices that are designed to be wearable and ambulatory, often as a bridge to transplant or destination therapy. Some research groups have constructed miniaturized hollow fiber ECMO units consisting of an oxygenator with integrated pump²⁰⁵⁻²⁰⁷, a few of which have been tested in preclinical trials. As a promising alternative to hollow fiber membranes, other researchers have been leveraging the miniaturization advantages of microelectromechanical systems (MEMS) technology to develop microfluidic artificial lungs. These devices consist of multiple layers of stacked polydimethylsiloxane (PDMS) forming parallel plate, capillary-like blood channels, which are optimized for minimal surface area, low priming volume, and low pressure drop^{106,110,121}. At present, manufacturing difficulties have prevented most of these devices from scaling up to support a full-size patient, although

they present a compelling solution to compaction by maximizing the amount of gas-diffusing surface area⁵⁵. In our lab, we have developed an alternative parallel plate microfluidic oxygenator based on silicon micropore membranes (S μ M) coated with a sub-5 μ m thin layer of PDMS¹⁴³. The rigidity imparted by the S μ M allows the composite S μ M-PDMS membranes to withstand very high (> 250 cmHg) oxygen sweep gas pressures to maximize the driving force of oxygen into the blood¹⁶⁰. In the future, these membranes can be arrayed in stacked parallel plate flow paths to create a larger oxygenator.

Ultimately, the most significant obstacle to designing a compact ECMO device is the high membrane area required for sufficient gas exchange. Typically, blood flow within oxygenators is kept in an entirely laminar flow regime to minimize the possibility of blood clotting in response to turbulent flow. Consequently, oxygen and carbon dioxide transport in ECMO are limited by a diffusional boundary layer within the blood, adjacent to the membrane surface. Due to this diffusion-limited process, hollow fiber ECMO oxygenators must be designed with large blood-contacting surface areas. As a reference point, the market-leading Maquet Quadrox-i adult model has a surface area of 1.8 m², translating to an area-normalized oxygenation efficiency of roughly 250 mL/min/m² if used at its average blood flow rate of 3.5 L/min⁴¹. One wearable ECMO device in prototype stage – the PAAL – provides a slightly higher oxygenation efficiency of 278 mL/min/m² in a device with 0.65 m² of surface area at the same 3.5 L/min blood flow rate⁸⁵. Microfluidic artificial lungs are similarly limited by boundary layer formation, since they maintain exceptionally laminar flow paths. Most of these devices have shown oxygenation exchange efficiency of below 250 mL/min/m²⁵⁵, with recent devices demonstrating 88 mL/min/m² and 130 mL/min/m²^{106,121}. Scale up to a larger device may alter the oxygen flux from these prototype measurements. Past results with our S μ M-PDMS oxygenator have shown a similar oxygenation efficiency in blood of 174 mL/min/m²¹⁴³. Despite design optimization efforts, most devices are unable to significantly surpass the gas exchange efficiency of the current hollow fiber technology, leading researchers to search for additional processes that enhance gas exchange.

Dating back to the inception of ECMO oxygenators, many researchers have sought solutions to overcoming the diffusion-limited transport in oxygenators, typically by introducing convective elements to the flow paths. Additional localized turbulence in the blood compartment can disrupt the diffusion boundary layer and strongly increase mass transfer, though possibly at the cost of considerable hemolysis and/or thrombosis²⁰⁸. For hollow fiber oxygenators, attempts have been made to introduce convection through oscillating hollow fibers⁸⁸, causing markedly increased hemolysis, or combining sinusoidal-shaped hollow fibers in conjunction with fluctuating liquid flows²⁰⁹, the effects of which have not been tested in blood. Researchers working with microfluidic oxygenators have used the machinability of PDMS to create various turbulence-promoting textures on their membranes. Some examples include furrowed membranes similar to those developed by Bellhouse, et al, in 1973, and embossed staggered herringbone trenches taken from the broader PDMS microfluidics fields^{123,210,211}. Although some of these methods have been promising *in vitro* with water, no results with blood have been published.

Another approach to improve transport is the use of fluidic spacer meshes inside parallel plate ECMO channels, as used in pre-hollow fiber ECMO devices^{54,212,213}. Fluidic spacers are known to promote increased transport through membranes by creating localized turbulence and disturbing the transport boundary layer near the membrane surface, even in flow conditions with low Reynolds numbers²¹⁴. Some materials used for the spacer meshes included nylon, vinyl-coated fiberglass, and polyvinylidene chloride. The landmark Kolobow oxygenator used reinforced silicone membranes wound in a spiral coil with a plastic spacer mesh in between the membrane layers²¹⁵. Similarly, the Travenol oxygenator used nylon screens to separate silicone parallel plate membranes²¹⁶. Using spacers helped overcome the diffusive difficulties (~50 μm thick membranes and large plate separations) imposed by manufacturing capabilities at the time⁵⁴. In addition to keeping the silicone layers apart for patency, the spacers improved gas transfer throughout the oxygenators and led to a twofold reduction in device size. However, hollow fiber oxygenators succeeded these early oxygenators in the late 1970s due to their lower

overall pressure drops, though they required a significantly higher membrane surface area. Given the recent interest in compact ECMO devices, spacers may be a concept to revisit for miniaturized parallel plate oxygenators such as our S μ M-PDMS oxygenator. Scale up of microfluidic oxygenators has proven difficult due to laborious manufacturing processes, and routing blood flow to many parallel channels. Using spacers – or turbulent mixing in general – should make scale-up much simpler by significantly decreasing the number of channels needed for sufficient respiratory support. A full-size oxygenator could be constructed with a fraction of the surface area and size of a hollow fiber device, making ambulatory use feasible.

The purpose of this work is to evaluate fluidic spacers as a method of improving mass transfer in the S μ M-PDMS oxygenator, with additional focus on any hemocompatibility consequences of the spacers. In this study, we constructed a prototype S μ M-PDMS oxygenator flow cell, and measured the spacers' impacts on O₂ transfer and pressure drop *in vitro*. Then, we exposed the flow cells to flowing porcine blood to simultaneously examine O₂ and CO₂ transfer *in vivo*, and hemocompatibility of the spacers. From this information, we speculated the size reduction of a hypothetical ECMO device using spacers, and if the spacers are a viable strategy for improving gas transfer in a parallel plate microfluidic oxygenator.

5.2 MATERIALS AND METHODS

5.2.1 Silicon Membrane Design

Planar silicon membranes can be used with spacers to determine the effects of spacers on blood oxygenation. Following prior work^{138,143,160}, silicon micropore membranes (S μ M) were fabricated through photopatterning 1000 nm-wide pores on one face of a silicon wafer. The wafer was diced into 1x6.5 cm² membrane pieces. For placement of the membrane inside the oxygenator flow cell, a soft silicone rubber gasket (BIHT6135, Marian Chicago, West Chicago, IL USA) was oxygen plasma-bonded to the nonporous face of the membrane (Harrick Plasma PDC-001, Harrick Plasma, Ithaca, NY USA).

After applying these “backside” gaskets, the porous face of the membranes was plasma bonded to a 5 μm thick layer of polydimethylsiloxane (PDMS), as in Dharia et al. 2017 and Abada et al. 2018. The combined $\text{S}\mu\text{M}$ -PDMS were then used as the gas exchange membranes in the oxygenator flow cell.

5.2.2 Spacers

Two mesh sheets made from FDA-compliant polypropylene were obtained to use as spacers in the oxygenator (Industrial Netting, Minneapolis, MN USA). Polypropylene is considered an inert biomaterial, and has been used as a membrane material for hollow fiber ECMO (Federspiel and Henchir 2004; Shimono et al. 1997). The meshes were considered as “coarse” or “fine” based on larger or smaller hole size, respectively (Fig. 5.1, Table 5.1). Each sheet was cut into pieces measuring 0.8x6.5 cm, which would fit over the entire membrane area inside of the oxygenator device.

For theoretical calculations of spacer performance, one cut spacer mesh of each type was massed and measured for volume using the volume displacement method ^{164,218}. Measurements of mass and calculated volume can be found in Table 5.1.

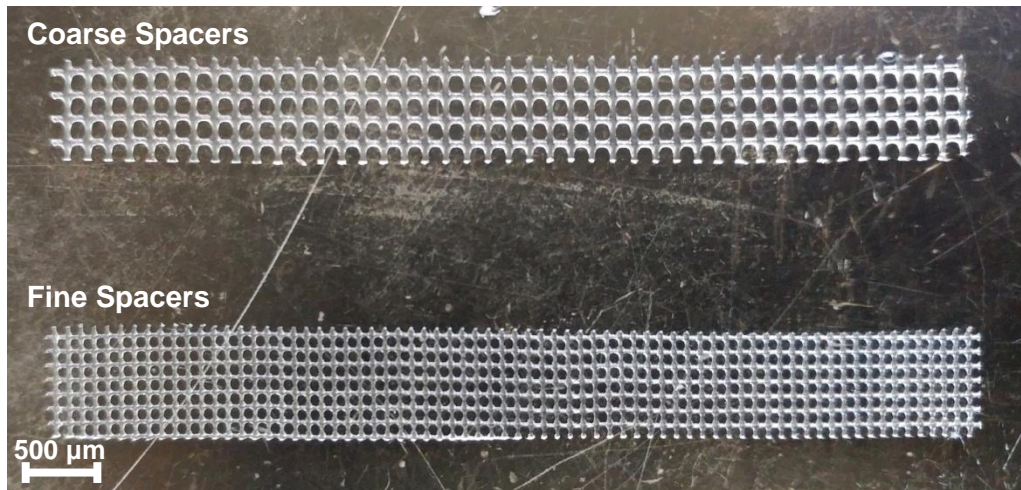


Fig. 5.1: Coarse and fine spacer meshes cut to fit in flow cell channels

Table 5.1: Dimensions of meshes used as spacers. Product Number, open area, hole size, and thickness are as stated by the manufacturer. Mass and calculated volume of a single cut mesh were measured for this study.

	Fine Spacers	Coarse Spacers
Product Number	XN6070	XN5170
Open Area (%)	35	50
Hole Size (mm)	0.635 x 0.762	1.016 x 1.346
Thickness (mm)	0.356	0.483
Measured Mass (g)	0.0504	0.0654
Calculated Volume (m ³)	1.06e-07	1.14e-07

5.2.3 Oxygenator Device Design and Assembly

A custom prototype flow cell was constructed from two stainless steel plates to house the S μ M and spacers (Hayes Manufacturing, Sunnyvale, CA USA). Each of the identical steel plates had a port for the liquid inlet or outlet and two slots for placing the S μ M (Fig. 5.2). With two steel plates forming a complete device, a total of four S μ M were used in each device. Underneath the membrane slots were the sweep gas channels, which were each accessible by two ports. The S μ M with backside gaskets were secured in their slots by applying a slight vacuum to the sweep gas channels to compress the backside gaskets. The liquid flow path was defined by a set of silicone gaskets to divide the liquid flow from the inlet into two channels over the membranes (R750009P, McMaster-Carr, Santa Fe Springs, CA USA). The liquid channel gasket was chosen to be 0.5 mm-thick and medium in stiffness to accommodate the thicknesses of both spacers within the liquid channel, and provide a fluidic seal around the device. Once the S μ M, gaskets, and spacers were placed, the steel plates were assembled together to yield a continuous flow path.

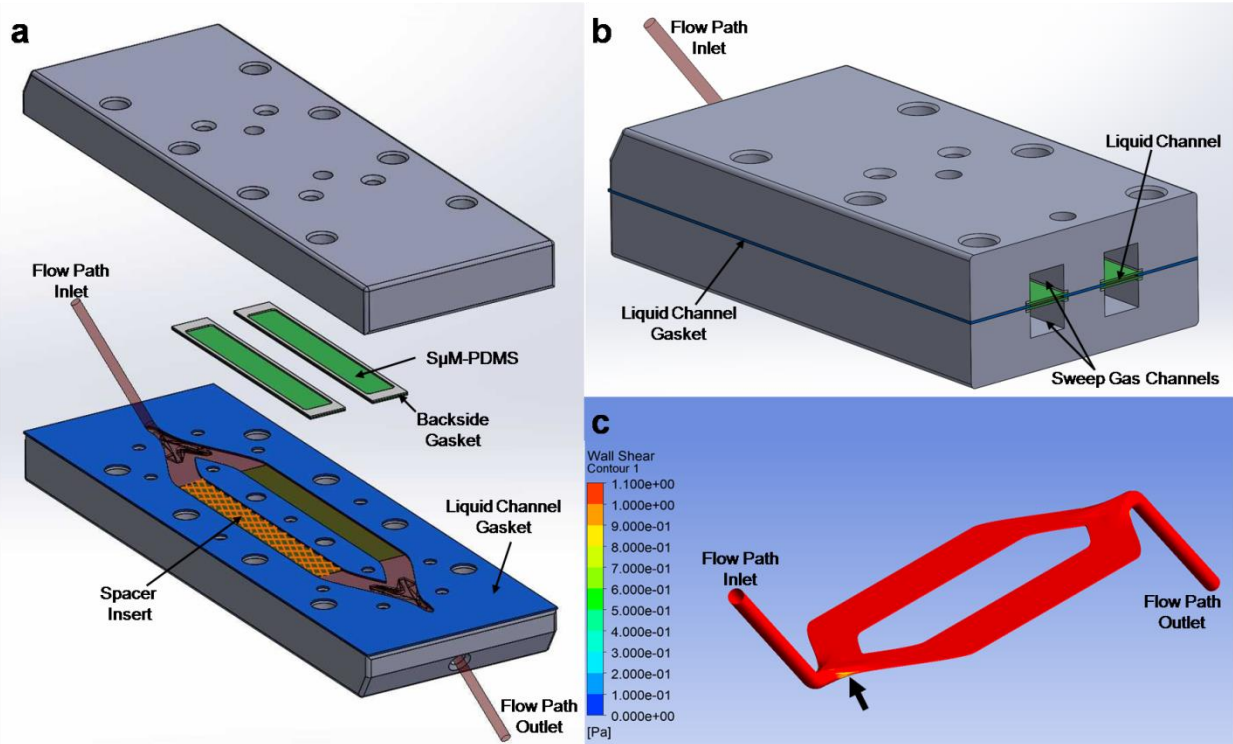


Fig. 5.2: Design views of oxygenator flow cell with spacers. (a) shows an exploded view of the oxygenator with a spacer and membranes in place, (b) shows a cross section with the sweep gas channels, and (c) shows computational modeling of the flow path at 50 mL/min with an arrow highlighting a region of low wall shear.

5.2.4 Oxygen Flux and Pressure Drop *In Vitro*

Three stainless steel flow cells were tested *in vitro* to determine the effects of the spacers on gas permeability and hydraulic pressure drop across the device (Fig. 5.3). Each device was tested with coarse spacers, with fine spacers, and without spacers. The flow cells were exposed to circulating, nitrogen-sparged water at flow rates of 10, 20, and 40 mL/min. A pressure gauge was placed upstream of the flow cell to detect hydrostatic pressure resulting from the spacers. Each membrane was supplied with flowing, pressurized oxygen sweep gas. An optical oxygen probe (NeoFox GT with FOSPOR probe, Ocean Optics, Dunedin, FL, USA) was placed downstream of the flow cell on the liquid side to detect oxygen transport across the membrane. The gas pressure of the oxygen sweep gas was raised to 10 cmHg, and oxygen flux into the water was measured by the probe. Area-normalized flux (J , mL O₂/min/m²) was

determined using the measured oxygen concentration in $\mu\text{mol/L}$ before and after adding oxygen to the circuit ($[O_2]_i$ and $[O_2]_f$, respectively), with a conversion of 22.4 L O_2 /mol at STP:

$$J = \frac{([O_2]_f - [O_2]_i) \cdot 10^{-6} \frac{\text{mol}}{\mu\text{mol}} \cdot 22.4 \frac{\text{L}}{\text{mol}} \cdot Q}{A_m}$$

Eq. 5.1

Where Q is the flow rate of water in mL/min, and A_m is membrane area in m^2 .

Based on the calculated oxygen flux, the impact of spacers can be compared to determine if spacers benefit gas transport.

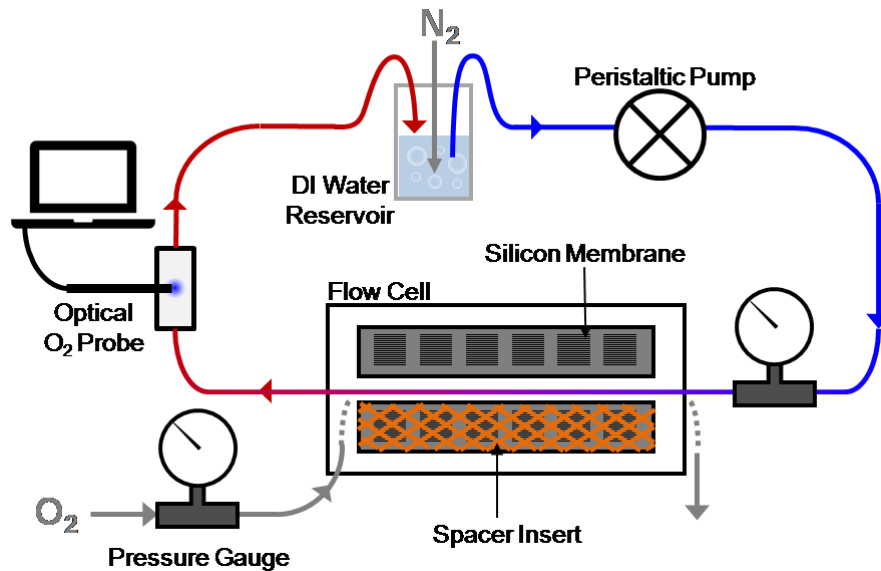


Fig. 5.3: Schematic of gas permeability testing setup, showing a spacer insert in one half of the flow cell.

5.2.5 Hemocompatibility *In Vivo*

The devices with and without spacers were tested for blood compatibility extracorporeally in a 40kg Yucatan minipig. Under general endotracheal anesthesia, a 15-French dialysis catheter (Arrow Cannon II, Teleflex, Wayne, PA USA) was inserted into the left external jugular vein using Seldinger

technique, with the tip positioned at the cavoatrial junction. Heparin (100u/kg) was administered intravenously and serially re-dosed to achieve ACT>300. The venous and arterial ports of the catheter were then attached to a closed flow circuit consisting of Tygon tubing (Masterflex L/S 16 Tygon E-LFL, Cole-Parmer, Vernon Hills, IL USA), with flow dividers to create three parallel blood channels, each containing one oxygenator device: one each with fine spacers, coarse spacers, and no spacers (Fig. 5.4). The circuit was primed with isotonic crystalloid solution prior to establishing blood flow by activation of a peristaltic pump. Three-way stopcocks were inserted in the Tygon tubing at the inlet and outlet of each oxygenator device to allow blood sample collection before and after exposure to the oxygenator's membranes.

After one hour of extracorporeal blood circulation at 20 mL/min without oxygenation, flowing oxygen sweep gas was supplied to any patent device at a flow rate of 3 L/min, and minimal pressure. Three blood samples were taken from the inlet and outlet of each patent device at 20 mL/min blood flow rate, for blood gas analysis to assess pO₂, pCO₂, pH, and HCO₃⁻ using an iSTAT handheld blood analyzer (Abbott Point of Care Inc., Princeton, NJ, USA). The blood flow rate was then decreased to 10 mL/min, and three inlet and outlet samples were collected from each patent device for blood gas analysis. After a total of three hours of blood exposure, the devices were flushed with saline and disassembled. Should any of the devices clot prior to the end of the experiment, they were removed from the circuit early. The devices were grossly inspected for clots, and the membranes were removed and broken into pieces. The experiment was conducted at a contract resource organization (PMI Preclinical, San Carlos, CA).

The area-normalized flux of O₂ and CO₂ through the membranes was calculated from the ABG or iSTAT readings at the inlet and outlet of each device. Inlet and outlet O₂ content ($[O_2]$, mL O₂/mL blood) was calculated as in Dharia, et al (2017)¹⁴³:

$$[O_2] = 1.36 \cdot Hg \cdot SaO_2 + 0.0031 \cdot PaO_2$$

Eq. 5.2

where Hg is the hemoglobin of the blood (mg/mL), SaO_2 is the percent of hemoglobin bound to oxygen, and PaO_2 is the partial pressure of oxygen in the blood (mm Hg). Similar to Eq. 5.1, the area-normalized flux of O_2 (J_{O_2} , mL O_2 /min/m²) is calculated by:

$$J_{O_2} = \frac{([O_2]_{outlet} - [O_2]_{inlet}) \cdot Q_{blood}}{A_m}$$

Eq. 5.3

where Q_{blood} is the flow rate of blood and A_m is the porous area of the membrane. The calculation of CO_2 flux – described in Douglas et al. (1988) – accounts for CO_2 stored as a dissolved gas (pCO_2), as bicarbonate ion (HCO_3^-), and bound to hemoglobin²¹⁹. First, inlet and outlet CO_2 concentration in plasma ($[CO_2]_{plasma}$, mL O_2 /mL blood) is calculated using the logarithmic form of the Henderson-Hasselbalch equation for plasma CO_2 :

$$[CO_2]_{plasma} = 2.226 \frac{mLCO_2 / 100mLblood}{mM} \cdot s \cdot pCO_2 \cdot (1 + 10^{pH - pK'})$$

Eq. 5.4

where s (plasma CO_2 solubility) and pK' (apparent pK) are known constants equal to 0.0307 mM CO_2 /mmHg CO_2 and 6.0907, respectively. The inlet and outlet CO_2 concentrations in blood ($[CO_2]_{blood}$, mL O_2 /mL blood) are then calculated using the McHardy-Visser equation:

$$[CO_2]_{blood} = [CO_2]_{plasma} \cdot \left[1 - \frac{0.0289 \cdot [Hb]}{(3.352 - 0.456 \cdot SO_2) \cdot (8.142 - pH)} \right]$$

Eq. 5.5

where SO_2 is the oxygen saturation of blood. The values of $[CO_2]_{blood}$ are used for the inlet and outlet content of blood CO_2 . Finally, the area-normalized CO_2 flux (J_{CO_2} , mL CO_2 /min/m²) is calculated as in Eq. 5.3:

$$J_{CO_2} = \frac{([CO_2]_{outlet} - [CO_2]_{inlet}) \cdot Q_{blood}}{A_m}$$

Eq. 5.6

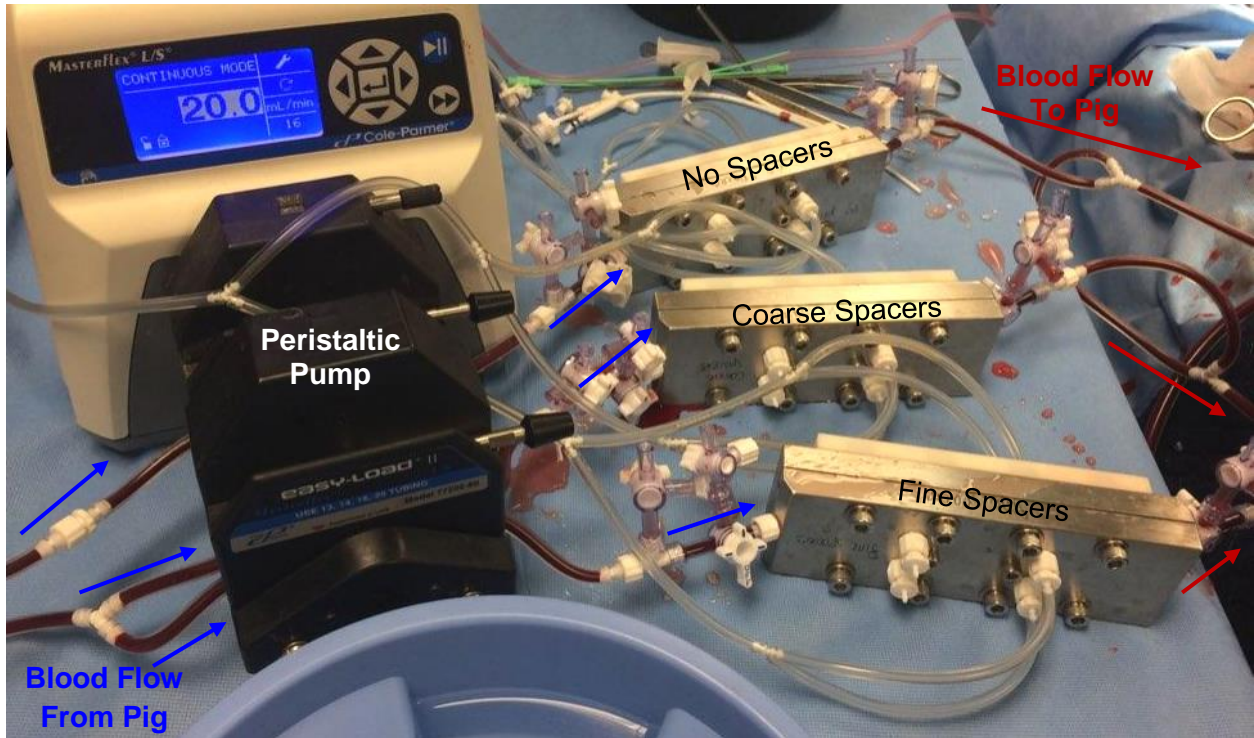


Fig. 5.4: *In vivo* testing of SµM-PDMS devices with spacers.

5.2.6 Scanning Electron Microscopy (SEM)

Two SµM were removed from each device, and each was broken into three representative pieces. These pieces were preserved for SEM through immersion in a fixative buffer for 48 hours. The buffer was composed of 3% glutaraldehyde (Sigma-Aldrich), 0.1 M sodium cacodylate (VWR), and 0.1 M sucrose in water. After 48 hours, the samples were washed twice with deionized water, and dehydrated through 10 minute immersions in ethanol/water (v/v%) mixtures of 35%, 50%, 70%, 95%, and twice with 100%

ethanol. The samples were dried overnight in air and then mounted on aluminum stubs for imaging using a Carl Zeiss Ultra 55 Field Emission Scanning Electron Microscope (Zeiss, Dublin, CA USA). Prior to imaging, the samples were sputter coated with gold.

5.3 RESULTS AND DISCUSSION

5.3.1 Oxygen Flux and Pressure Drop *In Vitro*

Three oxygenator devices were assembled using four S μ M each. The thickness of the center gasket was chosen to be 0.5 mm when uncompressed, making the channel height of the liquid flow path ~0.45 mm when the devices were assembled. Each of the devices was tested with three conditions: without spacers, with fine spacers, and with coarse spacers. For each condition, two measurements were taken of the oxygen flux and hydraulic transoxygenator pressure drop at water flow rates of 10, 20, and 40 mL/min. The measurements from all devices were averaged for each condition, and results are in Fig. 5.5.

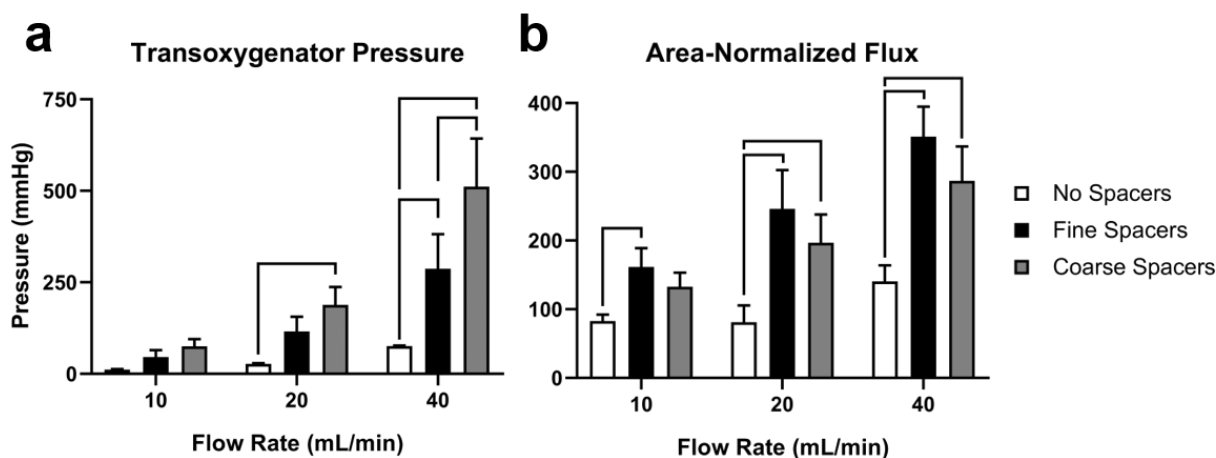


Fig. 5.5: (a) Transoxygenator pressure and (b) area-normalized flux of oxygenator with and without spacers. Bars indicate statistically significant difference in two-way ANOVA with Tukey post-hoc comparisons.

Overall, the device without spacers demonstrated a pressure drop of 11-33 mmHg, while the fine spacers showed a range of 46-240 mmHg and the coarse spacers showed between 75-470 mmHg (Fig. 5.5a). Compared to the no spacers condition, the presence of spacers strongly increased the hydraulic

pressure within the flow cells, mostly at higher water flow rates. For example, at 20 mL/min water flow, the pressure drops across the fine and coarse spacer conditions were 7.8 and 13 times greater, respectively, than without spacers. Given that the spacers present a physical obstruction to liquid flow in the channel, this elevated pressure drop would be expected by the Hagen-Poiseuille law. Additionally, the hydraulic pressure with coarse spacers was consistently higher than with fine spacers, though only statistically different at 40 mL/min. This result is consistent with the greater thickness of the coarse spacer mesh compared to the fine spacer mesh (Table 5.1).

While the increased gas transfer is a clear benefit to using spacers, higher pressure drop has been thought to cause hemolysis throughout ECMO circuits. As such, most oxygenators are designed to minimize transoxygenator pressure. For example, the market-leading Maquet Quadrox Adult has a relatively low pressure drop of ~67 mmHg at a blood flow rate of 5 L/min – an adult’s typical cardiac output^{27,220}. However, some studies dispute that hemolysis is correlated with transoxygenator pressure drop, and other oxygenators show higher pressure drops of up to nearly 300 mmHg at adult cardiac output²⁷. With the current S μ M-PDMS oxygenator design, most test conditions showed less than 300 mmHg of pressure drop, although the water flow rates tested were only 10-40 mL/min. Should the S μ M-PDMS oxygenator be expanded to a full-size device, multiple membrane channels would likely be arrayed in parallel to provide sufficient respiratory support. This would also reduce the pressure drop through each channel by distributing blood flow evenly. Until a full-size device is constructed, the pressure drop through each channel cannot be predicted. Still, testing spacer hemocompatibility in the current prototype S μ M-PDMS oxygenator may indicate a full-size oxygenator with spacers would be a viable concept.

In most cases, oxygen flux with either type of spacers was significantly increased compared to the no spacers condition, as assessed by two-way ANOVA with Tukey post-hoc analysis (Fig. 5.5b). Specifically, the fine spacers produced between 1.9-3.0 times greater oxygen flux, and the coarse spacers produced between 1.6-2.4 times greater flux. Though flux with the fine spacers was consistently higher

than with the coarse spacers, this difference was not statistically significant at any flow rate. Spacer meshes are known to create local vortices, which create convective “back mixing” and ultimately increased mass transfer²¹⁴. As such, both types of spacer meshes would be expected to increase mass transfer compared to the no spacers condition. The spacers are considerably different in all dimensions, so it is difficult to speculate which physical attributes led to both spacers yielding similar increases in mass transfer without computational modeling. Assuming these improvements, a S μ M-PDMS oxygenator using spacers would need only half the surface area of a device without spacers. For example, a device with fine spacers would need only 0.57 m² of surface area to completely support a 70 kg adult requiring ~210 mL O₂/min, while a no spacers device would need 1.3 m² (Fig. 5.5)¹⁵⁷. Compared to the market-leading Maquet Quadrox-i adult oxygenator with 1.8 m² of surface area, a S μ M-PDMS oxygenator using spacers would be less than one third of the size of the current standard of care.

The spacers can be evaluated from a theoretical standpoint to understand any differences in spacer performance. Calculations below are based on methods from Schock and Miquel; all constants and variables can be found in. Essentially, using measurements of the spacer meshes’ overall thickness, mass, and volume, the effective Reynolds and Sherwood numbers through the channel can be calculated. Results from these calculations can be found in Table 5.3, using a water flow rate of 20 mL/min through one channel of the S μ M-PDMS oxygenator (40 mL/min for the whole device). The Sherwood number of each spacer-filled channel represents the relative contributions of convection and diffusion to overall mass transfer, and may indicate which spacer type most strongly increases convective mass transfer in the oxygenator. Spacer thicknesses are already known from the manufacturer, and both the mass and volume of cut pieces of spacers were measured using a previously-described volume displacement method^{164,218}.

Table 5.2: Variables, geometric data of the S μ M-PDMS oxygenator, and constants used in calculations. Geometric data applies to one channel of each device, and one membrane.

Variable	Units
Flow Rate of Water (Q_{H_2O})	$m^3 s^{-1}$
Flow Rate of Gas (Q_{gas})	$m^3 s^{-1}$
Area-Normalized Flux (J)	$mL O_{2,STP} min^{-1} m^{-2}$
Oxygen Concentration ($[O_2]$)	$mol L^{-1}$
Pressure of CO ₂ (P_{CO_2})	mmHg
Pressure of Sweep Gas at Outlet ($P_{gas,outlet}$)	mmHg
Volume Flow Rate of CO ₂ (\dot{V}_{CO_2})	m^3/s
Volume Flow Rate of CO ₂ – Max ($\dot{V}_{CO_2,max}$)	m^3/s

Data	Units	Value
Channel Height (h)	m	5×10^{-4}
Channel Length (l)	m	8×10^{-3}
Channel Width (w)	m	6.5×10^{-2}
Channel Volume ($V_{channel}$)	m^3	2.60×10^{-7}
Membrane Area (A_m)	m^2	7.53×10^{-4}

Constants	Units	Value
Water Density (ρ)	$kg m^{-3}$	1000
Water Dynamic Viscosity (μ)	Pa s	8.90×10^{-4}
Water O ₂ Diffusivity at 20°C (D_{O_2})	$m^2 s^{-1}$	1.8×10^{-9}

Once the volume of each spacer (V_{spacer}) is known, the porosity of the spacer in the channel (ϕ)

can be calculated:

$$\phi = 1 - \frac{V_{spacer}}{V_{channel}}$$

Eq. 5.7

where $V_{channel}$ is the volume of the overall channel. From calculations in Schock and Miquel, the porosity

can be used to determine the effective area (A_{eff}), effective velocity (v_{eff}), and hydraulic diameter (d_h)

of the spacer-filled channel:

$$A_{eff} = w \times h \times \phi$$

Eq. 5.8

$$v_{eff} = \frac{Q_{H_2O}}{A_{eff}}$$

Eq. 5.9

$$d_h = \frac{4\phi}{2/h + 4(1-\phi)/d_f}$$

Eq. 5.10

where w is channel width [m], h is channel height [m], Q_{H_2O} is volumetric flow rate [m³/s], and d_f is the diameter of spacer filaments [m]. In this study, d_f is not known for either spacer. We have made an approximation of $d_f = h_{spacer}/2$, where h_{spacer} is the spacer height. Once the hydraulic diameter and effective velocity are known, the Reynolds number (Re) for the spacer-filled channel can be calculated:

$$Re = \frac{\rho v_{eff} d_h}{\mu}$$

Eq. 5.11

By comparing Reynolds numbers of the spacer-filled channels, the relative amount of turbulence caused by the spacers can be assessed. Subsequently, through additional calculation of the Schmidt number, the Sherwood number can be determined to relate convective to diffusive mass transfer. The Sherwood number can be expressed as a correlation between Reynolds number and Schmidt number, depending on the particular geometry of the channel. Eq. 5.12 is the Leveque correlation for laminar flow in a rectangular channel without spacers, and Eq. 5.13 is a correlation from Schock and Miquel for a spacer-filled channel.

$$Sc = \frac{\mu}{\rho D_{O_2}}$$

Eq. 5.12

$$Sh = 1.62 \left(Re Sc \frac{d_h}{l} \right)^{1/3}$$

Eq. 5.13

$$Sh = 0.065 Re^{0.875} Sc^{0.25}$$

Eq. 5.14

Table 5.3: Results of theoretical calculations for Reynolds number and Sherwood number for spacer-filled channels. Values for thickness, mass, and volume correspond to one cut spacer mesh. Values for effective area, effective velocity, and hydraulic diameter correspond to one channel of the S μ M-PDMS oxygenator.

Variable	Units	No Spacers	Fine Spacers	Coarse Spacers
Spacer Thickness (h_{spacer})	m	---	0.356	0.483
Spacer Mass (m_{spacer})	g	---	0.0504	0.0654
Spacer Volume (V_{spacer})	m ³	---	1.06×10^{-7}	1.14×10^{-7}
Porosity (ϕ)	%	100	42.5	57.6
Effective Area (A_{eff})	m ²	4.00×10^{-6}	1.21×10^{-6}	2.22×10^{-6}
Effective Velocity (v_{eff})	m s ⁻¹	0.0833	0.276	0.150
Hydraulic Diameter (d_h)	m	9.41×10^{-4}	4.25×10^{-4}	5.62×10^{-4}
Reynolds Number (Re)	---	78.4	58.6	42.1
Schmidt Number (Sc)	---	557	557	557
Sherwood Number (Sh)	---	13.6	20.4	15.3

Based on the calculated values in Table 5.3, information about spacer performance can be gleaned. First, the low porosity of the spacers strongly reduces the effective cross-sectional area and hydraulic diameter of the channels. Notably, the fine spacer has a lower porosity than the coarse spacer despite its relative thinness, which further reduces these variables. Due to the reduced effective area, the effective velocities of the spacer-filled channels are higher than a channel without spacers, which leads directly to higher Reynolds numbers for the spacer-filled channels. The higher Reynolds numbers –

especially for the fine spacers – are consistent with the knowledge that spacers are known to create local zones of non-laminar flow. Finally, the theoretical Sherwood number for the fine spacer-filled channel is considerably higher than the no spacer and coarse spacer channels, which are somewhat close. Ultimately, these calculations indicate that the spacers increase the non-laminar flow within the channels, leading to increased convective mass transfer. While the fine spacer is thinner than the coarse spacer and does not completely fill the channel, its lower porosity results in even more non-laminar flow and higher convective mass transfer. This result may indicate that mesh density may play a larger role in mass transfer than mesh size, although more systematic study of many spacer mesh types would be needed to examine this question. Since the fine spacers also yielded a lower pressure drop than the coarse spacers, the fine spacers were expected to yield superior gas exchange and hemocompatibility results *in vivo* compared to the coarse spacers.

5.3.2 Hemocompatibility *In Vivo*

The three devices with coarse, fine, and no spacers were connected to flowing, heparinized venous blood from the pig through a pump set to 20 mL/min. The 20 mL/min flow rate was chosen to maximize gas exchange, while preventing transoxygenator pressure in all devices from exceeding 300 mmHg. After 40 minutes of blood exposure, blood was exiting one of the sweep gas channels in the coarse spacers device, indicating that one of the S μ M-PDMS membranes may have broken. After 5 more minutes, the fine spacers device was leaking blood from the liquid channel gasket, likely due to occlusive clotting within the blood channel. Since both devices had shown blood leakage, they were removed from the circuit and saved for analysis. In this time, the device without spacers had not shown any signs of clotting, and flow was continued for a total of three hours. Blood gas readings were taken from only the device without spacers; raw data is in Table 5.4. Six total samples were taken: three at 20 mL/min, and three at 10 mL/min. After three hours, blood flow was discontinued, and the device was flushed with saline solution.

Table 5.4: Raw ABG data collected from no spacers device during *in vivo* experiment. Data is divided into pre- and post-device for the same time point.

Flow Rate (mL/min)	Pre-Device					Post-Device				
	pH	pCO ₂ (mmHg)	pO ₂ (mmHg)	HCO ₃ ⁻ (mmol/L)	SO ₂	pH	pCO ₂ (mmHg)	pO ₂ (mmHg)	HCO ₃ ⁻ (mmol/L)	SO ₂
20	7.37	51.8	52	29.9	0.85	7.373	45.3	52	26.3	0.85
20	7.364	52.9	55	30.2	0.87	7.369	47	55	27.1	0.87
20	7.363	53.3	60	30.3	0.89	7.365	48	59	27.4	0.89
10	7.363	52.3	63	29.8	0.9	7.37	50.2	64	29	0.91
10	7.362	54.6	66	31	0.91	7.372	48.1	74	27.9	0.94
10	7.362	51	69	29	0.93	7.366	47.3	77	27.1	0.95

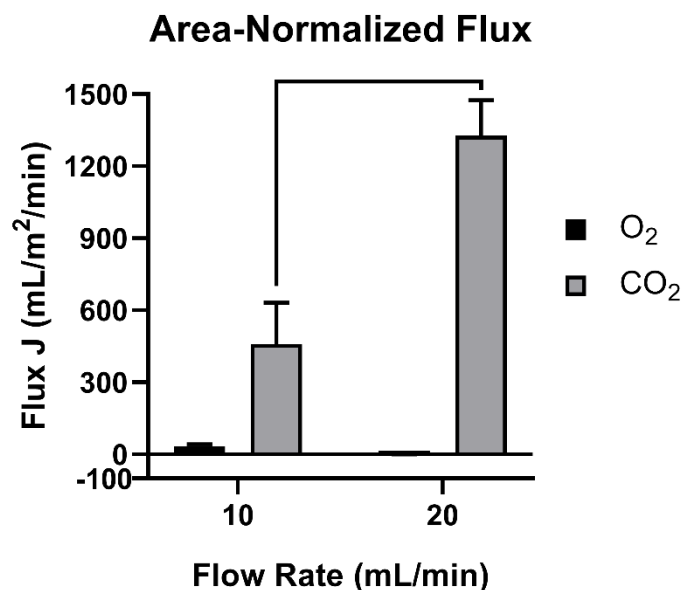


Fig. 5.6: *In vivo* flux of O₂ and CO₂ in device without spacers. The bar indicates statistically significant difference in two-way ANOVA with Tukey post-hoc comparisons.

Measurements of O₂ and CO₂ flux taken from the device without spacers are in Fig. 5.6.

Compared to the flux seen *in vitro* (Fig. 5.5), little to no O₂ flux was seen with blood regardless of flow rate. Earlier data collected with a different S μ M-PDMS oxygenator had demonstrated oxygen transport with blood, meaning that the low blood oxygenation may be exclusive to this experiment¹⁴³. In this experiment, the low O₂ flux was likely due to the minimal sweep gas pressure that was used, since sweep

gas pressure is the primary driving force of oxygen into blood. Despite the low oxygenation, considerable CO₂ removal was seen in the S μ M-PDMS device, particularly at 20 mL/min. Given that CO₂ removal is related to sweep gas flow rate, the high sweep gas flow rate relative to device size likely led to substantial CO₂ transfer. In calculations by Federspiel and Hattler (1996), the sweep gas flow rate (Q_{gas}) can be used to relate the measured CO₂ gas exchange rate (\dot{V}_{CO_2}) and the theoretical maximum CO₂ exchange rate ($\dot{V}_{CO_2,max}$):

$$\dot{V}_{CO_2} = J \times A_m$$

Eq. 5.15

$$\frac{\dot{V}_{CO_2}}{\dot{V}_{CO_2,max}} = 1 - \frac{P_{gas,outlet}}{2P_{CO_2,blood}} \frac{\dot{V}_{CO_2}}{Q_{gas}}$$

Eq. 5.16

where $P_{gas,outlet}$ is the total pressure of gas at the sweep gas outlet of the device and $P_{CO_2,blood}$ is the measured partial pressure of carbon dioxide in the blood (Table 5.2)²²¹. Considering that the sweep gas was vented into the ambient air, $P_{gas,outlet}$ should be equal to atmospheric pressure. Q_{gas} was set to 3 L/min. From Eq. 5.15 and Eq. 5.16, the calculated $\dot{V}_{CO_2}/\dot{V}_{CO_2,max}$ was 0.997 and 0.999 at blood flow rates of 20 and 10 mL/min, respectively. These values indicate that CO₂ removal was near the maximum possible with the oxygenator device, likely owing to the high Q_{gas} flow rate. The S μ M-PDMS membranes were able to sustain the high sweep gas flow rate without rupture, making the membranes suitable for use in a CO₂ removal device. Based on the measured CO₂ removal rate at 20 mL/min of blood flow, a total of 160 mL CO₂/min could be removed with only 0.12 m² of membrane surface area representing 484 membranes

⁷². However, these calculations are only based on this current prototype device, and further design of a CO₂ removal device using S μ M-PDMS membranes would be required to optimize CO₂ removal, blood flow rate, and surface area. Ultimately, future experiments and iterations of the S μ M-PDMS device would need to optimize O₂ exchange in addition to ensuring high CO₂ removal.

5.3.3 Examination of Devices

Upon disassembly, the three devices were grossly inspected for evidence of thrombosis (Fig. 5.7). Both of the devices with spacers showed considerable clotting within and around the spacer meshes, particularly at the distal end of the spacers near the device outlet. One of the membranes in the coarse spacers device had broken, as was speculated during the experiment. It was possible that occlusive clotting in the channel could have led to a pressure buildup inside the flow cell, causing the membrane to break. As a comparison, the device without spacers showed no gross clots anywhere in the device, despite exposure to flowing blood for two additional hours. The membranes were removed from the flow cells and rinsed in PBS to dislodge any non-adherent blood cells prior to SEM preservation. No gross clots were visible on any of the membranes themselves.

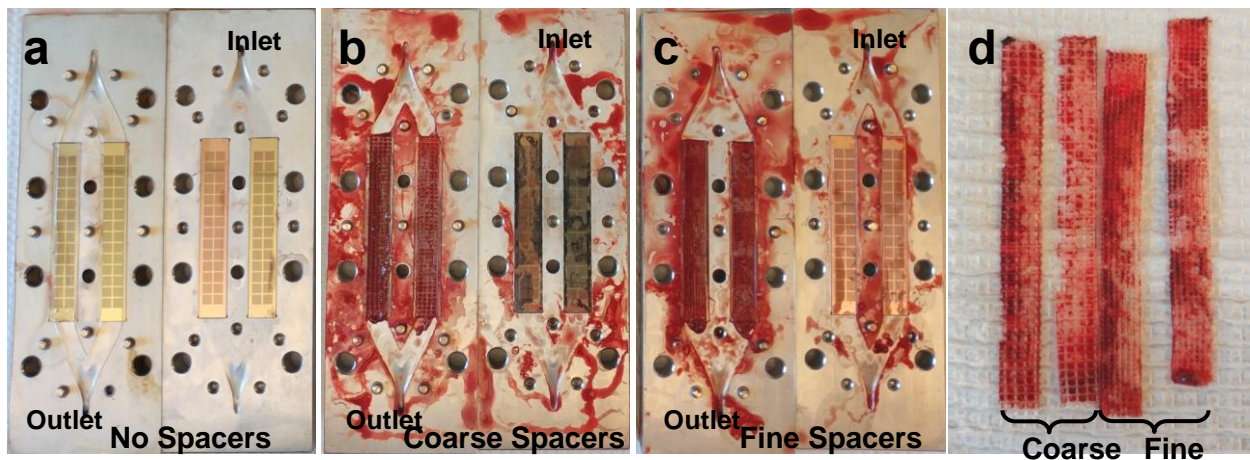


Fig. 5.7: Disassembled flow cells (a-c) and spacer meshes (d) after blood exposure

Overall, the spacers are likely responsible for all gross clotting observed in each device, since the no spacers device showed no gross clots despite using the same flow path geometry and membranes. Furthermore, the variety of clot patterns in the spacer meshes indicates that multiple factors influenced the distributions of clots. Most obvious are the clots at the end of each spacer mesh, closest to the outlet. Clotting at this location could mean that thrombosis was likeliest at the interface between the spacer and the rest of the channel, or that clots formed upstream and collected at the end of the spacer. Smaller clots were indeed seen at the inlet interface of some of the spacer meshes. However, the larger size of the outlet clots indicates that the spacers likely collected clots that formed upstream. As seen in Fig. 5.4, the flow cells were arranged with the membranes perpendicular to the table surface, and one of the channels above the other. Due to this positioning, the spacers show evidence of gravitational clot settling. In Fig. 5.7d, the spacers show increased clot deposition on their left sides, which was the side closer to the table. Additionally, the spacer in the lower channel of each device – those on the left side of the two sets in Fig. 5.7d – showed more clotting than the upper channel. Both patterns point to gravitational clot settling within the devices, and within the spacer meshes.

In some of the spacer meshes, a banding pattern was observed going down the mesh from inlet to outlet. Particularly in the fine mesh on the furthest right of Fig. 5.7d, the clots appeared to be deposited in evenly spaced regions. One possibility is that these regions may have formed because of the pulsatile flow of the peristaltic pump. In unpublished experiments, we have observed similar bands of clotting in tubing exposed to pulsatile pump flow. We speculate that the pulsatile flow leads to waves of stagnancy, which leads to clot formation in periodic intervals. Likely, the same stagnation effect led to the similar banded clot pattern seen in some of the spacer meshes. However, the banded pattern was not significantly visible in the coarse spacer meshes. Given the larger mesh size, we speculate that any small clots in the coarse spacer mesh may have migrated away from where they formed, reducing the visibility of any clot

patterns. Comparatively, the banded pattern was not seen in the device without spacers, even though the device was exposed to the same pulsatile flow.

5.3.4 Scanning Electron Microscopy (SEM)

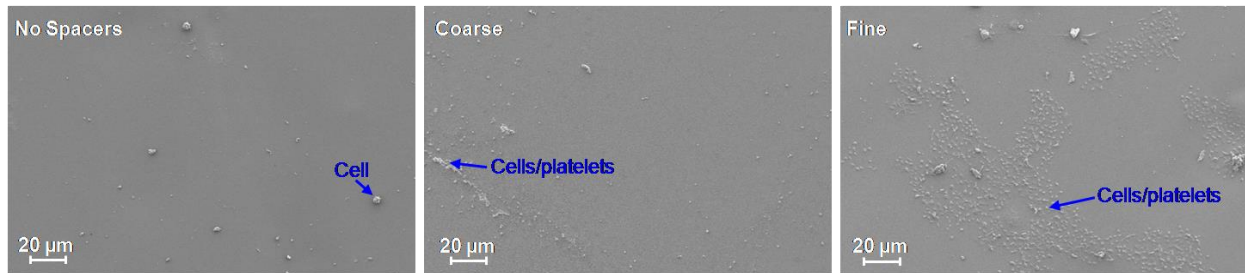


Fig. 5.8: Example SEM micrographs of S μ M post-blood exposure, taken at 500X magnification. Note that sample images from the coarse and fine spacers devices were selected to show regions where clots have formed, and are not necessarily representative of the overall surfaces.

Under SEM, the S μ M overall showed little deposition of clots, adhered cells, or adhered/activated platelets as seen in Fig. 5.8. Closer magnification showed that the surfaces all had an even layer of adsorbent proteins. In the no spacers device, the PDMS surface of the membranes showed only a few adherent non-erythrocyte cells. Considering the high hydrophobicity of PDMS, other studies have demonstrated considerable and platelet adhesion/activation on PDMS, even after similarly acute blood exposure. However, the incoming blood in this study was highly heparinized, likely preventing substantial platelet and cell adhesion. In both spacers devices, most SEM scans of the S μ M showed little evidence of clotting on the surface, similar to the no spacers condition. Some scans showed clot formation on the surfaces, which were selected for Fig. 5.8. Although these scans are not representative of the overall surface, they do show some linear patterns of adhered cells, activated platelets, and fibrous protein deposition, likely where the spacer meshes were in contact with the surface. The image of the fine spacer membrane in particular shows a right angle intersection of multiple clots, indicating the shape of the mesh. In these regions on the membrane surface, the spacers may have perpetuated sufficient stagnation to form these clots. Considering that the vast majority of the S μ M-PDMS surfaces showed little to no

clotting in any condition, it is likely that the membranes did not significantly contribute to the clot formation in the spacers devices.

Although the spacers in this study may not be suitable for turbulence inducement in ECMO, other strategies that are less intrusive may be more successful. Imprinting a texture onto parallel plate PDMS membranes, such as in Femmer et al. 2015, has been shown to improve gas exchange *in vitro* without raising the pressure drop. As with other turbulence-inducing strategies, applying a texture to PDMS membranes may lead to localized blood stagnation and clotting. However, optimization of the texture geometry could mitigate these effects.

5.4 CONCLUSION

In this work, two types of fluidic spacers were added to the $S_{\mu}M$ -PDMS oxygenator to evaluate impacts of the spacers on gas transfer efficiency and device hemocompatibility, with the overall goal of testing if turbulence inducement could benefit the $S_{\mu}M$ -PDMS oxygenator. Both types of spacers were shown to improve O_2 exchange in water by at least 50%, and more than doubled oxygen flux under most test conditions. Though the spacers improved gas exchange, they also led to a significantly higher trans-oxygenator pressure drop, which is often predicted to cause hemolysis and clotting in oxygenators. Theoretical analysis of the spacers showed that the spacers effectively increased the velocity of fluid through the oxygenator channels by decreasing hydraulic diameter, leading to more convective mass transfer with spacers.

Once the spacers were put in contact with *in vivo* blood flow, the devices with spacers clotted within less than an hour of exposure, with some of the clot patterns indicating that stagnant zones may have formed due to pulsatile pump flow through the spacer meshes. Interestingly, no evidence of clotting was observed on the $S_{\mu}M$ -PDMS surfaces in any device, meaning that the spacers were likely responsible for the entirety of the clotting. Overall, the patterns of clots indicate that the spacers strongly reduced the hemocompatibility of the $S_{\mu}M$ -PDMS oxygenator, while the membranes and flow path design were

overall non-detrimental to hemocompatibility. ECMO systems are typically rated for a minimum of 6 hours of use, and so the spacers as used in this study would be unsuitable for a full-scale device.

In conclusion, the spacers are likely not a viable strategy for enhancing gas exchange efficiency in parallel plate microfluidic ECMO devices due to the high likelihood of thrombosis. However, turbulence generation can significantly increase gas exchange *in vitro*, and non-invasive methods of inducing convective flows may be valuable to PDMS oxygenators. Also, the S μ M-PDMS membranes have shown considerable promise for a potential compact CO₂ removal device. Future work will use the gas exchange measurements from the S μ M-PDMS to continue developing a more advanced device for clinical gas exchange.

CHAPTER 6

CONCLUSIONS AND FUTURE DIRECTIONS

Current hollow fiber ECMO devices are unsuitable as a long-term lung replacement therapy due to a high risk of patient complications, restricting their use to only the most critically ill, bedbound patients with no other treatment options^{9,150}. The most common ECMO complications of thrombosis and bleeding stem from a lack of hemocompatibility throughout the large blood-contacting circuit. The complexity of pump-driven turbulent flow through the circuit – including the oxygenator – results in regions of stagnancy and uneven shear stresses, precipitating thrombosis. Additionally, to meet oxygenation and carbon dioxide removal needs, an adult-size oxygenator requires over 1 m² of membrane surface. Beyond the high blood-contacting surface area, the membranes can become fouled over time due to protein and cell adhesion, leading to gradually reducing performance of the oxygenator over time¹⁵. Ultimately, due to the cumbersome constraints on conventional ECMO, the therapy is unsuitable for most lung failure patients, especially in an ambulatory capacity.

Since ECMO is not intended to be a destination therapy for lung failure, a clinical need exists to treat many chronically ill lung failure patients who require indefinite respiratory assistance. For these patients, an ambulatory lung supplementation device could be used as a long-term destination therapy or bridge to transplant, using a similar approach to ECMO oxygenation^{6,14}. Such a device would be ideally compact and pumpless to minimize thrombosis risk^{52,222}. Given the thrombosis risks with hollow fiber

oxygenators, another type of membrane oxygenator may be more suitable to create a long-term ambulatory device.

This research work endeavors to implement a novel gas exchange technology – S μ M-PDMS membranes – in the design of an ambulatory lung assistance device, optimized for gas exchange efficiency and hemocompatibility. In this pursuit, multiple approaches were used to improve the functionality of the S μ M-PDMS oxygenator. First, different configurations of silicon membranes were characterized for mechanical strength and gas exchange capacity in order to determine the optimal platform for a robust, efficient oxygenator (Chapter 2). Following selection of S μ M-PDMS membranes, oxygenator prototypes were developed to simulate and validate these membranes' gas exchange performance, both *in vitro* and *in vivo* (Chapter 3). These *in vivo* experiments set an important performance benchmark for the S μ M-PDMS oxygenator concept by characterizing blood-gas exchange through the membranes. Additionally, this data provided significant insight into the design elements that affected the implementation of S μ M-PDMS membranes for gas exchange, and highlighted areas for future enhancement.

Two optimization objectives were defined: hemocompatibility of the device flow path and the membrane surfaces, and gas exchange (both O₂ and CO₂) through the S μ M-PDMS device. Since this work did not involve constructing a full-scale S μ M-PDMS oxygenator, hemocompatibility refinement of the prototype device flow path was not significantly prioritized at this stage of development. To improve the hemocompatibility of the S μ M-PDMS membrane surfaces, variations of a polyethylene glycol (PEG) coating was applied to silicon and PDMS surfaces using multiple liquid deposition protocols (Chapter 4). *In vitro* results indicated that, on silicon-PDMS composites specifically, no variation of the PEG coating yielded a stable antifouling coating. While thick multilayers of PEG (~15-20 nm) were highly effective at deterring protein fouling on cast PDMS, these benefits may have been observed due to instability of the coatings on cast PDMS specifically. In Chapter 5, convective mixing was introduced into the flow path of

a newer prototype S μ M-PDMS device in order to increase oxygen and carbon dioxide exchange, thereby enabling the design of a more compact oxygenator. Placement of mesh spacers in the liquid flow channels increased oxygen flux up to threefold *in vitro*, but caused occlusive thrombosis within the devices upon acute exposure to flowing blood.

Continuing from this early work with the functional coatings, further experiments are necessary to fully characterize and implement the coatings on S μ M-PDMS membranes. Much effort is still required to establish the impacts of the coatings on gas exchange and hemocompatibility with more rigorous *in vitro* and *in vivo* testing, assuming that the difficulties with *in vivo* testing can be addressed. If a biomolecule coating is selected, such as hyaluronic acid, additional experiments will be required to evaluate the coatings' stability and sterilizability prior to usage on a large-scale S μ M-PDMS oxygenator. Any impact of the selected coating on O₂ or CO₂ exchange through the membranes should be factored into the scaling of the full-size S μ M-PDMS oxygenator. Beyond using the functional coatings specifically on the S μ M-PDMS membranes, future work on the coatings could more deeply investigate the mechanisms by which the coatings impact gas exchange. Examining the interactions between the coatings and blood buffering systems could explain functional benefits of the coatings, and open up the possibilities for functional coatings on other medical devices.

While the spacer meshes may not have been a viable option for a S μ M-PDMS oxygenator, this study still justifies the need to improve gas exchange in an oxygenator through disruptive mixing. The addition of mixing in laminar flow blood channels could potentially reduce oxygenator size to a fraction of that of current hollow fiber devices, should thrombosis risk be mitigated. Through iterative optimization, future work can develop another type of thrombosis-minimizing mixer by reducing stagnant zones and controlling shear stress throughout the flow path. These structures can be simultaneously evaluated for improved gas exchange, ideally producing a mixing structure that meets both criteria. One potential solution could involve embossing mixing structures directly onto the membrane surfaces,

promoting mixing at the boundary layer region itself. Since the membrane surfaces are made of PDMS, soft lithography could be used to pattern a variety of structures onto the membrane surfaces, as described in other works^{123,223}. Usage of these structures throughout a S μ M-PDMS oxygenator could significantly reduce the membrane area and overall device size required for scale up to a full-size oxygenator.

Moving forward, development on the functional coatings and convective mixing can be leveraged to create a full-scale oxygenator capable of acting as a long-term lung assistance device. To prepare for scale up, mass transfer modeling and experimental validation can establish the ideal dimensions of a S μ M-PDMS oxygenator. Using methods from Chapter 2 and Chapter 3, continuing experimental work can focus on arranging multiple membranes in various series and parallel configurations, with the goal of determining the effects of channel geometry on gas exchange and pressure drop. Any alterations to gas exchange from functional coatings or mixing structures can be factored into calculations of final device size. Once a final device geometry has been conceived, the S μ M-PDMS can be stacked into an array of multiple membranes, achieving the required surface area for sufficient gas exchange. Using computational modeling, a manifold can be designed to house this membrane array and minimize thrombosis risk throughout the blood flow path. Finally, this full-scale oxygenator can be evaluated for gas exchange and hemocompatibility in a large-scale animal model, with the overarching goal of assessing its suitability as a long-term lung assistance therapy.

APPENDIX

A.1. FUNCTIONAL OXYGENATOR COATINGS FOR IMPROVED GAS EXCHANGE AND HEMOCOMPATIBILITY

Work in this chapter is ongoing and incomplete at the time of writing. This write up was included as an appendix for completeness.

A.1.1 INTRODUCTION

ECMO oxygenators have been constructed out of a variety of materials throughout their history, with certain material properties being particularly desirable for this specific application. First, the material must be sufficiently permeable to both O₂ and CO₂ gases to ensure that the oxygenator membranes can perform with maximum efficiency and minimum surface area. Liquid tightness is highly important to the blood oxygenator to prevent both gas emboli from forming in the blood, and plasma leakage into the sweep gas compartment. In addition, hemocompatibility of the material is essential to both prevent thrombus formation through platelet activation, and performance-reducing fouling of the membranes through protein adsorption. Furthermore, mechanical robustness is a significant concern to prevent membrane rupture; however, multiple materials can be used in a composite to reinforce a material that has insufficient mechanical strength on its own.

Some of the most common materials used in blood oxygenators are silicones because they feature high gas permeability to both O₂ and CO₂, biological inertness, and complete liquid tightness. Historically, silicone membranes were used as the basis for early parallel plate oxygenators^{54,212,216,224}, and subsequently silicones were used as coatings on porous hollow fiber oxygenators to prevent plasma leakage^{26,217}. More recently, research groups have constructed microfluidic capillary-like oxygenators using a silicone known as polydimethylsiloxane (PDMS), which has been extensively studied as a biomaterial in many applications^{55,109,120,225}. Similarly, our lab has developed novel membranes for blood-

gas exchange, based on the MEMS manufacturing of silicon from the integrated circuits industry. We have designed a composite membrane consisting of a silicon membrane surmounted with a 5 μm thick layer of PDMS; this structure is completely liquid-tight, and mechanically highly robust despite the thinness of the PDMS layer ^{143,160}.

Still, while silicones such as PDMS can be desirable for blood oxygenators, they are also susceptible to significant blood reactivity. PDMS and other silicones are bioinert but naturally hydrophobic, meaning that they attract significant adhesion of proteins – including fibrinogen – to the surface. Over time, adhesion of proteins to membranes reduces performance through fouling, and may also trigger platelet activation and eventually thrombus formation ^{183,226,227}. As such, surface modification of silicones is necessary for use in blood oxygenators. Through silane bonding chemistry, PDMS can be modified to have a variety of surface properties, especially hydrophilic or ionically charged groups, in order to reduce biofouling and thrombogenicity. Specifically for blood oxygenation, coatings that have been studied on PDMS include polyethylene glycol (PEG), zwitterionic polymers such as sulfobetaine, and endothelialization of the surface ^{124–127,180,227}. These coatings are often successful at stably improving hydrophilicity of PDMS, and reducing protein fouling and platelet responsiveness. Still, on an oxygenator, these coatings must demonstrate that they do not impede the transport of O_2 and/or CO_2 through the membranes, which most researchers on PDMS oxygenators have not addressed.

Research on hollow fiber ECMO devices can inform future work on coatings for silicone-based oxygenators, though generally these studies are limited. In some cases, coatings on hollow fibers have significantly reduced the gas permeability through the membranes, especially for endothelialized hollow fibers ⁸⁹. Other studies on polymeric coatings, such as zwitterionic coatings, have shown no change in permeability with the application of the coating ²²⁸. Interestingly, one particular coating on hollow fiber membranes was shown to significantly increase the removal of CO_2 from blood. In work by Arazawa, et al., researchers covalently attached the enzyme carbonic anhydrase to the surfaces of hollow fibers ⁷³;

physiologically, carbonic anhydrase maintains the buffering equilibrium between bicarbonate ion $[\text{HCO}_3]^-$ and CO_2 in blood. Along with the enzyme coating, a sweep gas containing sulfur dioxide (SO_2) was introduced into the system, causing dissolved sulfites to enter the bloodstream. Through lowering the pH of the blood local to the membrane surface, the balance between $[\text{HCO}_3]^-$ and CO_2 shifted in favor of dissolved CO_2 , which was increasingly driven out of the blood. Ultimately, the acidic sweep gas and the enzyme coating worked synergistically to drive increased CO_2 out of the bloodstream by interfering with the blood buffering system for CO_2 . This phenomenon, known as local acidification, demonstrates that the blood nearest to the membrane surface can strongly influence the gas permeability of the overall membrane. Interfering with the blood chemistry at this local level may provide options for improving gas flux through any type of oxygenator.

The purpose of this work is to apply biomolecule-based coatings to the surfaces of PDMS membranes intended for use in a blood-gas exchange device. Through chemical interactions between the coatings and the blood, these coatings were intended to both improve the hemocompatibility of the hydrophobic PDMS, and enhance gas exchange of O_2 and/or CO_2 through the membranes. In this study, we applied an amine precursor coating, and subsequently attached a number of biomolecule coatings on PDMS. We then characterized their effects on hydrophilicity and *in vitro* oxygen permeability, over the course of two major experiments. The coated membranes were then exposed to an *in vivo* porcine blood oxygenation circuit to determine the effects of the coatings on O_2 and CO_2 gas exchange. Post-analysis of adhered proteins and activated platelets was conducted to determine if the coatings had a beneficial effect on membrane hemocompatibility. Results are documented by individual experiment. Using these findings, we determine which, if any, of the coatings would be desirable on a blood-gas exchange device using PDMS as a membrane material.

A.1.2 MATERIALS AND METHODS

A.1.2.1 Substrates and Precursor Coatings

A.1.2.1.1 Substrates

Silicon micropore membranes, abbreviated as S μ M, were prepared for use as gas exchange membranes following prior work in this lab^{143,160}. Briefly, S μ M are created using silicon MEMS fabrication processes to yield flat-sheet membranes with highly organized, uniform pores. The membrane pores in this study were 1 μ m in width. A 5 μ m-thick layer of polydimethylsiloxane (PDMS) was formed from spin-coated Sylgard 184 PDMS (Dow Corning, Midland, MI, USA) mixed at a 10:1 elastomer-to-crosslinker ratio, and then diluted 1:1 with hexanes (Millipore Sigma, Burlington, MA, USA) as described in prior work. Each S μ M was bonded with PDMS through oxygen plasma treatment to yield the final membrane structure. These Si-PDMS membranes have been characterized in past work as both highly gas-permeable and structurally rigid – important qualities for designing a compact, efficient oxygenator.

Two additional substrates were created as materials controls for the Si-PDMS membranes. The first substrate (“Si”) consisted of 1 cm² pieces of silicon cut from 400 μ m-thick double side polished, p-type wafers. The second substrate (“PDMS”) consisted of undiluted Sylgard 184 PDMS mixed at a 10:1 elastomer-to-crosslinker ratio, which was cast into a 3 mm-thick sheet and cut into 1 cm² discs. Together, the Si-PDMS membranes and additional materials controls became the substrates for subsequent application of the biomolecule coatings.

A.1.2.1.2 Aminosilane Precursor Application

Prior to aminosilane application, all glassware was dried overnight in a 100°C oven. The aminosilane precursor was then applied to the surface of all substrates via silane bonding chemistry. The specific aminosilane chosen was N1-(3-Trimethoxysilylpropyl)diethylenetriamine, abbreviated as “DETA” (Millipore-Sigma). First, the substrates were treated with oxygen plasma (Harrick Plasma PDC-

001, Harrick Plasma, Ithaca, NY, USA) for 1 minute at high power (~30 watts) to produce reactive silanol groups on the surfaces. A solution of 5% DETA in anhydrous N,N-Dimethylformamide (DMF) was prepared (Millipore-Sigma). After activation, each substrate was individually placed into a reaction vessel: Si-PDMS membranes into 15 mL polypropylene conical tubes, and Si and PDMS substrates into 20 mL glass scintillation vials. 8 mL of DETA solution was added to the Si-PDMS membrane vessels, and 2 or 3 mL of the solution was added to the Si and PDMS vessels respectively. The reaction vessels were placed on a shaker and gently agitated for 3 hours at room temperature. Following the reaction, all substrates were washed 6 times: twice with DMF, twice with 1:1 DMF and methanol (VWR, Radnor, PA, USA), and twice with methanol. Substrates were dried in a desiccator overnight.

A.1.2.1.3 Poly(acrylic acid) (PAA) Immobilization

Prior to functionalization, poly(acrylic acid) (PAA) was modified to enable use in organic solvent systems. Poly(acrylic acid) sodium salt (3 g) was dissolved in 300 mL of deionized water. Following dissolution of polymer, HCl (3M) was added dropwise until pH of the solution reached 1, as monitored with litmus paper. This solution was stirred overnight at RT to allow the acidification of PAA (COO-Na to COO-H) to reach equilibrium. Following acidification of PAA, the reaction mixture was added dropwise to cold ethanol (500 ml) to precipitate the NaCl. Salt precipitate was filter by vacuum filtration, and the solvent was reduced by rotary evapoation until all ethanol was removed. Then water was removed by lyophilization and the product (white precipitate) was stored in a dry environment to prevent contamination of moisture.

To tether PAA to the aminated surface, 2 g of PAA (0.27 mol) was dissolved in 100 mL of anhydrous DMF at 70 C, then once dissolved 5.7 g of O-(7-Azabenzotriazol-1-yl)-N,N,N',N'-tetramethyluronium (HATU) (Thermo Fisher Scientific, Waltham, MA, USA) and 3 ml of DIPEA were added to the reaction solution and allowed to react for 30 minutes. HATU and DIPEA are amide coupling reagents which activate the carboxylate groups on PAA. After activation of PAA, the solution was added

to reaction vials containing the aminated substrates which reacted for at least 12 hours. Once finished the reaction solution was decanted and the substrates were thoroughly washed in excess solvent: twice with DMF, twice with 1:1 DMF:methanol, and twice with methanol. Thorough washing of the substrates with the reaction solvent is necessary to prevent deposition of reactants, which can be difficult to remove if formed. Substrates were then dried under vacuum and store in a desiccator until further reaction steps.

A.1.2.2 Secondary Reactions

A.1.2.2.1 Hyaluronic Acid Application

Hyaluronic acid (HA) was attached directly to the DETA-coated surfaces via EDC-NHS chemistry. 250 mg of HA (1.5-1.8 10E6 kDa, Millipore-Sigma) was dissolved in 50 mL MES buffer (50 mM, pH 5.5) to reach a final concentration of 5 mg/mL. The pH was adjusted with 1 M HCl to keep the solution at pH 5.5. Next, while stirring, 95.0 mg N-(3-Dimethylaminopropyl)-N'-ethylcarbodi-imide Hydrochloride (EDC, 0.50 mmol) (Thermo Fisher Scientific) and 12.0 mg N-Hydroxysuccinimide (NHS, 0.10 mmol) were added to the HA solution to activate the carboxylate side chains, which can then react with the primary amines on the substrates. This solution was reacted for 30 minutes. In parallel, the freshly silanized substrates were incubated in PBS (pH 7.4) for 30 minutes to partially deprotonate the amine groups: 1 mL for Si substrates, 2 mL for PDMS substrates, and 12 mL for Si-PDMS membranes. After activation, the same amounts of the HA solution were added to the pretreated substrate reaction vials and allowed to react overnight while stirring. The samples were then washed in 6 cycles of excess solvent to remove the unreacted HA/EDC/NHS: twice with MES Buffer pH 5.5, twice with deionized water, and twice with methanol. Then were subsequently dried under vacuum overnight and stored in a desiccator prior to characterization.

A.1.2.2.2 L-Histidine and Lysine Attachment to PAA

Histidine and lysine were modified for use in organic solvents to facilitate attachment to PAA. L-Histidine hydrochloride (Thermo Fisher Scientific) was purified using the same procedure as PAA.

To prepare the lysine for modification of PAA, the BOC protecting group of the lysine (Fmoc-Lys(Boc)-OH) was deprotected to free up the epsilon amine for further reactions. 1 g/21 mmol of Fmoc-Lys(Boc)-OH was dissolved in 25 mL of anhydrous DCM under stirring at 0°C. Second, 2.6 mL of trifluoroacetic acid (TFA) was added drop wise to the reaction mixture and allowed to react for 12 hours to remove the BOC protecting group. The reaction was then purified by rotary evaporation to remove the solvent and TFA salt byproducts. To achieve complete removal of TFA byproducts, the product was washed with dichloromethane and methanol two times.

A.1.2.3 Coating Characterization

A.1.2.3.1 Contact Angle – Wettability

Contact angle was used to assess successful application of the coatings at various stages of application (Fig. A. 1.1a). Changes to the contact angle after applying a coating would indicate if surface modification had occurred. Sessile drop measurements using deionized water were recorded for each sample using a Biolin Scientific Theta Lite optical tensiometer (Stockholm, Sweden) with OneAttension software¹⁴¹. Additional characterization via colorimetric staining for amine content (Coomassie staining, Fig. A. 1.1b) and carboxyl content (Toluidine Blue), as well as x-ray photoelectron spectroscopy, was conducted. However, these datasets were incomplete and therefore not included in this analysis.

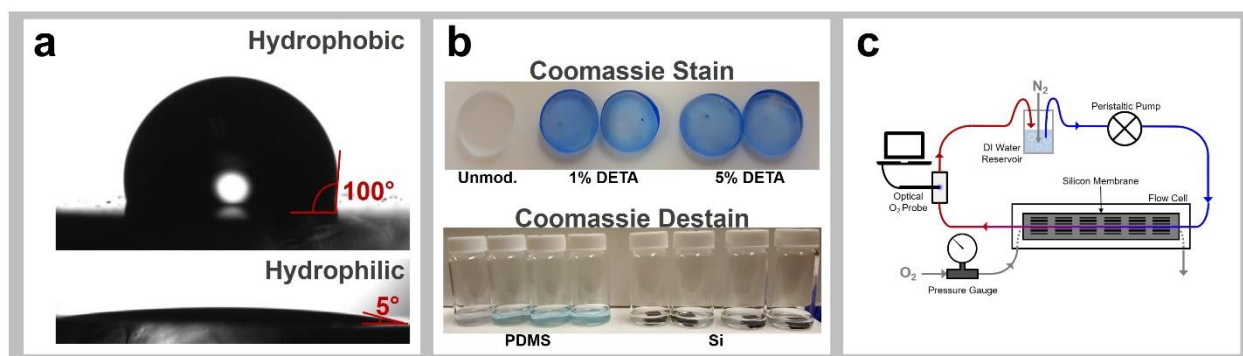


Fig. A. 1.1: *In vitro* testing methods for biomolecule-coated membranes: (a) contact angle for wettability, (b) Coomassie staining and destaining for amine content analysis, and (c) *in vitro* oxygen flux testing.

A.1.2.4 Gas Permeability and Hemocompatibility Evaluation

A.1.2.4.1 Oxygen Flux *In Vitro*

Following methods described in Abada, et al. (2018)¹⁶⁰, Si-PDMS membranes with each coating were evaluated for oxygen flux in an *in vitro* testing system (Fig. A. 1.1c). Briefly, deoxygenated water was pumped through a flow cell containing a single membrane, with oxygen sweep gas supplied to the opposite side of the membrane at a constant gauge pressure of 260 mmHg. Changes in oxygen concentration of the water as measured in $\mu\text{mol/L}$ are detected by an optical oxygen probe (NeoFoxGT with FOSPOR probe, Ocean Optics, Dunedin, FL, USA) before and after the sweep gas is supplied ($[O_2]_i$ and $[O_2]_f$, respectively). Three measurements were taken with each membrane at water flow rates varying from 5, 10, 20, 40, and 60 mL/min. Using measurements of $[O_2]_i$ and $[O_2]_f$, the area-normalized flux (J , mL O_2 /min/m²) was determined with a conversion of 22.4 L O_2 /mol at STP:

$$J = \frac{([O_2]_f - [O_2]_i) \cdot 10^{-6} \frac{\text{mol}}{\mu\text{mol}} \cdot 22.4 \frac{\text{L}}{\text{mol}} \cdot Q_{H_2O}}{A_m}$$

Eq. A. 1.1

where Q is the flow rate of water in mL/min and A_m is the porous area of the membrane in m². Through calculation of the area-normalized flux, the relative oxygen flux of each coating can be compared to determine if coating application compromises gas transport efficiency.

Experiment 1

The coatings tested in this experiment were unmodified PDMS, PAA-Lys, HA, and PAA-His. Membranes with these coatings were evaluated for O_2 flux individually at water flow rates of 5 and 10 mL/min. These flow rates were chosen to mimic previous studies on silicon membranes^{143,160}. Then, two membranes of a single coating were mounted into a parallel plate flow cell for *in vivo* use (Fig. A. 1.2). In this experiment, the membranes were mounted into a parallel plate flow cell as labeled in Fig. A. 1.2a,

with both membranes located on the same face of the device. Due to insufficient numbers of membranes, two materials controls without pores – unmodified silicon and unmodified Si-PDMS – were mounted on the opposing face of the device, with Si-PDMS at the inlet and Si at the outlet. This meant gas flow would only occur through the face of the device containing membranes. In this experiment, the coatings were only evaluated individually, and not in the assembled devices.

Experiment 2

The coatings tested in this experiment were unmodified PDMS, DETA, HA, Hemin, PAA alone, PAA-His, and PAA-Arg. Compared to Experiment 1, the inclusion of DETA and PAA alone ensured that the effects of these intermediates would be evaluated. Since sufficient membranes were available, four membranes with these coatings were tested individually at water flow rates of 10, 20, 40, and 60 mL/min. These flow rates were chosen to both encompass past *in vitro* data on silicon membranes at 10 mL/min, and also the possible flow rates that would be used in the *in vivo* experiment. Then, with the exception of PAA alone, the four membranes were assembled into the parallel plate flow cell seen in Fig. A. 1.2. When assembled with four membranes, the device effectively positions two Si-PDMS membranes in series, and two more membranes in opposition. The oxygen flux through this entire assembled devices were then evaluated at water flow rates of 20, 40, and 60 mL/min.

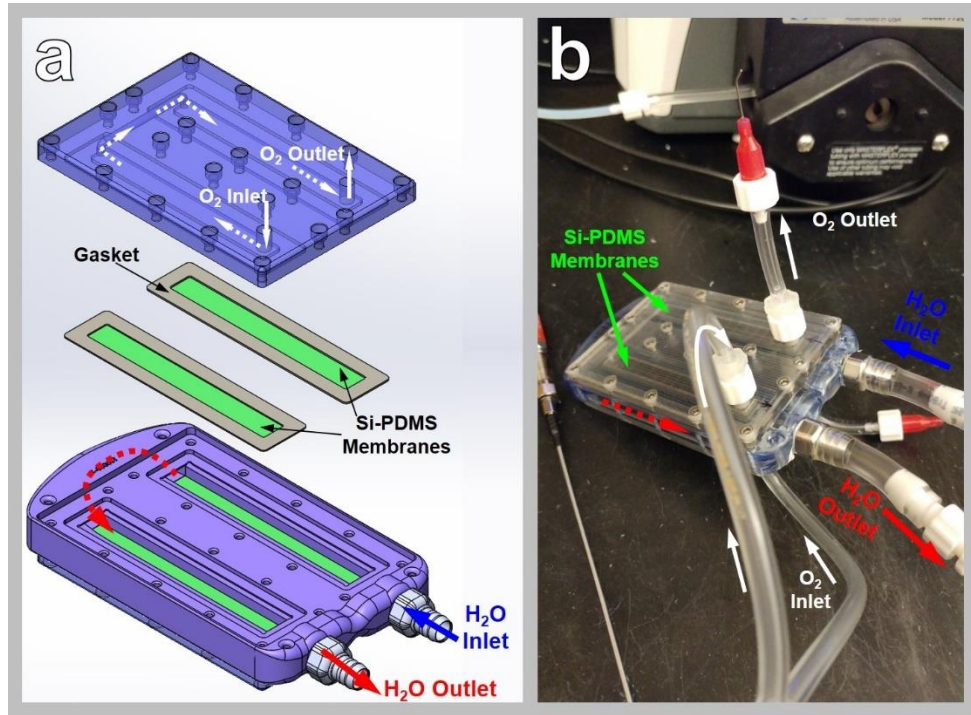


Fig. A. 1.2: Assembly of 4-membrane parallel plate flow cell used for *in vitro* and *in vivo* testing. (a) shows a diagram of the exploded flow cell, and (b) shows the assembled flow cell.

A.1.2.4.2 *In Vivo* Gas Exchange and Hemocompatibility

For both *in vivo* studies, devices with the coatings were evaluated for O₂ and CO₂ flux and hemocompatibility using an *in vivo* porcine model (~40 kg Yucatan minipig). Circuit setups for both experiments are in Fig. A. 1.3. By exposing the coatings to flowing blood, the functional impact of the coatings on gas exchange could be determined, as well as the hemocompatibility of the modified surfaces. The general procedure for both of the *in vivo* studies was as follows. Under general endotracheal anesthesia, a 15-French dialysis catheter (Arrow Cannon II, Teleflex, Wayne, PA USA) was inserted into the left external jugular vein using Seldinger technique, with the tip positioned at the cavoatrial junction. Heparin (100 U/kg) was administered intravenously and serially re-dosed to achieve ACT>300. At the beginning of each experiment, the pig was ventilated through a mechanical ventilator, supplied with 100% O₂. Near the beginning of each experiment, ventilation was removed and paralytics were

administered to prevent natural breathing. The pig was then ventilated by hand with room air to lower the pig's venous O₂ saturation to achieve slight hypoxia (SO₂ ~70%). The venous and arterial ports of the catheter were then attached to a closed flow circuit consisting of Tygon tubing (Masterflex L/S 25 Tygon E-LFL, Cole-Parmer, Vernon Hills, IL USA), divided into multiple channels (three for Experiment 1 and four for Experiment 2), and then passed through a peristaltic pump to control blood flow rate at 20 mL/min. Downstream of the peristaltic pump, each oxygenator device was connected to one of the blood flow channels, and flow from each channel was rejoined to return blood flow to the catheter. The circuit was primed with isotonic crystalloid solution prior to establishing blood flow. Three-way stopcocks were inserted in the Tygon tubing at the inlet and outlet of each oxygenator device to allow blood sample collection before and after exposure to the oxygenator's membranes.

Heparinized blood was flowed through the devices over a period of 2-4 hours, during which samples were taken from the inlet and outlet of each device. Blood gas analysis was conducted on these samples to assess pO₂, pCO₂, pH, and HCO₃⁻ using either an arterial blood gas machine (GEM3000, Instrumentation Laboratory, Bedford, MA, USA) or an iSTAT handheld blood analyzer (Abbott Point of Care Inc., Princeton, NJ, USA). After sufficient samples were collected, the devices were flushed with saline and then disassembled. The devices were grossly inspected for clots, and the membranes were removed, broken into pieces, and added to fixation buffers for hemocompatibility analysis. The experiment was conducted at a contract resource organization (PMI Preclinical, San Carlos, CA).

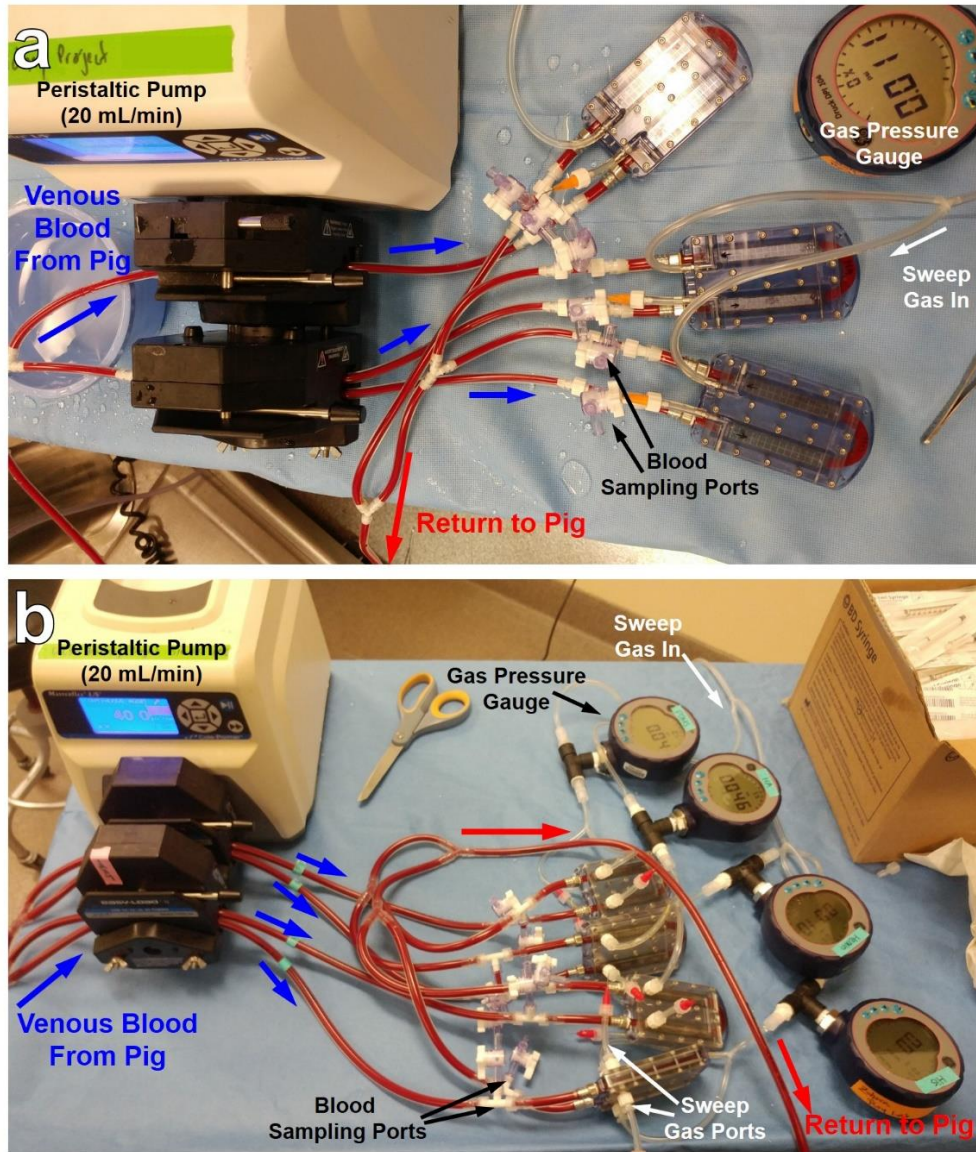


Fig. A. 1.3: Set up of *in vivo* gas exchange circuits for experiments 1 and 2. Devices in (a) from top to bottom: Lys, HA, His. Devices in (b) from top to bottom: unmodified PDMS, HA, Hemin, and PAA-His.

The area-normalized flux of O₂ and CO₂ through the membranes was calculated from the ABG or iSTAT readings at the inlet and outlet of each device. Inlet and outlet O₂ content ($[O_2]$, mL O₂/mL blood) was calculated as in Dharia, et al (2017)¹⁴³:

$$[O_2] = 1.36 \cdot Hg \cdot SaO_2 + 0.0031 \cdot PaO_2$$

Eq. A. 1.2

where Hg is the hemoglobin of the blood (mg/mL), SaO_2 is the percent of hemoglobin bound to oxygen, and PaO_2 is the partial pressure of oxygen in the blood (mm Hg). Similar to Eq. A. 1.1, the area-normalized flux of O₂ (J_{O_2} , mL O₂/min/m²) is calculated by:

$$J_{O_2} = \frac{([O_2]_{outlet} - [O_2]_{inlet}) \cdot Q_{blood}}{A_m}$$

Eq. A. 1.3

where Q_{blood} is the flow rate of blood and A_m is the porous area of the membrane. The calculation of CO₂ flux – described in Douglas et al. (1988) – accounts for CO₂ stored as a dissolved gas (pCO₂), as bicarbonate ion (HCO₃⁻), and bound to hemoglobin²¹⁹. First, inlet and outlet CO₂ concentration in plasma ($[CO_2]_{plasma}$, mL O₂/mL blood) is calculated using the logarithmic form of the Henderson-Hasselbalch equation for plasma CO₂:

$$[CO_2]_{plasma} = 2.226 \frac{mLCO_2 / 100mLblood}{mM} \cdot s \cdot pCO_2 \cdot (1 + 10^{pH - pK'})$$

Eq. A. 1.4

where s (plasma CO₂ solubility) and pK' (apparent pK) are known constants equal to 0.0307 mM CO₂/mmHg CO₂ and 6.0907, respectively. The inlet and outlet CO₂ concentrations in blood ($[CO_2]_{blood}$, mL O₂/mL blood) are then calculated using the McHardy-Visser equation:

$$[CO_2]_{blood} = [CO_2]_{plasma} \cdot \left[1 - \frac{0.0289 \cdot [Hb]}{(3.352 - 0.456 \cdot SO_2) \cdot (8.142 - pH)} \right]$$

Eq. A. 1.5

where SO_2 is the oxygen saturation of blood. The values of $[CO_2]_{blood}$ are used for the inlet and outlet content of blood CO_2 . Finally, the area-normalized CO_2 flux (J_{CO_2} , mL CO_2 /min/m²) is calculated as in

Eq. A. 1.3:

$$J_{CO_2} = \frac{([CO_2]_{outlet} - [CO_2]_{inlet}) \cdot Q_{blood}}{A_m}$$

Eq. A. 1.6

Experiment 1

Three of the coatings – HA, Lysine, and Histidine – were tested for O_2 and CO_2 flux, and hemocompatibility. In this experiment, two membranes with the same coating were mounted on the same side of the parallel plate device, and two materials controls (Si and Si+PDMS) were mounted on the opposing side as described above. Set up of the circuit is shown in Fig. A. 1.3a.

Blood was flowed through the circuit at a rate of 20 mL/min. Oxygen sweep gas was supplied to each device at a flow rate of 3 L/min between all devices and at a gauge pressure of 150 mmHg. Before taking measurements, blood was flowed through the circuit for one hour to stabilize the pig's ventilation status. After the pig's ventilation was stabilized, four samples were taken from the inlet and outlet of each device for blood gas analysis. After two total hours of blood flow, the devices were flushed with saline and disassembled.

Experiment 2

Four of the coatings – PDMS alone, HA, Hemin, and Histidine – were evaluated for O₂ and CO₂ flux, and hemocompatibility using an *in vivo* porcine model (40 kg Yucatan minipig). In this experiment, four membranes of a single coating were mounted into a parallel plate flow cell (Fig. A. 1.2a). Set up of the circuit is shown in Fig. A. 1.3b.

After one hour of extracorporeal blood circulation at 20 mL/min without oxygenation, flowing oxygen sweep gas was supplied at a flow rate of 3.5 L/min divided between all four devices, and gauge pressure of 220 mmHg. Five blood samples were taken from the inlet and outlet of each device for blood gas analysis to assess pO₂, pCO₂, pH, and HCO₃⁻ using either an arterial blood gas machine (GEM3000, Instrumentation Laboratory, Bedford, MA, USA) or an iSTAT handheld blood analyzer (Abbott Point of Care Inc., Princeton, NJ, USA). After nearly four hours of blood exposure, the devices were flushed with saline and disassembled.

A.1.2.4.3 Scanning Electron Microscopy (SEM)

After the porcine blood flow experiment, one fragment sample from each membrane was imaged for cell, platelet, and protein adhesion using scanning electron microscopy (SEM). Samples were placed in a solution of 3% glutaraldehyde (Millipore Sigma), 0.1 M sodium cacodylate (VWR), and 0.1 M sucrose (Millipore Sigma) at 4°C for 48 h. Then, the samples were washed twice with deionized water, and dehydrated by sequential 10 minute incubations with 35%, 50%, 70%, 90%, and two 100% ethanol/water (v/v%) solutions. The samples were dried in a desiccator overnight and mounted with conductive silver paint to aluminum SEM stubs. Finally, the samples were sputter coated with 4 nm of gold and imaged using a Carl Zeiss Ultra 55 Field Emission Scanning Electron Microscope (Zeiss, Dublin, CA, USA).

A.1.2.4.4 Platelet Immunohistochemistry (IHC)

Fluorescent immunohistochemistry (IHC) staining was only performed on samples from Experiment 2. Two membrane fragments from each coating set were imaged for platelet adhesion and activation using fluorescent staining of CD-41 (platelet identification marker) and CD-62p (platelet activation marker). Samples were placed in a 4% paraformaldehyde (Thermo Fisher Scientific) solution at 4°C until imaging (~2 weeks). The samples were washed and incubated with for an hour each with FITC-labeled anti-CD41 (orb181793, Biorbyt, Cambridge, UK) and Cy3-labeled anti-CD62p (bs-0561R-Cy3, Bioss Inc., Woburn, MA, USA). Samples were rinsed and imaged using a Nikon TI-E microscope (Nikon Instruments, Melville, NY, USA).

A.1.2.4.5 Statistical Analysis

For the Si-PDMS membranes, contact angle measurements were taken of at least three membranes, and each membrane was measured in three locations. A minimum of three sample measurements was taken for the Si and PDMS substrates in the contact angle, Coomassie staining, and TBO staining experiments. *In vitro* area-normalized flux was measured for four membranes of each coating. Statistical significance was determined using Graphpad Prism 8.2.0 (San Diego, CA, USA). Contact angle measurements were analyzed through one-way ANOVA. Tukey post-hoc tests were used to determine statistical difference ($p < 0.05$) between different coating conditions on the same substrate. Area-normalized flux was analyzed through two-way ANOVA for all flow rates and coating groups. Tukey post hoc tests were used to evaluate significant difference ($p < 0.05$) for all coating groups at the same flow rate, and for the same coating at different flow rates.

A.1.3 RESULTS

A.1.3.1 Coating Characterization

A.1.3.1.1 Contact Angle

Experiment 1

Measurements (average \pm SD) of contact angle after coating application on each substrate from Experiment 1 can be found in Fig. A. 1.4. The unmodified substrates showed similar contact angles to prior work in this lab: Si at 30.6° ¹⁴¹, Si-PDMS at 93.0° , and PDMS at 105° . In examining Si-PDMS specifically, DETA application did not alter the hydrophobicity of the surface. Once the coatings were applied on top of DETA, the HA and PAA-His coatings did significantly decrease the contact angle of the surface, with no difference between the two groups. PAA-Lys, on the other hand, did not significantly alter the contact angle of Si-PDMS. Compared to Si-PDMS, the Si material control showed a significant increase in contact angle with DETA application, while the PDMS material control showed no change in contact angle with DETA. On both materials controls, HA and PAA-His application on top of DETA significantly decreased contact angle in a manner similar to the Si-PDMS group. Also, PAA-Lys application on DETA for both materials controls remained hydrophobic compared to the other two biomolecule coatings.

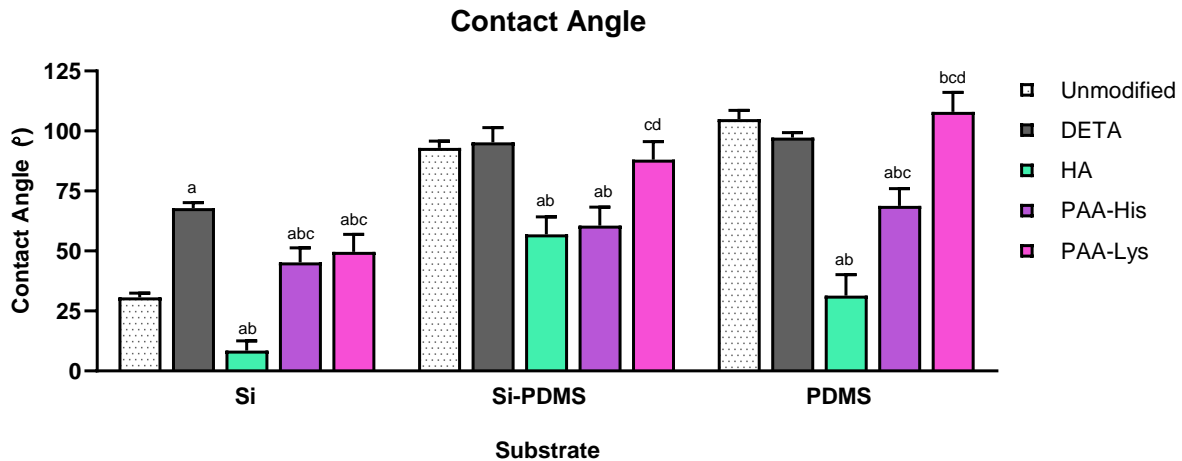


Fig. A. 1.4: Contact angle of biomolecule coatings on Si-PDMS membranes and Si and PDMS materials controls for Experiment 1. Significant difference ($p < 0.05$) is indicated above the columns: difference from the unmodified substrate is shown by (a), DETA shown by (b), HA shown by (c), and PAA-His shown by (d).

Experiment 2

Measurements (average \pm SD) of contact angle after coating application on each substrate from Experiment 2 can be found in Fig. A. 1.5. As in Experiment 1, all unmodified substrates showed similar contact angles to prior work in this lab: Si at 30.6° , Si-PDMS at 92.8° , and PDMS at 105° . Focusing on the Si-PDMS membranes, data showed only a slight difference in wettability with DETA application on the unmodified material, with both substrates remaining strongly hydrophobic²²⁹. However, the Si-PDMS showed significantly decreased contact angle with application of HA, PAA alone, and PAA bound to His (PAA-His). PAA bound to Arg (PAA-Arg) showed no difference from DETA alone, though more hydrophilic than the unmodified Si-PDMS. The Hemin coating did not significantly change wettability from the unmodified substrate, remaining strongly hydrophobic. The PDMS material control most of the same wettability trends as the Si-PDMS membranes, most notably significantly improved wettability with application of HA, PAA alone, PAA-His, and PAA-Arg. The Si material control exhibited different wettability changes than the Si-PDMS and PDMS substrates. DETA significantly increased contact angle

compared to unmodified Si, similar to values in prior literature²³⁰. All coatings on Si except HA remained more hydrophobic than the unmodified material: PAA-based coatings significantly reduced hydrophobicity from DETA alone, while Hemin was as hydrophobic as DETA.

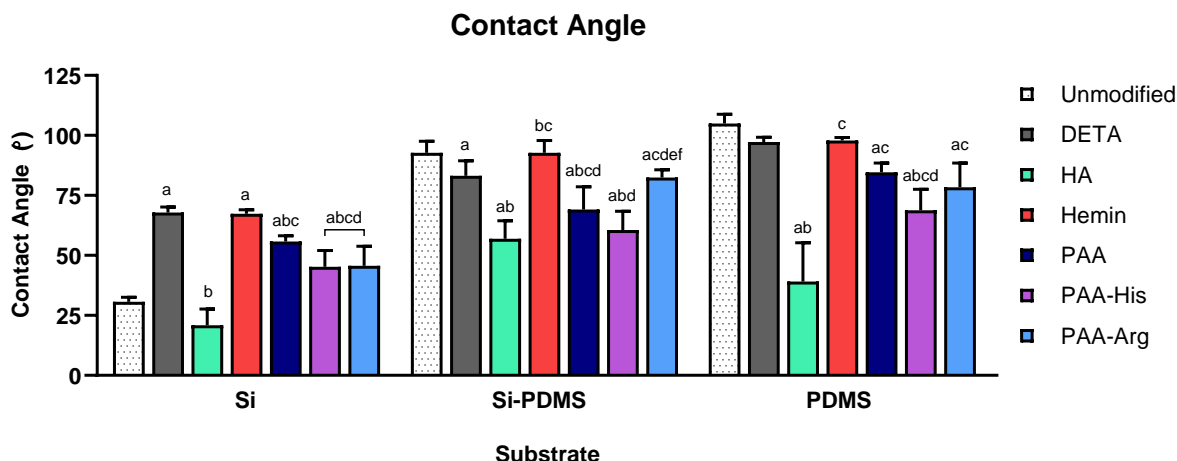


Fig. A. 1.5: Contact angle of biomolecule coatings on Si-PDMS membranes and Si and PDMS materials controls for Experiment 2. Significant difference ($p < 0.05$) is indicated above the columns: difference from the unmodified substrate is shown by (a), DETA shown by (b), HA shown by (c), Hemin shown by (d), PAA shown by (e), and PAA-His shown by (f).

Experiments 1 and 2

Between both Experiments 1 and 2, results from all three substrates indicate that DETA application likely caused the wettability of all substrates to converge to a certain contact angle, with an increase in hydrophobicity of Si and slight decreases in Si-PDMS and PDMS. Of the biomolecule coatings, HA was consistently the most hydrophilic of the coatings, with PAA-His also significantly improving hydrophilicity compared to DETA application. PAA-Arg was more hydrophilic on all substrates than the unmodified materials, though on both Si-PDMS and PDMS the PAA-Arg was not different from DETA alone. PAA-Lys and Hemin were consistently the most hydrophobic biomolecule coating, showing wettability similar to DETA alone (on Si) or the unmodified Si-PDMS and PDMS. Considering these trends in wettability, the biomolecule coatings expected to show the lowest cell,

platelet, and protein adhesion on any substrate would be HA and then PAA-His, as the most hydrophilic coatings. In contrast, PAA-Lys and Hemin – the most hydrophobic coatings – would demonstrate the most clotting and fouling on all substrates.

A.1.3.2 Gas Permeability and Hemocompatibility Evaluation

A.1.3.2.1 Oxygen Permeability *In Vitro*

Experiment 1

The area-normalized oxygen flux through the individual biomolecule-coated Si-PDMS membranes at water flow rates of 5 and 10 mL/min is shown in Fig. A. 1.6. At both of the tested flow rates, all of the substrates showed roughly equivalent O₂ flux. The flux of the unmodified PDMS group ranged from 81.3±28.1 to 130±15.5 mL/min/m². The flux ranges of the PAA-His (118±37.9 to 138±28.4 mL/min/m²) and PAA-Lys (114±25.1 to 131±17.9 mL/min/m²) coatings were similar. Only the HA group (range of 143±12.9 to 134±15.7 mL/min/m²). at a flow rate of 5 mL/min showed a significant increase in flux compared to the unmodified group. There was no difference in the flux of any group between the 5 and 10 mL/min flow rates. Generally, these results indicate that the coatings do not alter the inherent O₂ permeability of the Si-PDMS membranes. However, considerable variance in the flux measurements within each group may indicate that these results may not hold if more membranes were used. Furthermore, in this experiment, flux through the membranes was not measured at the *in vivo* flow rate of 20 mL/min, nor was flux measured through the assembled parallel plate devices. As such, for Experiment 2, the membranes were tested using a much wider range of flow rates, and were also tested in the parallel plate assembly that was used *in vivo*.

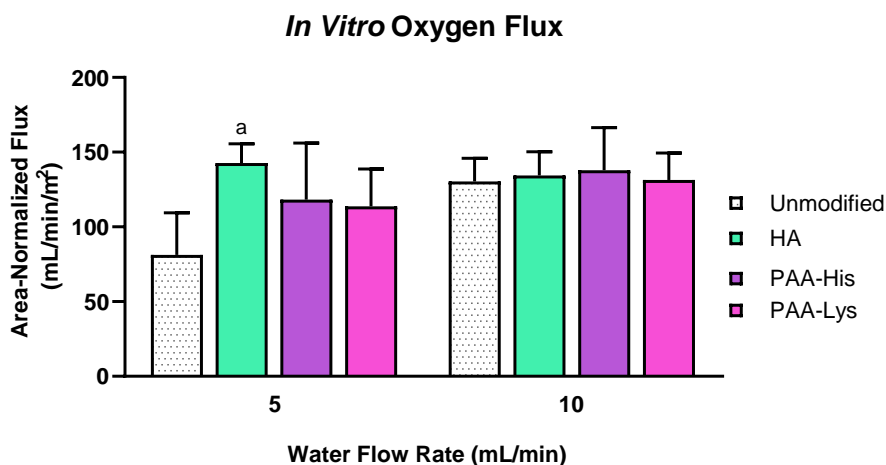


Fig. A. 1.6: *In vitro* oxygen flux of biomolecule coatings on individual Si-PDMS membranes from Experiment 1, normalized by membrane porous area. Significant difference ($p < 0.05$) between coating groups at the same flow rate is indicated by the letters above the columns: difference from the unmodified substrate is shown by (a).

Experiment 2

The area-normalized oxygen flux through the individual membranes at water flow rates of 10, 20, 40, and 60 mL/min is shown in Fig. A. 1.7. At all four flow rates, the unmodified Si-PDMS membranes showed the highest oxygen flux, ranging from 185 ± 24.7 to 361 ± 18.8 mL/min/m². Flux through these unmodified membranes significantly increased with each flow rate, consistent with boundary layer thinning and increased convective mass transfer at higher flow velocities. All the membranes with biomolecule coatings showed significantly lower oxygen flux than the unmodified substrate, with most coatings – DETA alone, HA, Hemin, and PAA-Arg – yielding around half the flux of the unmodified substrate. Membranes with DETA alone showed a range in flux of 108 ± 12.9 to 155 ± 32.5 mL/min/m², and the HA, Hemin, and PAA-Arg coatings were insignificantly different from DETA at each flow rate. PAA-His showed consistently lower flux than the other coatings, only around a quarter of the flux of the unmodified membranes (41.3 ± 4.56 to 45.7 ± 6.65 mL/min/m²). Interestingly, none of the biomolecule-

coated Si-PDMS membranes showed statistically significant increases in flux with higher water flow rates.

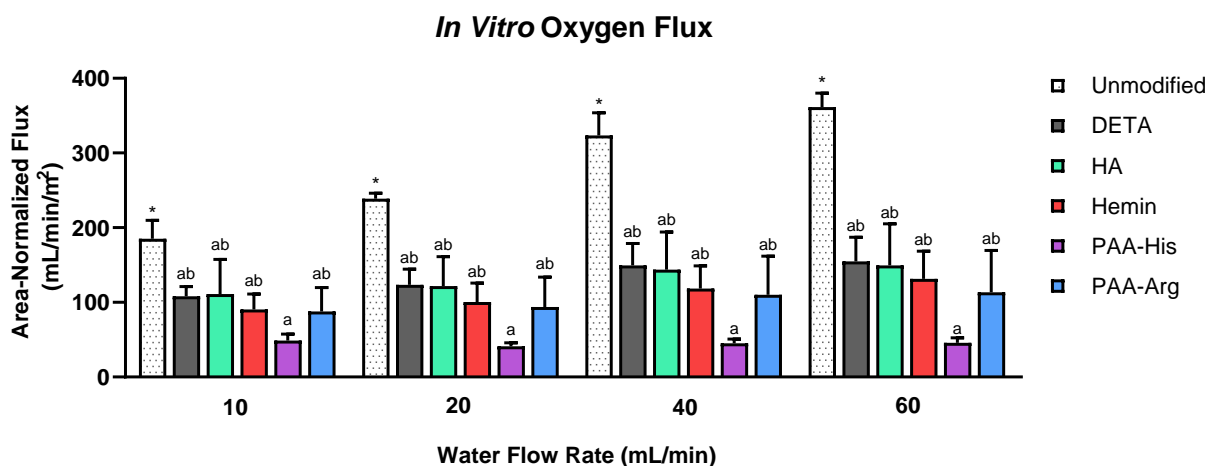


Fig. A. 1.7: *In vitro* oxygen flux of biomolecule coatings on individual Si-PDMS membranes from Experiment 2, normalized by membrane porous area. Significant difference ($p < 0.05$) between coating groups at the same flow rate is indicated by the letters above the columns: difference from the unmodified substrate is shown by (a), and PAA-His shown by (b). Significant difference of the same coating at different flow rates is indicated by (*).

Once the membranes were mounted into the 4-membrane parallel plate flow cell (Fig. A. 1.2), the oxygen flux throughout the assembled device was measured (Fig. A. 1.8). Compared to measuring the membranes individually, the flux measurements in the assembled device were much lower. For example, at 60 mL/min the individual unmodified membranes yielded 361 ± 18.8 mL/min/m² of O₂ flux while the assembled device yielded 129 ± 18.6 mL/min/m². Most likely, this discrepancy is due to the different channel dimensions between the flow cells. The channel height of the flow cell used for individual testing was 200 μ m, while the channel height of the flow cell in Fig. A. 1.2 was 3 mm, effectively 1.5 mm relative to each opposing chip. Considering that the flow rate through both devices was the same at 20, 40, and 60 mL/min, the freestream velocity in the large channel parallel plate device would be significantly lower by around an order of magnitude. The reduced freestream velocity (v , m/s) would

directly impact the mass transfer boundary layer thickness (δ , m) through the Reynolds number as follows:

$$\delta = \frac{4.91 \cdot x}{\sqrt{\text{Re}_x}}$$

Eq. A. 1.7

$$\text{Re}_x = \frac{\rho v x}{\mu}$$

Eq. A. 1.8

where x is any position along the surface of the membrane, ρ is the density of the fluid (kg/m^3), and μ is the dynamic viscosity of the fluid ($\text{kg}/\text{m}\cdot\text{s}$). With a lower freestream velocity in the larger channel, the Reynolds number decreases and the mass transfer boundary layer becomes thicker, leading to reduced oxygen flux in the larger channel.

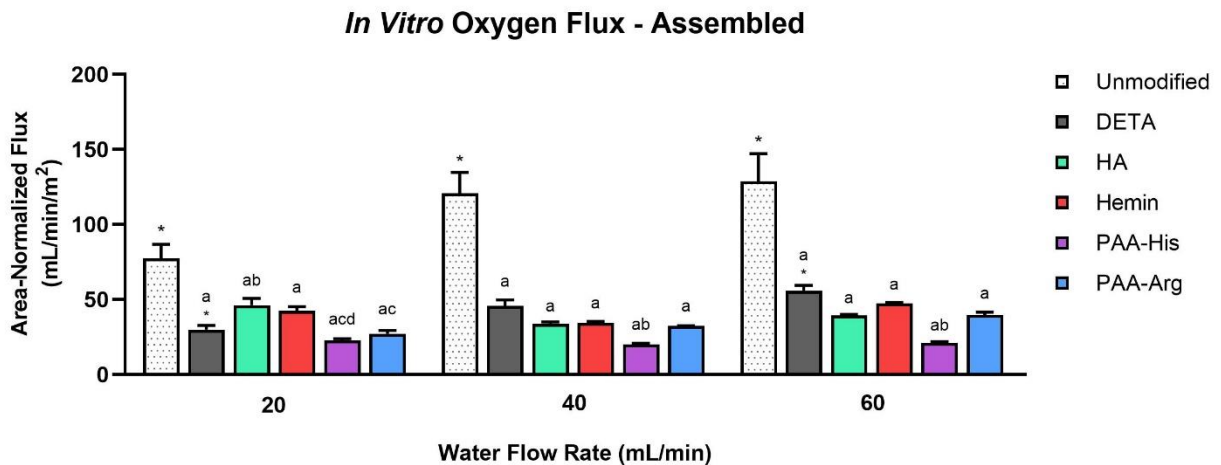


Fig. A. 1.8: Experiment 2 – *In vitro* oxygen flux of assembled parallel plate devices containing coated membranes, normalized by membrane porous area. Significant difference ($p < 0.05$) between coating groups at the same flow rate is indicated by the letters above the columns: difference from the unmodified substrate is shown by (a), DETA by (b), HA by (c), and Hemin by (d). Significant difference of the same coating at different flow rates is indicated by (*).

Experiments 1 and 2

Since the two experiments used a 10 mL/min flow rate, some comparisons between the two datasets can be made. Compared to Experiment 1, flux through the unmodified membranes at 10 mL/min was somewhat higher in Experiment 2, though not out of the range of error. Flux through the HA membranes was similar in both Experiments 1 and 2, but the flux through the PAA-His membranes was significantly lower in Experiment 2 compared to Experiment 1. The reason for this change may be due to variance in coating quality between the two datasets.

The *in vitro* O₂ flux results from Experiments 1 and 2 appear to contradict each other concerning whether the coatings impact the inherent O₂ permeability of the Si-PDMS membranes. Experiment 1 showed no significant difference in flux from the unmodified and coated membranes. However, from the *in vitro* results in Experiment 2, it is clear that application of any of the biomolecule coatings to Si-PDMS significantly reduces oxygen flux in water. Given that the dataset in Experiment 1 was more limited in scope, and did not test the membranes at higher flow rates, the dataset from Experiment 2 may be more reflective of the coatings' reduction of O₂ permeability. Most likely, the application of DETA to the surface is the primary driver of this reduction, since most of the biomolecule coatings added to DETA (HA, Hemin, and PAA-Arg) do not further reduce flux. Comparatively, PAA-His does seem to reduce flux beyond DETA alone. It is possible that the addition of PAA to DETA, which was not independently tested in this experiment, is responsible for this reduction in oxygen flux. However, since the PAA-Arg coating does not seem to impact oxygen flux through the membrane, it is unlikely that PAA addition alone reduces oxygen flux. Considering the *in vitro* data, it is possible that coated membranes will show a similar reduction when used *in vivo* with blood contact. Still, the coatings may provide some benefits over the unmodified PDMS substrate that will lead to better *in vivo* performance. The coatings may reduce biofouling on the surface – leading to higher gas transport with extended blood contact – or provide a functional benefit to gas exchange through ionic interference with blood buffering systems.

A.1.3.2.2 *In Vivo* Gas Permeability and Hemocompatibility

Experiment 1

All three of the coatings tested for contact angle and O₂ flux were tested in the *in vivo* oxygenation circuit: HA, PAA-His, and PAA-Lys. Insufficient resources were available to add the unmodified PDMS group into the circuit. Although this important control group was lacking in the circuit, testing the coatings together would permit comparison of these coatings *in vivo*.

After priming with saline, all three devices were connected to venous blood flow from the pig, circulating at 20 mL/min (Fig. A. 1.3). At the initial administration of blood flow, blood gas measurements indicated excessive oxygenation of the pig's blood from the mechanical ventilation system, with venous O₂ saturation of ~100%. Over the next hour, the pig's ventilation was altered to reduce the venous O₂ saturation to ~70%. During this time, the pig became significantly hypercarbic, with pH around 7.3 at the beginning of the measurement period, and 7.16 at the end of the period. With oxygen supplied through the sweep gas of each device, blood exiting the outlet of the devices became visibly brighter red in color, indicating some level of successful oxygenation and CO₂ removal (Fig. A. 1.9). Once the pig's ventilation had stabilized, a total of 4 measurement sets (inlet and outlet) were taken per device over an hour. In total, the membranes were exposed to flowing blood for 2 hours total during the experiment.

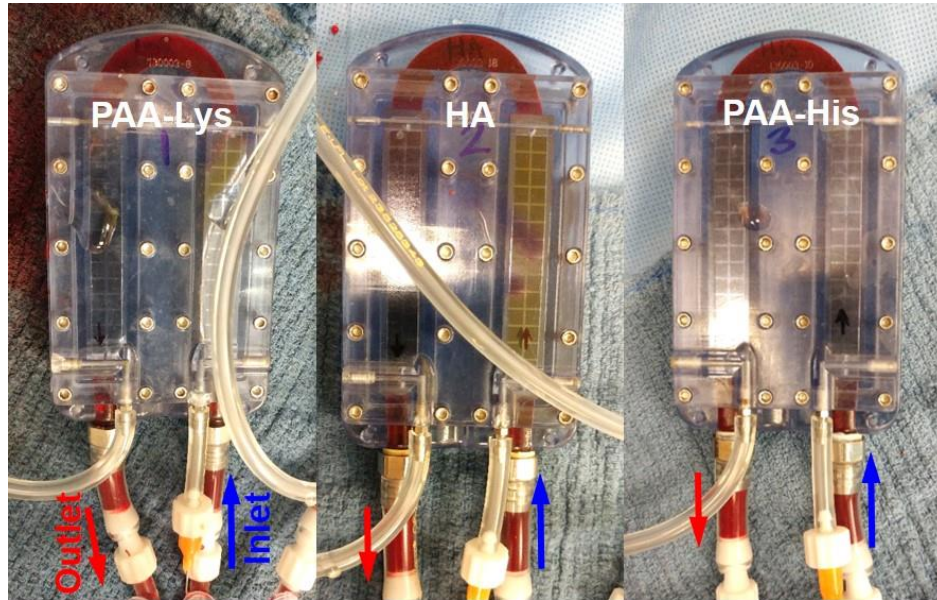


Fig. A. 1.9: Experiment 1 – Oxygenation of blood through assembled parallel plate devices *in vivo*. Inlets and outlets of each device are marked with blue and red arrows, respectively. Blood exiting the outlets was visibly brighter red in color compared to the inlets, indicating gas exchange of O₂ and CO₂.

The ABG measurements (Table A. 1.1) were used to calculate the O₂ and CO₂ flux through each device using Eq. A. 1.2-Eq. A. 1.6, shown in Fig. A. 1.10. Due to the high variance in measurements, no significant difference was found between any of the coating groups for either O₂ or CO₂ flux. For all coatings, the O₂ flux through the devices was negligible, with high variance in all measurements. The lack of blood oxygenation in this experiment may be attributable to the difficulty in controlling the ventilation to the pig throughout this experiment. However, the CO₂ flux through the coated membranes was strikingly high at ~8 L/min/m² for each of the devices. The CO₂ removal rates through the HA, PAA-His, and PAA-Lys devices were respectively 7.68±4.92, 7.84±4.52, and 8.90±0.439 L/min/m². Compared to other measurements of CO₂ flux through unmodified Si-PDMS membranes, such as in Chapter 5 (1.33±0.148 L/min/m²), the coatings' alteration of CO₂ flux is particularly dramatic. Given the severe hypercarbia of the pig in this experiment, it is possible that the CO₂ flux through the coatings was merely

elevated due to the significant excess of CO₂ in the blood. Without an unmodified PDMS control in this experiment, drawing conclusions from this data alone was unclear.

Table A. 1.1: Raw ABG data collected from the three coated devices during Experiment 1. Data is divided into pre- and post-device for the same time point.

Units	Flow Rate mL/min	Pre-Device					Post-Device				
		pH	pCO ₂ mmHg	pO ₂ mmHg	HCO ₃ ⁻ mmol/L	SO ₂	pH	pCO ₂ mmHg	pO ₂ mmHg	HCO ₃ ⁻ mmol/L	SO ₂
HA	20	7.23	71	52	29.7	079	7.23	51	57	21.4	0.83
	20	7.314	54.2	63	27.6	0.89	7.316	51.2	59	26.2	0.88
	20	7.257	65	41	29	0.67	7.234	34	38	14.4	0.64
	20	7.248	64.6	35	28	0.56	7.192	48.5	41	18.6	0.64
PAA-His	20	7.291	56.6	44	27.3	0.73	7.286	53.6	43	28.8	0.71
	20	7.32	56	56	28.9	0.86	7.32	31	60	16	0.88
	20	7.32	58	46	29.9	0.78	7.32	35	48	18	0.8
	20	7.23	72	44	30.2	0.7	7.24	51	39	21.9	0.63
PAA-Lys	20	7.265	61.3	50	27.8	0.79	7.261	41.1	53	18.5	0.82
	20	7.31	58	47	29.2	0.78	7.31	37	49	18.6	0.8
	20	7.27	67	32	30.8	0.52	7.27	46	34	21.1	0.56
	20	7.16	88	53	31.4	0.76	7.17	60	46	21.9	0.68

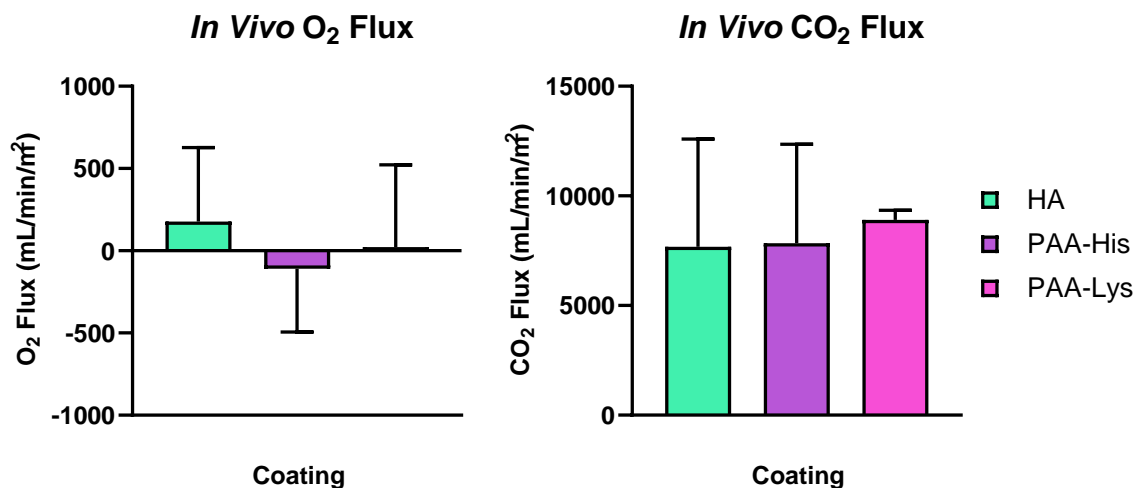


Fig. A. 1.10: Experiment 1 – Area-normalized O₂ and CO₂ flux *in vivo* of each parallel plate device, with a blood flow rate of 20 mL/min.

Experiment 2

From the *in vitro* testing of oxygen flux and contact angle, four coatings were downselected for *in vivo* testing: PDMS alone, HA, Hemin, and PAA-His. PDMS alone showed the highest oxygen flux *in vitro*, and would also act as a control group for the other three coatings. Both HA and Hemin showed comparable *in vitro* oxygen flux, but were strongly different in wettability. HA was the most hydrophilic, while Hemin was strongly hydrophobic. Despite its lower oxygen flux *in vitro*, PAA-His was selected due to its superior wettability compared to PAA-Arg. All three of the coatings together would permit comparison the effects of both gas permeability and hydrophilicity *in vivo*.

After priming with saline, all four devices were connected to venous blood flow from the pig, circulating at 20 mL/min (Fig. A. 1.3). During the first hour of blood flow, blood gas measurements indicated strong instability of the pig's ventilation regimen. pH values ranged from 7.3-7.7 throughout this period, and SO₂ ranged from 48-92%. Due to this instability, sweep gas oxygenation was not started until blood pH had stabilized to ~7.4 – around an hour after starting blood flow into the devices. Once the oxygen sweep gas was administered, blood exiting the outlet of the devices became visibly brighter red in color, again indicating some level of functional gas exchange (Fig. A. 1.11). Throughout the first hour of sweep gas administration, the incoming venous blood still showed significant instability in all ABG measurements – pH, pO₂, and pCO₂ – so only the measurements taken after 1 hour of oxygenation were used for subsequent calculations of O₂ and CO₂ flux. A total of 5 measurement sets (inlet and outlet) were taken per device over a period of an hour and 45 minutes. As such, the membranes were exposed to flowing blood for 3 hours and 45 minutes total during the experiment.

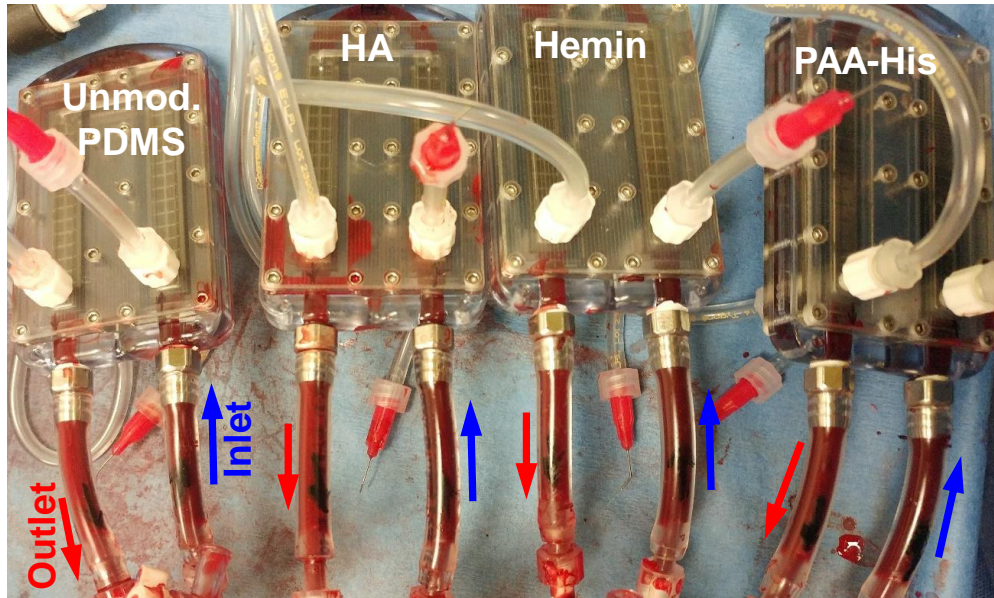


Fig. A. 1.11: Experiment 2 – Oxygenation of blood through assembled parallel plate devices *in vivo*.

Inlets and outlets of each device are marked. Blood exiting the outlets of some devices was visibly brighter red in color compared to the blood at the inlets.

The ABG measurements (Table A. 1.2) were used to calculate the O₂ and CO₂ flux through each device using Eq. A. 1.2-Eq. A. 1.6, shown in Fig. A. 1.12. Due to the high variance in measurements, no significant difference was found between any of the coating groups for either O₂ or CO₂ flux. In both flux calculations, the unmodified PDMS device showed less O₂ and CO₂ flux than most of the devices with coatings, though this difference was not significant due to the high measurement error. The unmodified PDMS device showed around half the O₂ flux *in vivo*, at 36.2 ± 37.3 mL/min/m², compared to *in vitro* at 77.4 ± 9.37 mL/min/m². Still, considering the measurement error of the *in vivo* data, it is likely these two values are not significantly different. The devices with coatings mostly showed much higher O₂ flux *in vivo* than *in vitro*, though these values are also unlikely to be significantly different.

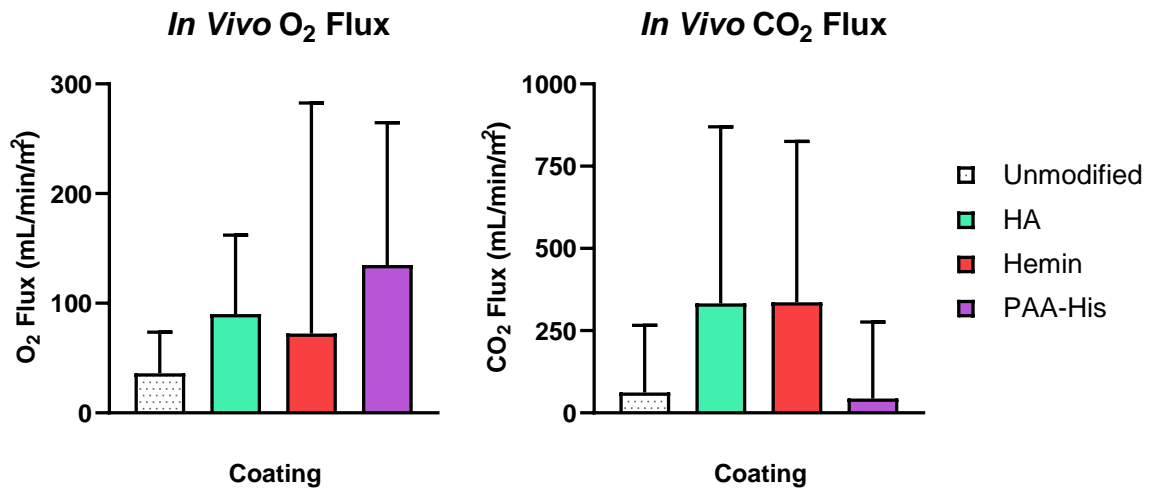


Fig. A. 1.12: Experiment 2 – Area-normalized O₂ and CO₂ flux *in vivo* of each parallel plate device, with a blood flow rate of 20 mL/min.

Table A. 1.2: Raw ABG data collected from the four devices during Experiment 2. Data is divided into pre- and post-device for the same time point.

Units	Flow Rate mL/min	Pre-Device					Post-Device				
		pH	pCO ₂ mmHg	pO ₂ mmHg	HCO ₃ ⁻ mmol/L	SO ₂	pH	pCO ₂ mmHg	pO ₂ mmHg	HCO ₃ ⁻ mmol/L	SO ₂
Unmod. PDMS	20	7.21	77	48	30.8	0.74	7.22	76	48	31.1	0.74
	20	7.22	74	54	30.3	0.8	7.22	74	54	30.3	0.8
	20	7.23	73	59	30.6	0.85	7.23	73	61	30.6	0.86
	20	7.24	69	59	29.6	0.84	7.24	69	60	29.6	0.86
	20	7.27	66	53	30.3	0.82	7.27	64	54	29.4	0.83
HA	20	7.2	77	53	30.1	0.78	7.22	75	53	30.7	0.79
	20	7.22	75	53	30.1	0.79	7.22	71	56	29.1	0.82
	20	7.22	74	56	30.3	0.82	7.23	73	58	30.6	0.84
	20	7.25	68	58	29.8	0.85	7.25	67	58	29.4	0.85
	20	7.27	65	48	29.8	0.77	7.24	64	52	29.4	0.81
Hemin	20	7.192	71.5	49	27.5	0.73	7.196	70.6	48	27.3	0.72
	20	7.191	72.4	49	27.7	0.73	7.148	71.8	54	27.9	0.78
	20	7.198	72.4	53	28.2	0.78	7.201	70.6	52	27.7	0.76
	20	7.219	67.6	55	27.6	0.8	7.239	63.8	51	27.2	0.78
	20	7.249	63.9	44	28	0.71	7.224	67.4	53	27	0.79
PAA- His	20	7.186	75.3	42	28.5	0.63	7.191	72.8	47	27.8	0.7
	20	7.194	71	50	27.4	0.75	7.191	71.1	50	27.2	0.74
	20	7.205	69.8	52	27.6	0.77	7.203	71.8	54	28.3	0.79
	20	7.217	67	52	27.3	0.77	7.223	66.3	55	27.3	0.8
	20	7.223	69	40	28.4	0.63	7.238	66	42	28	0.67

A.1.3.2.3 Scanning Electron Microscopy (SEM)

Experiment 1

Scanning electron micrographs of each coating after blood exposure from Experiment 1 are in Fig. A. 1.13. The scans were taken at 200X magnification to view the overall distribution of adherent cells or platelets, while still being able to visualize small-scale adherence or activation. As seen in Fig. A. 1.13a-c, the coated surfaces did show some diffuse cell and platelet adhesion across the surfaces, with some activated and spread platelets and fibrin clot formation. Debris from the underlying silicon structure was also present on the surface. Relative to the other coatings, the HA surface (Fig. A. 1.13a) showed the least amount of adhered material, while the PAA-His surface (Fig. A. 1.13b) and PAA-Lys surface (Fig. A.

1.13c) showed similar adhesion. Compared to the coated membranes, the Si material control (Fig. A. 1.13d) showed considerable platelet adhesion and activation, and the formation of larger fibrin networks. The unmodified PDMS surface in Fig. A. 1.13e showed considerable platelet and cell deposition across the entire surface. In general, the coated surfaces outperformed the material controls in terms of resisting cell and platelet adhesion, with the HA coating yielding the most resistance to adhesion.

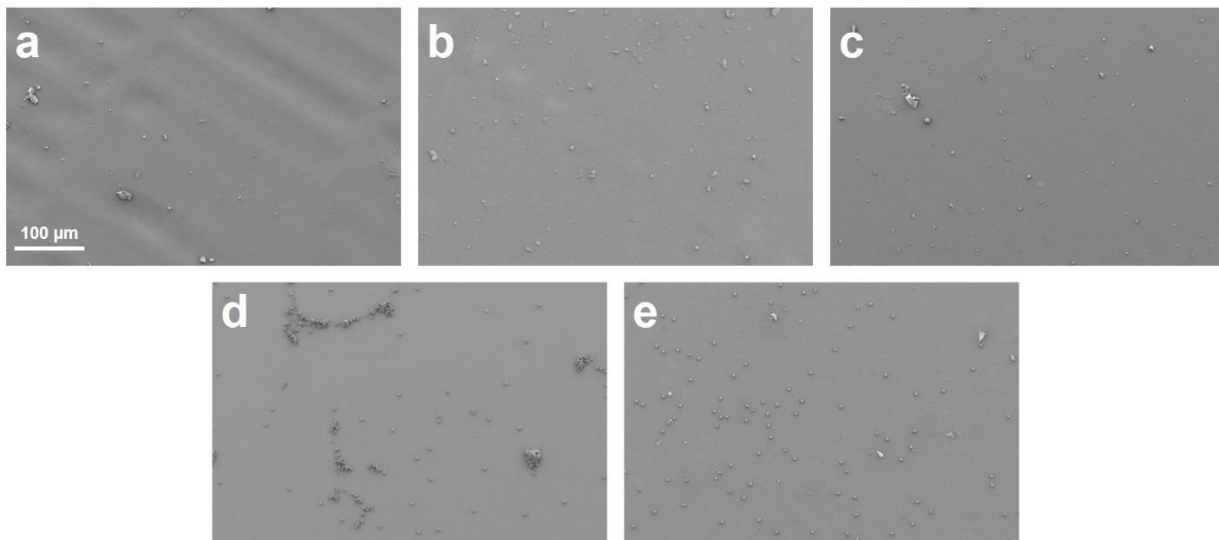


Fig. A. 1.13: Experiment 1 – 200X magnification SEM images of gross cell/platelet on membranes removed from the *in vivo* devices after 2 hours of blood contact. Coatings are: (a) HA, (b) PAA-His, (c) PAA-Lys, (d) unmodified Si, and (e) unmodified PDMS.

Experiment 2

Scanning electron micrographs of each coating after blood exposure are in Fig. A. 1.14. The scans were taken at 200X magnification. As seen in Fig. A. 1.14a, the unmodified PDMS surface had some adherence of biological material distributed across the surface, possibly with some activated and spread platelets. Debris from the underlying silicon structure was also present on the surface. The HA surface (Fig. A. 1.14b) showed much less adherence of biological material, and the PAA-His surface (Fig. A. 1.14d) showed similar adhesion to the unmodified PDMS. Comparatively, the Hemin surface (Fig. A. 1.14c) showed substantially more adhesion of cells and platelets, with many nascent thrombi visible

across the surface. Given their size and rounded shape, the largest adherent objects are likely leukocytes, some with projections attached to the surface. Closer inspection of the lower right corner of the image reveals a fibrous clot likely containing activated platelets. Overall, the HA surface had the least adhesion of cells and platelets out of all coatings.

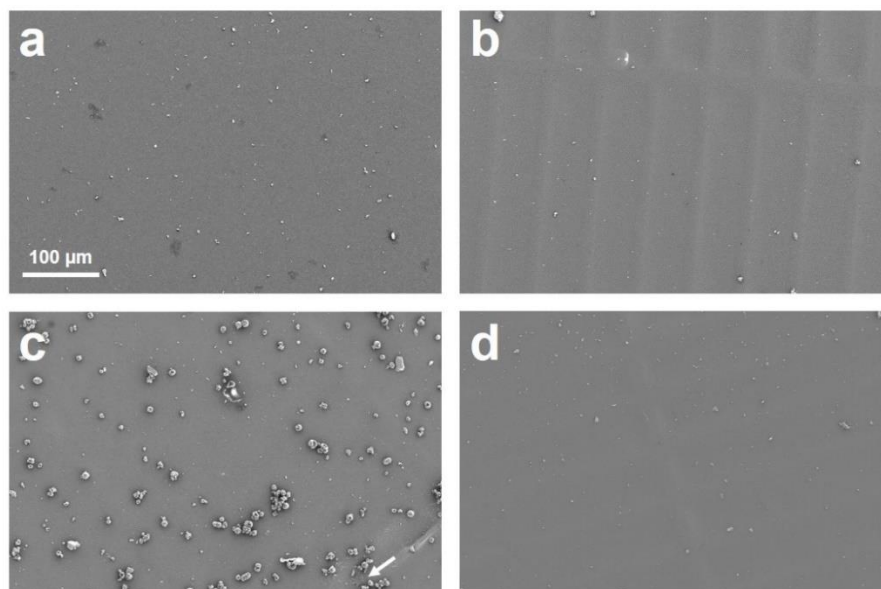


Fig. A. 1.14: Experiment 2 – 200X magnification SEM images of gross cell/platelet on membranes removed from the *in vivo* devices after nearly 4 hours of blood contact. Coatings are: (a) unmodified PDMS, (b) HA, (c) Hemin, and (d) PAA-His. The arrow in (c) indicates the formation of a fibrous clot.

A.1.3.2.4 Platelet Immunohistochemistry (IHC)

From Experiment 2, fluorescent images of platelet adhesion each coating after blood exposure are in Fig. A. 1.15, taken at 40X magnification to visualize a wide view of platelet distribution on the surfaces. On the unmodified PDMS surface (Fig. A. 1.15a), platelets can be seen distributed across the surface at a consistent, low density. Some platelets appear stained with only FITC, indicating adhesion but no activation, while some are also cross-stained with Cy-3, pointing to activation. Of the coatings, HA (Fig. A. 1.15b) shows the least platelet adhesion/activation, with only a few platelets present on the surface. The Hemin coated surface (Fig. A. 1.15c) shows a substantial increase in platelet adhesion and

activation compared to the unmodified PDMS surface, and the PAA-His surface (Fig. A. 1.15d) shows a modest increase. In particular, the Hemin surface is covered by a high density of cross-stained platelets, some of which have started to form larger aggregates. IHC imaging was not conducted on samples from Experiment 1.

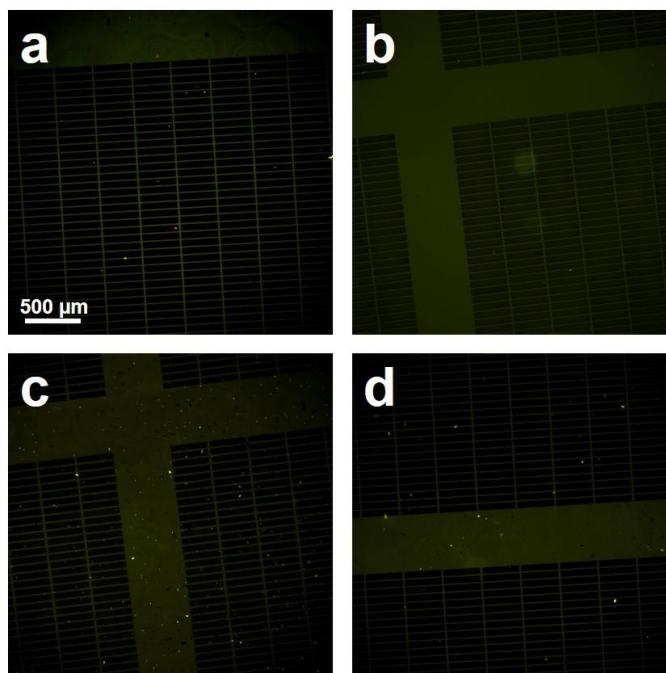


Fig. A. 1.15: Experiment 2 – 40X magnification IHC cross-stain of platelet adhesion (CD41, FITC green) and platelet activation (CD62p, Cy-3 red) on membranes removed from the *in vivo* devices after nearly 4 hours of blood contact. Coatings are: (a) unmodified PDMS, (b) HA, (c) Hemin, and (d) PAA-His.

A.1.4 DISCUSSION

Considering the data sets from all experiments, the biomolecule coatings strongly altered the hemocompatibility of the Si-PDMS membrane surfaces. Whether the benefit was positive or negative, the coatings generally showed consistent trends between *in vitro* wettability and *in vivo* hemocompatibility, and mostly differed from the unmodified PDMS surfaces. Between the two experiments, it is unclear if the coatings have a detrimental impact on the inherent gas permeability of the Si-PDMS membranes. Additional experiments would be necessary to increase sample numbers, and collect more conclusive

evidence. Although the coatings in Experiment 2 consistently decreased the *in vitro* O₂ flux through the membranes, it is unclear if this trend was also observed *in vivo* due to the high measurement error. As such, the biomolecule coatings demonstrated a clear hemocompatibility benefit compared to unmodified PDMS, but were unable to show any blood-gas exchange improvements on gas exchange membranes.

The presence of the biomolecule coatings on the surface was confirmed by contact angle changes. Characterization of the coatings was largely consistent with prior research on these coatings. To validate the presence of the coatings on the surface, two additional characterization techniques were employed in this study: colorimetric staining for amine and carboxyl groups and x-ray photoelectron spectroscopy. However, these datasets were not sufficiently complete to include in this analysis. As such, coating characterization in this study is currently limited to contact angle analysis. Still, other characterization techniques may have been useful to further define the functionality of the coatings. Data on thickness and conformity via ellipsometry could have identified possible links between coating thickness and thrombogenicity. Atomic force microscopy could have been used to image the topography of the coated surfaces, since surface roughness is also linked to thrombogenicity. Additionally, a technique to quantify the surface charge of the biomolecule coatings could have verified the charge state of the coatings under physiologic conditions.

Comparison of the characterization and hemocompatibility data revealed some trends consistent with all data sets. Namely, the HA coating was the most hydrophilic, and also the most resistant to cell and platelet adhesion. This finding was consistent between Experiments 1 and 2. Conversely, the most hydrophobic coatings – PAA-Lys and Hemin – were more thrombogenic than HA, but to different extents. PAA-His was intermediate in both regards. These comparisons indicated a strong connection between hydrophilicity and hemocompatibility with the coatings. However, if hydrophobicity alone determined hemocompatibility, the unmodified PDMS and PAA-Lys surfaces should have been as thrombogenic as Hemin. In Experiment 1, the PAA-Lys surface was less thrombogenic than the

unmodified PDMS material control despite being equally hydrophobic. Also, in Experiment 2, the unmodified PDMS surface attracted relatively few cells and platelets, comparable to the PAA-His surface and far less than Hemin. As such, factors beyond wettability likely contributed towards hemocompatibility, although hydrophilicity was a clear factor in preventing thrombosis.

Between all data sets, the influence of the coatings on gas permeability was unclear. The two *in vitro* data sets indicated opposite conclusions. Whereas Experiment 1 showed no significant difference with coating application, Experiment 2 showed a clear reduction in permeability with the application of any coating to the surface. Normalizing the flux measured through unmodified $S\mu\text{M}$ -PDMS membranes from Chapter 2 (Fig. 2.7) to surface area, the O_2 flux measured in prior studies at 10 mL/min flow rate was 306 ± 35.2 mL/min/m². Both datasets from Experiment 1 and 2 (Fig. A. 1.6 and Fig. A. 1.7) showed far less flux on the unmodified membranes than this study at the same flow rate, although the membranes used in these studies had different pore designs that may have influenced the normalization. Still, the flux measured in Experiment 2 was much closer to this previous measurement than Experiment 1, reaching close to the same flux at a higher water flow rate. Given the increased number of data points in Experiment 2, as well as the use of higher flow rates, the *in vitro* dataset in Experiment 2 is likely more reflective of the coatings' effect on the inherent gas permeability of the membranes. As such, the coatings appear to strongly decrease gas permeability of $S\mu\text{M}$ -PDMS membranes.

The reduction seen with DETA application alone may be the most significant contributor to the overall lower permeability of the coatings, since most of the coatings did not decrease flux further than DETA alone. One possibility for this observation may be related to the effects of the plasma treatment required to apply the DETA coating. Plasma treatment of PDMS causes the formation of a stiff, glassy SiO_2 layer on the PDMS surfaces, which has been shown to strongly reduce the gas permeability of PDMS^{115,117}. Usually, this SiO_2 layer dissipates over time due to surface rearrangement of the PDMS within around a week. However, these studies were conducted on bulk PDMS that was hundreds of

microns thick, unlike the ultrathin spin-coated layer on the $5\mu\text{M}$ -PDMS. It is possible that an SiO_2 layer on $5\mu\text{M}$ -PDMS membranes may not experience much surface rearrangement over time due to its thinness, and lack of sufficient PDMS required for rearrangement. Therefore, it is possible that the gas permeability reduction associated with plasma treatment may linger on $5\mu\text{M}$ -PDMS membranes for an indefinite amount of time. Plasma-treated PDMS without DETA application was not independently evaluated in this experiment, so further studies would need to confirm this observation.

The *in vivo* datasets from Experiments 1 and 2 were also unclear as to the impact of the coatings on gas exchange. Neither experiment was able to demonstrate oxygenation, unlike in Chapter 3. Lack of demonstrable oxygenation in both experiments is likely due to the instability of the ventilation regimen of the pigs. Unstable control over the incoming venous blood, and a limited collection of data points per device, resulted in high variance in O_2 flux measurements. Similarly, CO_2 flux measurements were affected by this instability in ventilation, particularly in Experiment 2 with the wide variation in blood pH (7.3-7.7 over the course of the experiment). Still, the extremely high CO_2 removal seen in Experiment 1 was striking, especially compared to past results from Chapter 5 under similar hypercarbic conditions. This CO_2 removal vastly exceeds data from Arazawa, et al. ($411\text{ mL}/\text{min}/\text{m}^2$), although – given the lack of a control uncoated device in this experiment – it is unclear if the coatings were the main driver of the high CO_2 removal. When a control device was added in Experiment 2, no significant difference in CO_2 removal was seen between uncoated and coated devices, possibly attributable to the inconsistency in the pig's ventilation. Considering all of the *in vivo* datasets, the impact of the coatings on *in vivo* gas exchange cannot be determined without additional experiments.

Future *in vivo* experiments would need to significantly modify the animal handling procedures in order to maintain consistent O_2 and CO_2 control over the incoming venous blood from the pig. In Experiments 1 and 2, the pig was ventilated with only O_2 because equipment to mix multiple gases for the ventilator, such as room air or N_2 , was not available. This led to the significant hyperoxia of the incoming

venous blood ($SO_2 \sim 100\%$), and the subsequent hand bag ventilation regimen to create a slightly hypoxic state. Titration of the inhaled ventilator gas with room air or N_2 would prevent this venous hyperoxia, and allow for controllable hypoxia within the venous blood. If such a ventilation regimen is used, better quality *in vivo* data could be collected to demonstrate O_2 and CO_2 transport.

A.1.5 CONCLUSION

Ultimately, the biomolecule coatings on $S\mu M$ -PDMS membranes did significantly improve the hemocompatibility of the surfaces, but were unable to demonstrate consistent impacts on gas exchange through the membranes. Of the coatings, the HA coating proved to be the most hydrophilic and hemocompatible when exposed to flowing blood. Oxygen flux *in vitro* may have been significantly lessened by the application of the coatings, possibly due to the plasma treatment required for surface modification. However, *in vivo* no difference was observed in oxygenation with or without coatings. Strikingly high CO_2 removal was seen in one of the experiments, signaling significant promise for the coatings in a CO_2 removal device. However, this result was not validated by the second experiment. Both of the experiments were impacted by the instability of the *in vivo* setup, and so neither experiment can conclusively demonstrate the impact of the coatings on *in vivo* gas exchange. Nonetheless, this work raises significant interest in the use of these coatings for improving PDMS-based oxygenator hemocompatibility, and possibly the gas exchange efficiency through the membranes. Future work will focus on increasing sample numbers to improve overall data quality for characterization and membrane performance, and also altering the *in vivo* experiment procedure to improve the quality of *in vivo* datasets.

A.2. *IN VIVO* GAS EXCHANGE THROUGH OXYGENATOR PROTOTYPES

A.2.1 INTRODUCTION

After completion of the *in vivo* experiment described in Chapter 5, further experiments with the prototype oxygenator were desired to better characterize transport through this particular device. As such, the purpose of this experiment was to collect additional *in vivo* data on the performance of the prototype oxygenator flow cell with greater sample numbers. In adding more replicates to the dataset, O₂ and CO₂ transport through the prototype could be further characterized.

A.2.2 METHODS

A.2.2.1 Oxygen Flux and Pressure Drop *In Vitro*

Four silicon micropores membranes (S μ M) were created for each device, and plasma bonded to a polydimethylsiloxane (PDMS) layer as described in Chapter 2^{143,160}. Three of the parallel plate oxygenator devices described in Chapter 5 (Fig. 5.2) were assembled using four S μ M-PDMS membranes each. No spacers were used in any of these devices, nor were the membranes coated with any surface modification. Essentially, all three devices were constructed in the same manner as the no spacers control device in Chapter 5.

Each device was placed in an *in vitro* oxygen flux testing circuit as described in 5.2.4, and shown in Fig. 5.3. The devices were subjected to flowing degassed water at 10, 20, and 40 mL/min and supplied with a pure oxygen sweep gas at 260 mmHg gauge pressure. Transoxygenator pressure was measured at each flow rate using the pressure gauge in the water circuit upstream of the device. Area-normalized

oxygen flux (J , mL O₂/min/m²) was determined using a downstream oxygen probe to measure concentration before and after supplying the sweep gas ($[O_2]_i$ and $[O_2]_f$, respectively), with a conversion of 22.4 L O₂/mol at STP:

$$J = \frac{([O_2]_f - [O_2]_i) \cdot 10^{-6} \frac{\text{mol}}{\mu\text{mol}} \cdot 22.4 \frac{\text{L}}{\text{mol}} \cdot Q}{A_m}$$

Eq. A. 2.1

where Q is the flow rate of water in mL/min, and A_m is the area of the membrane in m². The measurements of transoxygenator pressure and flux at each flow rate were compared to results from Chapter 5 (Fig. 5.5a and b, respectively) to determine repeatability.

A.2.2.2 Gas Exchange and Hemocompatibility *In Vivo*

All three devices were tested for gas exchange (O₂ and CO₂) and blood compatibility extracorporeally in a 40kg Yucatan minipig using the same circuit setup as in Chapter 5 (Fig. 5.4). The three devices were set up in parallel with each other. The pig used in this study was thought to have a naturally occurring respiratory deficiency, and so mechanical ventilation with inhaled pure O₂ was sufficient to achieve venous blood O₂ saturation of ~80%. Fully heparinized blood (ACT > 300 s) was flowed through the devices at a flow rate of 40 mL/min for 30 minutes, and flowing oxygen sweep gas was supplied to the devices at a pressure of 88 mmHg and a rate of 2 L/min (Fig. A. 2.1). Three blood samples from the inlet and outlet of each device were taken for blood gas analysis to assess pO₂, pCO₂, pH, and HCO₃⁻ using either an arterial blood gas machine (GEM3000, Instrumentation Laboratory, Bedford, MA, USA) or an iSTAT handheld blood analyzer (Abbott Point of Care Inc., Princeton, NJ, USA). After 30 minutes of blood flow at 40 mL/min, the blood flow rate was decreased to 20 mL/min for 30 minutes to mimic the flow rate used in Chapter 5. Three sets of inlet/outlet samples were taken from each device at this flow rate for blood gas analysis. After a total of two hours of blood exposure, the

devices were flushed with saline and disassembled. The devices were grossly inspected for clots, and the membranes were removed and broken into pieces. The experiment was conducted at a contract resource organization (PMI Preclinical, San Carlos, CA).

O₂ and CO₂ flux were calculated using equations Eq. 5.3 and Eq. 5.6, respectively.

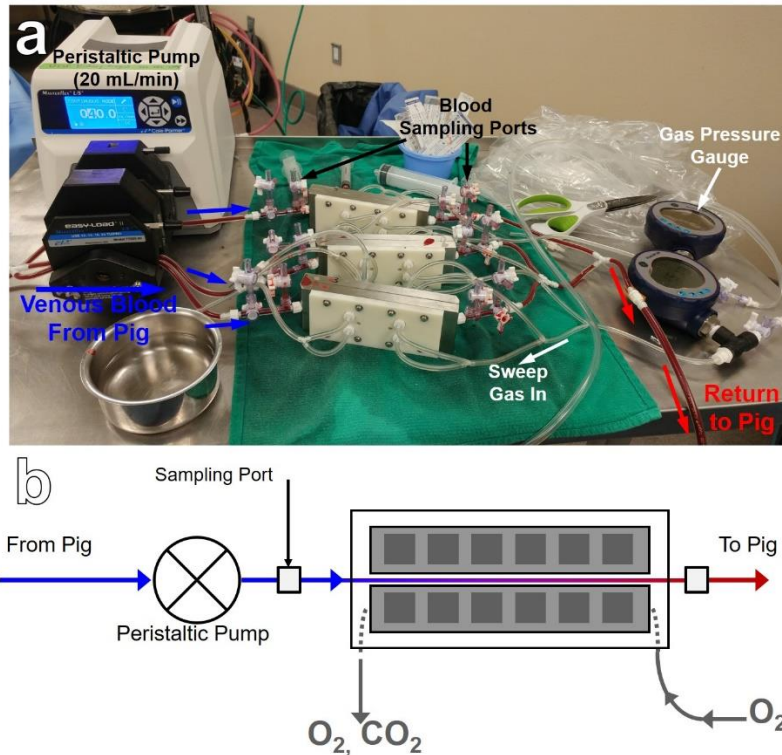


Fig. A. 2.1: Setup of *in vivo* testing circuit for replicates of the no spacers control device in Chapter 5. (a) shows a photograph of the setup, while (b) shows a simplified schematic.

A.2.2.3 Scanning Electron Microscopy (SEM)

After the porcine blood flow experiment, one fragment sample from each membrane was imaged for cell, platelet, and protein adhesion using scanning electron microscopy (SEM) as described in Chapter 5 and Appendix A.1. Samples were placed in a solution of 3% glutaraldehyde (Millipore Sigma), 0.1 M sodium cacodylate (VWR), and 0.1 M sucrose (Millipore Sigma) at 4°C for 48 h. Then, the samples were washed twice with deionized water, and dehydrated by sequential 10 minute incubations with 35%, 50%,

70%, 90%, and two 100% ethanol/water (v/v%) solutions. The samples were dried in a desiccator overnight and mounted with conductive silver paint to aluminum SEM stubs. Finally, the samples were sputter coated with 4 nm of gold and imaged using a Carl Zeiss Ultra 55 Field Emission Scanning Electron Microscope (Zeiss, Dublin, CA, USA).

A.2.2.4 Statistical Analysis

Statistical significance was determined using Graphpad Prism 8.2.0 (San Diego, CA, USA). For each of the three devices *in vitro*, two measurements were taken of transmembrane pressure and O₂ flux at each of the four flow rates tested. These measurements were averaged between all three devices at the same flow rate. Both the pressure and flux measurements from this experiment were compared to those from the no spacers control device in Chapter 5. The transmembrane pressure measurements were compared using two way ANOVA analysis with Tukey post-hoc tests for each experiment (Chapter 5 and Appendix A.2) and each flow rate (10, 20, and 40 mL/min). The area-normalized flux measurements were also compared using this method.

Flux measurements of O₂ and CO₂ *in vivo* at 20 mL/min were averaged for all three devices from this experiment. These measurements were compared to those from the no spacers control device in Chapter 5 using standard t-tests.

A.2.3 RESULTS

A.2.3.1 Oxygen Flux and Pressure Drop *In Vitro*

Measurements of transmembrane pressure drop and *in vitro* area-normalized oxygen flux are in Fig. A. 2.2, compared to the results from Chapter 5 (Fig. 5.5). Among the measurements of pressure, both experiments showed that there was significantly higher pressure in the circuit at 40 mL/min compared to 10 mL/min and 20 mL/min, which were not different. Also, there was no significant difference between the two experiments at 10 mL/min, but the original spacers study showed significantly higher pressure at 20 and 40 mL/min compared to the replicate study. It is possible that some variation in the *in vitro* testing

setup was behind this slight increase in pressure through the circuit in the original experiment. As such, the pressure data only shows some replicability between the experiments at the lower flow rates.

Between both experiments, area-normalized flux was not significantly different at any of the three flow rates tested, indicating strong replicability. In both experiments, the flux at 40 mL/min was significantly greater than at 10 mL/min, but only the original experiment showed a significant difference between flux at 40 and 20 mL/min. Still, the flux data shows significant replicability between trials.

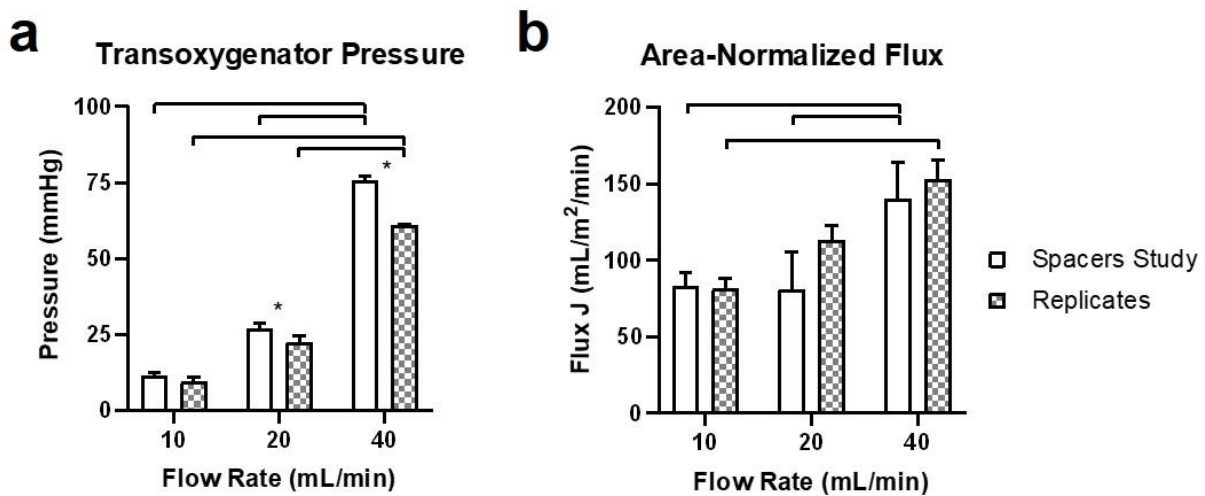


Fig. A. 2.2: *In vitro* testing comparison of replicate devices to the original data from Chapter 5 (Fig. 5.5). (a) shows transoxygenator pressure while (b) shows the area-normalized oxygen flux. Bars above the chart indicate significant difference between groups in the same experiment (spacers study or replicates) at different flow rates. The * symbol indicates significant difference between experiments at the same flow rate. Significant difference was determined using two-way ANOVA with Tukey post-hoc tests.

A.2.3.2 Gas Exchange and Hemocompatibility *In Vivo*

In vivo measurements of area-normalized O₂ and CO₂ flux can be found in Fig. A. 2.3, compared to results from Chapter 5 (Fig. 5.6). Raw ABG data used to calculate flux for all three devices can be found in Table A. 2.1. O₂ flux at blood flow rates of 20 and 40 mL/min was 63.7 ± 53.7 mL/min/m² and 111 ± 56.9 mL/min/m², respectively. CO₂ flux was 297 ± 366 mL/min/m² and 515 ± 668 mL/min/m², respectively. In this experiment, there was no significant difference between O₂ or CO₂ flux at 20 and 40

mL/min. This was likely related to the high variance within the blood gas samples. The data from the replicate experiment shows that O₂ flux was higher than in the original spacers study, though this difference at 20 mL/min was not significant. Likely, this lack of significant difference was due to the low sample size of the original study, and high variance within the datasets. Interestingly, CO₂ flux in the replicate experiment was significantly lower than in the original study, and also much more variable.

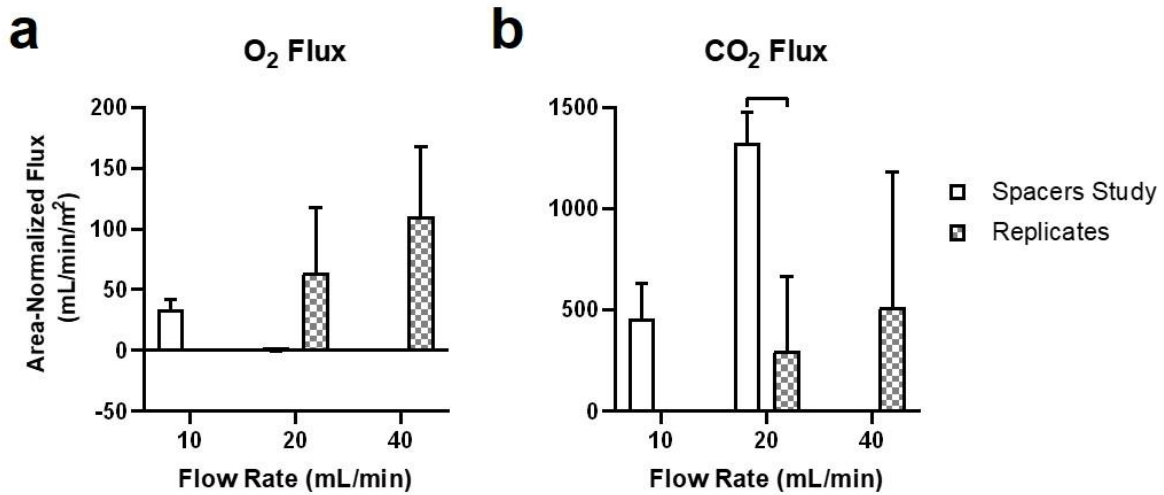


Fig. A. 2.3: *In vivo* O₂ and CO₂ area-normalized flux comparison of replicate devices to the original data from Chapter 5 (Fig. 5.5). (a) shows O₂ flux while (b) shows CO₂ flux. Bars above the chart indicate significant difference between groups at the same 20 mL/min flow rate as assessed by t-test.

Table A. 2.1: Raw ABG data collected from all three replicate devices during *in vivo* experiment. Data is divided into pre- and post-device for the same time point.

Units	Flow Rate mL/min	Pre-Device					Post-Device				
		pH	pCO ₂ mmHg	pO ₂ mmHg	HCO ₃ ⁻ mmol/L	SO ₂	pH	pCO ₂ mmHg	pO ₂ mmHg	HCO ₃ ⁻ mmol/L	SO ₂
Device 1	40	7.33	61	51	32.2	0.83	7.33	59	53	31.1	0.84
	40	7.327	52	52	27.3	0.84	7.326	51.6	53	27	0.84
	40	7.362	49.4	58	28	0.88	7.364	47.2	60	26.9	0.9
	20	7.359	49.1	59	27.7	0.89	7.363	49.2	64	28	0.91
	20	7.36	49.3	55	27.8	0.87	7.355	47.1	58	26.3	0.88
	20	7.39	50	61	30.3	0.91	7.4	48	65	29.7	0.92
Device 2	40	7.34	56	52	30.2	0.84	7.35	55	54	30.4	0.86
	40	7.38	52	62	30.8	0.91	7.39	50	66	30.3	0.93
	40	7.39	51	59	30.9	0.9	7.39	49	64	29.7	0.92
	20	7.39	51	63	30.9	0.92	7.38	51	67	30.2	0.93
	20	7.361	48.1	56	27.2	0.87	7.357	46	69	25.8	0.93
	20	7.367	47.8	58	27.4	0.89	7.369	45.9	62	26.5	0.9
Device 3	40	7.309	53.9	49	27.1	0.8	7.312	54.9	51	27.8	0.81
	40	7.36	54	55	30.5	0.87	7.37	53	60	30.6	0.9
	40	7.39	51	58	30.9	0.89	7.39	49	62	29.7	0.91
	20	7.38	52	62	30.8	0.91	7.4	50	67	31	0.93
	20	7.38	51	58	30.2	0.89	7.38	49	62	29	0.91
	20	7.38	49	63	29	0.91	7.38	50	65	29.6	0.92

The disassembled devices after 2 hours of exposure to fully-heparinized blood can be seen in Fig. A. 2.4. Within each device, there was one gross clot visible at the same location within all three of the flow paths. This location was within the stainless steel header region leading into the silicon membranes, just prior to the parallel split over the two membranes. These clots were only observed at the inlet, and were largely “white” (fibrinous) in composition rather than “red” (hemolytic). Other than these inlet clots, no other gross thrombi were observed in the channels, including over the membranes themselves.

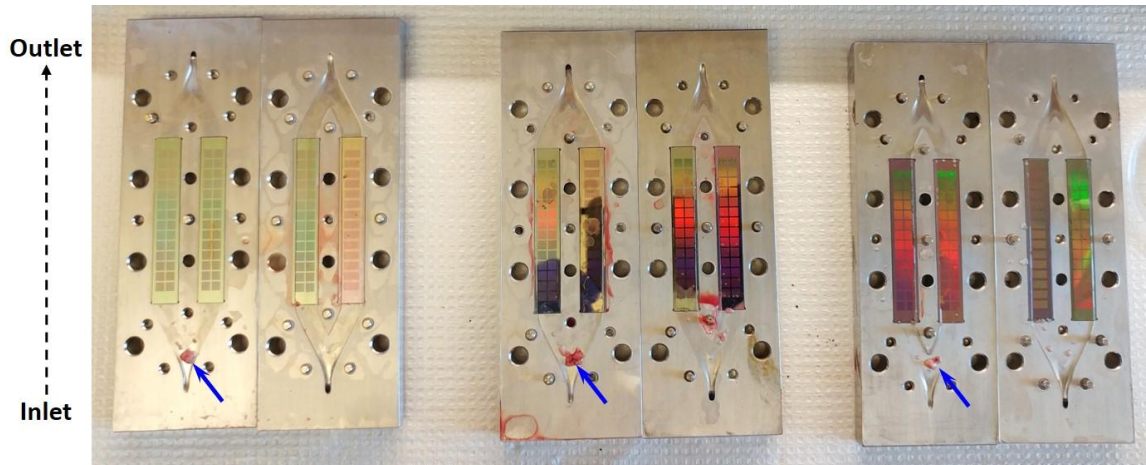


Fig. A. 2.4: Disassembly of oxygenator devices after 2 hours of exposure to heparinized blood. Each device is oriented with the blood flow inlet at the bottom of the image. Blue arrows indicate clot formation.

A.2.3.3 Scanning Electron Microscopy (SEM)

Scanning electron microscopy images at 200X and 1000X can be found in Fig. A. 2.5. From the micrographs, the surfaces are largely free of significant platelet and cell adhesion. Still, some adhesion of cells and thrombi can be seen on the surfaces. In some of the closer magnification images, some fibrous protein adhesion was observed, possibly indicating the potential for thrombus formation.

Compared to the SEM images in Chapter 5, the surfaces in the replicate study showed slightly less adhesion than the control sample in the original experiment. Little adhesion of cells and proteins was seen overall in both experiments, though. Given that the replicate devices were exposed to only 2 hours of blood flow instead of 3, there may have been less adhesion on these samples due to the reduced contact time with blood. All samples in the original and replicate experiments were the same unmodified PDMS.

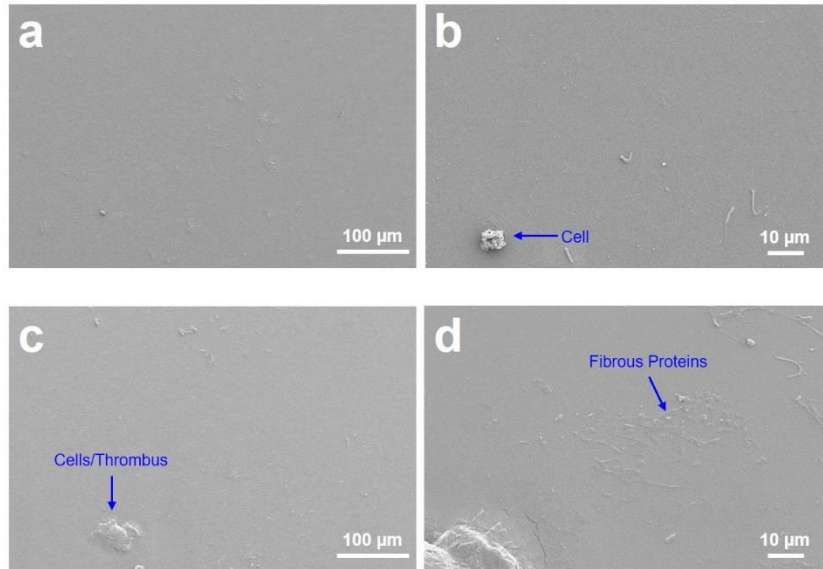


Fig. A. 2.5: SEM micrographs of replicate devices at 200X and 1000X magnification. (a) and (b) show the same sample at both magnifications, as do (c) and (d). Blue arrows indicate notable adhesion of cells or proteins.

A.2.4 DISCUSSION

This study was an attempt to replicate data from the control device in Chapter 5, with moderate success. Overall, the *in vitro* data was reasonably replicable between experiments, especially the area-normalized oxygen flux. Both experiments saw pressure drop and oxygen flux significantly increase with higher water flow rates. Although transoxygenator pressure differed between experiments at 20 and 40 mL/min, increased sample numbers could potentially reduce this difference.

However, the *in vivo* data was not consistent between experiments. O₂ flux may not have shown a significant difference between experiments, but flux in the replicate experiment was generally higher than in the original study. The reason for this difference is likely the higher sweep gas pressure used in the replicate experiment compared to the original (88 mmHg vs minimal pressure, respectively). Oxygen flux into the blood is driven by pressure gradients between the sweep gas and the venous blood. Most likely, little oxygenation was seen in the original experiment since no sweep gas pressure was applied beyond atmospheric pressure. In contrast, the replicate experiment increased the O₂ driving pressure into blood by

elevating the sweep gas pressure. Comparatively, CO₂ removal in the original experiment was significantly higher than the replicate study. Since CO₂ removal is driven by sweep gas flow rate, the higher O₂ sweep flow rate used in the original study for the control device (3 L/min) is likely responsible for the increased CO₂ removal. The replicate study used only 2 L/min of O₂ sweep gas flow, which was further split amongst three devices to yield ~0.67 L/min of sweep gas flow per device. This difference in CO₂ flow rate between experiments was likely the reason for the discrepancy in flux.

In all *in vivo* experiments described, especially in Chapter 5 and Appendix A.1, considerable variance in the measured O₂ and CO₂ flux limited the significance of the datasets. Much of the variance is attributable to the instability of the ventilation regimen of the pig and resulting effects on venous O₂ blood saturation. Ultimately, the testing protocol used for future *in vivo* oxygenator experiments must establish a stable ventilation regimen to ensure consistent, slight hypoxia of the venous blood. However, the ventilation of the pig was not an issue in this experiment due to the compromised respiratory physiology of the pig. Essentially, beyond the instability of the pig, other factors may be contributing to the high variance in gas flux. Given the small membrane area in these prototypes, the surface area of these devices may be low to allow for a significant, repeatable signal to be observable by the ABG data. For example, the observable differences in pO₂ pre- and post-device are often less than 10% of the total pO₂ readings. This means that any variability within sample sets of the same device (i.e. differences in pO₂ of 2 vs. 4 mmHg) become amplified in the flux calculations to yield an overall high variance in gas flux. Future scaled up devices with higher area would yield a larger difference in O₂ and CO₂ flux, and would likely produce more consistent ABG data.

In summary, all three devices in this study showed replicability to the control device of Chapter 5 *in vitro*, but did not replicate *in vivo* gas flux results for O₂ or CO₂ due to the differences in testing protocol and high variance. Future work should emphasize the establishment of a stable *in vivo* testing protocol, and the use of larger silicon membrane oxygenators to improve measurement quality.

REFERENCES

1. Lequier, L., Horton, S., McMullan, D. & Bartlett, R. H. Extracorporeal membrane oxygenation circuitry. *Pediatr. Crit. care ...* **14**, 1–10 (2013).
2. Frenckner, B. & Radell, P. Respiratory failure and extracorporeal membrane oxygenation. *Semin. Pediatr. Surg.* **17**, 34–41 (2008).
3. Thiagarajan, R. R. *et al.* Extracorporeal Life Support Organization Registry International Report 2016. *ASAIO J.* **63**, 60–67 (2017).
4. Extracorporeal Life Support Organization. ECLS Registry Report. (2019).
5. Rais Bahrami, K. & Van Meurs, K. P. ECMO for neonatal respiratory failure. *Seminars in Perinatology* **29**, 15–23 (2005).
6. Bartlett, R. H. ECMO: The next ten years. *Egypt. J. Crit. Care Med.* **4**, 7–10 (2016).
7. Peek, G. J. *et al.* CESAR: conventional ventilatory support vs extracorporeal membrane oxygenation for severe adult respiratory failure. *BMC Health Serv. Res.* **13**, 163 (2006).
8. Peek, G. J. *et al.* Efficacy and economic assessment of conventional ventilatory support versus extracorporeal membrane oxygenation for severe adult respiratory failure (CESAR): a multicentre randomised controlled trial. *Lancet* **374**, 1351–1363 (2009).
9. Marasco, S. F., Lukas, G., McDonald, M., McMillan, J. & Ihle, B. Review of ECMO (Extra Corporeal Membrane Oxygenation) Support in Critically Ill Adult Patients. *Hear. Lung Circ.* **17**, (2008).
10. Esper, S. A., Levy, J. H., Waters, J. H. & Welsby, I. J. Extracorporeal membrane oxygenation in the adult: A review of anticoagulation monitoring and transfusion. *Anesth. Analg.* **118**, 731–743 (2014).
11. Brogan, T. V, Thiagarajan, R. R., Rycus, P. T., Bartlett, R. H. & Bratton, S. L. Extracorporeal membrane oxygenation in adults with severe respiratory failure : a multi-center database. *Intensive*

- Care Med* **35**, 2105–2114 (2009).
12. Hayes, D. *et al.* Active rehabilitation with venovenous extracorporeal membrane oxygenation as a bridge to lung transplantation in a pediatric patient. *World J. Pediatr.* **9**, 373–374 (2013).
 13. Bain, J. C. *et al.* Economic Outcomes of Extracorporeal Membrane Oxygenation With and Without Ambulation as a Bridge to Lung Transplantation. *Respir. Care* **61**, 1–7 (2016).
 14. Jenkins, C. S. & Van Berkel, V. Taking Your ECMO with You: Continued Progress Toward an Ambulatory Goal. *ASAIO J.* **63**, 521–522 (2017).
 15. Lehle, K. *et al.* Efficiency in extracorporeal membrane oxygenation-cellular deposits on polymethylpentene membranes increase resistance to blood flow and reduce gas exchange capacity. *ASAIO J.* **54**, 612–617 (2008).
 16. De Biasi, A. R., Manning, K. B. & Salemi, A. Science for surgeons: Understanding pump thrombogenesis in continuous-flow left ventricular assist devices. *J. Thorac. Cardiovasc. Surg.* **149**, 667–673 (2015).
 17. Kormos, R. L. Left ventricular assist device pump thrombosis: Understanding mechanisms as a key to causality. *J. Thorac. Cardiovasc. Surg.* **149**, 673–674 (2015).
 18. Beely, B. M. *et al.* Electron microscopy as a tool for assessment of anticoagulation strategies during extracorporeal life support: the proof is on the membrane. *ASAIO J.* 525–532 (2016).
doi:10.1097/MAT.0000000000000394
 19. Williams, B. & Bernstein, W. Review of venoarterial extracorporeal membrane oxygenation and development of intracardiac thrombosis in adult cardiothoracic patients. *J. Extra. Corpor. Technol.* **48**, 162–167 (2016).
 20. Williams, D. C. *et al.* Circuit Oxygenator Contributes to Extracorporeal Membrane Oxygenation-Induced Hemolysis. *ASAIO J.* **61**, 190–195 (2015).
 21. Yasuda, T. *et al.* Influence of Static Pressure and Shear Rate on Hemolysis of Red Blood Cells.

- ASAIO J.* **47**, 351–353 (2001).
22. Zwischenberger, J. B. *et al.* Development of an implantable artificial lung: Challenges and progress. *ASAIO J.* **47**, 316–320 (2001).
 23. Burgreen, G. W., Antaki, J. F., Wu, Z. J. & Holmes, A. J. Computational fluid dynamics as a development tool for rotary blood pumps. *Artif. Organs* **25**, 336–340 (2001).
 24. Hastings, S. M., Ku, D. N., Wagoner, S., Maher, K. O. & Deshpande, S. Sources of Circuit Thrombosis in Pediatric Extracorporeal Membrane Oxygenation. *ASAIO J.* **63**, 86–92 (2017).
 25. Gartner, M. J., Wilhelm, C. R., Gage, K. L., Fabrizio, M. C. & Wagner, W. R. Modeling flow effects on thrombotic deposition in a membrane oxygenator. *Artif. Organs* **24**, 29–36 (2000).
 26. Kawahito, S. *et al.* Hemolytic Characteristics of Oxygenators During Clinical Extracorporeal Membrane Oxygenation. *ASAIO J.* 636–639 (2002). doi:10.1097/01.MAT.0000033860.20288.DD
 27. Stanzel, R. D. & Henderson, M. Clinical evaluation of contemporary oxygenators. *Perfusion* (2015). doi:10.1177/0267659115604709
 28. Greenberg, C. S., Miraglia, C. C., Rickles, F. R. & Shuman, M. A. Cleavage of blood coagulation Factor XIII and fibrinogen by thrombin during in vitro clotting. *J. Clin. Invest.* **75**, 1463–1470 (1985).
 29. Gorbet, M. B. & Sefton, M. V. Biomaterial-associated thrombosis: Roles of coagulation factors, complement, platelets and leukocytes. *Biomater. Silver Jubil. Compend.* **25**, 219–241 (2006).
 30. Sivaraman, B. & Latour, R. A. The relationship between platelet adhesion on surfaces and the structure versus the amount of adsorbed fibrinogen. *Biomaterials* **31**, 832–839 (2010).
 31. Jung, S.-Y. THE VROMAN EFFECT: A MOLECULAR LEVEL DESCRIPTION OF FIBRINOGEN DISPLACEMENT. (2003). doi:10.1017/CBO9781107415324.004
 32. Wertz, C. F. & Santore, M. M. Adsorption and relaxation kinetics of albumin and fibrinogen on hydrophobic surfaces: Single-species and competitive behavior. *Langmuir* **15**, 8884–8894 (1999).

33. Vroman, L., Adams, A. L., Fischer, G. C. & Munoz, P. C. Interaction of High Molecular Weight Kiniogen, Factor XII, and Fibrinogen in Plasma at Interaces. *Blood* **55**, 156–159 (1980).
34. Vilaseca, P., Dawson, K. a. & Franzese, G. Understanding surface-adsorption of proteins: the Vroman effect. 1–9 (2012).
35. Stevens, M. M. & George, J. H. Exploring and Engineering the Cell Surface Interface. *Science (80-.)*. **310**, 1135–1138 (2005).
36. Roach, P., Farrar, D. & Perry, C. C. Surface tailoring for controlled protein adsorption: Effect of topography at the nanometer scale and chemistry. *J. Am. Chem. Soc.* **128**, 3939–3945 (2006).
37. Scopelliti, P. E. *et al.* The effect of surface nanometre-scale morphology on protein adsorption. *PLoS One* **5**, 1–9 (2010).
38. Linneweber, J. *et al.* The effect of surface roughness on activation of the coagulation system and platelet adhesion in rotary blood pumps. *Artif. Organs* **31**, 345–351 (2007).
39. Chen, L., Han, D. & Jiang, L. On improving blood compatibility: From bioinspired to synthetic design and fabrication of biointerfacial topography at micro/nano scales. *Colloids Surfaces B Biointerfaces* **85**, 2–7 (2011).
40. Extracorporeal Life Support Organization (ELSO) General Guidelines for all ECLS Cases. **Version 1.**, (2013).
41. Maquet. QUADROX-i Small Adult and Adult Choose maximum safety . (2015). Available at: <http://www.maquet.com/int/products/quadrox-i-adult-and-small-adult/>. (Accessed: 6th April 2016)
42. Lund, L. W. & Federspiel, W. J. Removing extra CO₂ in COPD patients. *Curr. Respir. Care Rep.* **2**, 131–138 (2013).
43. Collins, J. A., Rudenski, A., Gibson, J., Howard, L. & O’Driscoll, R. Relating oxygen partial pressure, saturation and content: The haemoglobin-oxygen dissociation curve. *Breathe* **11**, 194–201 (2015).

44. Patel, S. & Majmundar, S. H. Physiology, Carbon Dioxide Retention. in *StatPearls [Internet]* (StatPearls Publishing).
45. Arthurs, G. J. & Sudhakar, M. Carbon dioxide transport. *Contin. Educ. Anaesthesia, Crit. Care Pain* **5**, 207–210 (2005).
46. Pittman, R. N. Chapter 4: Oxygen transport. in *Regulation of Tissue Oxygenation* (Morgan & Claypool Life Sciences, 2011). doi:10.4199/C00029ED1V01Y201103ISP017
47. Federspiel, W. & Henchir, K. Lung, Artificial: Basic Principles and Current Applications. in *Encyclopedia of Biomaterials and Biomedical Engineering* 910–920 (2004). doi:10.1081/E-EBBE
48. Huxley, V. H. & Kutchai, H. The effect of the red cell membrane and a diffusion boundary layer on the rate of oxygen uptake by human erythrocytes. *J. Physiol.* **316**, 75–83 (1981).
49. Huxley, V. H. & Kutchai, H. Effect of diffusion boundary layers on the initial uptake of O₂ by red cells. Theory versus experiment. *Microvasc. Res.* **26**, 89–107 (1983).
50. Puttkammer, P. P. Boundary layer over a flat plate. *BSc Report, Univ. Twente* (2013).
51. R. Goerke, A., Leung, J. & R. Wickramasinghe, S. Mass and momentum transfer in blood oxygenators. *Chem. Eng. Sci.* **57**, 2035–2046 (2002).
52. Fernando, U. P. *et al.* A Membrane Lung Design Based on Circular Blood Flow Paths. *ASAIO J.* **63**, 637–643 (2017).
53. Dutton, R. C. *et al.* Development and Evaluation of a New Hollow-Fiber Membrane Oxygenator. *ASAIO J.* **17**, 331–336 (1971).
54. Yeager, T. & Roy, S. Evolution of Gas Permeable Membranes for Extracorporeal Membrane Oxygenation. *Artif. Organs* **41**, (2017).
55. Potkay, J. A. The promise of microfluidic artificial lungs. *Lab Chip* **14**, 4122–4138 (2014).
56. Müller, T. *et al.* A new miniaturized system for extracorporeal membrane oxygenation in adult respiratory failure. *Crit. Care* **13**, R205 (2009).

57. Abramson, M. Experimental lung device kept wounded British soldier alive. *Stars and Stripes* (2009). Available at: <https://www.stripes.com/news/experimental-lung-device-kept-wounded-british-soldier-alive-1.94046>. (Accessed: 12th April 2019)
58. Panigada, M. *et al.* Comparison between clinical indicators of transmembrane oxygenator thrombosis and multidetector computed tomographic analysis. *J. Crit. Care* **30**, 441.e7-441.e13 (2015).
59. Membrana, 3M. 3M Membrana OXYPLUS , TM TM TM Capillary Membrane, Type PMP 90/200 Chemical. (2019). doi:10.1007/978-3-662-44324-8_100061
60. Peinemann, K.-V. & Pereira Nunes, S. Membranes for Artificial Lungs. in *Membranes for Life Sciences* 56–67 (2007).
61. Silvetti, S., Koster, A. & Pappalardo, F. Do We Need Heparin Coating for Extracorporeal Membrane Oxygenation? New Concepts and Controversial Positions About Coating Surfaces of Extracorporeal Circuits. *Artif. Organs* **39**, 176–179 (2015).
62. Kristensen, E. M. E. *et al.* Heparin coating durability on artificial heart valves studied by XPS and antithrombin binding capacity. *Colloids Surfaces B Biointerfaces* **49**, 1–7 (2006).
63. Böning, A. *et al.* Phosphorylcholine or heparin coating for pediatric extracorporeal circulation causes similar biologic effects in neonates and infants. *J. Thorac. Cardiovasc. Surg.* **127**, 1458–1465 (2004).
64. Gorman, R. C. *et al.* Surface-Bound Heparin Fails to Reduce Thrombin Formation During Clinical Cardiopulmonary Bypass. *J Thorac Cardiovasc Surg* **111**, 1–12 (1996).
65. Ukita, R. *et al.* Zwitterionic poly-carboxybetaine coating reduces artificial lung thrombosis in sheep and rabbits. *Acta Biomater.* **92**, 71–81 (2019).
66. Fukui, T., Nishida, H. & Takanashi, S. Biocompatibility of cardiopulmonary bypass circuit with new polymer Senko E-Ternal Coating. *Perfusion* **30**, 572–579 (2015).

67. Teligui, L. *et al.* An ex vivo evaluation of blood coagulation and thromboresistance of two extracorporeal circuit coatings with reduced and full heparin dose. *Interact. Cardiovasc. Thorac. Surg.* **18**, 763–769 (2014).
68. Liebold, A. Biocompatibility of a new synthetic oxygenator coating (SOFTLINE COATING): A multicenter clinical evaluation. *Thorac Cardiovasc Surg* **55**, P_93 (2007).
69. Madhani, S. P., D'Aloiso, B. D., Frankowski, B. J. & Federspiel, W. J. Darcy permeability characterization of PMP hollow fiber membrane bundles. *ASAIO J.* **62**, 329–331 (2016).
70. Morales-Quinteros, L., Del Sorbo, L. & Artigas, A. Extracorporeal carbon dioxide removal for acute hypercapnic respiratory failure. *Ann. Intensive Care* **9**, (2019).
71. Boyle, A. J. *et al.* Extracorporeal carbon dioxide removal for lowering the risk of mechanical ventilation: research questions and clinical potential for the future. *Lancet Respir. Med.* **6**, 874–884 (2018).
72. Jeffries, R. G., Lund, L., Frankowski, B. & Federspiel, W. J. An extracorporeal carbon dioxide removal (ECCO2R) device operating at hemodialysis blood flow rates. *Intensive Care Med. Exp.* **5**, 1–12 (2017).
73. Arazawa, D. T., Kimmel, J. D., Finn, M. C. & Federspiel, W. J. Acidic sweep gas with carbonic anhydrase coated hollow fiber membranes synergistically accelerates CO₂ removal from blood. *Acta Biomater.* **25**, 143–149 (2015).
74. Pettenuzzo, T., Fan, E. & Del Sorbo, L. Extracorporeal carbon dioxide removal in acute exacerbations of chronic obstructive pulmonary disease. *Ann. Transl. Med.* **6**, 31–31 (2018).
75. Ki, K. K. *et al.* Low flow rate alters haemostatic parameters in an ex-vivo extracorporeal membrane oxygenation circuit. *Intensive Care Med. Exp.* **7**, (2019).
76. Trials.gov, C. Extracorporeal CO₂ Removal With the Hemolung RAS for Mechanical Ventilation Avoidance During Acute Exacerbation of COPD (VENT-AVOID). *National Institute of Medicine*

- Available at: <https://clinicaltrials.gov/ct2/show/NCT03255057>. (Accessed: 12th January 2019)
77. ALung Announces the Achievement of a Key Milestone in the U.S. Based VENT-AVOID Trial and Continued Progress Towards Completion of the Trial. *Business Wire* (2019). Available at: <https://www.businesswire.com/news/home/20190711005540/en/ALung-Announces-Achievement-Key-Milestone-U.S.-Based>. (Accessed: 12th January 2019)
 78. Lawson, D. S. *et al.* Hemolytic characteristics of three commercially available centrifugal blood pumps. *Pediatr. Crit. Care Med.* **6**, 573–577 (2005).
 79. Thompson, A. J. *et al.* A low resistance, concentric-gated pediatric artificial lung for end-stage lung failure. *J. Hear. Lung Transpl.* **37**, 1029–1034 (2018).
 80. Hamid, I. A., Hariharan, A. S. & Ravi Shankar, N. R. The advent of ECMO and pumpless extracorporeal lung assist in ARDS. *J. Emergencies, Trauma Shock* **4**, 244–250 (2011).
 81. Bein, T., Scherer, M. N., Philipp, A., Weber, F. & Woertgen, C. Pumpless extracorporeal lung assist (pECLA) in patients with acute respiratory distress syndrome and severe brain injury. *J. Trauma - Inj. Infect. Crit. Care* **58**, 1294–1297 (2005).
 82. Kopp, R. *et al.* Hemocompatibility of a miniaturized extracorporeal membrane oxygenation and a pumpless interventional lung assist in experimental lung injury. *Artif. Organs* **34**, 13–21 (2010).
 83. Fischer, S. *et al.* Bridge to lung transplantation with the novel pumpless interventional lung assist device NovaLung. *J. Thorac. Cardiovasc. Surg.* **131**, 719–723 (2006).
 84. Orizondo, R. A. *et al.* In Vitro Characterization of the Pittsburgh Pediatric Ambulatory Lung. *ASAIO J.* **64**, 806–811 (2018).
 85. Madhani, S. P., Frankowski, B. J. & Federspiel, W. J. Fiber Bundle Design for an Integrated Wearable Artificial Lung. *ASAIO J.* **63**, 631–636 (2017).
 86. May, A. G., Orizondo, R. A., Frankowski, B. J., Wearden, P. D. & Federspiel, W. J. Acute In Vivo Evaluation of the Pittsburgh Pediatric Ambulatory Lung. *ASAIO J.* **65**, 395–400 (2019).

87. Schraven, L. *et al.* Effects of Pulsatile Blood Flow on Oxygenator Performance. *Artif. Organs* **42**, 410–419 (2018).
88. Orizondo, R. A. *et al.* Effects of Hollow Fiber Membrane Oscillation on an Artificial Lung. *Ann. Biomed. Eng.* **46**, 762–771 (2018).
89. Polk, A. A. *et al.* A biohybrid artificial lung prototype with active mixing of endothelialized microporous hollow fibers. *Biotechnol. Bioeng.* **106**, 490–500 (2010).
90. Wiegmann, B. *et al.* Developing a biohybrid lung – sufficient endothelialization of poly-4-methyl-1-pentene gas exchange hollow- fiber membranes. *J. Mech. Behav. Biomed. Mater.* **60**, 301–311 (2016).
91. Iqbal, Z. *et al.* In vitro and in vivo hemocompatibility assessment of ultrathin sulfobetaine polymer coatings for silicon-based implants. *J. Biomater. Appl.* **0**, (2019).
92. Jiang, S. & Cao, Z. Ultralow-fouling, functionalizable, and hydrolyzable zwitterionic materials and their derivatives for biological applications. *Adv. Mater.* **22**, 920–932 (2010).
93. Ye, S. *et al.* Hollow Fiber Membrane Modification with Functional Zwitterionic Macromolecules for Improved Thromboresistance in Artificial Lungs. *Langmuir* **31**, 2463–2471 (2015).
94. Huang, X. *et al.* Surface monofunctionalized polymethyl pentene hollow fiber membranes by plasma treatment and hemocompatibility modification for membrane oxygenators. *Appl. Surf. Sci.* **362**, 355–363 (2016).
95. Wang, Y. B., Shi, K. H., Jiang, H. L. & Gong, Y. K. Significantly reduced adsorption and activation of blood components in a membrane oxygenator system coated with crosslinkable zwitterionic copolymer. *Acta Biomater.* **40**, 153–161 (2016).
96. Annich, G. M. *et al.* Reduced platelet activation and thrombosis in extracorporeal circuits coated with nitric oxide release polymers. *Crit. Care Med.* **28**, 915–920 (2000).
97. Frost, M. C., Rudich, S. M., Zhang, H., Maraschio, M. A. & Meyerhoff, M. E. In vivo

- biocompatibility and analytical performance of intravascular amperometric oxygen sensors prepared with improved nitric oxide-releasing silicone rubber coating. *Anal. Chem.* **74**, 5942–5947 (2002).
98. Major, T. C., Brant, D. O., Reynolds, M. M., Bartlett, R. H. & Mark, E. The attenuation of platelet and monocyte activation in a rabbit model of extracorporeal circulation by a nitric oxide releasing polymer. *Biomaterials* **31**, 2736 (2011).
 99. Skrzypchak, A. M. *et al.* Effect of varying nitric oxide release to prevent platelet consumption and preserve platelet function in an in vivo model of extracorporeal circulation. *Perfusion* **22**, 193–200 (2007).
 100. Amoako, K. A. *et al.* Fabrication and In vivo Thrombogenicity Testing of Nitric Oxide Generating Artificial Lungs. *J Biomed Mater Res A.* **101**, (2013).
 101. Lai, A. *et al.* 72-Hour in vivo evaluation of nitric oxide generating artificial lung gas exchange fibers in sheep. *Acta Biomater.* **90**, 122–131 (2019).
 102. Pflaum, M., Peredo, A. S., Dipresa, D., De, A. & Korossis, S. *Membrane bioreactors for (bio-)artificial lung. Current Trends and Future Developments on (Bio-) Membranes* **2016**, (2020).
 103. Pflaum, M. *et al.* Endothelialization and characterization of titanium dioxide-coated gas-exchange membranes for application in the bioartificial lung. *Acta Biomater.* **50**, 510–521 (2017).
 104. Zwirner, U. *et al.* Identifying an optimal seeding protocol and endothelial cell substrate for biohybrid lung development. *J. Tissue Eng. Regen. Med.* **12**, 2319–2330 (2018).
 105. Hoganson, D. M. *et al.* Branched vascular network architecture: a new approach to lung assist device technology. *J. Thorac. Cardiovasc. Surg.* **140**, 990–995 (2010).
 106. Thompson, A. J., Ma, L. J., Plegue, T. J. & Potkay, J. A. Design Analysis and Optimization of a Single Layer PDMS Microfluidic Artificial Lung. *IEEE Trans. Biomed. Eng.* (2018).
doi:10.1109/TBME.2018.2866782

107. Dabaghi, M. *et al.* An artificial placenta type microfluidic blood oxygenator with double-sided gas transfer microchannels and its integration as a neonatal lung assist device. *Biomicrofluidics* **12**, 044101 (2018).
108. Lee, J. K., Kung, M. C., Kung, H. H. & Mockros, L. F. Microchannel Technologies for Artificial Lungs: (3) Open Rectangular Channels. *ASAIO J.* **54**, 390–395 (2008).
109. Kniazeva, T., Hsiao, J. C., Charest, J. L. & Borenstein, J. T. A microfluidic respiratory assist device with high gas permeance for artificial lung applications. *Biomed. Microdevices* **13**, 315–323 (2011).
110. Kniazeva, T. *et al.* Performance and scaling effects in a multilayer microfluidic extracorporeal lung oxygenation device. *Lab Chip* **12**, 1686–1695 (2012).
111. Gimbel, A. A., Flores, E., Koo, A., Garcia-Cardena, G. & Borenstein, J. T. Development of a biomimetic microfluidic oxygen transfer device. *Lab Chip* **16**, 3227–3234 (2016).
112. Wu, W.-I. *et al.* Lung assist device: development of microfluidic oxygenators for preterm infants with respiratory failure. *Lab Chip* **13**, 2641–50 (2013).
113. Potkay, J. A., Magnetta, M., Vinson, A. & Cmolik, B. Bio-inspired, efficient, artificial lung employing air as the ventilating gas. *Lab Chip* **11**, 2901–2909 (2011).
114. Kovach, K. M. *et al.* In vitro evaluation and in vivo demonstration of a biomimetic, hemocompatible, microfluidic artificial lung. *Lab Chip* **15**, 1366–75 (2015).
115. Houston, K. ., Weinkauff, D. . & Stewart, F. . Gas transport characteristics of plasma treated poly(dimethylsiloxane) and polyphosphazene membrane materials. *J. Memb. Sci.* **205**, 103–112 (2002).
116. Firpo, G., Angeli, E., Repetto, L. & Valbusa, U. Permeability thickness dependence of polydimethylsiloxane (PDMS) membranes. *J. Memb. Sci.* **481**, 1–8 (2015).
117. Markov, D. A., Lillie, E. M., Garbett, S. P. & McCawley, L. J. Variation in diffusion of gases

- through PDMS due to plasma surface treatment and storage conditions. *Biomed. Microdevices* **16**, 91–96 (2014).
118. Merkel, T. C., Bondar, V. I., Nagai, K., Freeman, B. D. & Pinnau, I. Gas Sorption, Diffusion, and Permeation in Poly(dimethylsiloxane). *J. Polym. Sci. Part B Polym. Phys.* **38**, 415–434 (2000).
119. Thompson, A. J., Marks, L. H., Goudie, M. J. & Handa, H. A small-scale , rolled-membrane microfluidic artificial lung designed towards future large area manufacturing. *Biomicrofluidics* **11**, 024113 (2017).
120. Matharoo, H. *et al.* Steel reinforced composite silicone membranes and its integration to microfluidic oxygenators for high performance gas exchange. *Biomicrofluidics* **12**, (2018).
121. Dabaghi, M. *et al.* An Ultra-thin Highly Flexible Microfluidic Device for Blood Oxygenation. *Lab Chip* (2018). doi:10.1039/C8LC01083H
122. Rochow, N. *et al.* An integrated array of microfluidic oxygenators as a neonatal lung assist device: In vitro characterization and in vivo demonstration. *Artif. Organs* **38**, 856–866 (2014).
123. Femmer, T., Eggersdorfer, M. L., Kuehne, A. J. C. & Wessling, M. Efficient gas–liquid contact using microfluidic membrane devices with staggered herringbone mixers. *Lab Chip* **15**, 3132–3137 (2015).
124. Kovach, K. M., Capadona, J. R., Gupta, A. Sen & Potkay, J. A. The effects of PEG-based surface modification of PDMS microchannels on long-term hemocompatibility. *J. Biomed. Mater. Res. - Part A* **102**, 4195–4205 (2014).
125. Plegue, T. J., Kovach, K. M., Thompson, A. J. & Potkay, J. A. Stability of Polyethylene Glycol and Zwitterionic Surface Modi fi cations in PDMS Micro fl uidic Flow Chambers. *Langmuir* **34**, 492–502 (2018).
126. Dietrich, M. *et al.* ENDOXY - Development of a Biomimetic Oxygenator-Test-Device. *PLoS One* **10**, e0142961 (2015).

127. Klein, S. *et al.* EndOxy: Dynamic Long-Term Evaluation of Endothelialized Gas Exchange Membranes for a Biohybrid Lung. *Ann. Biomed. Eng.* (2019). doi:10.1007/s10439-019-02401-2
128. Roy, S. *et al.* Silicon nanopore membrane technology for an implantable artificial kidney. in *TRANSDUCERS 2009 - 15th International Conference on Solid-State Sensors, Actuators and Microsystems* 755–760 (2009). doi:10.1109/SENSOR.2009.5285603
129. Conlisk, A. T., Datta, S., Fissell, W. H. & Roy, S. Biomolecular transport through hemofiltration membranes. *Ann. Biomed. Eng.* **37**, 722–736 (2009).
130. Fissell, W. H., Fleischman, A. J., Humes, H. D. & Roy, S. Development of continuous implantable renal replacement: past and future. *Transl. Res.* **150**, 327–336 (2007).
131. Fissell, W. H. *et al.* High-performance silicon nanopore hemofiltration membranes. *J. Memb. Sci.* **326**, 58–63 (2009).
132. Yeager, T. High Efficiency Asymmetric Membranes for Extracorporeal Membrane Oxygenation. (University of California, San Francisco, 2017).
133. Feinberg, B. J. *et al.* Silicon nanoporous membranes as a rigorous platform for validation of biomolecular transport models. *J. Memb. Sci.* **536**, 44–51 (2017).
134. Kanani, D. M. *et al.* Permeability-selectivity analysis for ultrafiltration: Effect of pore geometry. *J. Memb. Sci.* **349**, 405–410 (2010).
135. Kim, S. *et al.* Diffusive Silicon Nanopore Membranes for Hemodialysis Applications. *PLoS One* **11**, (2016).
136. Kim, S. *et al.* Preliminary Diffusive Clearance of Silicon Nanopore Membranes in a Parallel Plate Configuration for Renal Replacement Therapy. *ASAIO J.* 169–175 (2015).
doi:10.1097/MAT.0000000000000311
137. Kensinger, C. *et al.* First Implantation of Silicon Nanopore Membrane Hemofilters. *ASAIO J.* 1 (2016). doi:10.1097/MAT.0000000000000367

138. Song, S. *et al.* Silicon nanopore membrane (SNM) for islet encapsulation and immunoisolation under convective transport. *Sci. Rep.* **6**, 1–9 (2016).
139. Song, S. *et al.* An intravascular bioartificial pancreas device (iBAP) with silicon nanopore membranes (SNM) for islet encapsulation under convective mass transport. *Lab Chip* **17**, 1778–1792 (2017).
140. Jayagopal, A. In Vitro Modeling of the Kidney for Drug Transport and Toxicity Testing. (2017).
141. Iqbal, Z. *et al.* Sterilization effects on ultrathin film polymer coatings for silicon-based implantable medical devices. *J. Biomed. Mater. Res. Part B Appl. Biomater.* **00B**, 000–000 (2017).
142. Li, L., Marchant, R. E., Dubnisheva, A., Roy, S. & Fissell, W. H. Anti-biofouling Sulfobetaine Polymer Thin Films on Silicon and Silicon Nanopore Membranes. *J. Biomater. Sci. Polym. Ed.* **22**, 91–106 (2011).
143. Dharia, A. *et al.* Silicon Micropore-Based Parallel Plate Membrane Oxygenator. *Artif. Organs* **42**, 166–173 (2017).
144. Fissell, W. H. *et al.* High Knudsen number fluid flow at near-standard temperature and pressure conditions using precision nanochannels. *Microfluid Nanofluid* 425–433 (2011).
doi:10.1007/s10404-010-0682-4
145. Yeager, T., Kant, R., Goldman, K., Fissell, W. & Roy, S. Planar PDMS/Silicon Asymmetric Membranes for Extracorporeal Membrane Oxygenation. *ASAIO 59th Annu. Conf. Abstr.* 67 (2013).
146. Kaesler, A. *et al.* Experimental Approach to Visualize Flow in a Stacked Hollow Fiber Bundle of an Artificial Lung With Particle Image Velocimetry. *Artif. Organs* **41**, 529–538 (2017).
147. Technologies, Al. About the Hemolung RAS. (2019). Available at:
<https://www.alung.com/hemolung-ras-us/>. (Accessed: 12th April 2019)
148. Vaquer, S., Haro, C. De, Peruga, P., Oliva, J. C. & Artigas, A. Systematic review and meta -

- analysis of complications and mortality of veno - venous extracorporeal membrane oxygenation for refractory acute respiratory distress syndrome. *Ann. Intensive Care* **7**, 51 (2017).
149. Brown, K. L. & Goldman, A. P. Neonatal extra-corporeal life support : Indications and limitations. *Early Hum. Dev.* **84**, 143–148 (2008).
 150. Gaffney, A. M., Wildhirt, S. M., Griffin, M. J., Annich, G. M. & Radomski, M. W. Extracorporeal life support. *Br. Med. J.* **341**, c5317 (2010).
 151. Kanani, D. M., Fissell, W. H., Roy, S., Dubnisheva, A. & Zydney, A. L. Permeability - Selectivity Analysis for Ultrafiltration: Effect of Pore Geometry. *J. Memb. Sci.* **349**, 1–13 (2010).
 152. Smith, R. A., Fleischman, A. J., Fissell, W. H., Zorman, C. A. & Roy, S. A system to measure minute hydraulic permeability of nanometer scale devices in a non-destructive manner. *Meas. Sci. Technol.* **22**, 045802 (2011).
 153. Zeman, L. Characterization of microfiltration membranes by image analysis of electron micrographs . Part II . Functional and morphological parameters. *J. Memb. Sci.* **71**, 233–246 (1992).
 154. Morley, S. W., Bieniek, P. & Rosenberg, M. METHOD AND SYSTEM FOR PURGING MOISTURE FROM AN OXYGENATOR. (2013).
 155. Alexander, J. V, Neely, J. W. & Grulke, E. A. Effect of Chemical Functionalization on the Mechanical Properties of Polypropylene Hollow Fiber Membranes. *J. Polym. Sci. Part B Polym. Phys.* **52**, 1366–1373 (2014).
 156. Potkay, J. A. A simple, closed-form, mathematical model for gas exchange in microchannel artificial lungs. *Biomed. Microdevices* **15**, 397–406 (2013).
 157. Paden, M. L., Conrad, S. a, Rycus, P. T. & Thiagarajan, R. R. Extracorporeal Life Support Organization Registry Report 2012. *ASAIO J.* **59**, 202–10 (2013).
 158. Gerke, A. K., Tang, F., Cavanaugh, J. E., Doerschug, K. C. & Polgreen, P. M. Increased trend in

- extracorporeal membrane oxygenation use by adults in the United States since 2007. *BMC Res. Notes* **8**, 686 (2015).
159. Esper, S. A., Levy, J. H., Waters, J. H. & Welsby, I. J. Extracorporeal membrane oxygenation in the adult: a review of anticoagulation monitoring and transfusion. *Anesth. Analg.* **118**, 731–43 (2014).
160. Abada, E. N., Feinberg, B. J. & Roy, S. Evaluation of silicon membranes for extracorporeal membrane oxygenation (ECMO). *Biomed. Microdevices* **20**, (2018).
161. Vaslef, S. N., Mockros, L. F., Anderson, R. W. & Leonard, R. J. Use of a mathematical model to predict oxygen transfer rates in hollow fiber membrane oxygenators. *ASAIO J.* **40**, 990–6
162. Hewitt, T. J., Hattler, B. G. & Federspiel, W. J. A mathematical model of gas exchange in an intravenous membrane oxygenator. *Ann. Biomed. Eng.* **26**, 166–78 (1998).
163. Fournier, R. L. *Basic transport phenomena in biomedical engineering*. (CRC Press, 2011).
164. Schock, G. & Miquel, A. Mass transfer and pressure loss in spiral wound modules. *Desalination* **64**, 339–352 (1987).
165. Spaeth, E. E. & Friedlander, S. K. The diffusion of oxygen, carbon dioxide, and inert gas in flowing blood. *Biophys. J.* **7**, 827–51 (1967).
166. Lee, C. Y., Wang, W. T., Liu, C. C. & Fu, L. M. Passive mixers in microfluidic systems: A review. *Chemical Engineering Journal* **288**, 146–160 (2016).
167. Parvizian, F., Rahimi, M., Hosseini, S. M., Madaeni, S. S. & Alsairafi, A. A. The effect of high frequency ultrasound on diffusion boundary layer resistance in ion-exchange membrane transport. *Desalination* **286**, 155–165 (2012).
168. Mata, A., Fleischman, A. J. & Roy, S. Characterization of Polydimethylsiloxane (PDMS) Properties for Biomedical Micro / Nanosystems. *Biomed. Microdevices* **7**, 281–293 (2005).
169. Abbasi, F., Mirzadeh, H. & Katbab, A.-A. Modification of polysiloxane polymers for biomedical

- applications: a review. *Polym. Int.* **50**, 1279–1287 (2001).
170. Epshteyn, A. A., Flores, E., Koo, A., Garcia-Cardena, G. & Borenstein, J. T. Development of a Biomimetic Microfluidic Oxygen Transfer Device. *Lab Chip* **16**, 3227–3234 (2016).
 171. Murakami, T., Kuroda, S. & Osawa, Z. Dynamics of Polymeric Solid Surfaces Treated with Oxygen Plasma : Effect of Aging Media after Plasma Treatment. *J. Colloid. Interface Sci.* **202**, 37–44 (1998).
 172. Zhang, Z. *et al.* Polybetaine modification of PDMS microfluidic devices to resist thrombus formation in whole blood. *Lab Chip* **13**, 1963–8 (2013).
 173. Ellis, A. V. Recent developments in PDMS surface modification for microfluidic devices. *Electrophoresis* **31**, 2–16 (2010).
 174. Zhang, H. & Chiao, M. Anti-fouling coatings of poly(dimethylsiloxane) devices for biological and biomedical applications. *J. Med. Biol. Eng.* **35**, 143–155 (2015).
 175. Hillborg, H. *et al.* Crosslinked polydimethylsiloxane exposed to oxygen plasma studied by neutron reflectometry and other surface specific techniques. *Polymer (Guildf)*. **41**, 6851–6863 (2000).
 176. Bodas, D. & Khan-malek, C. Hydrophilization and hydrophobic recovery of PDMS by oxygen plasma and chemical treatment — An SEM investigation. *Sensors Actuators B* **123**, 368–373 (2007).
 177. Eddington, D. T., Puccinelli, J. P. & Beebe, D. J. Thermal aging and reduced hydrophobic recovery of polydimethylsiloxane. *Sensors Actuators B* **114**, 170–172 (2006).
 178. Hemmilä, S., Cauich-rodríguez, J. V, Kreutzer, J. & Kallio, P. Rapid, simple, and cost-effective treatments to achieve long-term hydrophilic PDMS surfaces. *Appl. Surf. Sci.* **258**, 9864–9875 (2012).
 179. Yeh, S. B., Chen, C. S., Chen, W. Y. & Huang, C. J. Modification of silicone elastomer with zwitterionic silane for durable antifouling properties. *Langmuir* **30**, 11386–11393 (2014).

180. Keefe, A. J., Brault, N. D. & Jiang, S. Suppressing Surface Reconstruction of Superhydrophobic PDMS Using a Superhydrophilic Zwitterionic Polymer. (2012).
181. Zhang, Z. *et al.* Surface modification of PDMS by surface-initiated atom transfer radical polymerization of water-soluble dendronized PEG methacrylate. *Colloids Surfaces B Biointerfaces* **88**, 85–92 (2011).
182. Riedel, T. *et al.* Complete identification of proteins responsible for human blood plasma fouling on poly(ethylene glycol)-based surfaces. *Langmuir* **29**, 3388–3397 (2013).
183. Zhang, M., Desai, T. & Ferrari, M. Proteins and cells on PEG immobilized silicon surfaces. *Biomaterials* **19**, 953–960 (1998).
184. Uthsubramaniam, L. A. M. *et al.* Hemocompatibility of Silicon-Based Substrates for Biomedical Implant Applications. *Ann. Biomed. Eng.* **39**, 1296–1305 (2011).
185. Kim, J., Chaudhury, M. K. & Owen, M. J. Hydrophobic Recovery of Polydimethylsiloxane Elastomer Exposed to Partial Electrical Discharge. *J. Colloid. Interface Sci.* **226**, 231–236 (2000).
186. Bodas, D., Rauch, J. Y. & Khan-Malek, C. Surface modification and aging studies of addition-curing silicone rubbers by oxygen plasma. *Eur. Polym. J.* **44**, 2130–2139 (2008).
187. Mills, K. L., Zhu, X., Takayama, S. & Thouless, M. D. The mechanical properties of a surface-modified layer on poly (dimethylsiloxane). *J Mater Res.* **23**, 37–48 (2009).
188. Meng, Y., Li, Z. B., Chen, X. & Chen, J. P. Reducing wrinkles and cracks of metal films on PDMS substrate by hexane extraction and oxygen plasma etching. *Microelectron. Eng.* **130**, 8–12 (2014).
189. Liu, M., Sun, J., Sun, Y., Bock, C. & Chen, Q. Thickness-dependent mechanical properties of polydimethylsiloxane membranes. *J. Micromech. Microeng.* **19**, 035028 (2009).
190. Papra, A., Gadegaard, N. & Larsen, N. B. Characterization of Ultrathin Poly (ethylene glycol) Monolayers on Silicon Substrates. *Langmuir* **17**, 1457–1460 (2001).

191. Wen, K. *et al.* Postassembly Chemical Modification of a Highly Ordered Organosilane Multilayer: New Insights into the Structure, Bonding, and Dynamics of Self-Assembling Silane Monolayers. *ACS Nano* **2**, 579–599 (2008).
192. Maoz, R. & Sagiv, J. Hydrogen-bonded multilayers of self-assembling silanes: structure elucidation by combined Fourier transform infra-red spectroscopy and X-ray scattering techniques. *Supramol. Sci.* **2**, 9–24 (1995).
193. Wang, A., Tang, H., Cao, T., Salley, S. O. & Ng, K. Y. S. In vitro stability study of organosilane self-assemble monolayers and multilayers. *J. Colloid. Interface Sci.* **291**, 438–447 (2005).
194. Vickers, J. A., Caulum, M. M. & Henry, C. S. Generation of Hydrophilic Poly (dimethylsiloxane) for High-Performance Microchip Electrophoresis. *Anal. Chem.* **78**, 7446–7452 (2006).
195. Efimenko, K., Wallace, W. E. & Genzer, J. Surface Modification of Sylgard-184 Poly (dimethyl siloxane) Networks by Ultraviolet and Ultraviolet / Ozone Treatment. *J. Colloid. Interface Sci.* **254**, 306–315 (2002).
196. Hendricks, T. R., Wang, W. & Lee, I. Buckling in nanomechanical films. *Soft Matter* **6**, 3701–3706 (2010).
197. Song, J. *et al.* Buckling of a stiff thin film on a compliant substrate in large deformation. *Int. J. Solids Struct.* **45**, 3107–3121 (2008).
198. Chen, C. & Yang, S. Wrinkling instabilities in polymer films and their applications. *Polym. Int.* **61**, 1041–1047 (2012).
199. Blummel, J. *et al.* Protein repellent properties of covalently attached PEG coatings on nanostructured SiO₂ -based interfaces. *Biomaterials* **28**, 4739–4747 (2007).
200. Mei, H., Huang, R., Chung, J. Y., Stafford, C. M. & Yu, H.-H. Buckling modes of elastic thin films on elastic substrates. *Appl. Phys. Lett.* **90**, 151902 (2007).
201. Iqbal, Z. Ultrathin Zwitterionic Polymer Coatings to Improve Hemocompatibility for Silicon-

- based Implantable Medical Devices. (2018).
202. Thorslund, S., Sanchez, J., Larsson, R., Nikolajeff, F. & Bergquist, J. Functionality and stability of heparin immobilized onto poly(dimethylsiloxane). *Colloids Surfaces B Biointerfaces* **45**, 76–81 (2005).
 203. Rajagopal, K. & Hoepfer, M. M. State of the Art: Bridging to lung transplantation using artificial organ support technologies. *J. Hear. Lung Transplant.* **35**, 1385–1398 (2016).
 204. Ko, Y. J. *et al.* Feasibility and safety of early physical therapy and active mobilization for patients on extracorporeal membrane oxygenation. *ASAIO J.* **61**, 564–568 (2015).
 205. Madhani, S. P. *et al.* In Vivo 5 Day Animal Studies of a Compact, Wearable Pumping Artificial Lung. *ASAIO J.* 1 (2017). doi:10.1097/MAT.0000000000000740
 206. Akiyama, D. *et al.* Development of an ultra compact durable ECMO system and evaluation in a chronic animal experiment for 4 weeks. *J. Hear. Lung Transplant.* **37**, S262 (2018).
 207. Wu, Z. J. *et al.* Thirty-day in-vivo performance of a wearable artificial pump-lung for ambulatory respiratory support. *Ann. Thorac. Surg.* **93**, 274–281 (2012).
 208. Hendrix, R. H. J., Ganushchak, Y. M. & Weerwind, P. W. Contemporary Oxygenator Design: Shear Stress-Related Oxygen and Carbon Dioxide Transfer. *Artif. Organs* **42**, 611–619 (2018).
 209. Luelf, T., Tepper, M., Breisig, H. & Wessling, M. Sinusoidal shaped hollow fibers for enhanced mass transfer. *J. Memb. Sci.* **533**, 302–308 (2017).
 210. Bellhouse, B. J. *et al.* A High Efficiency Membrane Oxygenator and Pulsatile Pumping System, and its Application to Animal Trials.
 211. Neußer, C., Bach, C., Doeringer, J. & Jockenhoevel, S. Processing of membranes for oxygenation using the Bellhouse-effect. *Curr. Dir. Biomed. Eng.* **1**, 108–111 (2015).
 212. Mockros, L. F. Artificial lung design : sheet-membrane units *. 425–435 (1975).
 213. Galletti, P. M. Applications of plastics in membrane oxygenators. *J. Biomed. Mater. Res.* **5**, 129–

- 134 (1971).
214. Li, F., Meindersma, W., De Haan, A. B. & Reith, T. Optimization of commercial net spacers in spiral wound membrane modules. *J. Memb. Sci.* **208**, 289–302 (2002).
215. Kolobow, T. Artificial organ for membrane dialysis of biological fluids. (1970).
216. Housman, L. B. & Braunwald, N. S. Experimental Evaluation of the Travenol and Landé-Edwards Membrane Oxygenators for Use in Neonate Perfusions. *Ann. Thorac. Surg.* **14**, 150–158 (1972).
217. Shimono, T. *et al.* Silicone-Coated Polypropylene Hollow-Fiber Oxygenator: Experimental Evaluation and Preliminary Clinical Use. *Ann Thorac Surg* **63**, 1730–6 (1997).
218. Siddiqui, A. *et al.* Porosity of spacer-filled channels in spiral-wound membrane systems: Quantification methods and impact on hydraulic characterization. *Water Res.* **119**, 304–311 (2017).
219. Douglas, AR; Jones, NL; Reed, J. Calculation of whole blood CO₂ content. *J Appl Physiol* **65**, 473–477 (1988).
220. Guan, Y. *et al.* Evaluation of Quadrox-i adult hollow fiber oxygenator with integrated arterial filter. *J. Extra. Corpor. Technol.* **42**, 134–138 (2010).
221. Federspiel, W. J. & Hattler, B. G. Sweep gas flowrate and CO₂ exchange in artificial lungs. *Artif. Organs* **20**, 1050–1052 (1996).
222. Alghanem, F. *et al.* Pediatric Artificial Lung: A Low-Resistance Pumpless Artificial Lung Alleviates an Acute Lamb Model of Increased Right Ventricle Afterload. *ASAIO J.* **63**, 223–228 (2017).
223. Borenstein, J. T., Charest, J. L., Dibiasio, C. & Finley, V. MICROFLUDIC ORGAN ASSIST DEVICE INCORPORATING BOUNDARY LAYER DISRUPTERS. US 9,597,441 B2 (2017).
224. Gaylor, J. D. S. & Mockros, L. F. Artificial-lung design: Sheet-membrane units. *Med. Biol. Eng.* **13**, 425–435 (1975).

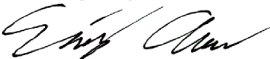
225. Wu, W. *et al.* Development of Microfluidic Oxygenators as Lung Assisting Devices for Preterm Infants. *15th Int. Conf. Miniaturized Syst. Chem. Life Sci.* 550–552 (2011).
226. Lehle, K. *et al.* Efficiency in extracorporeal membrane oxygenation-cellular deposits on polymethylpentene membranes increase resistance to blood flow and reduce gas exchange capacity. *ASAIO J.* **54**, 612–617 (2008).
227. Kuo, W. H. *et al.* Surface modification with poly(sulfobetaine methacrylate-co-acrylic acid) to reduce fibrinogen adsorption, platelet adhesion, and plasma coagulation. *Biomacromolecules* **12**, 4348–4356 (2011).
228. Ye, S. H. *et al.* Hollow fiber membrane modification with functional zwitterionic macromolecules for improved thromboresistance in artificial lungs. *Langmuir* **31**, 2463–2471 (2015).
229. Yue, Z., Liu, X., Molino, P. J. & Wallace, G. G. Bio-functionalisation of polydimethylsiloxane with hyaluronic acid and hyaluronic acid - Collagen conjugate for neural interfacing. *Biomaterials* **32**, 4714–4724 (2011).
230. Demirel, G., Çağlayan, M. O., Garipcan, B., Duman, M. & Pişkin, E. Formation and organization of amino terminated self-assembled layers on Si(001) surface. *Nanoscale Res. Lett.* **2**, 350–354 (2007).

Publishing Agreement

It is the policy of the University to encourage the distribution of all theses, dissertations, and manuscripts. Copies of all UCSF theses, dissertations, and manuscripts will be routed to the library via the Graduate Division. The library will make all theses, dissertations, and manuscripts accessible to the public and will preserve these to the best of their abilities, in perpetuity.

Please sign the following statement:

I hereby grant permission to the Graduate Division of the University of California, San Francisco to release copies of my thesis, dissertation, or manuscript to the Campus Library to provide access and preservation, in whole or in part, in perpetuity.

DocuSigned by:

EC77DC25735B4DD...

Author Signature

12/6/2019

Date